Wireless Power Transfer for Implantable Medical Devices

Wireless Power Transfer for Implantable Medical Devices
High-Power and Midfield Considerations

PROEFSCHRIFT

ter verkrijging van de graad van doctor aan de
Technische Universiteit Eindhoven, op gezag van de
rector magnificus, prof.dr.ir. F. P. T. Baaijens, voor een
commissie aangewezen door het College voor
Promoties in het openbaar te verdedigen op
dinsdag 8 februari 2023 om 16:00 uur

door

Thomas Petrus Gerardus van Nunen

geboren te Helmond

Dit proefschrift is goedgekeurd door de promotoren en de samenstelling van de promotiecommissie is als volgt:

voorzitter:	prof.dr.ir. A.B. Smolders
1e promotor:	prof.dr.ir. H. J. Visser
2e promotor:	prof.dr.ir. M. J. Bentum
copromotor:	dr.ir. R. M. C. Mestrom
leden:	prof.dr. P. D. Mitcheson (Imperial College London)
	prof.dr.ir. W. A. Serdijn (Technische Universiteit Delft)
	prof.dr.ir. P. G. M. Baltus
adviseur:	prof.dr. P. Roelfsema (Netherlands Institute for Neuroscience)

Het onderzoek of ontwerp dat in dit proefschrift wordt beschreven is uitgevoerd in overeenstemming met de TU/e Gedragscode Wetenschapsbeoefening.

Wireless Power Transfer for Implantable Medical Devices
High-power and midfield considerations
T.P.G. van Nunen
Technische Universiteit Eindhoven, 2023

A catalogue record is available from the Eindhoven University of Technology Library
ISBN: 978-90-386-5663-2
NUR: 959

This work was performed in the Electromagnetics group of the Eindhoven University of Technology.

This research is supported by the Dutch Technology Foundation STW, which is part of the Netherlands Organization for Scientific Research (NWO), project 5 of the NESTOR program (P15-42).

This thesis was prepared with the LaTeX 2ε documentation system
Reproduction: Ipskamp printing B.V., Enschede, The Netherlands
Cover: Design by T.P.G. van Nunen, inspired by the album cover of Inside Out by Michael Giacchino, and by the AIVD Kerstpuzzel. Hint: BROWN = WHITE. Good luck!

To those who have taught valuable life lessons
in the most unexpected ways

Contents

Summary

Globally, more than 43 million people are blind. Over the last 30 years, the blind population increased by roughly 50%, and a similar growth is foreseen for the coming 30 years. The global annual cost of blindness (COB) is tens of billions of dollars per year. The majority of the blind population was born with normal sight, and lost its sight throughout their life through medical causes or accidents. In most of these cases, the visual cortex in the brain is still capable of interpreting electrical signals, but the eyes or the connection between the eyes and the visual cortex are damaged or lost.

It is known that electrical stimulation of the visual cortex can lead to the perception of visual stimuli, called phosphenes, even in blind individuals. By establishing a connection between an external image source, such as a camera, and electrodes implanted in the visual cortex, a blind individual can experience a crude form of vision with these phosphenes. The NESTOR project, of which the research described in this thesis is part, aims to create such a visual prosthesis.

In this thesis, the design of a class-E/DE wireless power transfer (WPT) link is described, with a focus on the application in implantable medical devices (IMDs). A complete set of design equations is presented. This design process is applied to a case study for which a WPT link for the NESTOR project is designed; one that transfers 80 mW, operating at 6.78 MHz. The design is simulated in a circuit simulator, and a prototype is manufactured and verified. The match between the simulations and the measurements is considered acceptable. The total system efficiency, including oscillator and gate driver, is 39.1 and 56.6%. The system tolerates misalignments up to 16 mm for realistic implantation depths. Thermal and full-wave electromagnetic (EM) simulations are used to show compliance with (medical) standards IEEE Std C95.1, ICNIRP, ETSI EN 303 417, EN-45502-1, and ISO 14708-3.

Validation of electronics intended for use in or near the human body should be performed in a realistic environment, as the presence of tissue can have a significant impact on the behavior. Biomedical phantoms can be used to create such a tissue-mimicking environment quickly, cheaply, and reliably. It is required that their dielectric properties are in the correct range and remain constant for an extended period of time. This thesis presents recipes for several biomedical phantoms that can be generated using standard kitchen equipment using commonly available ingredients that are safe to handle. Their dielectric properties are measured from 4 MHz to 20 GHz, using a commercial probe, and remain stable for at least 10 days. The influence of the different ingredients on the (dielectric) properties is discussed. To measure the dielectric properties, the design of a cheap and simple dielectric probe is presented, made from a piece of solid-screen coaxial cable. Its performance is compared to a commercial probe.

For certain experiments, using one homogeneous type of biomedical phantom might be sufficient. In other cases, however, it might be beneficial to increase the level of detail to achieve a more realistic environment. One approach is to add artificial bones to the phantom, for example created with 3D-printing technology. This thesis presents the dielectric properties of several commercially available 3D-printing filaments, measured from 4 MHz to 20 GHz, using a commercial probe. Some of these materials have dielectric properties that are close to those of bone for certain frequency bands, and can thus be used in biomedical experiments.

Miniaturization is an ongoing trend in the development of IMDs. Nowadays, IMDs with sizes in the order of 1 mm^3 or less are becoming available, enabling new areas of application. As batteries are too large in this case, WPT is required. For cases where the receiver size is much smaller than the implant depth, research suggests that WPT at GHz frequencies is more efficient than at the commonly used MHz frequencies. This operation regime is called midfield wireless power transfer (MF-WPT), where power is transferred using propagating waves, rather than inductively, using evanescent waves. However, as the efficiency is inherently very low in these cases, it is interesting to investigate at which frequencies the most power can be received while staying below the specific absorption rate (SAR) limits. This thesis describes two analytical models that can be used to answer this question.

These models can be used to calculate the EM fields generated by a magnetic point dipole (MPD) located near or inside lossy medium, such as the human body. The first model is limited to two half spaces, i.e. air and tissue, with the MPD located in either one of them. The second model generalizes this to an arbitrary number of layers, with the MPD located in any layer. The two outer layers are half spaces, and all layers are planar. The former model is more limited in terms of applicability, but is simpler to implement. The models execute in seconds to minutes, depending on the number of layers, the frequency, and the required spatial resolution, making them considerably faster than (commercial) full-wave EM solvers, and thus very suitable for rapid design iteration. The fields generated by the analytical models are compared to those generated by the commercial full-wave solver Simulia CST Studio Suite®, for frequencies ranging from 100 kHz to 5 GHz. The average differences are below 9% (typically below 4%), with just a few exceptions.

This thesis also describes how the models are extended to calculate the generated SAR, received power, and total dissipated power in the tissue. These data can be used to determine the maximum transmit power such that the SAR safety limits are not exceeded. This can then be used to determine the maximum power that can be received by a mm-sized implant located multiple cm inside the human body, as well as the corresponding transfer efficiency. Both were calculated for frequencies ranging from 10 kHz to 10 GHz. It turns out that both the highest received power and the highest transfer efficiency are found at 10 kHz, the lowest frequency investigated. Additionally, the performance is approximately equal for frequencies up to 300 kHz; the difference is less than 4%.

Acronyms

ASA	acrylate styrene acrylonitrile
CI	cochlear implant
COB	cost of blindness
COTS	commercial off-the-shelf
CSF	cerebro-spinal fluid
DBS	deep brain stimulation
DC	direct current
EM	electromagnetic
EMI	electromagnetic interference
EPD	electric point dipole
ESR	equivalent series resistance
FD	finite difference
FDA	Food and Drug Administration
FDM	fused deposition modeling
FEM	finite element method
FFF	fused filament fabrication
FFT	fast Fourier transform
GaN	gallium nitride
HMD	horizontally oriented magnetic point dipole
ICD	implantable cardioverter defibrillator
IMD	implantable medical device
ISM	industrial, scientific and medical
LVAD	left ventricular assist device

MF-WPT	midfield wireless power transfer
MPD	magnetic point dipole
MPL	maximum power on the load
MPTE	maximum power transfer efficiency
MRI	magnetic resonance imaging
MWR	millimeter wave radar
MWT	microwave tomography
PC	personal computer
PCB	printed circuit board
PEC	perfect electric conductor
PETG	polyethylene terephthalate glycol
PLA	polylactic acid
PML	perfectly matched layer
PTC	perfect thermal conductor
PTE	power transfer efficiency
RMS	root mean square
Rx	receiver
SAR	specific absorption rate
SLA	stereolithography apparatus
SRF	self-resonance frequency
TSL	tissue simulating liquid
TU/e	Eindhoven University of Technology
Tx	transmitter
VMD	vertically oriented magnetic point dipole
VNA	vector network analyser
WPT	wireless power transfer
ZDS	zero-derivative switching
ZVS	zero-voltage switching

Chapter one

Introduction

1.1 Societal impact of visual impairment

Reading these words in a book or on a screen, finding a place to sit down, maneuvering through a building, traveling to the supermarket or to your work or studies; these activities probably sound very trivial to you and many people around you. Nevertheless, there is a significant amount of people for whom even these kinds of activities pose a big challenge.

Globally, over 43 million people are blind. Between 1990 and 2020, the blind population increased by just over 50%. By the year 2050, the total number of blind people is expected to have reached 61 million [19].

In more than 90% of the blind population, blindness is caused by (age-related) disease, rather than being congenital [19, 59, 73, 205]. There are substantial regional differences in prevalence of blindness, which can be over twelve times lower in high-income regions compared to lesser developed regions. Common causes of blindness are cataract, uncorrected refractive error, macular degeneration, glaucoma, and diabetic retinopathy. Whilst the precise distribution of causes differs per region, the above conditions account for 71% of the blind population worldwide [59, 132], with regional prevalence ranging from 52% in North Africa and Middle East, to 82% in South Asia.

Blindness has a range of effects on both the daily life of the individual, and on society in general, such as decreased chances on the job market and productivity loss, increased dependence on others, difficulties in engaging in social activities, increased chance of subthreshold depression and anxiety, increased chance in mortality, and a general decrease in (health-related) quality of life [51, 84, 132, 214, 237]. According to research conducted in the US, losing visual acuity is considered one of the four worst things that could happen to someone [58], and is feared more than the loss of memory, hearing, or speech.

Already in the year 2000, the global cost of blindness (COB), or loss of productivity, was estimated to be US$ 19 billion per year. In 2011, the combined COB of nine sample countries (Japan, Brazil, Nigeria, United States, Mexico, Pakistan, Honduras, Australia, Malaysia) was estimated to be between US$ 8 and 22 billion per year, depending on the method of estimation used [51]. Even though prevalence of blindness is higher in developing countries, the per capita COB is higher in high-income countries. With the increasing prevalence of blindness, as discussed above, it can safely be assumed that the current worldwide COB is several tens of billions of dollars per year.

1.2 Artificial vision for the blind

In normally sighted individuals, light that enters the eye and hits the retina, is converted into electric pulses that exit the eye through the optic nerve. These pulses travel through the visual pathway and arrive in the primary visual cortex, as depicted in Figure 1.1. From there, they are transmitted to deeper regions of the visual cortex, and to other parts of the brain to integrate with other inputs, such as memory. Eventually, this allows the individual to experience the surrounding environment and to act accordingly [237].

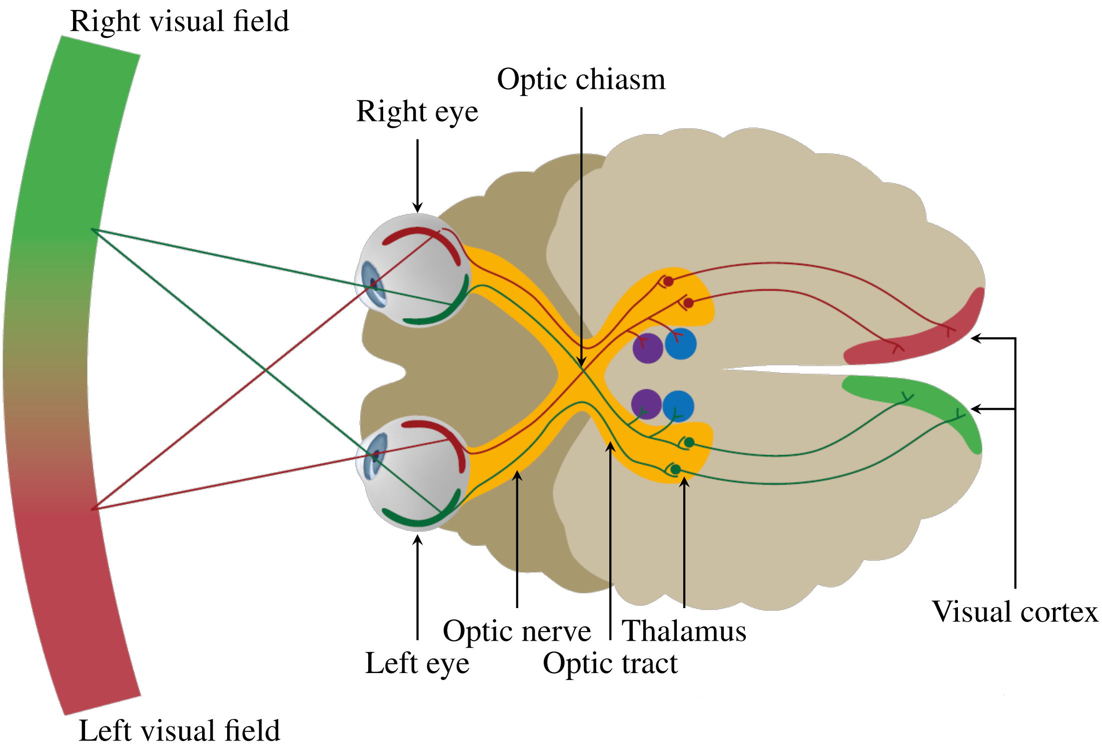

Figure 1.1: Simplified representation of the visual pathway, where electric impulses travel from the eyes through the optic nerve to the primary visual cortex. Figure adapted from [237].

When the eyes or optic nerves are severely damaged, either by natural causes or trauma, the situation might occur where electric pulses are no longer generated in the eye, or where these pulses are unable to reach the visual cortex. In that case, the individual no longer experiences visual stimuli, and can be considered blind.

Already in the 18th century, Benjamin Franklin discussed the idea that electrical current could be used to restore vision in blind individuals [231]. Indeed, the fact that electric pulses no longer arrive at the visual cortex does not imply that the visual cortex is unable to interpret these pulses. In fact, electrical activity in the visual cortex can still be perceived by the individual. Experiments in rats [170], cats [222], monkeys [26, 215], and humans [18, 45, 46] have shown that electrical stimulation of the retina or primary visual cortex leads to the perception of small dots of light, called ‘phosphenes’. This implies that it is possible to create artificial vision for the blind, where the signals generated by an external camera are transmitted to implanted electronics that are connected to, for example, the retina or visual cortex, effectively bypassing the damaged parts of the visual pathway. Each implanted electrode corresponds to one phosphene that can be individually controlled. By eliciting phosphenes in certain patterns, based on the camera image, the patient can experience the surrounding environment again, albeit in a crude fashion. Some form of image processing is required [137] to adopt the multi-megapixel image from the camera to the limited number of phosphenes that can be generated, which currently ranges from below one hundred to several thousand.

We can distinguish several main approaches in the implementation of artificial vision [132, 191, 194], of which two have received the vast majority of recent research: cortical implants [18, 26, 33, 45, 46, 153, 184], and retinal implants [48]. The latter can be further divided into epiretinal [25, 123, 140, 185], subretinal [197, 206], and suprachoroidal transretinal [9, 108, 222] implants.

Cortical implants stimulate the visual cortex directly. Stimulation can happen through surface electrodes, or intracortical electrodes. The latter are much smaller and activate a smaller part of the cortex, resulting in a reduction in the current required to elicit a phosphene of about two orders of magnitude, in less interference between adjacent electrodes, and in smaller phosphenes, enabling a higher spatial resolution [26, 153]. The fact that this method does not rely on the functioning of any other part of the visual pathway makes it the approach with the largest range of applicability. There is a known relation between the location in the primary visual cortex and the location in the visual field, making it relatively easy to determine suitable locations to place the electrodes. The surface area of the V1 region of the visual cortex is between 12 and 40 cm^2 [16], which is much larger than the surface area of the macula, which measures less than 24 mm^2 [142]. This means more electrodes can be used and these can be positioned more precisely, resulting in an accuracy which outperforms that of the retinal implants. However, the surgery required is much more severe, leading to an increased risk of complications and longer recovery times. Furthermore, one of the main challenges is to prevent deterioration of the electrode-brain interface and encapsulation of the electrodes and wires [14, 132, 146, 187, 191].

Retinal implants have received most attention of any type of visual prosthesis over the past years, and some have even been approved for commercial use [140, 167]. They are placed in the eye, where they stimulate the retina with (arrays of) electrodes. These electrodes are relatively easy to implant. There is a known relation between the location on the retina and the location in the visual field, making it relatively easy to determine suitable locations to place the electrodes. However, the limited size of the retina (in particular the macula) means that the electrodes should be sufficiently small and have a high density in order to obtain high accuracy: a system capable of producing 1000 phosphenes would require over 40 electrodes/mm^2 to cover the macula. Furthermore, high positioning accuracy is required. Long term safety has been demonstrated in the Argus I epiretinal implants, some of which have now been implanted for almost 15 years [8].

Challenges of retinal implants are in fabricating electrodes with the right curvature that matches that of the eye. Furthermore, the use of these electrodes relies on most parts of the visual pathway to be still intact, making its range of applicability smaller than that of other types of visual prostheses. Of the aforementioned five most common causes of blindness, only patients with blindness caused by cataract, un-corrected refractive error and macular degeneration can benefit from a retinal implant. Retinal implants can be epiretinal, subretinal, or suprachoroidal. The differences between these options will be covered next.

Epiretinal implants, such as the commercially available Argus®II by Second Sight Medical Products [140], are placed on the retinal surface from the inside of the eye, where they stimulate the retina from the top side. The surgery involved is arguably one of the least technically challenging of the implants discussed in this section, although fixing the implant in place can be challenging. Several device or surgery related adverse events have been reported [186].

Subretinal implants, such as the commercially available Alpha-IMS and AMS by Retina Implant AG [206, 207] (now discontinued), and the Prima System implant® by Pixium Vision [167], are placed under the retina, where it replaces the function of the damaged photoreceptors. The implant is kept in place by intraocular pressure. The surgery is more complicated than for the epiretinal implant.

Suprachoroidal transretinal implants consist of electrode arrays located in the sclera, the tissue covering the outermost part of the eye, and return electrodes placed in the vitreous humor, the liquid center of the eye. Electrical stimulation thus passes through the retina from behind. The advantage of this method is that the electrodes are located in a more durable part of the eye, which results in a better reliability and is also safer for the retina. Additionally, the surgical procedure is less technically challenging than required for the other retinal prostheses. Successful medical trials have been conducted [9, 108], but commercial devices have not been found.

The NESTOR project [154], of which the research discussed in this thesis is a part, aims to develop a cortical implant with 1024 intracortical electrodes. This should, for example, provide sufficient information for mobility in a simple environment [40]. Successful experiments have already been conducted on rhesus monkeys [26], however, the electrodes were wired to external stimulation equipment. The final product will require wireless data transfer, the research and development of which was carried out at Eindhoven University of Technology (TU/e) [161, 162, 163, 164], and wireless power transfer (WPT), which is the subject of this thesis.

1.3 Wireless power transfer to biomedical implants

Biomedical implants play an increasingly prominent role in healthcare, with a wide range of applications, such as diagnosing, monitoring, and treating diseases and disorders [39, 117, 208]. Already in the year 1932 the first artificial cardiac pacemaker was introduced [78], and currently over 750,000 cardiac pacemakers are implanted each year in the US alone [41]. Research on cochlear implants (CIs) started in the 1950's, and the first commercial devices have been approved by the Food and Drug Administration (FDA) in the mid-1980's [20, 63, 202]. Other common examples of implantable medical devices (IMDs) are left ventricular assist devices (LVADs) [139], implantable cardioverter defibrillators (ICDs) [236], and deep brain stimulation (DBS) devices [74, 136].

Challenges in the further development of IMDs include those related to the powering of the devices [7]. Battery powered cardiac pacemakers have a typical lifespan of up to 10 years [41], after which the device can be replaced through a relatively simple surgical procedure. This approach is not suitable for very small IMDs, or IMDs that consume a more considerable amount of power, such as CIs and LVADs, as the battery would need to be replaced often, or the physical size of the battery would become impractically large. In these cases, the battery can be charged periodically using a transcutaneous WPT link [4, 7, 13, 39, 109, 180]. Alternatively, the IMD can be powered directly through the WPT link, eliminating the need for an implanted battery. This reduces the cost and size of the implant, as well as the risks associated with the presence of a battery. Powering the IMD with a percutaneous cable is not recommended, as this creates a permanent opening in the skin that is prone to infection.

Already in the year 1831, Michael Faraday and Joseph Henry independently from each other discovered that it is possible to transfer energy through the air by magnetic induction, thus laying the foundation for inductive WPT. A lot has happened in the meantime. Nowadays, there are many options regarding the implementation of WPT to an IMD, each of which has their own advantages and downsides [4, 7, 13, 39, 54, 117]. Which technique is most suitable depends highly on the application.

Ultrasonic WPT operates on the principle of acoustic waves traveling through the tissue, usually in the frequency range from 50 kHz to several MHz [4, 13, 47, 117, 166]. At the receiver, these waves are converted into electrical energy through a piezoelectric transducer. The small wavelength in the millimeter or sub-millimeter range makes this technique particularly suitable for directional WPT. Ultrasonic WPT can achieve an acceptable power transfer efficiency (PTE) of over 25% [166, 178] and penetration depths of up to 10 cm [47, 201]. The size of its receivers is small, i.e. ranging roughly from below 1 mm^2 to 500 mm^2 [39, 166, 178], and received power levels of sub-μW up to several hundred mW have been demonstrated [13, 178]. The transmitter needs to be acoustically matched to the skin, which requires a mechanical connection between the transmitter and the skin [13]. Power cannot be transferred through the skull [4].

Capacitive WPT is the transfer of power through time-varying electric fields between two pairs of capacitor plates, using for example the skin and/or air as the dielectric material in between them [4, 117]. Two pairs of plates are required; one for the forward current path and one for the return path. Capacitive WPT can achieve received power levels of several hundred mW [53, 98], and a PTE of over 50% [98]. The in-body penetration depth is limited to a few mm due to the weak coupling between the plate pairs at increased distance [53, 98, 109], making this method mainly suitable for subcutaneous implants [4]. Furthermore, the required receiver size is relatively large, i.e. several hundred mm^2 for each of the plate pairs [53, 98].

Optical WPT has a photovoltaic cell integrated into the IMD, which is illuminated by an external light source. This technique is well suited for miniaturization, enabling it to be used for the powering of very small implants, i.e. for dimensions in the 100 μm range [158]. An acceptable penetration depth of about 10 mm can be achieved [39, 189]. The PTE of optical WPT is limited to a few percent [7, 75, 158, 189], as well as the received power level, which is generally limited to a few 100 μW [7, 75, 189], and the method is sensitive to misalignment [109].

Mid-field WPT uses propagating modes of electromagnetic (EM) radiation inside the tissue to transfer energy, contrary to the evanescent modes present in commonly used near-field (inductive) WPT. The frequency that yields maximum WPT efficiency inside the human body is in the GHz range [64, 174, 175], corresponding to a wavelength in the cm range inside the tissue. By optimizing the excitation of these fields, a region with high energy density can be created, achieving penetration depths of over 5 cm [4, 39, 141, 174]. Within this region, the receiver can be made very small, i.e. in the mm range [4, 39, 175]. With adaptive excitation, this region can be steered. The PTE of mid-field WPT is in the order of 0.1% or lower [141, 174], and the received power level is low, i.e. at most a few mW [64, 141]. Furthermore, rectifiers that operate at GHz frequencies have limited efficiency, especially at low power levels [90], which is the case here. This will negatively affect the overall WPT efficiency.

Far-field WPT is intended to be used in situations where the patient is located a few meters away (i.e. in the far-field) from the transmitter, and is not required to remain stationary. Additionally, it could be used when the receiver is moving through the human body, such as in smart pills [200], as this method is less sensitive to misalignment. The receiver can be made very small, i.e. in the mm range [90, 133, 200]. The PTE of far-field WPT is in the order of 0.1% or lower [90, 133], and the received power levels are in the order of 100 μW [90, 200]. Furthermore, operation at GHz frequencies limits the rectification efficiency, especially at low power levels [90].

Inductive WPT is arguably the most common implementation of biomedical WPT. Commercially available CIs use inductive WPT. Outside of the medical domain, inductive WPT is widely used to charge for example mobile phones and electric toothbrushes. Power and/or data can be transferred from an external coil to an implanted coil, and optionally data can be transmitted back using reverse telemetry [156]. A pair of coils is required, but additional relay coils can be added for improved distance, tolerance to load variation, and higher PTE [13, 54, 109, 156], at the cost of complexity and volume. The receiver size is usually in the range from mm to several cm, and penetration depths are in the range from mm to several cm [4, 109]. Over 100 mW can be transferred at over 50% PTE [4, 109, 169]. Some misalignment is tolerated, usually limited to roughly the largest coil radius [38].

Alternatively, energy can be harvested from processes taking place inside the human body, using for example a bio-fuel cell to convert glucose and oxygen from blood into electrical energy, thermoelectricity to obtain energy from temperature differences, piezoelectricity to harvest energy from body movement or blood flow, or electromagnetic generators to harvest energy from body movement [7, 150, 156]. However, the output power levels of these solutions are low, generally in the sub-mW region, and additional challenges regarding for example size and biocompatibility have to be addressed.

Safety is of utmost importance in biomedical WPT systems; they should not cause harm to the human body or nearby devices. International standards have been composed to define safe operation conditions. For example, introduced electric fields should not heat up the tissue beyond certain limits (IEEE Std C95.1, ICNIRP) [213, 245], magnetic fields should not interfere with nearby devices (ETSI EN 303 417) [55], and implanted electronics should not generate too much heat (EN-45502-1, ISO 14708-3) [52, 95]. Full-wave and thermal simulations can be used to assess whether or not the specific limits posed in each of the standards are met.

For the NESTOR project [154], the required level of received power is expected to be around 50 mW, as will be explained in more detail in Chapter 2. Ultrasonic, capacitive, and inductive WPT are viable candidates for the power delivery in this case, as these techniques are able to transfer this level of power, as described above. Ultrasonic WPT has the lowest PTE of the three techniques, and is therefore not preferred. Furthermore, the required acoustical match between the transmitter and the human body might be difficult to realize properly in practice. Both capacitive and inductive WPT can achieve similar PTE and the required area is comparable, but capacitive WPT is more sensitive to misalignment and more limited in terms of distance between the transmitter and receiver.

In the NESTOR project, the distance between the transmitter and receiver is expected to be between 8 and 15 mm, and the radial misalignment is expected to be less than 15 mm, as will be explained in Chapter 2. Considering these requirements, inductive WPT is expected to outperform its capacitive counterpart. For these reasons, inductive WPT was chosen for the NESTOR project.

The work in this thesis presents a complete design approach for an inductive WPT system comprising of a class-E inverter and a class-DE rectifier, which is optimized for maximum power transfer efficiency (MPTE). This design approach is used to design a WPT system for the NESTOR project [154]. The design is simulated in circuit simulation software, manufactured, and validated. Special attention was paid to the behavior of the system when the transmitter (Tx) and receiver (Rx) coils are misaligned, and when the load resistance changes. The presented WPT system transfers at least 80 mW at 6.78 MHz for a realistic range of distance and misalignment between the coils. This is more than the 50 mW required for the NESTOR project, which leaves room for a possible increase in electrodes in the future without the need for a new design. Compliance with the international standards mentioned above is demonstrated with the aid of EM and thermal simulation software.

Biological tissue affects the behavior of implanted coils. Compared to a coil in free space, the relative permittivity of the tissue lowers the self-resonance frequency (SRF) of the coil, and the conductivity increases the losses. A WPT that performs well in free space could hence exhibit a vast decrease in performance when the receiver is surrounded by biological tissue, even at MHz frequencies. This work gives insight in the influence of the relative permittivity and conductivity on the behavior of a wire-wound coil, and elaborates on the effect of embedding the coil in a coating layer.

1.4 Midfield Wireless Power Transfer (MF-WPT)

With the recent developments in miniaturization of IMDs, the range of applicability is ever expanding, and new possibilities open [39, 50, 120, 148]. Sub-mm size implants can be used in neural recording and stimulation, or can be used to measure certain physiological parameters, for example the glucose concentration or oxygenation [103, 158, 201]. Their size makes it possible to conveniently implant these IMDs, for example using a syringe or a small incision, such that the patient might experience only little discomfort from the implantation procedure [196]. Multiple devices can be implanted to create a network of sensors, recorders, or stimulators, without the need for interconnecting wires.

The development of (sub-)mm-size IMDs, located deep (i.e. multiple cm) inside the body, poses new challenges, one of which is related to power delivery. The devices are generally too small for a battery to be included. Harvesting energy from biological processes taking place inside the body, as described in the previous section, is a technique not yet considered mature enough. Furthermore, some kind of wireless link could still be necessary to transfer the data to or from the implant. WPT is a suitable solution.

Capacitive WPT is not suitable for small receivers located deep inside the body. Ultrasound [201] and optical [158] WPT can be used in some applications, but have severely limited capabilities to transfer through bone, and are therefore not suitable for (sub-)mm-size IMDs located in the brain. The efficiency of inductive WPT will be low when the receiver size is much smaller than the transmitter size and the transfer distance, which is the case here [62]. The use of midfield wireless power transfer (MF-WPT) can result in an increase in efficiency.

Research has suggested the optimal frequency for biomedical inductive WPT to be in the (sub-)GHz range, rather than at the commonly used frequencies of 13.56 MHz and below [87, 141, 157, 174, 175]. This might sound counter-intuitive, as the attenuation in biological tissue is known to increase with frequency [68]. However, in MF-WPT, the energy is mainly transferred in propagating modes, contrary to the transfer through evanescent modes in near-field inductive WPT, making it more efficient than inductive WPT in this case. Furthermore, as the received power is proportional to the rate of change of the magnetic field, the use of a higher frequency should be beneficial [175].

An additional advantage of using (sub-)GHz frequencies is the fact that the wavelengths are smaller than at MHz frequencies. Inside human tissue, these are in the cm range. This enables the use of field-shaping techniques to focus the fields, creating regions of high energy density at the location of the receiver. MF-WPT, is expected to play a vital role in the field of biomedical WPT in the future [113, 119]

In this work, 'midfield' denotes the region where both the reactive and radiative fields contribute (significantly) to the transfer of energy. An IMD located multiple cm inside the human body will be in the midfield at GHz frequencies, but in the near field at several MHz. In this work, we compare operation at different frequencies. At some frequencies, the receiver will be in the midfield, whereas at other frequencies it will be in the near field.

Multiple sources have used theoretical models to demonstrate the WPT efficiency to be optimal at (sub-)GHz frequencies, when optimizing for maximum power transfer efficiency (MPTE). Nonetheless, the efficiency is very small, i.e. below 1% [87, 157, 174, 175]. One could argue whether optimizing such a low efficiency is the best approach, or that it would be better to maximize the absolute received power within the specific absorption rate (SAR) limits. It was demonstrated that, when optimizing for maximum power on the load (MPL), there is little benefit of using MF-WPT at (sub-)GHz frequencies versus traditional inductive coupling at low-MHz frequencies [64]. However, the model used in [64] considers the human body to be a half-space consisting of one single tissue, which is a simplified representation. The environment under consideration can be more accurately represented by layered media, which will introduce additional reflections and refractions of the EM fields inside the tissue. This might change the theoretical optimal frequency for MPL.

As it is impossible to describe the EM fields inside layered media in closed form equations, an analytical model comprising a numerical procedure is required. This thesis describes a model that can be used to determine the theoretical optimal frequency for MPL in a multi-layer environment.

1.5 Analytical models for electromagnetic field modeling

Existing work on MF-WPT relies mainly on full-wave computer simulations [43], sometimes combined with measurements in animal tissue [88, 159, 240] or SAR measurements in biomedical phantoms [88, 141]. Additionally, mathematical models are used [64, 121, 157, 175], but they are limited to the use of two layers, focus only on the power transfer efficiency, lack details about (numerical) implementation, or focus on achieving MPTE instead of maximum power on the load (MPL). Research on MF-WPT could benefit from the availability of a general analytical model that can be used to calculate the EM fields in a layered environment with an arbitrary number of layers. This will be useful for solving more fundamental problems, such as determining the optimal frequency for WPT into the human body, while taking into account the effects of biological tissue.

Basing any biomedical WPT design solely on full-wave simulations is not advisable, as this is an inefficient approach for rapid prototyping. Especially when the designer starts performing full-wave simulations from scratch, the number of iterations required can be high. Even when rapid prototyping is not of key importance, the use of an analytical model is advised as a point of departure. Otherwise, errors in full-wave results might go unnoticed. Full-wave simulations can be used in a later stage to fine-tune the results, and to improve their accuracy.

Using an analytical model can be a more efficient start of a design process. It can provide very useful and speedy information that gives the designer a head start, possibly at the cost of (known) reduced applicability. Such rapid design iterations provide quick insight in, for example, the expected field distribution, SAR levels in each tissue layer, and received power. In addition, sensitivities in the design may be studied efficiently. Eventually, after this initial design, a full-wave solver can be used to fine-tune the design, requiring only a few iterations.

In this thesis, the application of two analytical models that can be used to calculate the EM fields generated by a magnetic point dipole (MPD) located inside or in the presence of planarly layered media is described. These can be used to approximate the fields generated by a small coil located outside the human body, or a small coil embedded inside the human body. Alternatively, using the reciprocity theorem, it can be used to determine the external coil current distribution required to focus the fields at a specific location inside the human body where a receiver coil will be located [121].

The first model is limited to two half-spaces, where the MPD can be located in either one of them. The second model is applicable to the situation with an arbitrary number of planar layers, each of which can have any combination of dielectric properties, as long as they are isotropic and uniform throughout the layer. The top and bottom layer are half-spaces. The former model is more limited than the latter, but it is also much easier to implement numerically, and it executes faster. The two-layer model can be used for a fast, initial design, by replacing the human body by a single, equivalent half-space with average dielectric properties. Consequently, the multi-layer model can be used to increase the level of detail, and thus the accuracy.

All essential steps for an efficient numerical implementation of the models are presented, and the results are compared systematically to those generated by a commercial EM field solver. Also the execution time is compared, which shows a large speedup. Although this thesis focuses on biomedical applications, this is by no means a limitation. In fact, the model is applicable to any situation that contains (locally approximated) planarly layered media.

Another advantage of the analytical models is that the calculation of the fields at a certain coordinate is completely independent of the calculation of the fields at another coordinate, contrary to finite difference (FD) or finite element method (FEM) solvers used in the calculation schemes of commercial software. This implies, for example, that the fields outside of the human body do not have to be calculated, and that the results need to be evaluated only at locations of interest, which leads to additional speedup using less memory, compared to conventional field solvers. This is in sharp contrast with commercial FD or FEM solvers, where the complete volume has to be analyzed, and a minimum (local) mesh size is required to ensure convergence of the algorithms. Additionally, this means that, in a multicore system, each processor can be assigned the task of computing the EM fields at a different spatial coordinate, eliminating the need for extensive communication and other time consuming dependencies between processors. This suggests that the speed-up in execution time of our method scales approximately linearly with the amount of processors[1], whereas the speedup of, for example, Simulia CST Studio Suite® stalls above a certain number of processors [3, 21, 36, 239].

Furthermore, this thesis presents an extension to the models, such that they can be used to calculate the received power, SAR, and total dissipated energy in the tissue. Based on the SAR results, the transmit power of the source can now be increased such that the generated SAR is just below the relevant safety limit [213, 245]. This transmit power can then be used to determine the maximum power that can be received within the safety limits. The analysis is repeated for frequencies ranging from 10 kHz to 10 GHz, such that the optimal frequency for MPL can be determined. Based on this analysis, WPT to a mm-sized receiver, located multiple cm deep inside the human body, achieves MPL at 10 kHz, where it should be noted that the performance is approximately constant for frequencies ranging from 10 kHz to 300 kHz. The same goes for the power transfer efficiency.

1.6 Realistic environment for bioelectronics experiments

When designing an IMD, or in fact any piece of electronics that is intended for use in or near the human body, it is important to test it in a realistic environment. It is known that the presence of human tissue affects the behavior of antennas, for example [71, 104, 199, 242]. The

[1] We were able to verify this for up to 64 CPU cores.

operation of such antennas can only be verified reliably when they are positioned in an environment that mimics the intended environment [83]; in free-space, the antenna might behave poorly. Examples of cases where a realistic measurement environment is preferred include data transfer in or near the human body, various kinds of WPT, experiments with imaging techniques such as magnetic resonance imaging (MRI), millimeter wave radar (MWR), microwave tomography (MWT), and ultrasound [102, 124, 151], but also communication in mines, buildings, or urban areas. In this Thesis, the focus is on biomedical experiments, although some of the presented results can be used in other kinds of experiments as well.

1.6.1 Liquid-based phantoms

Some research uses meat or actual animal carcasses [4, 24, 98, 148, 176, 178, 201, 203] for validation. The advantage of this approach is that the dielectric, mechanical, and thermal properties will be as desired, and these properties will be accurate over a broad frequency range. However, the properties of biological tissue might change rapidly when not perfused or preserved well, and the properties are temperature dependent, which makes refrigeration troublesome [203]. This makes the method unreliable and poorly repeatable, and preservation of the material challenging.

Another option is to use biomedical phantoms; materials or combinations of materials with properties that mimic those of human tissue as closely as possible. Advantages of this approach are repeatability, easier preservation, and reliability over a longer period of time, usually ranging from several days to months [212, 242]. Furthermore, virtually any shape and material can be created, thus the user is not limited to the availability of specific biological materials. Using commonly available ingredients like deionized water, sugar, salt, agar, gelatin, polyethylene, and sodium alginate, already a broad range of biological tissues can be mimicked [42, 70, 107, 155, 173, 203, 212]. However, available recipes focus on mimicking only one type of biological tissue in a limited frequency range.

Drawbacks of the use of biomedical phantoms include the fact that the properties of the phantom might only be as desired for a limited frequency range. Additionally, some available recipes require ingredients that are expensive, difficult to obtain, or dangerous to handle [15, 242]. Furthermore, it can be difficult to generate phantoms that mimic a combination of properties of the biological tissue at the same time, such as dielectric, thermal, and acoustic properties. The recipe of a phantom is focused on achieving correct values for one specific property. It can already be challenging to achieve the desired values for both ε_r' and σ at the right frequency. This might become near impossible if additional requirements are set.

In this thesis, new recipes for biomedical phantoms are presented, using only commonly available and easy to handle ingredients, and requiring standard kitchen equipment. The dielectric properties are measured from 4 MHz to 20 GHz, using a commercial probe. The influence of the individual ingredients on the dielectric properties is presented, and the shelf life is determined.

A commercial dielectric probe can cost several ten thousand euros, which might be above budget for certain research facilities. In essence, a commercial dielectric probe is nothing more than a well-characterized piece of coaxial cable, accompanied by a mathematical procedure tailored to that probe. We present the design of a simple dielectric probe, made from a piece of semi-rigid solid-screen coaxial cable. Its performance is compared to the commercial probe.

1.6.2 Solid-based phantoms

An increase in the level of detail of these phantoms, by for example a more realistic geometry or multiple tissue layers, will result in more reliable measurements and will broaden the range of applications. To achieve more detail, it can be beneficial to add solid structures to the phantom, for example bone or teeth structures. Alternatively, molds can be used to create organ phantoms with realistic shapes [173], filled with a tissue simulating liquid (TSL) with the desired dielectric properties.

This thesis presents the measured dielectric properties of a variety of commercial off-the-shelf (COTS) 3D printing materials, including some commonly used plastics, as well as plastics enriched with various kinds of carbon, metal, and stone particles. The dielectric properties are measured from 4 MHz to 20 GHz, using a commercial probe.

1.7 Research questions and outline of the thesis

The following research questions are addressed and answered in this thesis:

- Can we improve on the state-of-the-art overall efficiency of WPT to IMDs, taking into account biomedical safety, size restrictions and misalignment, next to the powering requirements?
- Can we adapt and apply a mathematical model, developed for EM field calculation in layered media, to calculate fields and power transfer into the human body in an accurate and time-efficient way?
- What is the optimal frequency for WPT to IMDs?
- Can we use commonly available ingredients to create materials with dielectric properties that resemble those of human tissue, to validate WPT prototypes in a realistic environment and to experimentally determine the optimal frequency for WPT?

Chapters 2 and 3 regard the design of a WPT link for biomedical applications. The design requirements, such as available link budget, for WPT in biomedical applications are discussed in Chapter 2. It supports Chapter 3, which describes the design process of a complete inductive WPT system consisting of a class-E inverter and class-DE rectifier. A case study is performed to design a WPT system suitable for the NESTOR project [154], which is capable of transferring over 80 mW at 6.78 MHz. The design includes circuit simulations, and the prototype is manufactured and validated. Compliance with relevant international standards is shown. Special attention is paid to the design of the Tx and Rx coils, and on how the link can be designed such that it can be used for a broad range of the coupling factor k.

In **Chapters 4 and 5**, two analytical models that model the EM fields of an MPD above dispersive media are presented. The model in Chapter 4 is applicable to the situation with two half-spaces, with the dipole located in either one of them. The model in Chapter 5 is applicable to the situation with an arbitrary number of planer layers, each of which can have any combination of dielectric properties, as long as they are isotropic and uniform throughout the layer. The top and bottom layer are half-spaces. The former model is more limited than the latter, but it is also much easier to implement numerically. The two-layer model from Chapter 4 can be used for a fast, initial design, by replacing the human body by a single equivalent half-space with average dielectric properties. Consequently, the multi-layer model from Chapter 4 can be used to increase the level of detail, and thus the accuracy. Details regarding the numerical implementation are presented, and the results are validated using commercial full-wave EM solver software.

These models can be used to make estimations on the expected EM field distribution when sources are located near or inside the human body. They execute in tens to hundreds of seconds, depending on the number of layers, the frequency, and the desired spatial resolution, even on a regular desktop personal computer (PC). This is much faster than commercial full-wave EM solver software, which can take several hours to perform the same task, even on a high-power server. Therefore, these models can be time-saving tools in iterative design processes. Furthermore, they can be used to find the optimal frequency for MF-WPT for a given layered geometry, much faster than a commercial solver.

In **Chapter 6**, the models are extended such that they can calculate the SAR, the received power, and the total power dissipated in the tissue. These are used to determine the maximum power that can be transmitted whilst the SAR level is below the safety limit. This maximum power is then used to determine the frequency at which WPT to a mm-sized implant, located multiple cm deep inside the body, is optimal, both in terms of received power, and transfer efficiency. Both are in the $10-300$ kHz range. (Chapter 6)

Chapters 7 and 8 regard the creation of biomedical phantoms to create a realistic environment for biomedical experiments. Various recipes for liquid biomedical phantoms are presented in Chapter 7. The ingredients for these phantoms are commonly available, cheap, and easy to handle. Only standard kitchen equipment is required to manufacture the phantoms. A commercial dielectric probe was used to measure the dielectric properties from 4 MHz to 20 GHz, and the shelf-life was determined.

Additionally, the design of a cheap and easy dielectric probe is presented, which can be used to measure the dielectric properties of liquid phantoms when a COTS dielectric probe is not available. The performance of this probe is compared to that of the COTS one, and although the difference is notable, it can still be used to get an estimate that is accurate enough for most biomedical experiments.

An additional level of detail in biomedical phantoms can be achieved by adding solid structures, for example bone or teeth. Chapter 8 describes the measured dielectric properties of various COTS 3D printing materials, including materials enriched with carbon, metal, and stone particles. These materials can be used to generate solid phantom parts with dielectric properties that mimic those of real biological solids. 3D printing can also be used to create molds for liquid phantoms, for example to realise organs.

The structure and coherence of Chapters 2 through 8 is summarized in Table 1.1. Finally, conclusions are drawn in **Chapter 9**, where also recommendations for future work are made.

Table 1.1: Structure and coherence of Chapters 2 through 8.

Part	Specification	Chapter	Publication
WPT hardware	Design requirements	2	[P1, P5]
	Design process and realization	3	[P1]
Optimal frequency	Two-layer analytical field model	4	[P4]
	Multi-layer analytical field model	5	-
	Calculation of optimal frequency	6	[P2]
Realistic measurements	Liquid-based phantoms	7	[P3]
	Solid-based phantoms	8	[P6]

1.8 Original contributions of the thesis

The work that is presented in this thesis contains the following original contributions.

- The design process of a complete inductive WPT system consisting of a class-E inverter and class-DE rectifier, including the driver. The WPT system is designed for MPTE (Chapter 3)

- A complete prototype for WPT to a visual neuroprosthesis. The case study includes circuit simulations, and the prototype is manufactured and validated. Compliance with relevant international standards is shown. It is possible to transfer $\geq$ 80 mW safely to a subcutaneous receiver, with an efficiency that is better than the state of the art, for distances between the coils from 8 to 15 mm, and misalignment up to 16 mm. (Chapter 3)

- Two analytical models that model the EM fields generated by a MPD located in a planarly layered environment are presented: one for an environment consisting of two half-spaces, and one for an arbitrary number of layers. The generated EM fields are compared to those generated by commercial full-wave EM solver software. The differences in field distribution are small. The analytical model executes much faster (up to 400 times) than the commercial full-wave EM solver software. (Chapters 4 and 5)
- The analytical models are extended such that they can calculate the SAR, the received power, and the total power dissipated in the tissue. These are used to determine the maximum received power, as well as the transfer efficiency, of WPT to a mm-sized implant, located multiple cm inside the human body, whilst the generated SAR is at the limit value. Both are highest in the $10 - 300$ kHz range. (Chapter 6)
- Recipes for several biomedical phantoms using cheap, commonly available and easy to handle ingredients, having a shelf life of over 10 days. The dielectric properties are measured from 4 MHz to 20 GHz, using a commercial probe. (Chapter 7)
- A simple permittivity probe was built from a semi-rigid solid-screen coaxial cable. The performance of this probe is compared to a commercial dielectric probe. It is not as accurate as the commercial probe, but is nonetheless considered accurate enough for the creation of liquid biomedical phantoms. (Chapter 7)
- Measurement of the dielectric properties of various COTS 3D printing materials, including common plastics and plastics enriched with carbon, metal, and stone particles. The dielectric properties are measured from 4 MHz to 20 GHz, using a commercial probe. Considerations for manufacturing solid biomedical phantoms are presented. (Chapter 8)

Chapter two

System level requirements

Before the actual design of the WPT hardware can start, the system level requirements have to be defined. The requirements presented in this chapter assume a total of 1024 electrodes to be implanted in the visual cortex for the NESTOR project [154], as was introduced in Chapter 1.

The brain implant can either be battery powered, which means a battery is implanted that is charged during the night, and the stored energy is used by the IMD during the day. As percutaneous wires, i.e. wires that penetrate the skin, introduce health issues such as increased chances of infection, the charging of the battery will need to take place wirelessly. Alternatively, the implant can be directly wirelessly powered. In both cases, WPT is needed.

Besides a stimulating part, the IMD is assumed to include a recording part [26, 161]. The purpose of the recording part is twofold. On the one hand, recorded signals can be used for calibration of the stimulation part. On the other hand, recorded signals can be used to monitor the IMD and the surrounding tissue over an extended period of time. During stimulation, unexcited electrodes can be used to record activity in the visual cortex. Besides, in absence of any electrical stimulation, cortical background activity can be recorded. Furthermore, the electrode impedance can be measured. Changes in these measurements can indicate malfunction of the device, or changes in the surrounding tissue [49, 228].

2.1 Power consumption of the implant

An initial estimation of the required output power of the WPT link was based on the power consumption of related work [181, 192], which was extrapolated to 1024 electrodes. Based on this estimation, the stimulation part is initially expected to consume a total of 15 mW, and the recording part is estimated to consume 18 – 35 mW. The brain implant is thus expected to consume a total of 50 mW. The initial estimation of the power consumption is listed in the second column of Table 2.1.

For a detailed estimation of the power consumption of the brain implant, some details have to be clarified. The implanted electrodes have an impedance of 50 kΩ [234] and require a bipolar current with a maximum amplitude of 50 μA to elicit a phosphene. This corresponds to a symmetrical power supply voltage of ± 2.5 V. A headroom of 1 V is added to each power supply rail to cover the voltage drop over the amplifiers, resulting in a required voltage at the receiver of ± 3.5 V, or 7 V in total. The electrode impedance might vary over time, which influences the required stimulation power. On the long term, however, the impedance, as well as the current required to elicit a phosphene, are expected to remain approximately constant [229].

The waveform for each electrode is 200 μs positive, 200 μs negative, and has a period of 3 ms. The positive and negative parts of the waveform of two distinct electrodes are allowed to overlap, meaning that the duty cycle is effectively $\frac{200}{3000} = \frac{1}{15} \approx 6.7\%$.

The efficiency of the amplifiers is assumed to be better than 50% [192]. When we assume that simultaneous activation of at most 20% of the 1024 electrodes at any given time is sufficient to produce a useful image in the patient, the maximum power consumption of the stimulation electronics is

$$P_{sim} = 7\ \text{V} \cdot 50\ \mu\text{A} \cdot 6.7\% \cdot \frac{1}{50\%} \cdot 20\% \cdot 1024 = 9.6\ \text{mW}. \tag{2.1}$$

The downlink receiver developed for the NESTOR project consumes 0.2 mW [165]. Unpacking the data and controlling the stimulation part is expected to consume 0.8 mW [33]. The uplink transmitter consumes 0.3 mW [165]. This number assumes at most 10% of the recording electrodes, i.e. 103, to be active simultaneously at any given time. Neural recording of a single channel is assumed to consume $5.7 - 15.5$ μW or less [131, 192], resulting in at most $0.6 - 1.6$ mW for all channels combined. Additionally, 1.4 mW should be sufficient to control the recording part [23, 126].

The detailed estimation of the power consumption is listed in the fourth column of Table 2.1. In retrospect, using the results from research performed by the other NESTOR team members, as well as other recent work, the stimulation part is now expected to consume a total of 10.6 mW, and the recording part is expected to consume a total of 3.3 mW.

The design in Chapter 3 is based on the initial estimation of 50 mW, whilst in retrospect only 13.9 mW is required. It should therefore be possible to, sticking to this 50 mW, increase the number of implanted electrodes without requiring a redesign of the WPT system. When the power consumption is assumed to scale linearly with the number of electrodes, the available 50 mW should be sufficient to supply over 3600 electrodes.

2.2 Receiver coil requirements

The available space for a subcutaneous Rx coil is limited. Consultations with a neurosurgeon, regarding his experience with the surgical procedure to implant an IMD, made us decide for an Rx coil diameter less than 40 mm and a thickness (including biocompatible coating) of at

Table 2.1: Estimated power consumption of the implanted electronics.

Subsystem	Initial estimation	Specification	Final estimation
Stimulation	15 mW	Electrodes + amplifiers	9.6 mW
		Downlink receiver	0.2 mW
		Stimulation controller	0.8 mW
Recording	18 – 35 mW	Amplifiers + digitizing	0.6 – 1.6 mW
		Uplink transmitter	0.3 mW
		Recording controller	1.4 mW

most 3 mm. A possible material for the biocompatible coating is Parylene-C, which can be applied with a thickness of 6 μm [195]. Copper wire cannot be used in the final product, as copper is a neurotoxin. Gold (Au) can be used safely in the final product, but this is not used in this prototype for economical reasons.

The Rx coil should preferably be located away from the stimulation electronics, as these electronics could experience interference from the magnetic fields associated with WPT.

The Tx coil should be as large as possible, and the number of turns should be as high as possible [171], within practical limits. There are no set constraints regarding the size of the Tx unit. A thicker wire than in the Rx coil can be used, as this reduces the losses, and there is no need for this coil to be flexible. However, using too thick a wire can result in a bulky coil.

2.3 Coil misalignment

The Rx coil will be located between the scalp and the skull. The distance between the Tx and Rx coils thus depends on the thickness of the scalp, as well as possible additional materials.

The normal thickness of the human scalp is 2 to 5 mm [89, 160, 235], although it can be thicker in the days after surgery. To prevent the risk of skin irritation, the Tx coil will not be placed directly on the skin. A comfortable headband with a thickness of 4 to 8 mm is assumed to hold the Tx unit. The enclosure of the Tx unit is chosen to be 2 mm thick, such that it can be 3D-printed easily. This is in line with the IEC 60601 standard [91]. This means that the height h between the external Tx coil and implanted Rx coil is in the range from 8 to 15 mm. Figure 2.1 shows a representation of the positioning of the coils. As both the headband and the enclosure are expected to be constructed from non-magnetic materials, they are not expected to impact the behavior of the WPT link.

The Tx unit will be mounted on a headband, which will be positioned by the patient. This introduces uncertainty in the exact location of the Tx coil relative to the Rx coil. Furthermore, the headband could move slightly over time. It is yet unclear what values can be expected for the radial misalignment, but for now we assume choosing the upper bound for the radial misalignment d at 15 mm will be sufficient.

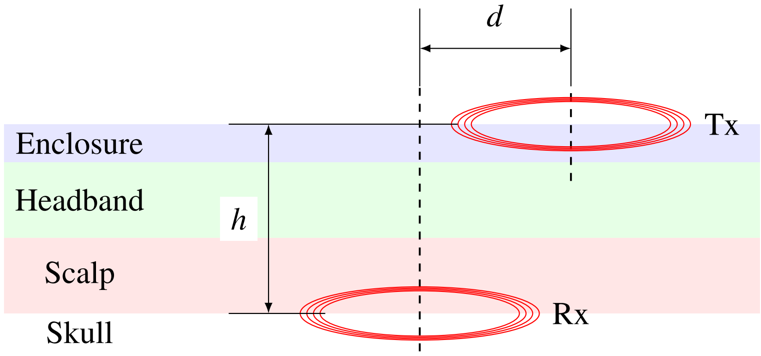

Figure 2.1: Separation h and radial misalignment d between the coils.

2.4 Frequency of operation

WPT is only allowed in specific frequency bands. According to ETSI EN 303 417 [55], WPT is permitted in five bands below 30 MHz, given in Table 2.2, where it is noted that other frequency bands may be available in some countries. Several other bands are used in some cases, but these are not (yet) fully harmonized [56]. As we aim to develop a WPT link that can be used in commercial products with broad applicability, we restrict ourselves to the frequencies listed in Table 2.2. Note that the widely used Qi Low Power standard [233] and the upcoming AirFuel™ standard [232] operate in WPT bands 4 and 5, respectively.

Table 2.2: Frequency bands allowed for WPT, according to ETSI EN 303 417 [55].

WPT band	Frequency range	Commercial standard
1	19 – 21 kHz	
2	59 – 61 kHz	
3	79 – 90 kHz	
4	100 – 300 kHz	Qi Low Power [233]
5	6.765 – 6.795 MHz	AirFuel™ [232]

Higher frequencies are associated with smaller coils, which is advantageous in this case. However, with increasing frequency, the losses in the coil also increase [238]. When the frequency of operation is chosen too high, the losses start to dominate. In practice, the WPT frequency of inductive links like the one under consideration, designed for the transfer of tens to hundreds of mW over a distance smaller than the coil radius, is therefore often chosen below 30 MHz [117, 190].

Considering the above, we have chosen to operate the WPT link for the NESTOR project at 6.78 MHz.

2.5 Biomedical safety standards for tissue heating

EM fields and waves interact with biological tissue. One of the effects is heating of the tissue. Sufficiently high field levels can cause damage to the cells. International standards define guidelines to limit human exposure to EM fields, such as IEEE Std C95.1 [213] and ICNIRP [245].

This poses an upper limit to the amount of EM power that can be transmitted to a receiver located inside the human body. Recent results from literature can be used to get an indication of the maximum power level that can be achieved whilst complying to the standards.

It was shown that at 5 MHz, 1 W can be transferred safely to a brain implanted visual prosthesis [105]. However, the analysis includes only the fields generated by the transmitter in absence of a receiver. From other related work, we know that tissue absorption can be high around the receiver coil [99, 211]. It is therefore assumed that the actual power limit will be well below 1 W.

It was shown that, at 1 MHz, 100 mW can be received by an IMD, with an external transmit power of 180 mW, while staying below the SAR limit [99]. Additionally, at 40 MHz, 319 mW can be received by an IMD, with an external transmit power of 676 mW, while staying below the SAR limit [211]. No related work for operation at 6.78 MHz was found. It should be noted that these references regard one specific tissue layer composition, and as such do not take into account, for example, the variability in skin thickness. Furthermore, in the latter, the IMD is located at a depth of 10 mm inside the human body, which is much deeper than in our application. Therefore, it might be less relevant to our application.

Based on these data, it is assumed that, at 6.78 MHz, a maximum power somewhere between 100 and 319 mW can be received while staying below the SAR limit. To be on the safe side, we assume it should be possible to transfer at least 100 mW at 6.78 MHz safely.

Besides tissue heating caused by EM fields, electronics heat up during operation. Consequently, the tissue around the implant will heat up as well. The increase in temperature should be limited, to prevent damage to the tissue. According to ISO 14708-3 [95] and EN-45502-1 [52], the outer surface of any implantable neurostimulator should never exceed the normal surrounding body temperature by more than 2°C.

Energy is dissipated in the Rx coil and in the rectifier electronics. This energy, combined with their surface area, results in the heat flux. When the final dimensions and losses of both are determined, thermal simulations can be performed to assess whether the heat flux is low enough. Based on related work, we assume that a heat flux below 22.3 mW/cm^2 should be low enough to meet the standards [139].

2.6 Battery versus wireless power delivery

Batteries belonging to the current range of available implantable types [94] are likely too bulky to fit within the 3 mm thickness requirement. Thinner batteries are available [77], but these are not approved for implanted use. Let us, for now, assume a battery is available that is safe for implantation, such that we can compare battery versus wireless powering of the IMD.

We consider a system where the battery is charged during the night, for example by a charger embedded in the pillow, and the battery supplies the IMD during the day. The battery would need to have sufficient capacity for about 16 hours of continuous operation during the day, considering a regular day, and needs to be charged in about 8 hours during sleep. We can thus say that the power required to charge the battery is roughly twice the power consumption of the IMD. A WPT link to charge the battery would thus need to transfer roughly twice the amount of power than in the case where the IMD is directly wirelessly powered. This implies that the field strengths required to charge the battery, and thus the associated risks of introducing adverse health effects, are higher for the battery powered case than for the case where the IMD is directly wirelessly powered.

In Section 2.5, we have seen that it should be possible to transfer 100 mW while staying below the SAR limit. This suggests that it should just be possible to charge the battery wirelessly during the sleep, given that a suitable battery is available.

However, a person can be expected to move during sleep. To fully charge the battery, 100 mW should be transferred continuously for 8 hours. The WPT system should thus maintain the transfer regardless of the movement, position, and orientation of the receiver. This could for example be achieved by a 3D receiver, consisting of three mutually orthogonal receiver coils [117]. It was shown that it is possible to transfer over 100 mW to an IMD with arbitrary orientation, whilst complying to the SAR regulations, using Helmholtz-style transmitter coils [100]. However, the transfer efficiency is low ($\eta \approx 5\%$). Additionally, Helmholtz-style transmitter coils might be difficult to install around a human head without affecting the comfort of the user. Furthermore, as the receiver consists of three orthogonal coils, its shape is approximately cubical. The receiver presented in [100] measures $12 \times 12 \times 12$ mm^3, which is too bulky for our application.

Considering the presented disadvantages of battery powered operation, the choice is made to power the IMD wirelessly.

In retrospect, the expected power consumption of the IMD is much lower than the initial estimation, as described in Section 2.1. To supply the IMD with 13.9 mW during 16 hours, a battery with a capacity of about 222 mWh is needed, and the charging power would need to be 27.8 mW. A battery measuring $2.5 \times 14 \times 24$ mm^3 is available which has sufficient capacity [77]. It likely fits inside the IMD enclosure, although the specific battery is not approved for implantation. This suggests that, in the future, battery powered operation of similar IMDs could be a viable option. However, a suitable WPT configuration has to be found.

2.7 Conclusion

This chapter has presented the design requirements for the WPT system which is to be designed for the NESTOR project. They are listed in Table 2.3. The Rx coil diameter should be kept below 40 mm, its thickness below 3 mm. The distance between the Tx and Rx coils is 8 to 15 mm, the misalignment is expected to be at most 15 mm.

The power will be transferred wirelessly at 6.78 MHz. At this frequency, it should be possible to transfer at least 100 mW safely. Initially, not all data required to predict the power consumption of the implant was available, as part of it was still being researched by others in the NESTOR project. Based on related work, the power consumption of the implant was initially estimated to be about 50 mW. In retrospect, with the results of the other NESTOR team members available, as well as based on recent related work, the expected power consumption of the IMD is only 13.9 mW.

Table 2.3: Design requirements for power delivery to the brain implant.

Parameter	Requirement
Power delivery mechanism	Direct WPT
Frequency of operation	6.78 MHz
Power consumption of implant (initial estimate)	50 mW
Power consumption of implant (final estimate)	13.9 mW
Received power within SAR limits	$\leq$ 100 mW
Heat flux of implanted electronics	$\leq$ 22.3 mW/cm^2
Rx coil diameter	$\leq$ 40 mm
Rx coil thickness	$\leq$ 3 mm
Distance between coils	8 – 15 mm
Misalignment between coils	$\leq$ 15 mm

Chapter three

Wireless power transfer to implantable medical devices using a class E inverter and a class DE rectifier[1]

3.1 Introduction

Wires penetrating the skin can cause serious infection, and are thus to be avoided in (semi-)permanent IMDs. For many applications, including the one in the NESTOR project [154], adding a battery is undesired, due to the physical size increase of the IMD. Therefore, the IMD will be powered wirelessly.

Much progress has been made in the field of inductive WPT in recent years and impressive results have been achieved, which are summarized in [4, 13, 109, 188]. For the WPT system for the NESTOR project, as was introduced in Chapter 1, the requirements for which were discussed in Chapter 2, related work is not directly applicable, because either the validation is performed in air rather than in a representative environment, SAR simulations or measurements are not performed [213, 245], the reported PTE does not include the transmit and receive electronics, the used frequency band is not allowed for WPT in Europe [31, 55], or the distance or transferred power is too small for our application. Table 3.1 lists relevant related work, the gray colored cells correspond to one of the reasons for non-applicability in our situation as mentioned above. Work that does not include an inverter has been left out of the comparison. None of the listed sources mention the heat generation in the IMD [52, 95].

This chapter presents a complete mathematical framework for the design of a 2-coil WPT system consisting of a class E inverter and a class DE rectifier, which is optimized for MPTE. The presented framework is used to design a WPT prototype intended for use in the NESTOR project [154], the requirements for which were discussed in Chapter 2. The prototype is val-

[1]This chapter is based on [P2] and [P5].

Table 3.1: Related work specitifactions for WPT systems for IMDs.

Ref.	f [MHz]	P [mW]	η [%]	d [mm]	Env.	SAR	Other
[10]	6.785	$1-10$	$51-74$	$1-10$	Saline	N/A	η without controller
[22]	0.7	50	36	30	Air	N/A	η without controller
[99]	1	100	≤ 65.8	$5-10$	Rat	HFSS + meas.	η without controller and rectifier
[101]	13.56	100	≤ 66.4	$5-15$	Air	N/A	
[114]	1	250	≤ 67	$2-15$	Air	N/A	
[135]	10	24	$35-42$	$4-8$	Air	N/A	η without controller
[169]	$6.5-7.5$	115	≤ 52.9	$5-8$	Pork	N/A	
[211]	39.86	115	47.2	10	Pork	HFSS	

idated in a realistic environment. EM and thermal simulations show compliance with the relevant SAR regulations [213, 245], field strength regulations [31, 55], and thermal regulations [52, 95].

Section 3.2 describes the choice of the inverter and rectifier classes. The required design equations for the complete WPT system are given in Section 3.3. These equations are used to design a WPT system for the NESTOR project in Section 3.4, including EM and thermal simulations to show compatibility with the relevant safety standards. The performance of the WPT prototype is evaluated in Section 3.5. Section 3.6 contains the discussion, and Section 3.7 concludes this chapter.

3.2 Design considerations

A general inductive WPT system comprises an inverter, two coils, and a rectifier. The inverter generates an approximately sinusoidal signal from the incoming direct current (DC) power, which is fed to the Tx coil. This current generates a time-harmonic magnetic field in and around the coil. The Rx coil captures part of this field, which is converted back to an electrical current. The rectifier then converts this sinusoidal signal back into DC, where it can be consumed by the load.

Inverter and rectifier designs can be divided into various classes, each with a characteristic standard design, and each having certain characteristic properties, regarding for example efficiency, susceptibility to load variations, required control signals, and design complexity (or part count) [125]. Which class is most suitable depends highly on the application; one application might require the highest possible efficiency at the cost of size, while another might sacrifice some efficiency to achieve the smallest possible form factor. Suppression of harmonics and robustness for variation in the load or coupling factor, also influence the selection of a suitable class. In biomedical WPT applications, it is beneficial to have a small size, high efficiency, and limited design complexity. Limiting the level of generated higher harmonics is also important, but as we will see later in this chapter, this requirement will already be met without additional measures.

3.2.1 Inverter classes

Inverters of classes A to C use transistors in their active region, which can be beneficial for achieving low harmonic distortion. However, this means that the voltage over the transistor is higher than when the transistor is used as a switch. This implies higher losses in classes A to C [80]. These classes are thus not optimal for use in efficient power inverters, and should therefore be avoided in WPT [125].

Classes D to F use transistors as switches, which reduces the losses significantly, as this means that the voltage drop over the transistors is low [125]. The transistors are loaded with higher-order passive circuits to obtain an output waveform with low harmonic distortion. The Tx coil doubles as a part of the filter in this case.

Class D inverter

A class D inverter is easy to design, and it operates on a duty cycle of 50%, making it simple to control [34]. However, it uses a high-side transistor, which means that it requires additional level shifting circuitry to drive the gate. Furthermore, the parasitic capacitor inside each transistor is charged and discharged each cycle, causing losses [80]. It is challenging to use a class D inverter at MHz frequencies, as these losses increase with frequency [34].

Class E inverter

The part count of the class E inverter is lower than that for the class D. It uses zero-voltage switching (ZVS) and zero-derivative switching (ZDS), meaning that the voltage over the transistor, as well as the derivative of this voltage, are zero when the transistor is opened or closed [80, 112]. This eliminates the losses associated with the (dis)charging of the parasitic capacitors in the transistors, resulting in a higher efficiency than class D [34, 125]. It can operate at a range of duty cycles, including 50%. It is less robust to changes in the coupling factor k.

Class F inverter

The efficiency of class F is a few percent higher than class E [6, 34]. Additional LC-filters on the output result in its waveform being less distorted than classes D and E, resulting in lower harmonics, and in less voltage stress on the transistor. However, the part count is higher [34], and the duty cycle for optimum operation is lower [6], which can be more difficult to realise in practice. As we will see in Section 3.3.4, the generation of a signal with a 50% duty cycle requires only three basic components.

3.2.2 Rectifier classes

In WPT applications, the most common rectifier classes are D to F, just as with the inverters [190].

Class D rectifier

Class D rectifiers have a low part count. Their output voltage is relatively high, compared to other rectifier classes. Just as the class D inverter, the class D rectifier suffers from losses associated with parasitic capacitances, causing the efficiency to drop at MHz frequencies [190].

Class E rectifier

The class E rectifier also has a low part count. Just as with the inverters, the efficiency of the class E rectifier is higher than class D, because the losses associated with the parasitics are eliminated [111, 190]. However, its output voltage is much lower (roughly half) than that of a class D rectifier.

Class DE rectifier

Class DE rectifiers combine the advantages of both the class D and E rectifier: the output voltage of class D, together with the efficiency of class E rectifier, at the cost of a slight increase in part count [65, 66, 80].

Rectifiers of higher class

Rectifiers of higher class exist, which might add a few percent efficiency, but they add components to the receiver side, and require additional control signals. This is not desired in our application, as the implanted receiver should be kept small in size.

3.2.3 Inverter and rectifier selection

The WPT link for the NESTOR project should have high efficiency, and limited design complexity. Furthermore, the system should be robust against misalignment between the Tx and Rx unit, meaning it should work for a broad range of k. Also, it should not malfunction when the Tx unit is suddenly removed (i.e. $k = 0$). The receiver should have a small form factor. Considering these requirements, a class E inverter and a class DE rectifier were chosen. As we will see in this chapter, the combination of the class E inverter and the class DE rectifier can be designed to be sufficiently robust for the broad range for k that we encounter in this application.

3.3 Design equations

Pinuela *et al.* [171] describe an approach for maximizing the end-to-end efficiency of a WPT system with a class E inverter at MHz frequencies. In particular, they state that, for achieving MPTE, the coils should be as large as possible, have as many turns as possible, and have a wire diameter as large as possible. However, part of their optimization relies on choosing an optimal frequency, whereas the legally permitted range of operating frequencies is often severely limited [31, 55].

Kazimierczuk and Czarkowski [112] have presented a set of equations that can be used to design a class E inverter. Fukui and Koizumi [65] have presented a set of equations that can be used to design a class DE rectifier. Nagashima *et al.* [152] used both to design a WPT system consisting of a class E inverter and a class DE rectifier. However, the design process mentioned in [152] is not complete.

Namely, the maximum efficiency is determined empirically, instead of analytically. A range of WPT systems is designed, each for a different value of the receiver diode duty cycle[2] ζ_d, and each design is simulated in a circuit simulator, after which the solution that yields the highest efficiency is chosen. Secondly, the choice of the input voltage V_{dc} is not discussed. Furthermore, it is unclear how the behavior of the WPT system changes when the coupling factor k or the load R_L deviate from their optimal value.

Inaba *et al.* [93] also used the equations mentioned in [65] and [112] to design a WPT system comprising a class E inverter and class DE rectifier. It is shown that the system can achieve acceptable efficiency over a broad range for k. However, it is not optimized for MPTE, and therefore this design strategy is not adopted.

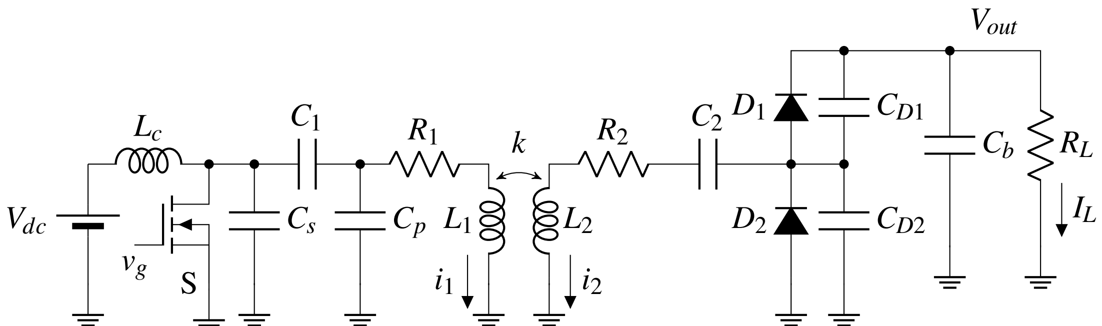

Figure 3.1: Schematic of the WPT link, consisting of a class E inverter (left) and a class DE rectifier (right). The wireless coupling (k) occurs through coils L_1 and L_2.

The circuit of a typical class E/DE WPT system is depicted in Figure 3.1, where lowercase letters denote time-harmonic signals, and uppercase letters denote (quasi-)DC signals. To obtain the design equations for the class E/DE WPT system, the following initial assumptions

[2]We have chosen to use the letter ζ for the duty cycle, to avoid confusion with the annotation of diodes.

are made:

- switch S and diodes D_1 and D_2 are ideal, i.e. they have zero resistance or voltage drop in the ON-state, they have no leakage current in the OFF-state, and switching ON or OFF happens instantaneously;
- the passive components are ideal;
- L_c is sufficiently large for the input current to be considered DC, and C_b is large enough for the current and voltage consumed by R_L to be constant;
- currents i_1 and i_2 are perfectly sinusoidal;
- the parasitic capacitance of switch S is completely absorbed by C_s;
- the parasitic capacitance of diode D_n is completely absorbed by C_{Dn}, $n = 1, 2$.

The components depicted in Figure 3.1 will be introduced throughout the following subsections. The effect of the losses that are associated with the components being not ideal, will be ignored for now. This will be taken into account later in this chapter. Considerations regarding the choice of physical components are discussed in more detail in relation to the case study in Section 3.4.

The procedure described hereafter is iterative in general. It is possible that a solution is found on the first try, but it is also possible that no solution can be found immediately. At the end of this section, an iteration strategy will be discussed.

3.3.1 Coils

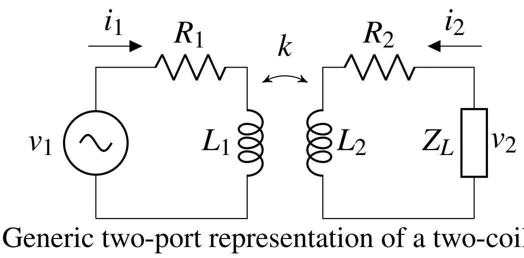

Figure 3.2: Generic two-port representation of a two-coil WPT system.

The MPTE of the system is determined by the load impedance and the coil parameters. As the load impedance is determined by the system requirements, the design process starts with the selection of the coils. Consider a Tx and an Rx coil, with self inductances L_1 and L_2, respectively, and with equivalent series resistances (ESRs) R_1 and R_2, respectively, as depicted in Figure 3.2. Note that the ESR of a coil is frequency dependent, and should thus be determined at the desired operating frequency $\omega = 2\pi f$. The coupling factor between the coils is k, and the mutual inductance is given as

$$M = k\sqrt{L_1 L_2}, \tag{3.1}$$

and the (unloaded) quality factor Q of each coil is given as

$$Q_i = \frac{\omega L_i}{R_i}, \qquad i = 1, 2... \tag{3.2}$$

Coil size and alignment

The available space for coils is often severely limited in WPT systems for biomedical applications. It is important to determine how large the coils can be. In general, larger diameter circular coils have a better coupling factor k, which is beneficial for the overall efficiency of the system [171]. Adding turns will also improve k, but will additionally increase the ESR, and lower the SRF of the coil.

Software like FastHenry [106] can be used to obtain values for the inductances and ESRs, as well as the coupling factor. These values can be used to get insight in the maximum achievable efficiency of the link, as will be shown later on. The effect of increasing the coil diameter or number of turns can also be calculated, using such a software tool.

Depending on the application, the alignment of the coils can be subject to variation every charge cycle or even during one charge cycle, and consequently the WPT link is required to operate efficiently over a range of k. Larger diameter coils generally have a better tolerance for misalignment. Tools like FastHenry [106] can be used to obtain an estimate for the range in k that can be expected.

Maximum power transfer efficiency

For the two-coil system[3], shown in Figure 3.2, the impedance matrix is given as

$$\begin{aligned} \begin{bmatrix} v_1 \\ v_2 \end{bmatrix} &= \begin{bmatrix} z_{11} & z_{21} \\ z_{12} & z_{22} \end{bmatrix} \begin{bmatrix} i_1 \\ i_2 \end{bmatrix} = \begin{bmatrix} r_{11} + \mathrm{j}x_{11} & r_{21} + \mathrm{j}x_{21} \\ r_{12} + \mathrm{j}x_{12} & r_{22} + \mathrm{j}x_{22} \end{bmatrix} \begin{bmatrix} i_1 \\ i_2 \end{bmatrix} \\ &= \begin{bmatrix} R_1 + \mathrm{j}\omega L_1 & \mathrm{j}\omega M \\ \mathrm{j}\omega M & R_2 + \mathrm{j}\omega L_2 \end{bmatrix} \begin{bmatrix} i_1 \\ i_2 \end{bmatrix}, \end{aligned} \tag{3.3}$$

where the system is reciprocal, i.e. $z_{21} = z_{12}$, and where $r_{12} = 0$ [44]. The input impedance $\frac{v_1}{i_1}$ is given as

$$Z_{in} = z_{11} - \frac{z_{12}^2}{z_{22} + Z_L}. \tag{3.4}$$

[3]The reader is referred to Dionigi [44] for cases with more than two coils.

Dionigi [44] states that it is possible to determine a unique optimal load impedance $Z_{L,opt}$ for any n-coil system, such that the PTE for that particular setup is maximized[4]. The PTE is given as

$$\eta = \frac{P_{out}}{P_{in}} = \frac{\mathrm{Re}\{Z_L\}}{\mathrm{Re}\{Z_{in}\}} \left| \frac{z_{12}}{z_{22} + Z_L} \right|^2. \tag{3.5}$$

The PTE for any two-port network is maximized by finding the load impedance that yields $\delta\eta/\delta\mathrm{Re}\{Z_L\} = 0$ and $\delta\eta/\delta\mathrm{Im}\{Z_L\} = 0$. Solving for those two conditions results in the load resistance and reactance that yield MPTE as

$$R_{L,opt} = R_2\sqrt{1 + \frac{\omega^2 M^2}{R_1 R_2}}, \tag{3.6}$$

$$X_{L,opt} = -\omega L_2, \tag{3.7}$$

with the corresponding efficiency

$$\eta_{max} = \frac{\frac{\omega^2 M^2}{R_1 R_2}}{\left(\sqrt{1 + \frac{\omega^2 M^2}{R_1 R_2}} + 1\right)^2} = \frac{k^2 Q_1 Q_2}{\left(\sqrt{1 + k^2 Q_1 Q_2} + 1\right)^2}. \tag{3.8}$$

Note that this is the efficiency of the two port network only, i.e. the coils and their ESRs, as depicted in Figure 3.2, and as such does not incorporate losses in the inverter or rectifier. These will be added later.

3.3.2 Class DE rectifier

The rectifier should be designed such that its input impedance is equal to the optimal load $Z_{L,opt} = R_{L,opt} + \mathrm{j}X_{L,opt}$, as given in Eqs. (3.6) and (3.7). $Z_{L,opt}$ can be represented by an optimal resistor $R_{L,opt}$ in series with an optimal capacitor $C_{L,opt} = (-\omega X_{L,opt})^{-1} = (\omega^2 L_2)^{-1}$.

The input impedance of a class DE rectifier can be approximated by an equivalent circuit, as shown in Figure 3.3, consisting of a resistor R_i in series with a capacitor C_i [66]. The rectifier shall be designed such that its input resistance R_i is equal to $R_{L,opt}$, using the diode duty cycle ζ_d as tuning element. The corresponding input capacitance C_i can then be determined, and a series capacitor C_2 can be added, such that the series combination of C_i and C_2 is equal to $C_{L,opt}$.

The input resistance of a class DE rectifier is given as [152]:

$$R_i = \frac{R_L[1 - \cos(2\pi\zeta_d)]^2}{2\pi^2}, \tag{3.9}$$

[4] Solutions for maximum power on the load (MPL) are also presented by Dionigi [44].

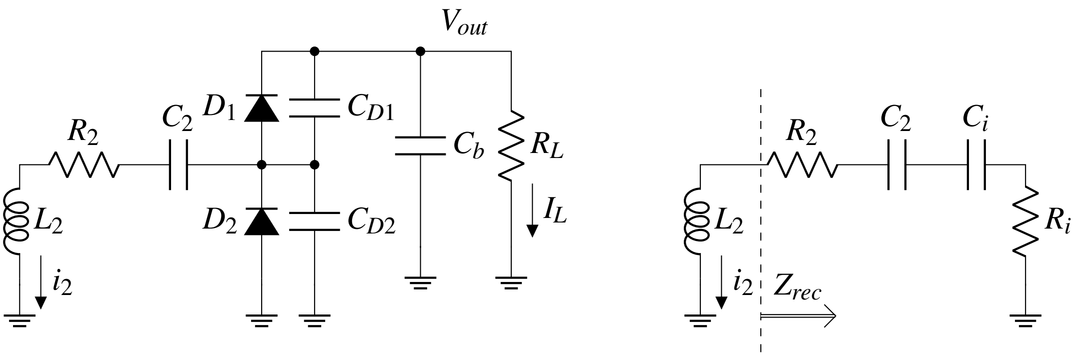

Figure 3.3: class DE rectifier (left) and its equivalent circuit (right).

where ζ_d is the duty cycle of both diodes D_1 and D_2. By substituting the value of $R_{L,opt}$ found in Eq. (3.6) for R_i, the value of the diode duty cycle that results in MPTE, $\zeta_{d,opt}$, can be found. Using this value, the required values for C_{D1} and C_{D2} can be calculated as [152]:

$$C_{D1} = C_{D2} = \frac{\pi[1 + \cos(2\pi\zeta_{d,opt})]}{\omega R_L[1 - \cos(2\pi\zeta_{d,opt})]}, \tag{3.10}$$

which allows us to determine the value of the equivalent input capacitance of the rectifier as [152]:

$$C_i = \frac{2\pi(C_{D1} + C_{D2})}{\sin(4\pi\zeta_{d,opt}) + 2\pi(1 - 2\zeta_{d,opt})}. \tag{3.11}$$

Using circuit theory and Eq. (3.7), the value of C_2 can now be determined as

$$C_2 = \frac{C_i}{\omega^2 L_2 C_i - 1}, \tag{3.12}$$

and the equivalent capacitance of the series connection of C_i and C_2 can be defined as

$$C_r = \frac{C_i C_2}{C_i + C_2}. \tag{3.13}$$

The amplitude of the rectifier input current equals [65]:

$$i_2 = \frac{2\pi I_L}{1 - \cos(2\pi\zeta_{d,opt})}, \tag{3.14}$$

where I_L is the DC output current flowing through R_L. For this analysis, the output voltage and current are assumed to be DC, but in reality, they will contain a small RF ripple. The value of C_b influences the amplitude of this ripple. Using circuit theory, the minimum value of buffer capacitor C_b, which corresponds to a maximum peak-to-peak output voltage ripple ΔV, can be determined using

$$C_b \geq \frac{I_L}{\omega \Delta V}. \tag{3.15}$$

When the receiver is in resonance, the impedance of C_2 in series with C_i cancels the impedance of L_2. The induced secondary voltage can thus be expressed as

$$v_{ind} = (R_2 + R_i)i_2. \tag{3.16}$$

The rectifier impedance as seen by L_2 can be expressed as

$$Z_{rec} = R_2 + R_i + \frac{1}{\mathrm{j}\omega C_r}. \tag{3.17}$$

The quantities introduced in this subsection will be used in the design of the inverter, which will be outlined next.

3.3.3 Class E inverter

The current through the Tx coil can be expressed as [152]:

$$i_1 = \frac{v_{ind}}{\omega M}, \tag{3.18}$$

where v_{ind} is the induced secondary voltage, as given by Eq. (3.16).

Figure 3.4(a) shows the class E inverter [152], and Figures 3.4(b)-(d) show three equivalent circuits. The real and imaginary parts of the equivalent impedance $Z_{eq} = R_{eq} + \mathrm{j}\omega L_{eq}$ of the coupled rectifier as seen by the inverter, depicted in Figure 3.4(c), can be expressed as

$$R_{eq} = \frac{k^2\omega^2 L_1 L_2 (R_2 + R_i)}{(R_2 + R_i)^2 + \left(\omega L_2 - \frac{1}{\omega C_r}\right)^2}, \tag{3.19}$$

$$L_{eq} = L_1(1 - k^2) + \frac{k^2 L_1 \left[(R_2 + R_i)^2 - \frac{L_2}{C_r} + \left(\frac{1}{\omega C_r}\right)^2\right]}{(R_2 + R_i)^2 + \left(\omega L_2 - \frac{1}{\omega C_r}\right)^2}. \tag{3.20}$$

The load impedance $R_1 + Z_{eq} = R_1 + R_{eq} + \mathrm{j}\omega L_{eq}$ is transformed into $Z_{inv} = R_{inv} + \mathrm{j}\omega L_{inv}$ by the impedance transformation component[5] $X_p = (-\omega C_p)^{-1}$, resulting in the typical class E inverter circuit shown in Figure 3.4(d). By comparing with Figure 3.4(b), we find

$$Z_{inv} = R_{inv} + \mathrm{j}\omega L_{inv} = \frac{1}{\frac{1}{R_1 + R_{eq} + \mathrm{j}\omega L_{eq}} + \mathrm{j}\omega C_p}, \tag{3.21}$$

which results in

[5] In practice, Eq. (3.30), in which the value for X_p is determined, will often result in a negative value, meaning that X_p will be a capacitor. This will be the assumption in this thesis. It is left to the reader to adapt the equations in the rare case that X_p is inductive.

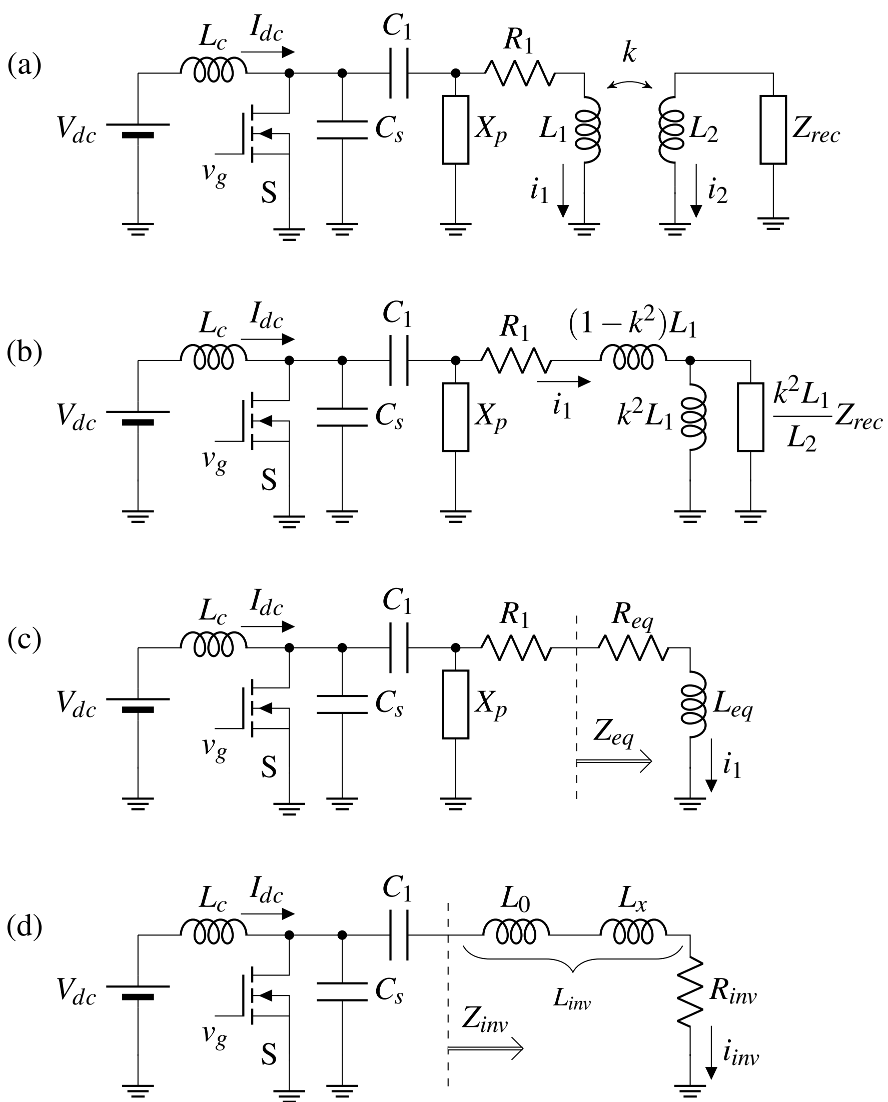

Figure 3.4: Class E inverter (a), equivalent circuit including the coupled rectifier (b), simplified equivalent circuit (c), and equivalent typical circuit (d).

$$R_{inv} = \frac{R_{eq}+R_1}{\omega^2 C_p^2\left[(R_{eq}+R_1)^2+\left(\omega L_{eq}-\dfrac{1}{\omega C_p}\right)^2\right]}, \tag{3.22}$$

$$L_{inv} = \frac{L_{eq}(1-\omega^2 L_{eq}C_p)-C_p(R_{eq}+R_1)^2}{\omega^2 C_p^2\left[(R_{eq}+R_1)^2+\left(\omega L_{eq}-\dfrac{1}{\omega C_p}\right)^2\right]}. \tag{3.23}$$

As the inverter circuit is now the typical class E layout, many design strategies can be applied from this point onwards [112]. It is even possible to design the system for an inverter from a different class by using Z_{inv} as the load impedance. We shall follow the approach from [112].

The magnitude of the inverter output current i_{inv} relates to the power supply voltage V_{dc}, when ZVS and ZDS conditions are satisfied [112], as

$$i_{inv} = -\frac{2\sin(\pi\zeta_s)\sin(\pi\zeta_s+\varphi_1)}{\pi(1-\zeta_s)R_{inv}}V_{dc}, \tag{3.24}$$

where ζ_s is the duty cycle of the switch, and φ_1 is the phase-shift between the inverter output current i_{inv} and the switch drive signal v_g, which can be expressed as

$$\varphi_1 = \pi + \arctan\left[\frac{\cos(\pi\zeta_s)-1}{2\pi(1-\zeta_s)+\sin(2\pi\zeta_s)}\right]. \tag{3.25}$$

The power supply current I_{dc} is given as [112]:

$$I_{dc} = \frac{\cos(2\pi\zeta_s+\varphi_1)-\cos\varphi_1}{2\pi(1-\zeta_s)}i_{inv}. \tag{3.26}$$

To meet the ZVS and ZDS conditions, the load of the inverter should be inductive [112]. For the sake of analysis, L_{inv} was virtually divided into two series inductances L_0 and L_x, the first of which is resonant with C_1 at operation frequency ω. The excess inductance L_x realizes the phase shift required to meet ZVS and ZDS conditions, its value can be found using Eq. (3.27), see also [112]:

$$L_x = \frac{R_{inv}}{\omega}\left[\frac{2(1-\zeta_s)^2\pi^2-1+2\cos\varphi_1\cos(2\pi\zeta_s+\varphi_1)}{4\sin\pi\zeta_s\cos(\pi\zeta_s+\varphi_1)\sin(\pi\zeta_s+\varphi_1)[(1-\zeta_s)\pi\cos\pi\zeta_s+\sin\pi\zeta_s]}\right.$$
$$\left.-\frac{\cos[2(\pi\zeta_s+\varphi_1)][\cos2\pi\zeta_s-\pi(1-\zeta_s)\sin2\pi\zeta_s]}{4\sin\pi\zeta_s\cos(\pi\zeta_s+\varphi_1)\sin(\pi\zeta_s+\varphi_1)[(1-\zeta_s)\pi\cos\pi\zeta_s+\sin\pi\zeta_s]}\right]. \tag{3.27}$$

The value of R_{inv}, which can be found using Eq. (3.22), depends on C_p, which is yet to be determined. An extra constraint should be put on the value of R_{inv}, which can be derived from Figure 3.4. The power in the equivalent circuits can be equated to obtain

$$i_1^2(R_{eq}+R_1) = i_{inv}^2R_{inv}, \tag{3.28}$$

such that it can be used together with Eq. (3.24) to get

$$R_{inv} = \frac{2\sin^2(\pi\zeta_s)\sin^2(\pi\zeta_s+\varphi_1)V_{dc}^2}{\pi^2(1-\zeta_s)^2i_1^2(R_{eq}+R_1)}, \tag{3.29}$$

which can be equated to Eq. (3.22) such that the value for impedance X_p can be obtained as

$$X_p = \frac{-R_{inv}\left[(R_{eq}+R_1)^2+\omega^2L_{eq}^2\right]}{\omega L_{eq}R_{inv} \pm \sqrt{R_{inv}(R_{eq}+R_1)\left[(R_{eq}+R_1)(R_{eq}+R_1-R_{inv})+\omega^2L_{eq}^2\right]}}. \tag{3.30}$$

The equation has two solutions, of which the one that satisfies $L_0 = L_{inv} - L_x > 0$ should be chosen, as the value of L_0 can not be negative.

As stated before, the series capacitor C_1 resonates with L_0 [112]. Its value follows from

$$C_1 = \frac{1}{\omega^2 L_0} = \frac{1}{\omega^2 (L_{inv} - L_x)}. \tag{3.31}$$

The value of the shunt capacitor C_s can be calculated as [112]:

$$C_s = \frac{2 \sin \pi\zeta_s \cos(\pi\zeta_s + \varphi_1) \sin(\pi\zeta_s + \varphi_1)[(1-\zeta_s)\pi \cos \pi\zeta_s + \sin \pi\zeta_s]}{\omega\pi^2(1-\zeta_s)R_{inv}}. \tag{3.32}$$

The current through the shunt inductor L_c is assumed to be constant, which can in fact only be valid if its inductance is infinite. In practice, when a finite value is used, there will always be a ripple on the current I_{dc}. How much ripple is acceptable, depends on the application. When we want to limit this ripple to, for example, 10% of the DC current, the required minimum inductance can be found using [112]:

$$L_c \geq \frac{2\pi R_{inv}}{\omega} \left(\frac{\pi^2}{2} + 2 \right). \tag{3.33}$$

It should be noted that choosing a smaller value might also work, but can have some drawbacks. Firstly, the peak current through L_c increases, which increases its required current handling capabilities. Secondly, the ripple current in the circuit increases, possibly causing unwanted electromagnetic interference (EMI) effects. Lastly, as the design equations are based on the assumption that the current through L_c is DC, an increase in ripple current might cause the realised WPT link to not behave exactly as designed.

Finally, the required power supply voltage V_{dc} can be determined as [112]:

$$V_{dc} = \frac{I_{dc}}{\omega C_1} \frac{(1-\zeta_s)[\pi(1-\zeta_s)\cos \pi\zeta_s + \sin \pi\zeta_s]}{\tan(\pi\zeta_s + \varphi_1) \sin \pi\zeta_s}, \tag{3.34}$$

where it should be noted that this value is not very critical; changing V_{dc} will influence the output voltage, but was found to have hardly any effect on the efficiency. More details can be found in Section 3.3.6.

3.3.4 Controller

We choose to operate the switch of the inverter at a duty cycle of 50%, as this drive signal can be generated with just three basic components. The circuit in Figure 3.5 shows a circuit that creates a 6.78 MHz gate drive signal with $\zeta_s = 0.5$.

A crystal oscillator creates a 13.56 MHz signal, the waveform shape of which is not critical. This signal is fed into the edge-triggered clock-pin of a D-type flip-flop. In this configuration, the flip-flop toggles the logic level of the output every period of the input

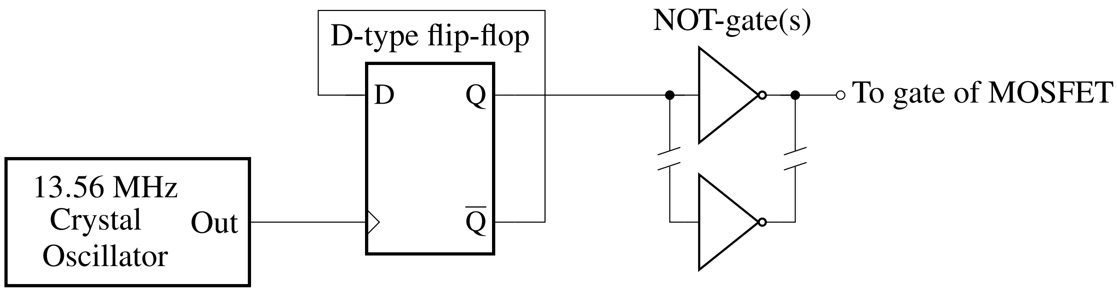

Figure 3.5: 50% duty cycle 6.78 MHz oscillator and gate driver.

signal, effectively halving the input frequency and creating a square wave with a 50% duty cycle. The output of the flip-flop is fed to n parallel NOT-gates, that together can supply the current required to drive the gate of MOSFET S in the class E inverter in Figure 3.1. The required number of NOT-gates depends on the output current capability of each NOT-gate, and on the current required to drive the gate of the MOSFET.

We assume the amplitude of the gate-source voltage required to drive the MOSFET can be supplied directly by the NOT-gate. If this is not the case, the NOT-gate can be replaced either by a NOT-gate that accepts a higher supply voltage, combined with a level shifter to increase the input voltage swing, or by a dedicated gate driver chip.

It is possible to add extra safety features to the circuit, such as a current sensor that measures whether or not the input current I_{dc} (see Figure 3.1) is within predefined safety limits, or a temperature sensor. The output of such a sensor can be connected to the reset pin of the flip-flop (not shown in the circuit), such that the gate voltage becomes zero when an unsafe condition is detected. For the proof of concept demonstrator, designed in this chapter, these safety features are not included.

3.3.5 Efficiency

The power dissipation in the system can be approximated analytically, and the efficiency can be derived from it. To do so, the first two assumptions made in the beginning of Section 3.3 are abandoned, i.e. the components are no longer ideal.

The power dissipated in the input choke inductor L_c (see Figure 3.1) is

$$P_{Lc} = R_{Lc} I_{dc}^2, \tag{3.35}$$

where R_{Lc} is the ESR[6] of L_c.

The root mean square (RMS) value of the current through the MOSFET $I_{S,rms}$, and through the shunt capacitor $I_{Cs,rms}$, depicted in Figure 3.4, are given by [112]:

[6]Note again that the resistance of a coil is frequency dependent, and should thus be determined at the operating frequency.

$$i_{S,rms} = \frac{i_{inv}}{2}\sqrt{\frac{\pi^2+28}{\pi^2+4}}, \tag{3.36}$$

$$i_{Cs,rms} = \frac{i_{inv}}{2}\sqrt{\frac{\pi^2-4}{\pi^2+4}}, \tag{3.37}$$

resulting in dissipation in the MOSFET and shunt capacitor as follows:

$$P_S = R_{DS} i_{S,rms}^2 = \frac{R_{DS} i_{inv}^2}{4}\frac{\pi^2+28}{\pi^2+4}, \tag{3.38}$$

$$P_{Cs} = R_{Cs} i_{Cs,rms}^2 = \frac{R_{Cs} i_{inv}^2}{4}\frac{\pi^2-4}{\pi^2+4}, \tag{3.39}$$

where R_{DS} is the drain-source ON-resistance of the MOSFET, and R_{Cs} is the ESR of C_s. Note that Eqs. (3.38) and (3.39) are valid for $\zeta_s = 0.5$ only.

The currents through the Tx and Rx coil are assumed to be sinusoidal. Therefore, we can define the losses in the Tx and Rx coils, and in capacitors C_1, C_p, and C_2 as

$$P_{R1} = \frac{R_1 i_1^2}{2}, \qquad P_{R2}, = \frac{R_2 i_2^2}{2}, \tag{3.40}$$

$$P_{C1} = \frac{R_{C1} i_{inv}^2}{2}, \qquad P_{C2} = \frac{R_{C2} i_2^2}{2}, \tag{3.41}$$

$$P_{Cp} = \frac{R_{Cp}(i_{inv}-i_1)^2}{2}, \tag{3.42}$$

where R_{Ca} is the ESR of capacitor C_a, $a = 1, p, 2$.

The combined loss in the two rectifier diodes D_1 and D_2, assuming both are identical, is [65]:

$$P_D = 2I_L V_{th} + \pi I_L^2 R_D \frac{4\pi\zeta_d - \sin 4\pi\zeta_d}{(1-\cos 2\pi\zeta_d)^2}, \tag{3.43}$$

where V_{th} is the diode threshold voltage, and R_D is its ON resistance.

The combined loss in the two shunt capacitors C_{D1} and C_{D2}, assuming both are identical, is given by [65]:

$$P_{Cd} = \pi I_L^2 \frac{R_{Cd}}{2}\frac{2\pi(1-2\zeta_d)+\sin 4\pi\zeta_d}{(1-\cos 2\pi\zeta_d)^2}, \tag{3.44}$$

where R_{Cd} is the ESR of capacitors C_{D1} and C_{D2}.

To drive MOSFET S, its gate is charged and discharged each cycle. The power this takes is

$$P_G = \frac{v_g Q_{G(tot)} \omega}{4\pi}, \tag{3.45}$$

where v_g is the amplitude of the gate drive voltage, and $Q_{G(tot)}$ is the total gate charge.

We can now get an estimate of the power dissipation in the inverter P_{inv}, the link P_{link}, and the rectifier P_{rect} by calculating

$$P_{inv} = P_G + P_S + P_{Lc} + P_{Cs} + P_{C1} + P_{Cp}, \tag{3.46}$$

$$P_{link} = P_{R1} + P_{R2}, \tag{3.47}$$

$$P_{rect} = P_D + P_{C2} + P_{Cd}. \tag{3.48}$$

The theoretical efficiency of the WPT system is then

$$\eta_{tot} = \frac{I_L^2 R_L}{I_L^2 R_L + P_{inv} + P_{link} + P_{rect}}. \tag{3.49}$$

3.3.6 Iteration strategy

To solve the above equations, an initial guess for the input voltage V_{dc} is required in Eqs. (3.24) and (3.29), as the optimal value for V_{dc} is only calculated as the final step in Eq. (3.34). In the best case scenario, the initial guess is (approximately) equal to the result of Eq. (3.34), in which case the design is complete. However, chances are that the difference is significant, and further steps are required.

One approach is to change the initial guess for V_{dc} and iterate until it is (approximately) equal to the result of Eq. (3.34). However, this assumes that it is actually possible to generate this value for V_{dc} in your transmitter. This might not always be the case.

A different approach allows for some freedom in the choice of V_{dc}. When the actual input voltage of the inverter differs from the optimal value calculated in Eq. (3.34), the link will still perform and be efficient, only the voltages and currents will be different. If we supply the inverter with a higher voltage than designed, the output voltage will also be higher. Consequently, when we would design the WPT system to have an output voltage that is lower than actually desired, and supply it with a higher voltage than it was designed for – or vice versa – we could eventually end up with a system that outputs the required voltage, without compromising the efficiency. The iteration procedure is described in Figure 3.6.

When the WPT system is supplied with a different voltage than designed, one should pay attention when calculating the losses using Eqs. (3.35) through (3.44), as the currents in the system change accordingly.

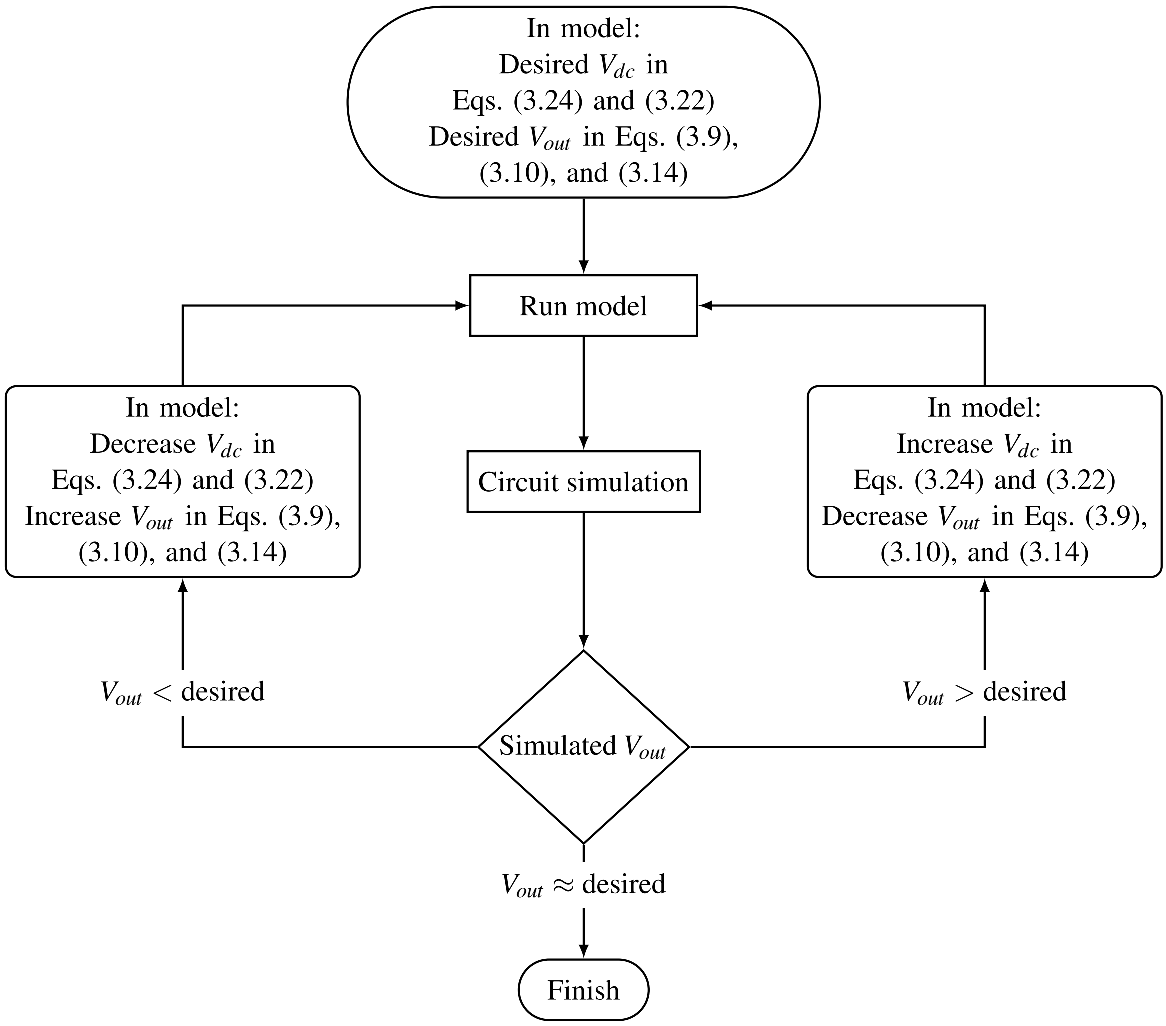

Figure 3.6: Iteration procedure to achieve efficient operation at arbitrary input and output voltage levels. For Eqs. (3.9), (3.10), and (3.14), use $V_{out} = R_L I_L$.

3.4 Case study: WPT to visual prosthesis

As described in Chapter 2, the visual prosthesis that is being designed in the NESTOR project [154] is expected to consume approximately 50 mW. If possible, we would like to transfer more power, to create some headroom, such that the system does not need a redesign when more electrodes are added to increase the phosphene count, when the electrode impedance is lowered, or when additional functionality is added. Based on experience gained during this research, we assume it should be possible to transfer 90 mW to a neuroprosthesis within the relevant safety standards, for a realistic range in distance and misalignment between the Tx and Rx coils. The inverter will be powered with $V_{dc} = 5$ V, which is directly available from a standard USB port.

3.4.1 Coil size

The design process starts with the selection of the coils. Their size, wire diameter, and turn count should be chosen such that the highest efficiency can be achieved. Note that optimizing the link efficiency is not a guarantee: the complete system should be optimized. Furthermore, the coils should be designed such that the system is robust against changes in distance and misalignment between the two coils, within realistic limits.

Available space for a subcutaneous Rx coil is limited, as described in Chapter 2. The maximum Rx coil diameter is 40 mm, and the thickness (including biocompatible coating) should be kept below 3 mm. Increasing the diameter or adding turns will improve k. Although adding turns will also increase the ESR and lower the SRF, we found that the increase in k outweighs the increase in ESR unless the operation frequency is too close to the SRF. During this research, we found that an operation frequency about $2-4$ times lower than the SRF is optimal in this respect. The Rx coil should thus have as much turns as possible with as thick wire as possible, without exceeding the size constraints, and whilst making sure the SRF is not too low (i.e. $2-4$ times higher than 6.78 MHz).

With software like FastHenry [106], inductances, ESRs and coupling factors can be calculated. With these values, the maximum achievable link efficiency - i.e. coils only - can be calculated or simulated [44]. FastHenry cannot calculate the coil's SRF, and the given ESR will be too low if the frequency of operation is close to the SRF (i.e. less than 4 times lower). Furthermore, the influence of the surrounding biological tissue is not taken into account. The influence of surrounding tissue can be lowered by coating the final coil, or by sealing it in a plastic film, as will be described later in this chapter.

Multiple Rx coils with a diameter of 35 mm were manufactured, with wire thicknesses of 0.25 and 0.6 mm, and 3 to 10 turns in 1 turn increments. They were sealed in a 2×125 μm thick PET pouch. Their properties were measured in a 0.9% (0.154 M) saline solution [104]. The Rx coil with 7 turns of 0.25 mm wire yields the highest maximum achievable efficiency. As explained in Chapter 2, copper wire cannot be used in the final product. A 0.25 mm diameter copper (Cu) wire corresponds to a 0.30 mm diameter gold (Au) wire, which can be used safely, but is not used in this prototype for economical reasons.

As explained in Chapter 2, the Tx coil should be as large as possible, within practical limits. With the aid of FastHenry [106], it was found that a flat coil with an inner diameter of 35 mm is sufficient to allow for a radial misalignment d of up to 15 mm, which is expected to be sufficient for aligning the coils in practice. As explained in Chapter 2, a thicker wire than in the Rx coil can be used, and the number of turns should be as high as possible. A flat Tx coil of 10 turns was chosen, with a wire diameter of 1.0 mm, resulting in an outer diameter of 55 mm, which is considered acceptably small. The measured ESR and SRF, which will be discussed next, are considered acceptable.

The candidate coils were modeled in FastHenry, and measured using a Keysight P5004A vector network analyser (VNA). The results are listed in Table 3.2. The increase in ESR of the Tx coil, compared to the simulations, is believed to be caused by the fact that the coil operates relatively close to its SRF, the effects of which FastHenry is unable to model accurately. The increase in ESR of the Rx coil is believed to be caused by both the fact that the coil operates relatively close to its SRF, and the fact that the measured coil is submerged in a 0.9% saline solution, instead of in air. Even though the Rx coil is sealed in a PET pouch, as described earlier, the measured parameters of the coil are negatively affected by submerging it into the saline solution, albeit the influence is much smaller than without the seal.

Table 3.2: Simulated and and measured Tx and Rx coil parameters at 6.78 MHz.

Coil	Calculated L	Measured L	Calculated R	Measured R	Measured SRF
Tx	6.90 μH	6.81 μH	1.16 Ω	3.00 Ω	25.5 MHz
Rx	4.86 μH	4.51 μH	2.91 Ω	3.54 Ω	23.0 MHz

3.4.2 Coil alignment

As discussed in Chapter 2, the height h between the external Tx coil and implanted Rx coil is in the range from 8 to 15 mm. The misalignment d between the coils is expected to be at most 15 mm. Figure 3.7 shows the positioning of the two coils.

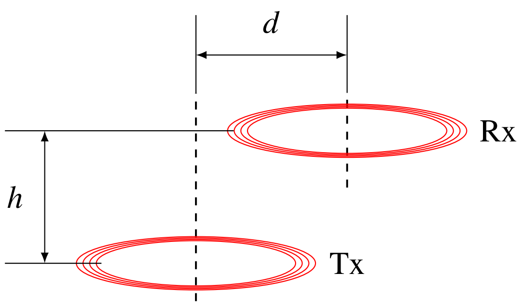

Figure 3.7: Separation h and radial misalignment d between the coils.

For different values of h and d, see Figure 3.7, the mutual and self inductances M and L and the ESRs of the coils are measured using a Keysight P5004A VNA. Next, the expected maximum theoretical link efficiency η_{max} is calculated using Eq. (3.8). The link has to operate for $8 \leq h \leq 15$ mm and $0 \leq d \leq 15$ mm, which can be seen to correspond to a range for the coupling factor k of roughly $0.14 \leq k \leq 0.37$, see Figure 3.8(a). The corresponding maximum theoretical link efficiency η_{max} is between 86 and 95%, see Figure 3.8(b).

The value for η_{max} is an indicative upper bound only, and will not be met in practice, because losses in the inverter and rectifier are present. Furthermore, the load is assumed to be optimized for each value of k, whereas in practice, only a single value can be chosen[7], and all other cases will implicitly operate with a load that is (slightly) less optimal.

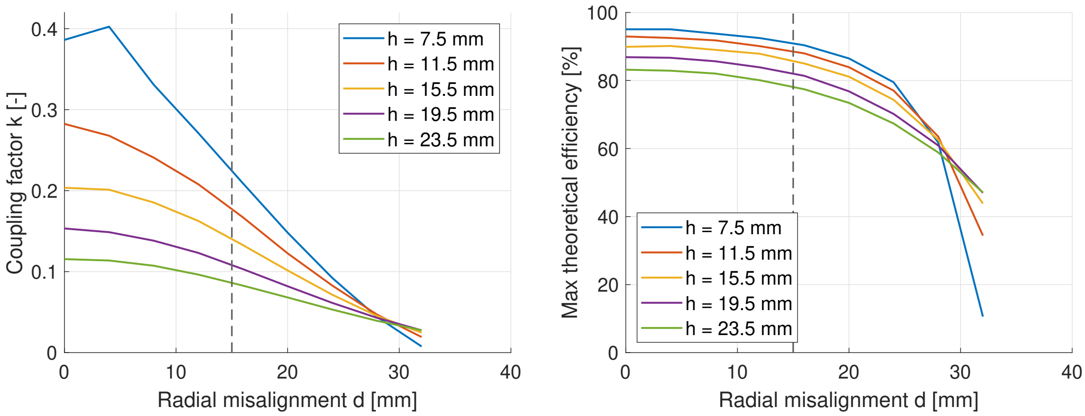

(a) Measured coupling factor. **(b)** Maximum theoretical efficiency.

Figure 3.8: Measured coupling factor k and maximum theoretical link efficiency η_{max} for different combinations of separation distance h and radial misalignment d. The dashed line denotes $d = 15$ mm, the upper limit of the required radial misalignment range.

Coupling factor

Even though the link will be optimized for a single value k_{opt} only, it should be designed such that its performance is acceptable for the full range of k.

The initial guess for k_{opt} was 0.25, as this is in the middle of the required range. The results of the design process , as described in Section 3.3, were simulated in LTspice [138], as will be explained in more detail next. It was found that the required output voltage of 7 V, as explained in Chapter 2, could not be reached for the required range of k, and therefore $k_{opt} = 0.25$ was rejected. After some iteration, the value $k_{opt} = 0.20$ was chosen, as the resulting in an output voltage above 7 V for the required range of k.

The described iteration procedure of Section 3.3.6 is not followed for this prototype. The

[7] It is possible to design a WPT system for coupling-independent operation, but this requires a variable frequency of operation [32], which is not desired in a medical application [55].

reason is that, even without iteration, the minimum required output voltage can be received for the required range of k, and hence no further iteration is required. Consequently, at $k = k_{opt}$, the actual output voltage is higher than the required value. The increase in output voltage appears to be proportional to the difference between the actual and optimal value of the input voltage, i.e. when the applied input voltage is $X\%$ higher than the optimal value, calculated in Eq. (3.34), the actual output voltage will also be approximately $X\%$ higher than the output voltage for which the link was designed.

3.4.3 Electronics design

The measured coil parameters were subsequently used in the design equations of Section 3.3. The resulting design was simulated in LTspice [138]. Table 3.3 lists the calculated component values for the inverter and rectifier, and the ones used in the circuit simulation. Three simulated values notably differ from their calculated values: C_s, $C_{D1,2}$ and L_c. C_s is smaller than calculated to compensate for the output capacitance of MOSFET S, which is in the same order of magnitude. L_c is smaller than calculated, because available discrete parts with an inductance larger than 47 μH are not suitable, since their size is too large, their losses are too high, or their SRF is too low. The difference in the value of $C_{D1,2}$ has a different nature.

The capacitance of the diodes $D_{1,2}$ is much lower than $C_{D1,2}$, so these do not need to be compensated for. The sensitivity of the simulation to tolerances in the component values was investigated. For all components, a 5% change does not significantly influence the result. However, during this process, it was found that lowering $C_{D1,2}$ resulted in a slightly better efficiency, and in a slightly higher output voltage at higher values of k. The best efficiency could be achieved for $C_{D1,2} = 36$ pF, although it has to be noted that the improvement in efficiency is less than 3% compared to the $C_{D1,2} = 63$ pF case.

Table 3.3: Calculated component values, and those used in the circuit simulation.

Component	Calculated value	Value used in simulation
C_1	82.6 pF	82 pF
C_2	166.1 pF	168 pF
C_p	17.0 pF	15 pF
C_s	61.8 pF	22 pF
$C_{D1,2}$	63.0 pF	36 pF
L_C	71.7 μH	47 μH

The simulated output voltage is shown as a function of k in Figure 3.9(a). At $k = k_{opt}$, the output voltage is 9.91 V, which corresponds to an output power of 181 mW. This is higher than designed, which is caused by the fact that the link operates at an input voltage $V_{dc} = 5.0$ V, being about 35% higher than the optimal value calculated in [65]. The simulated output voltage is about 42% higher than the output voltage for which the link was designed, which is in the same order of magnitude as the previously mentioned 35%.

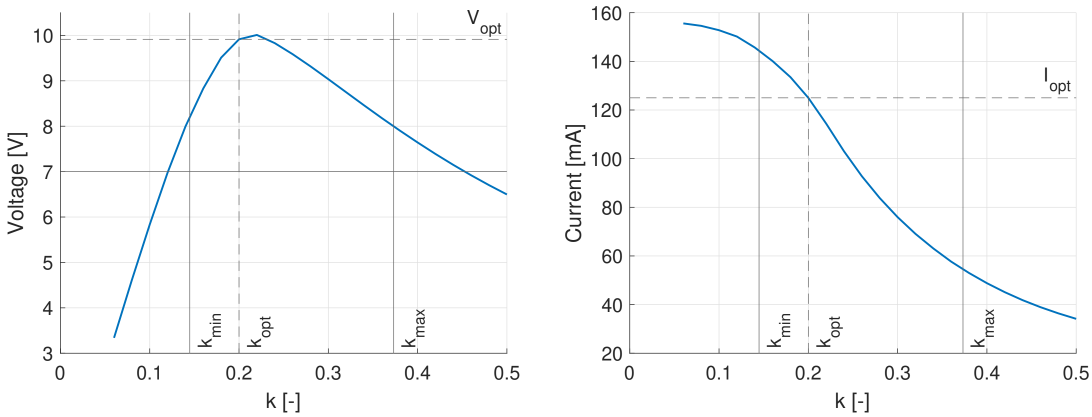

(a) Simulated DC output voltage. **(b)** Simulated Tx coil current.

Figure 3.9: Simulated DC output voltage and Tx coil current as a function of k.

The advantage of this higher output voltage is that the required 7.0 V is achieved for a range of values for k, rather than only at $k = k_{opt} = 0.20$. Circuit simulations show this range to be $0.12 \leq k \leq 0.45$, which includes the complete design range $0.14 \leq k \leq 0.37$, as shown in Figure 3.9(a).

The amplitude of the current through the Tx coil I_1, at $k = k_{opt}$, is calculated to be 68.9 mA. As can be seen in Figure 3.9(b), circuit simulations show it to be about 81% higher. This suggests that the Tx coil current scales with the square of the power supply voltage V_{dc}, which would be 82% in this case.

3.4.4 Selection of parts

MOSFETS and diodes have parasitic capacitances, which add to the capacitors that are connected parallel to them. The MOSFET and diodes should thus be chosen such that their parasitic capacitances are (well) below the values of C_s and $C_{D1,2}$, respectively. For the diode, a Schottky diode with $C_j < 3.6$ pF was chosen, and the MOSFET has $C_{oss} < 50$ pF. As these values are voltage dependent, it requires some fine tuning in LTspice to find the optimal value for C_s and $C_{D1,2}$. Table 3.4 shows the components used in the final prototype. The capacitors have a tolerance of $\pm 5\%$ or better. The oscillator and each of the chips (flip-flop, NOT-gate, 3.3 V regulator) have a decoupling capacitor connected at the power pins, as specified in their respective data sheets. In case no value is specified in the data sheet, 100 nF is used.

The prototype should preferably be as small as possible, yet the components should not be too small, as they will be soldered by hand. Therefore, SMD capacitors with a 0603 form factor were used, and chips with a pitch of at least 0.5 mm.

Components such as capacitors and inductors are not ideal in practice. They are chosen such that their SRF is at least twice the operating frequency. Furthermore, they are chosen to

Table 3.4: Components used in the prototype.

Component	Value	Part number
C_1	82 pF	251R14S820JV4T
C_2	168 pF	CBR06C680F5GAC
	$(100+68)$	06031A101JAT2A
C_p	15 pF	SQCSVA150JAT1A
C_s	22 pF	251R14S220JV4T
$C_{D1,2}$	36 pF	CBR06C360F5GAC
C_b	2×100 nF	GRM188R72A104KA35D
L_C	47 μH	DS1608C-473MLC
R_L	544.4 Ω	560 // 22K // 180K Ω
S	GaN MOSFET	GS-065-004-1-L
$D_{1,2}$	Schottky	BAS40-04
Oscillator	13.56 MHz	X1G004451007312
Flip-flop	D-type	NC7SZ74K8X
NOT-gate	Triple	74LVC3G14DC,125
Voltage regulator	3.3 V	MIC5504-3.3YM5-TR
Decoupling capacitor	100 nF	GRM188R72A104KA35D
Decoupling capacitor	1 μF	GCM188R71C105KA64D

have an ESR as low as possible, and a Q-factor as high as possible.

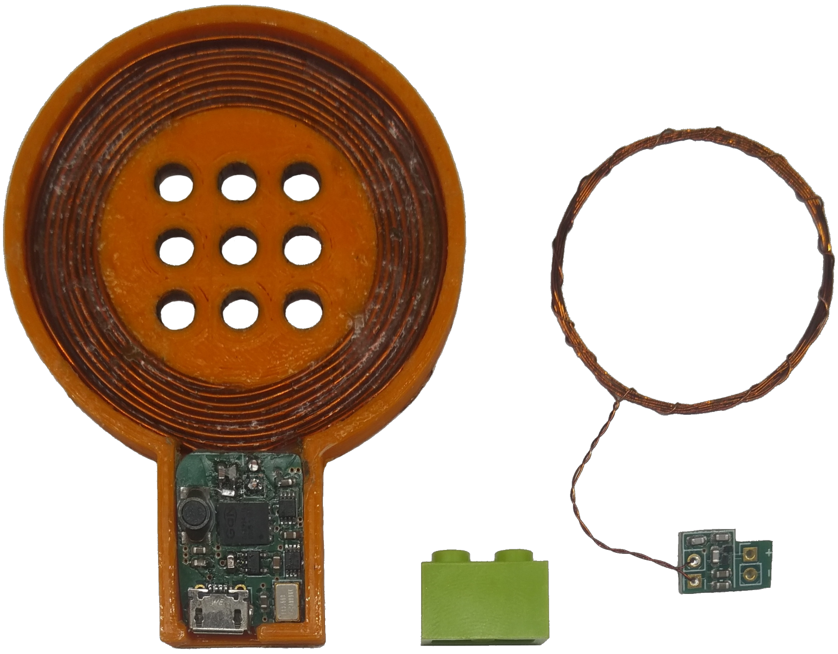

Figure 3.10: Realized transmitter (left) and receiver (right) prototypes. Standard 2×1 LEGO® brick for size.

Figure 3.10 shows the finished prototype. A detailed analysis of the performance under different load conditions is presented in the next section. The total printed circuit board (PCB) area of the inverter prototype measures $21.0 \times 16.0 = 336$ mm^2, including a micro-USB connector for power. The rectifier measures $7.2 \times 8.3 = 59.76$ mm^2. The combined cost of the components, excluding the PCB and Tx and Rx coils, is less than €10,- in bulk manufacture.

The size of the receiver PCB can be decreased to $7.4 \times 6.4 = 47.36$ mm^2 when the BAS40-04 diode is replaced by the PMEG6002ELDYL diode. An additional advantage is that the circuit simulations show an increase in efficiency of up to 6.5%, depending on k. The PMEG6002ELDYL, however, measuring only $1.0 \times 0.6 \times 0.4$ mm, was found to be very hard to solder by hand. Therefore, the presented results are generated with the BAS40-04.

3.4.5 Safety limits

A biomedical implant should meet several exposure limits before it can be considered safe. In particular, tissue should not heat up too much as a result of generated EM fields [213, 245] and heat generation in the implant [52, 95], and the transmitted magnetic fields should stay below certain limits at a distance [31, 55].

Tissue heating by EM fields

When EM fields interact with biological tissue, energy is absorbed in the tissue, which consequently heats up. The specific absorption rate (SAR) of the tissue can be calculated by averaging $\frac{1}{2}\sigma|\vec{E}|^2$ over a defined mass. According to [213, 245], the SAR limit for continuous local exposure of the human head is 2 W/kg, to be averaged over a 10 g cubic volume.

The coils were simulated in Simulia CST Studio Suite®, using the dielectric properties of Table 3.5 [68] for the human tissues involved. The Rx coil is assumed to be flat. The Tx coil current amplitude was obtained through the LTspice simulation described earlier and depends on the distance h and misalignment d between the coils, as can be deduced from Figures 3.8(a) and 3.9(b). The corresponding SAR was obtained for a planarly layered model with a scalp thickness of 2 to 4 mm, a skull thickness of 6.5 mm, and a cerebro-spinal fluid (CSF) thickness of 3.2 mm [89, 160, 235]. The worst-case SAR occurs when the scalp thickness is 2 mm. A total of 40 simulations were performed, for $8 \leq h \leq 15$ and $0 \leq d \leq 16$ mm.

The simulated SAR is between 0.38 and 0.58 W/kg. Hence, the designed WPT link complies with the standard for the complete range of h and d, with a fair margin. The natural uncertainty in dielectric properties, caused by for example natural inhomogeneity of the tissue and other physiological processes, is estimated to be $\pm 15-25\%$ [67] at 6.78 MHz. Since the SAR limit is 2 W/kg [213, 245], the uncertainty is expected to be sufficiently low for the simulated SAR not to exceed the limit value.

Table 3.5: Thermal and dielectric tissue properties at 6.78 MHz [68, 129].

Parameter	Scalp	Skull	CSF	Grey matter
Relative permittivity ε_r	478	47.6	109	397
Conductivity σ [S/m]	0.147	0.0392	2.00	0.252
Mass density ρ [kg/m^3]	1010	1810	1007	1039
Specific heat C [J/kgK]	3500	1300	4096	3680
Thermal conductivity K [W/mK]	0.420	0.300	0.57	0.565
Blood perfusion B [W/m^{3}K]	9100	1000	0	35000
Metabolic rate A_0 [W/m^3]	1000	0	0	10000

Magnetic field limits

A WPT link operating at 6.78 MHz should not generate magnetic fields that are stronger than 42 dBμA/m at a distance of 10 m, according to ERC Recommendation 70-03 [31] and ETSI EN 303 417 [55]. The Tx coil was simulated in Simulia CST Studio Suite®, driven by a current of 150 mA. The simulation volume is $2 \times 2 \times 2$ m.

The simulated magnetic field strength at 10 cm is 117.7 dBμA/m, and at 1 m it is 58.6 dBμA/m, a difference of almost 60 dB. According to the Biot-Savart law, the (static) magnetic field on the axis of a circular loop decays with r^3, which corresponds to the 60 dB difference mentioned above. The field at 10 m would thus be -1.4 dBμA/m, hence the prototype complies with ERC Recommendation 70-03 [31] and ETSI EN 303 417 [55] regarding radiated emissions, even in the worst case.

Effect of harmonics

The output waveform of the class E inverter is not a perfect sine, some harmonics are present at multiples of 6.78 MHz. According to ETSI EN 303 417 [55], harmonics between 10 and 30 MHz should not exceed -3.5 dBμA/m.

A fast Fourier transform (FFT) was performed on the circuit simulation results in LTspice. For all values of k, the signal component at 13.56 MHz was found to be at least 21.7 dB lower than the maximum value of the Tx coil current at 6.78 MHz (which occurs at $k = 0$). This implies that the associated magnetic field is also at least 21.7 dB weaker than the field strength at 6.78 MHz. The magnetic field strength at 13.56 MHz would thus be at most -23.1 dBμA/m. The components at 20.34 and 27.12 MHz are at least 38.4 and 43.8 dB lower than the maximum value of the Tx coil current at 6.78 MHz, respectively. The higher harmonics are even weaker. This means that the prototype complies with ETSI EN 303 417 [55] regarding spurious emissions.

This part does not take into account the frequency-dependent behavior of the Tx coil. The measured SRF of the Tx coil is about 25.5 MHz. Already at frequencies about half of the SRF, the behavior of the coil is found to be notably affected. This means that the Tx coil will be a less efficient radiator at 13.56 MHz compared to 6.78 MHz. In practice, the spurious emissions will thus be even lower than mentioned above.

Tissue heating by heating of components

According to ISO 14708-3 [95] and EN-45502-1 [52], the outer surface of any implantable neurostimulator should never exceed the normal surrounding body temperature by more than 2°C.

The heat generated by the implanted receiver is equal to the dissipated power. For the current design, the computed losses are 14.7 mW for $k = k_{opt}$. The volume of the rectifier is taken to be $7.4 \times 6.4 \times 2.0$ mm^3, corresponding to a surface area of 150 mm^2. This corresponds to a maximum heat flux of 9.7 mW/cm^2.

A thermal simulation was performed in Simulia CST Studio Suite®, similar to [122], using the thermal properties of human tissue from [129], listed in Table 3.5. The thermal source was a perfect thermal conductor (PTC) volume with the same dimensions as the rectifier. The rectifier is assumed to be located on the skull-scalp boundary. A range of simulations was performed, with the scalp thickness varying from 2 to 4 mm, the skull thickness varying from 3 to 6.5 mm, and the CSF layer being 3.2 mm thick [89, 160, 235].

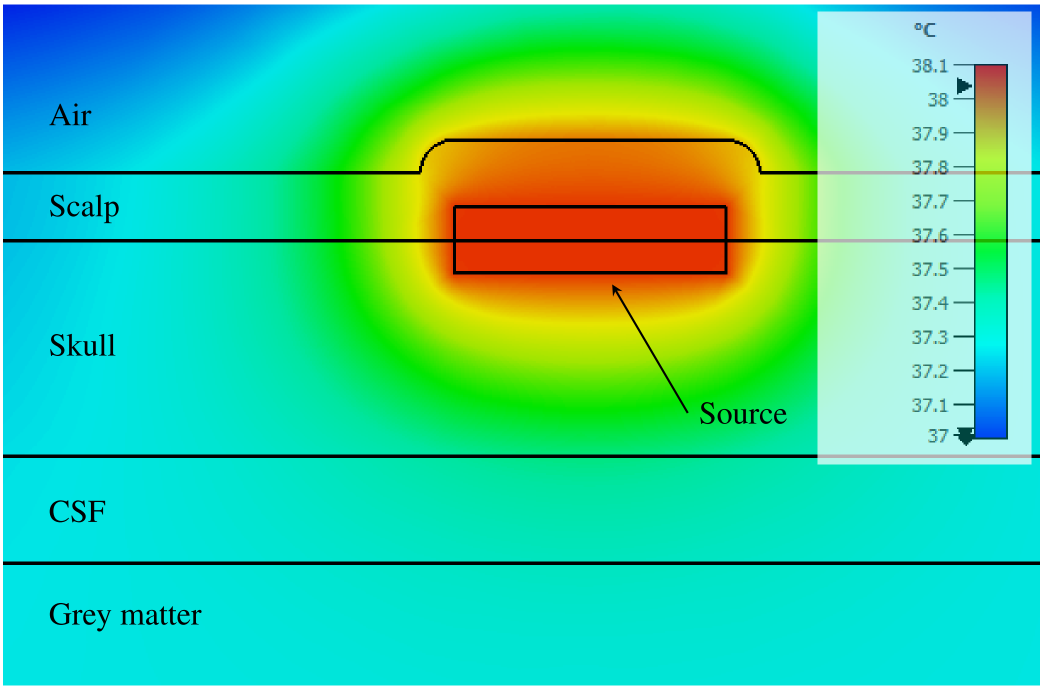

Figure 3.11: Thermal simulation of the implanted receiver, generating 14.7 mW, performed in CST Studio Suite®. The temperature ranges from 37.0 (blue) to 38.1°C (red).

Figure 3.11 shows the resulting temperature distribution for the worst-case scenario; a skull thickness of 6.5 mm, and a scalp thickness of 2 mm. The maximum temperature increase, compared to the case without an active thermal source, is 0.86°C. As can be seen in the Figure, the scalp is assumed to warp around the implant, maintaining its thickness. If the outer surface of the scalp is assumed to stay flat, the resulting maximum temperature changes less than 0.01°C.

According to the simulation, the receiver can dissipate about 36.0 mW before the 2°C limit is reached. This implies the prototype complies with ISO 14708-3 and EN-45502-1, even in the worst case. In practice, an enclosure will be added to the rectifier, enlarging the surface area, hence lowering the heat flux, meaning that even more energy can be dissipated before the 2°C limit is reached.

The heat flux of the Rx coil is over 10 times lower than that of the rectifier. It thus complies with the standard.

3.5 Results

The prototype described in the previous Section is validated for $R_L = 544$, 700, and 980 Ω, corresponding to 90, 70, and 50 mW received power at $V_{out} = 7$ V, respectively. As the link is designed to deliver 90 mW, the analysis is focused mainly at $R_L = 544$ Ω. Figure 3.12 shows the simulated and measured efficiency η, input current I_{dc}, and output voltage V_{out} and power P_{out}, as a function of the coupling factor k.

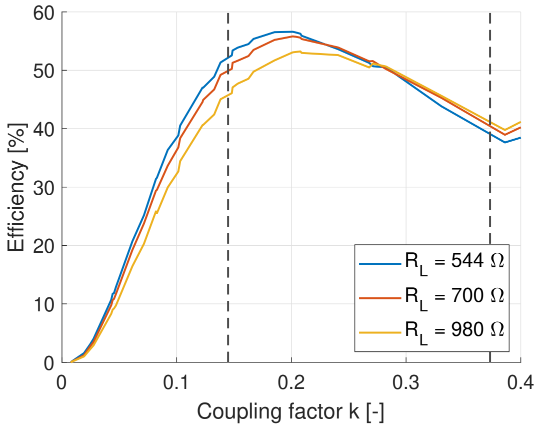

(a) End-to-end efficiency (full system).

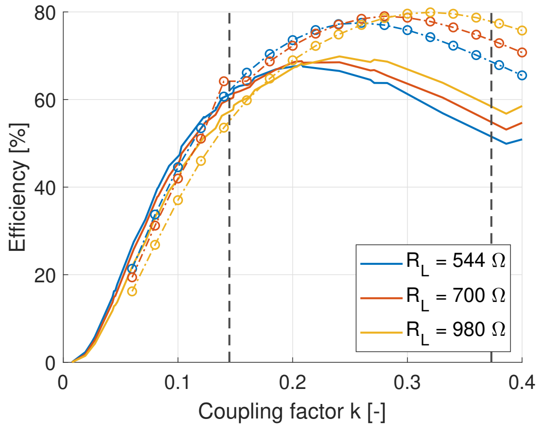

(b) Transfer efficiency (without controller).

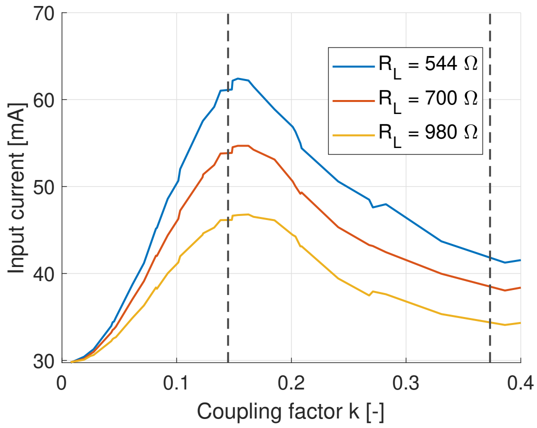

(c) Input current, full system.

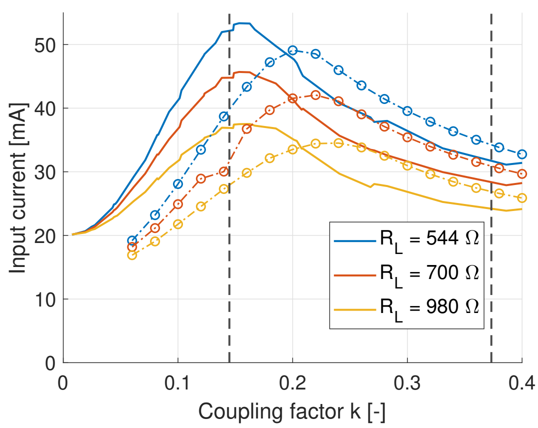

(d) Input current, without controller.

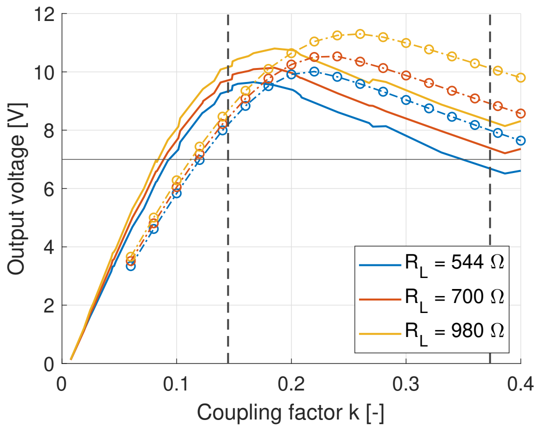

(e) Output voltage.

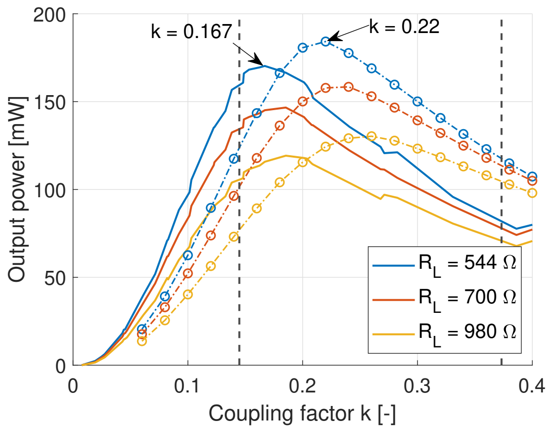

(f) Output power.

Figure 3.12: Simulated and measured efficiency, output power, input current, and output voltage of the manufactured prototype for $V_{in} = 5V$ and three different load resistances. Solid line = measured, dashed line with circular markers = simulated.

From Figure 3.12, it can be observed that the shape of the curves from the simulations and measurements shows similar behavior. However, the measured peak in output power in the prototype occurs at a coupling factor around 0.053 lower than the simulations. Additional measurements have shown that the spice model of the MOSFET is inaccurate in terms of parasitics, at least at the relatively low voltage and current levels at which the MOSFET operates (it operates at max 4% of its rated voltage and current). Additionally, the parasitics of the three coils L_c, L_1, and L_2 are significant at 6.78 MHz. These observations could explain the shift in behavior. Furthermore, the coupling factor was measured with the Rx coil submerged in a 0.9% saline solution. This might have unintentionally influenced the result, in the sense that the measured coupling factor might not be directly relatable to the simulated coupling factor.

From Figure 3.12(f), it can be seen that the prototype is able to deliver at least 80 mW power to the load for $8 \leq h \leq 15$ mm and $0 \leq d \leq 15$ mm. The end-to-end efficiency is between 39 and 57%. When the cause of the $\Delta k = 0.053$ shift, as explained above, is adequately resolved, is it expected that the system would be able to transfer the full 90 mW for which it was designed, with a higher efficiency.

In literature, the power consumption of the controller and gate driver are often ignored in the reported efficiency. The measured efficiency of the link without oscillator and gate driver, also referred to as the transfer efficiency, is between 52 and 68%. Up to 170 mW can be transferred when $k = 0.167$, with a transfer efficiency of 65%.

The mismatch in output voltage between the prototype and the simulation is up to 17%. However, when the measured curve is shifted by $\Delta k = 0.053$, as discussed above, the difference drops below 4%. In that case, the difference in input current is at most 8%.

The oscillator and gate driver, depicted in Figure 3.5, produce a clean square wave with a duty cycle $\zeta_s = 50\%$. However, no additional research was performed to improve this part. It is possible that an increase in end-to-end efficiency can be achieved by choosing more energy efficient components. Furthermore, it could be the case that the number of NOT-gates that was used to drive the gate of the MOSFET is not the optimal one, which would mean that changing the number of NOT-gates would result in higher efficiency for the overall system.

3.6 Discussion

Some additional aspects should be taken into consideration for the successful implementation of a WPT system for IMDs.

3.6.1 Output voltage stabilization

The output voltage ranges to over 9 V, depending on k. Increasing the value of R_L, thus lowering the load, results in a higher output voltage: over 11 V can be received. If the output voltage is required to remain constant, independent of R_L and k (within the ranges specified), a

DC-DC buck converter could be added after the rectifier, delivering a constant output voltage irrespective of the input voltage, at the cost of a slight decrease in system efficiency and an increase of the implant volume. Alternatively, one could adapt the inverter such that the input voltage V_{dc} of the power stage becomes variable (for example with a DC-DC converter with a controllable output voltage), and change this voltage according to the output voltage on the load, such that the output voltage remains constant. This requires a communication link from the receiver to the transmitter. In the NESTOR project [154], a communication link is already envisioned for neural recording [164]. This link could also be used to send the messages required to control V_{dc}.

3.6.2 Thermal considerations

The designed WPT link complies with the relevant standards regarding tissue heating as a result of SAR and as a result of heat generation in the implant. However, when the implant and the Rx coil are physically close to one another, both effects start to add up. The temperature increase as a result of the combination of both heat sources might exceed the limits posed in the standards. Therefore, it is advised to physically separate both the implant and the Rx coil. Based on the temperature profile in Figure 3.11, we conclude that a separation of at least 7 mm should be sufficient.

3.6.3 Maximum received power

Rather than designing the WPT system for MPTE, it is possible to optimize the presented system for MPL [44]. This was found to result in about half the efficiency at optimal coupling ($k = k_{opt}$), and a significant increase in input power when the value of the coupling factor k deviates from its optimal value k_{opt}. Therefore, this design strategy was not adopted. It turns out that optimizing for MPTE results in a maximum tolerance for misalignment as well [224].

3.7 Conclusion

An approach for the design of a WPT system consisting of a class E inverter, a class DE rectifier, and two coupled coils, optimized for MPTE, was presented. Circuit diagrams are given, including those for the oscillator and gate driver. A complete set of design equations is presented, including the losses for each component.

The design was validated in a case study, for which circuit simulations were performed, and a prototype was manufactured. There is a mismatch of up to 17% in output voltage between the simulations and the measurements. However, when the measurement results are shifted by $\Delta k = 0.053$, the difference drops to 4%. In the latter case, the difference in input current is at most 8%. This shift of $\Delta k = 0.053$ is believed to be caused by inaccuracies in the spice models for the MOSFET, and by the fact that the SRFs of the coils is close to the frequency of operation.

The WPT link designed for the case study can transfer 80 mW at 7 V transcutaneously to a biomedical brain implant at 6.78 MHz. In designing such a system, the end-to-end efficiency needs to be optimized, not just the link efficiency. In our system, the latter is 86 to 95%, depending on the misalignment. The end-to-end efficiency is 39 to 57%. The transfer efficiency, where the controller and gate driver are ignored, is 52 and 68%.

The system was designed to maximize the transfer efficiency, including the inverter and the rectifier, rather than maximizing the efficiency of the individual sub-systems separately.

Misalignment tolerance should be part of the design. This was found to affect the compliance with the relevant (medical) standards. The designed WPT system complies with IEEE Std C95.1, ICNIRP, ETSI EN 303 417, EN-45502-1 and ISO 14708-3 standards for distances between the coils of $8 \leq h \leq 15$ mm, and misalignment from $0 \leq d \leq 15$ mm.

CHAPTER FOUR

Electromagnetic field calculation for biomedical wireless power transfer in two-layer applications[1]

4.1 Introduction

Research on WPT, as well as other EM-related applications, such as data transfer, in or near the human body, relies partly on numerical tools for modeling the EM fields inside the biological tissue. These tools give insight in the field distribution inside the tissue, verifying that the energy is delivered to the desired location or traveling in the desired direction, and making sure the SAR limits are not exceeded. Additionally, they can be used to compare the behavior of different WPT techniques, or to determine which operational frequency yields the best performance.

For WPT to mm-sized implants, located at a depth of several centimeters inside the human body, research suggests that the use of (sub-)GHz frequencies outperforms traditional inductive WPT at MHz frequencies [85, 141, 175]. However, other research contradicts this claim [64]. The work presented in this chapter and the next one is aimed at settling the debate, based on modeling tools. Furthermore, these tools can be used to speed up the design process of both traditional and midfield WPT systems, and to investigate WPT transmitters with a more complex architecture, such as phased arrays or complex shapes.

Modeling the fields of an external (magnetic) source transmitting energy into a biological tissue, or vice versa, is not a trivial task. Standard equations, like the well known Helmholtz equation, are no longer valid in the presence of discontinuities in the surrounding medium, and incorporating losses in them might not be straightforward. Various software tools are available on the market to aid one into creating a successful WPT link, such as full-wave

[1]This chapter is based on [P4].

solvers like Simulia CST Studio Suite® [35] and Sim4Life [198]. The main disadvantages of those tools are that they are costly, and can require many hours of computation time per simulation, even on dedicated high-performance computers. Additionally, it can take a considerable amount of time before the user has gained enough experience to create models that are accurate and efficient.

We believe a speedup in the design process of these links can be achieved by properly incorporating suitable analytical models. However, describing the fields in mathematical terms, both inside and outside the tissue, can not be done in closed form. Nonetheless, we show that it is possible to numerically implement an analytical model that accurately predicts these fields and executes much faster than commercial full-wave solvers.

We present an analytical model to accurately predict the EM fields inside and outside conductive tissue, caused by a vertically oriented magnetic point dipole (VMD) located outside this tissue. The model is easy to implement, and can be adapted to a magnetic source of arbitrary shape via the superposition principle. With minor changes, the model can also be used for sources with arbitrary orientation, or sources inside the tissue. Additionally, it can be adapted for electric sources.

The model presented in this chapter is limited to two layers, i.e. one air and one tissue layer. The model presented in the next chapter applies to a setup with an arbitrary number of layers, with the source located in any of them. The former model is easier to implement, and despite its limited applicability, it can be used to get useful insight in the generated EM fields within typically tens to hundreds of seconds.

4.2 Analytical model

Any magnetic source can be modeled by a superposition of MPDs, each assigned its own location, orientation, magnitude and phase. Here, we focus on one of these building blocks: the fields generated by a single VMD with magnetic moment M, located in air at location $(0,0,h)$ above conductive tissue, see Figure 4.1. The air and tissue shall be referred to as layer 0 and 1, respectively. The tissue, located at $z < 0$, has relative permittivity $\varepsilon_{r,1}$, relative permeability $\mu_{r,1} = 1$, and conductivity σ_1. For reasons that will become obvious later, an image source is introduced, located at $(0,0,-h)$.

4.2.1 Mathematical framework

Baños [12] has constructed a mathematical framework to calculate the fields for various setups that involve a conductive half-space, including the one under consideration. The context of his work was not related to biomedical applications, but rather directed towards communication through air at relatively low frequencies over long distances, in the presence of a lossy ground, lake, or sea. Although Baños states his method is valid for low frequencies, we show here that the performance is good for frequencies up to 5 GHz. Validation of the model above 5 GHz was not possible, as we were unable to generate reference data in CST Studio Suite®[35], because the memory requirements for those full-wave simulations were beyond our system specifications. This is not believed to be a limitation of the analytical model, and is in fact an argument in favor of using the analytical model, as it runs on a regular PC. Note that Baños considered a setup where the top half-space contains conductive material, whereas this work assumes the bottom half-space to consist of conductive material. For this reason, the equations presented in this chapter are slightly altered versions or those in [12].

Figure 4.1 depicts the situation under consideration; layer 0 and 1 are two half-spaces, the VMD is located in the former, indicated as Source. Note that this setup is axially symmetric around the z-axis. The choice of a cylindrical coordinate system is therefore obvious. The numerical implementation of his method does not converge for media with a conductivity that is strictly zero, so layer 0 (air) has an arbitrary low conductivity. Any value below $\sigma_0 = 10^{-7}$ Sm^{-1} was observed to work fine, ensuring convergence of the algorithms without notably changing the result.

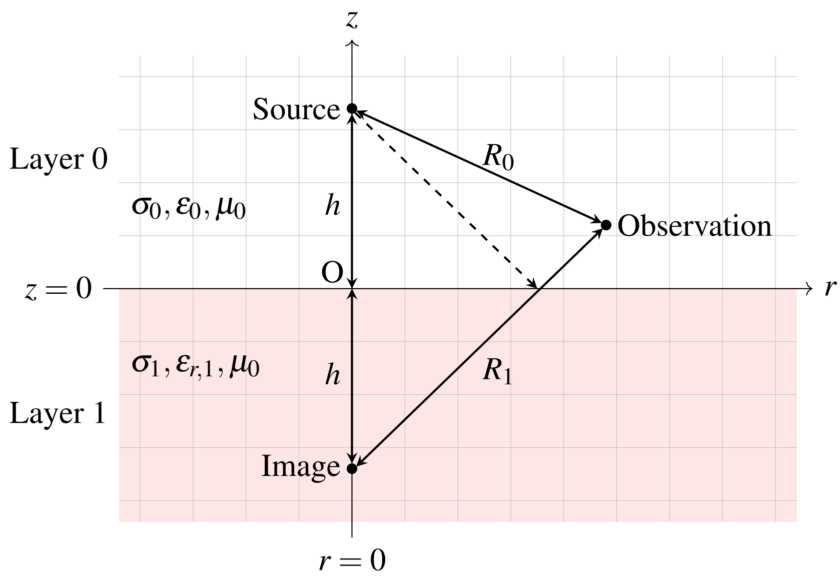

Figure 4.1: Schematic representation of the setup for the analytical model.

The fields in layer 0 are a combination of those coming directly from the source, and those reflected off the boundary between the two layers. In Figure 4.1, these are represented by the solid line R_0, and the dashed line, respectively. The reflected fields can be regarded as fields originating from the mirrored image of the source. The fields in layer 1 are only those transmitted through the boundary.

The distances from the source and image points to the observation point (r, z), which can be in any of the two layers, are given as

$$R_0 = \sqrt{r^2 + (h-z)^2}, \tag{4.1}$$

$$R_1 = \sqrt{r^2 + (h+z)^2}. \tag{4.2}$$

The wave number, or propagation constant, in layer n is defined in terms of its dielectric properties as

$$k_n^2 = \omega^2 \mu_0 \varepsilon_n \varepsilon_0 + \mathrm{j}\omega\mu_0\sigma_n. \tag{4.3}$$

The scalar Green's function for a point dipole, commonly known as $\frac{\mathrm{e}^{\mathrm{j}kr}}{r}$ [76], is adapted slightly, such that we can distinguish between the wave coming directly from the source, and the one reflected off the boundary, as

$$G_{ij} = \frac{\mathrm{e}^{\mathrm{j}k_iR_j}}{R_j}, \tag{4.4}$$

which will be used in the expressions for the generated EM fields next. Throughout this work, the subscript $\{ij\}$ denotes a source located in layer i, and the observation point in layer j.

4.2.2 Expression of the field components

We can now write the fields in layer 0 as

$$H_{0r} = \frac{M}{4\pi}\left\{\frac{\partial^2}{\partial r \partial z}\left[G_{00} - G_{01} + U_{00}\right]\right\}, \tag{4.5}$$

$$H_{0z} = \frac{M}{4\pi}\left\{\left(\frac{\partial^2}{\partial z^2} + k_0^2\right)\left[G_{00} - G_{01} + U_{00}\right]\right\}, \tag{4.6}$$

$$E_{0\varphi} = \frac{-\mathrm{j}\omega M\mu_0}{4\pi}\left\{\frac{\partial}{\partial r}\left[G_{00} - G_{01} + U_{00}\right]\right\}. \tag{4.7}$$

Because we consider a VMD, the other three field components are zero. The fields in layer 1 can be written as

$$H_{1r} = \frac{M}{4\pi}\left\{\frac{\partial^2}{\partial r \partial z}U_{01}\right\}, \tag{4.8}$$

$$H_{1z} = \frac{M}{4\pi}\left\{\left(\frac{\partial^2}{\partial z^2} + k_1^2\right)U_{01}\right\}, \tag{4.9}$$

$$E_{1\varphi} = \frac{-\mathrm{j}\omega M\mu_0}{4\pi}\left\{\frac{\partial}{\partial r}U_{01}\right\}. \tag{4.10}$$

The other three field components are again zero.

In the above equations, U_{00} and U_{01} are so-called essential integrals. Their derivation is done extensively in [12], Equation (2.68), hence this will not be repeated here. They are given as:

$$U_{00}(r,z) = \int_0^\infty \frac{2\mathrm{e}^{-\gamma_0(h+z)}}{\gamma_0+\gamma_1} J_0(gr) g \mathrm{d}g, \tag{4.11}$$

$$U_{01}(r,z) = \int_0^\infty \frac{2\mathrm{e}^{\gamma_1 z-\gamma_0 h}}{\gamma_0+\gamma_1} J_0(gr) g \mathrm{d}g, \tag{4.12}$$

where $J_0()$ is the Bessel function of the first kind and order zero, g is the integration variable, and we have for the attenuation factor γ_n, in accordance with [12]:

$$\gamma_n = \sqrt{g^2 - k_n^2}. \tag{4.13}$$

4.3 Numerical implementation

The essential integrals in Eqs. (4.11) and (4.12) have no closed-form solution, and thus have to be solved numerically. The same holds for their derivatives, needed for Eqs. (4.5) — (4.10).

The integrands of Eqs. (4.11) and (4.12) are not smooth, and contain at least one sharp peak. The behavior for small g, and around the peaks, requires sufficient detail to capture. For g sufficiently large, the integrands are smooth and approach zero. An integral with these properties can not be solved successfully by just an arbitrary numerical method.

For the numerical evaluation of the integrals, the built-in `integral` function of MATLAB [145, 193] is used, which is based on an adaptive Gauss-Kronrod (7 Gauss nodes, 15 Kronrod nodes) quadrature method. It combines the general advantages of quadrature integration with the ability to adaptively refine the subintervals. This allows capturing of peaks and other non-smooth behavior in the integrand with greater detail.

The first step is to divide the integration domain into two subintervals: one running from 0 to the location of the sharp peak, the other running from the peak to infinity. Both resulting subintervals are now smooth, and can thus be integrated easily. An additional advantage of this approach is that it results in an additional speedup of about 10%. The absolute and relative tolerances of the `integral` function are both set to 10^{-10}. This results in sufficient accuracy, as the result does not change notably when the tolerances are set even stricter. Higher values result in errors for some combinations of parameters, causing the integration routine to complete before sufficient level of accuracy was achieved.

The derivatives of Eq. (4.4) are easily found analytically, but finding those of Eqs. (4.11) and (4.12) is less straightforward. These derivatives are approximated using finite differences as [118]

$$\frac{\partial f(r,z)}{\partial r} \approx \frac{f(r+\delta,z)-f(r-\delta,z)}{2\delta}, \tag{4.14a}$$

$$\frac{\partial^2 f(r,z)}{\partial z^2} \approx \frac{f(r,z+\delta)-2f(r,z)+f(r,z-\delta)}{\delta^2}, \tag{4.14b}$$

$$\frac{\partial^2 f(r,z)}{\partial r \partial z} \approx \frac{f(r+\delta,z+\delta)-f(r-\delta,z+\delta)-f(r+\delta,z-\delta)+f(r-\delta,z-\delta)}{4\delta^2}, \tag{4.14c}$$

where δ is identical for both coordinates (r,z), and should be chosen sufficiently small. The approximation error is of order $\mathscr{O}(\delta^2)$. $\delta = 10^{-5}$ is used, resulting in an acceptably low error for all combinations of parameters used, which will be elaborated upon next. Note that this approach requires each integral to be evaluated nine times for each point (r,z).

4.4 Validation of the model

The analytical model has been run for a VMD for frequencies $f = 13$ MHz, 100 MHz, 1 GHz, 2.45 GHz, and 5 GHz. The dipole is located at $h = 10$ mm above tissue with $\varepsilon_{r,1} = 40$ and $\sigma = 1$ Sm^{-1}. These values are chosen to lie in the range of many kinds of human tissue [67].

The validation is performed by comparing the results generated by the analytical model to those generated by full-wave simulations performed in Simulia CST Studio Suite®[35]. Since MPDs do not exist in CST, the CST-model consists of a single-turn perfect electric conductor (PEC) circular loop with a wire diameter of 15 μm and an loop radius of 107.5 μm (corresponding to an inner radius of 100 μm), with a 2 μm slit that contains the current source. Figure 4.2 shows the CST model of the coil.

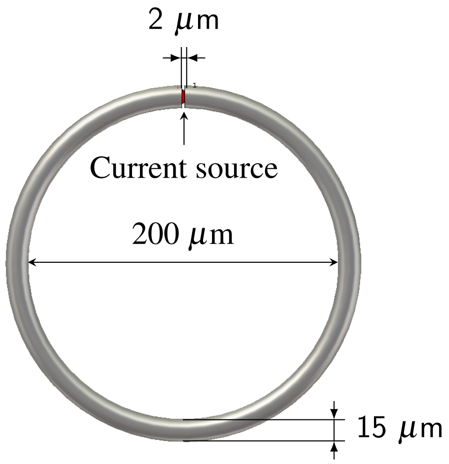

Figure 4.2: Single-turn wire loop used for validation in CST Studio Suite®[35].

Having such a small loop circumference allows us to treat it as an MPD [223]. The current through the loop is 1 A, thus the magnetic moment M is $3.63 \cdot 10^{-8}$ Am^2. This value is used as M in the analytical field calculations (4.5) — (4.10).

The fields generated by the analytical model and those generated by CST are interpolated to identical grids. This enables the calculation of the relative difference between the two on each point (r,z) in the grid as

$$\text{diff}(r,z) = \frac{\big||H_{model}(r,z)| - |H_{CST}(r,z)|\big|}{|H_{CST}(r,z)|}, \tag{4.15}$$

and an equivalent approach can be used for the electric field. The relative difference is then averaged over the entire layer, for each field component. Instead of field interpolation, it is also possible to choose identical grids already beforehand, which should work equally well. The described approach, however, allows for a bit more freedom in the calculation process.

For the validation procedure, the air and tissue half-spaces were initially chosen to measure $100 \times 100 \times 80$ mm each. This corresponds to $0 \leq r \leq 50$ and $-80 \leq z \leq 80$ mm in the analytical model, which, based on related work, we believe is a realistic range for mid-field wireless power transfer (MF-WPT) [87, 141, 157, 174, 175], at least for the purpose of validation.

When the CST simulation volume is taken equal to the analytical calculation dimensions, it quickly becomes clear that the boundaries of the simulation volume introduce unwanted effects. Presumably, the error generated by the perfectly matched layer (PML) boundaries is high enough to be noticeable. To reduce these effects, the simulation volume was extended by 20 — 80% in all directions, as a padding to accommodate for the boundary conditions. Used only the original volume is used in the comparison between CST and the analytical model, ignoring the added volume. The larger the simulation volume is chosen, the smaller the difference becomes, at the cost of increased computation time and memory usage. For lower frequencies, more extension is needed before an acceptably low difference is achieved.

4.5 Results

The model was compared to CST simulations for the five different frequencies mentioned. The analytical model was implemented in MATLAB®[145]. It calculates a planar cut of the three field components (H_r, H_z, E_φ) in the two layers, with 50×50 grid points in each layer. This gives sufficient detail in this case. The analytical model took about 90 seconds to execute.[2] The CST model took about 7 hours to execute.[3]

Figure 4.3 shows the results for $f = 1$ GHz in layer 0, and the corresponding relative differences, calculated using Eq. (4.15). Figure 4.4 shows the same for layer 1. All three field components are depicted. The source can be clearly distinguished at $(r,z) = (0, 0.01)$. The

[2]The analytical model was executed on a notebook computer with a quad-core 2.80 GHz Intel® i7-7700 processor, using less than 3.5 GB RAM.

[3]The CST simulation was executed on a server with two hexa-core 2.79 GHz Intel® Xeon® X5660 processors, using up to 70 GB RAM.

H_z component is strongest along the r and z-axes, as is expected. The H_r and E_φ components are approximately zero along the z-axis, as is also expected [11]. The E_φ field of a MPD located in vacuum exhibits a doughnut-shaped radiation pattern [11], which can be observed in Figure 4.4 as well, although it is clearly distorted by the presence of the layer.

Table 4.1 lists the average relative differences between the fields generated by the analytical model and those generated by CST for both layers, calculated using Eq. (4.15). In general, for all frequencies, the largest relative differences can be found nearest to the source. The fields close to the source are outside the scope of this work, for the purpose of WPT. Therefore, we chose to ignore a small region around the source during the calculation of the relative differences. Defining the region to extend 4 mm in the r-direction and 2 mm in the z-direction was found to mitigate negative effects introduced by the wire loop not being an ideal MPD for all frequencies mentioned. This region is shown in black in Figure 4.3. We believe that, for the purpose of WPT, this region can be considered irrelevant, and can thus be ignored without affecting the applicability of the analytical model. Table 4.1 also contains the average differences between the fields generated by the analytical model and the CST simulation when this small volume near the source is excluded. When the simulation volume is extended by 20% in all directions, to reduce the negative effect of the boundaries, the simulation time for CST roughly doubles, as does the memory usage.

Although the wire loop is assumed to behave as an MPD [223], this has to be validated. Therefore, the wire loop radius was changed to values 1.5 and 2.0 times larger, and the magnetic moment M was updated accordingly. The resulting CST results do not show a significant change, validating that indeed the wire loop behaves as an MPD.

4.6 Discussion

The fields computed with the analytical model, and those from the CST simulation match quite closely, as is shown in Table 4.1. For all frequencies considered, the relative difference is acceptably low (on average below 8.1%).

The difference is generally highest near the source. This can be explained by the fact that, even though the fields generated by the small wire loop are very similar to those generated by an MPD, the near-field behavior is not expected to be identical; a wire loop with finite radius in the near-field is simply not the same as an elementary point dipole. This effect is observed only very close to the source, i.e. at a distance less than 4 mm in the r-direction and 2 mm in the z-direction, for frequencies from 13 MHz to 5 GHz. A detailed analysis of the frequency and permittivity related nature of this phenomenon was not performed, as we believe this is not relevant for the intended application of this analytical model, being the purpose of (biomedical) WPT. Nonetheless, a small wire loop can be considered to behave as an MPD when evaluated not too close to the source.

The computational resources required to use the model are significantly lower than those required to run a CST simulation; after a correction for the number of cores, the model runs

Table 4.1: Average relative differences[%] between the results generated using CST and those generated by the analytical model, with and without the volume near the source.

	Layer 0 with source	Layer 0 source excluded	Layer 1
		$f = 13$ MHz	
H_r	37.3	2.3	1.8
H_z	9.6	7.6	7.3
E_φ	2.4	2.2	3.0
		$f = 100$ MHz	
H_r	27.1	2.7	1.9
H_z	8.2	8.1	4.3
E_φ	3.2	3.0	1.4
		$f = 1$ GHz	
H_r	112.8	2.9	2.3
H_z	6.1	6.1	3.1
E_φ	5.0	4.6	2.5
		$f = 2.45$ GHz	
H_r	12.7	7.3	2.6
H_z	5.0	3.9	1.8
E_φ	3.1	3.1	2.3
		$f = 5$ GHz	
H_r	12.2	4.9	5.2
H_z	9.8	5.9	5.9
E_φ	7.3	7.3	4.6

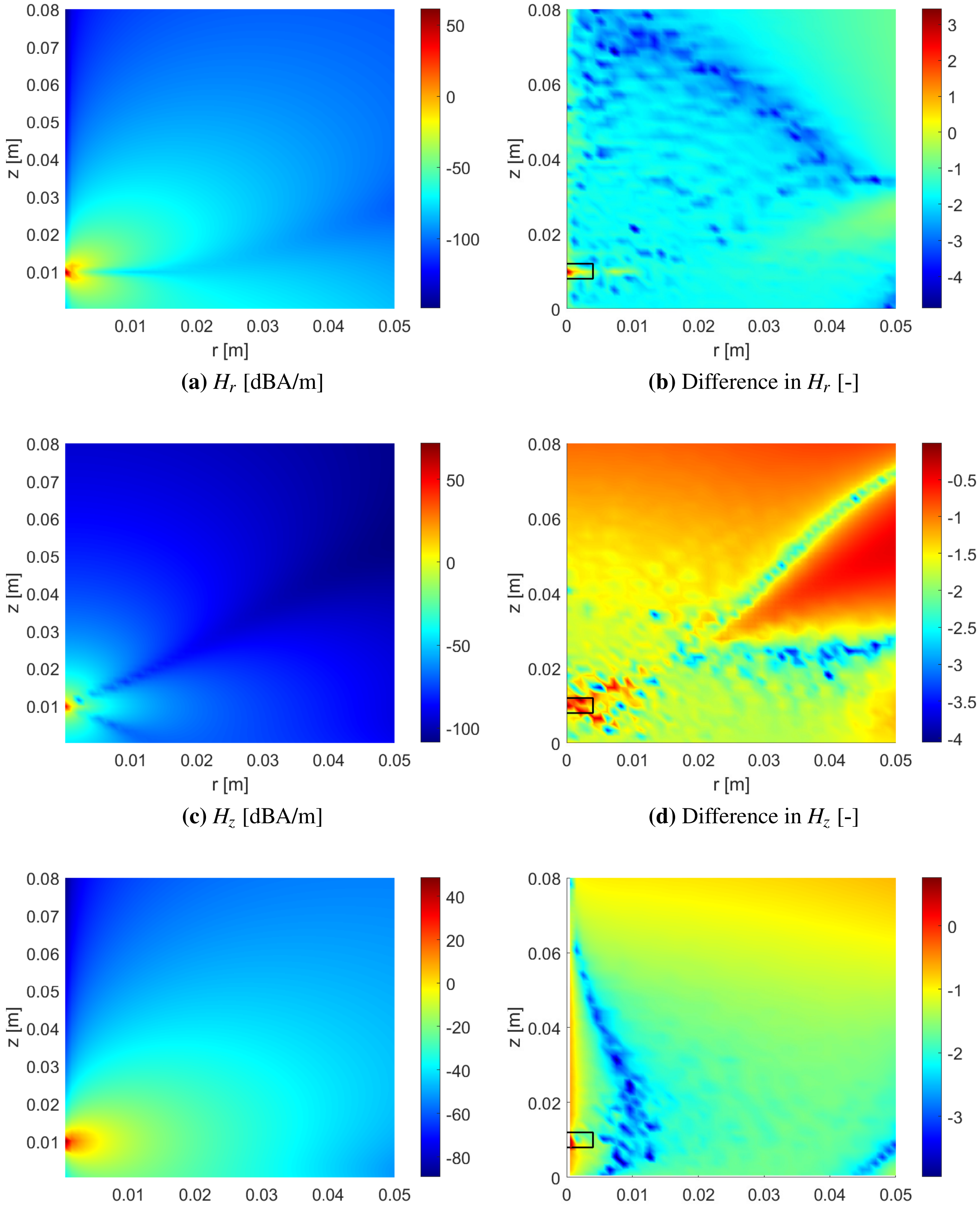

(a) H_r [dBA/m] **(b)** Difference in H_r [-]

(c) H_z [dBA/m] **(d)** Difference in H_z [-]

(e) E_φ [dBV/m] **(f)** Difference in E_φ [-]

Figure 4.3: Results generated by the analytical model for $f = 1$ GHz in layer 0 (left) and the relative difference between the analytical model and the CST simulation (right), plotted on a logarithmic scale: $\log_{10}(\text{diff})$. The region bounded by the black lines is excluded from the analysis, as described in Section 4.5. Note that each plot has different scaling.

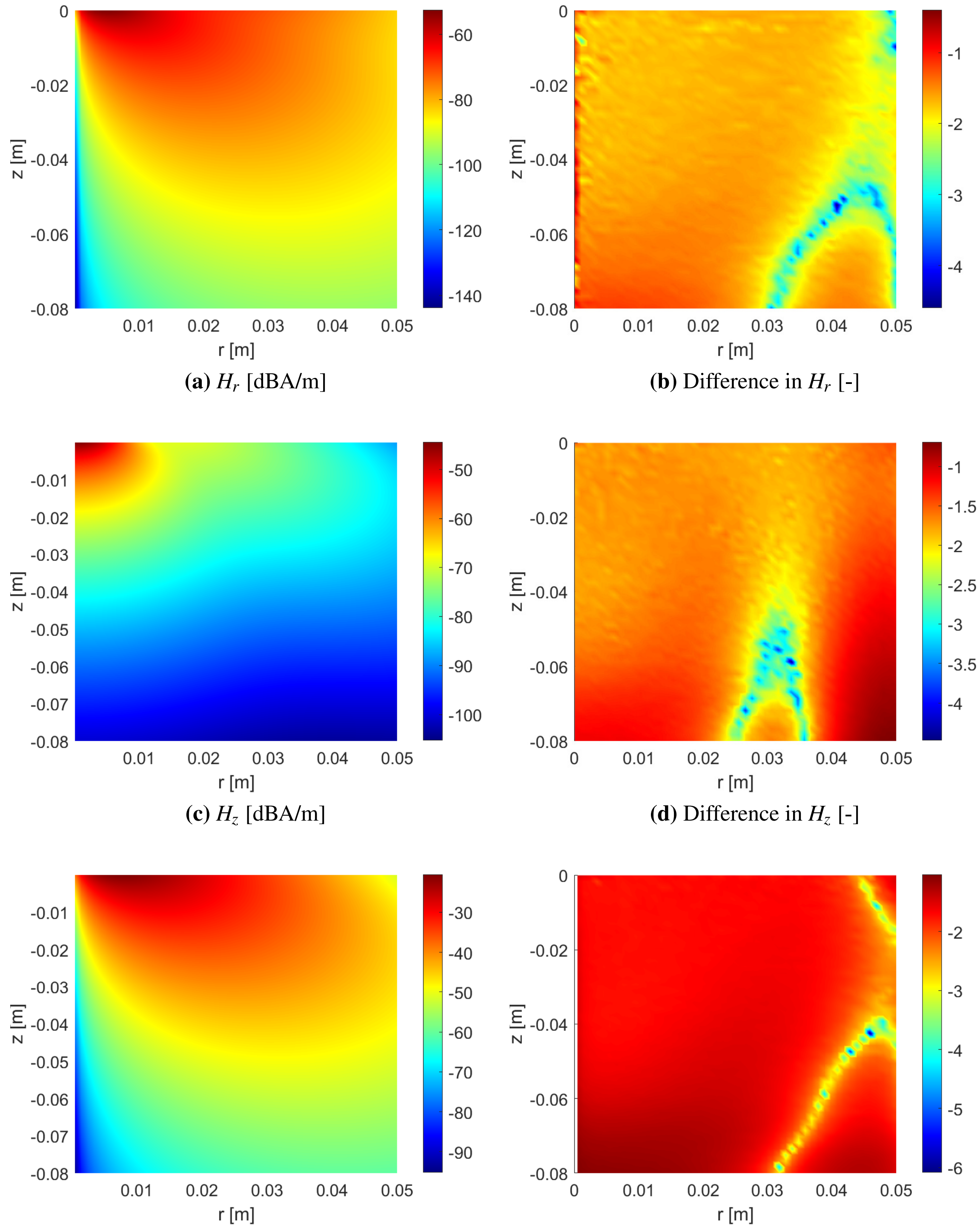

(a) H_r [dBA/m]

(b) Difference in H_r [-]

(c) H_z [dBA/m]

(d) Difference in H_z [-]

(e) E_φ [dBV/m]

(f) Difference in E_φ [-]

Figure 4.4: Results generated by the analytical model for $f = 1$ GHz in layer 1 (left) and the relative difference between the analytical model and the CST simulation (right), plotted on a logarithmic scale: $\log_{10}(\text{diff})$. Note that each plot has different scaling.

more than 800 times faster and uses about 20 times less memory. This also means that the analytical model can easily run on a standard desktop PC. The model is well suitable for parallelization, since all grid points can be calculated independently.

If one wishes to model more practical situations that can not be represented by a single magnetic dipole, the superposition principle can be used, stating that any magnetic source can be represented by a superposition of MPDs, located at certain positions, each with its specific magnitude and phase. This extension of the model does not mean a huge increase in computation time, since the layers are half-spaces. One has to calculate the fields only once, and can then freely shift them through the xy-(or $r\varphi$-)plane, changing the magnitude A_m and phase ϕ_m of the magnetic moment accordingly, as $M = A_m e^{j\phi_m}$. If a source with nonzero height is to be modeled, the fields have to be calculated once for each value of h, and can be shifted accordingly.

4.7 Conclusion

An analytical model was presented that models the EM-fields generated by a VMD located over a conductive half-space, for instance (equivalent) biological tissue. The model was compared with simulations with CST, a commercial full-wave solver. In that model, the fields are generated by an electrically small wire loop, that was shown to behave as an MPD. The relative differences are small, i.e. below 8.1% on average, hence the model can be said to perform well. The model was verified for frequencies ranging from 13 MHz to 5 GHz.

The analytical model executes more than 800 times faster than the CST simulation, and uses about 20 times less memory. The model can be easily extended to more realistic sources by the superposition principle. This requires only a small increase in computational cost.

This model can be used to speed up the design process of biomedical WPT devices significantly. It can be used stand-alone, or as a preliminary tool for rapid design iteration.

Chapter five

Electromagnetic field calculation for biomedical wireless power transfer in multi-layer applications[1]

5.1 Introduction

In this chapter, we present the application of an analytical model to calculate the EM fields generated by a MPD located in the presence of planarly layered media. This can be used to approximate the fields generated by a small coil located outside the human body, or a small coil embedded inside the human body. Alternatively, based on the principle of reciprocity, it can be used to determine the external coil current distribution required to focus the fields at a specific location inside the human body where a receiver coil will be located [121]. The model is intended as a practical design tool for simulations of biomedical WPT systems, but is applicable to any setup where a (point) source generates EM fields in the presence of planarly layered media.

The model was introduced by Wait [226] in 1962, and was aimed specifically at wave propagation in the terrestrial atmosphere or the Earth's crust. The general motivation was that many natural environments can be approximated by planarly layered media, such as the environments in long-distance communication, communication with submarines, communication in mines, or geophysical research. Wait [226] modeled the EM fields generated by a MPD in the presence of planarly layered isotropic media.

In the model presented in this chapter, there is no limit on the number of layers, the source can be located in any layer, and can have any orientation. Furthermore, we provide all essential steps for an efficient numerical implementation of the model, and we systematically compare the results to those generated by a commercial full-wave EM field solver. Although

[1]This chapter is based on [P1].

this work focuses on biomedical applications, this is by no means a limitation. In fact, the model is applicable to any situation that contains (locally approximated) planarly layered media. Even though Wait developed his model with a focus on long distances, we show that it also performs well in centimeter and millimeter ranges.

An advantage of the analytical model is that the calculation of the fields at a certain coordinate is completely independent of the calculation of the fields at another coordinate, contrary to, for example, FDTD calculation schemes. This implies, for example, that the fields outside the human body do not have to be calculated, and that the results can be evaluated only at locations of interest, which leads to faster computation using less memory. This is in sharp contrast with most commercial EM field simulation software, where the complete volume has to be analyzed, and a minimum (local) mesh size is required to ensure convergence of the algorithms. Additionally, this means that, in a multicore system, each processor can be assigned the task of computing the EM fields at a unique spatial coordinate, eliminating the need for extensive communication and other time consuming dependencies between processors. This suggests that the speed-up in execution time scales approximately linearly with the amount of processors[2], whereas the speedup of Simulia CST Studio Suite® decreases above a certain number of processors [3, 21, 36, 239].

Results can be generated orders of magnitude faster than with full-wave methods, and in many practical situations require just a few minutes for a single frequency, even on a standard PC. Furthermore, the model can be implemented in almost any programming language.

5.2 Mathematical Model

We consider an MPD located in horizontally layered media. The field distribution of an MPD can be expressed in terms of Green's functions [76, 210] to which the effects of the discontinuities at the layer interfaces, and the losses, are added later [226].

The generated EM-fields at an arbitrary point are a superposition of the fields following the direct path from the source, and all fields following an indirect path. The direct path is the shortest path, which is only refracted at layer boundaries. The indirect paths include one or more reflections off boundaries, and can also include refractions. There is one direct path and an infinite number of indirect paths. Figure 5.1 shows the propagation along some of these paths in a layered environment, with the layers stacked in the z-direction of a rectangular or cylindrical coordinate system.

The mathematical model we use to describe the EM fields was introduced by Wait [226]. This work is based on the implementation of Wait's model as presented by Stoyer [209], as it summarizes the essential equations for a magnetic or electric dipole in horizontally stratified media. However, even though Wait mentions applications like communication at kHz frequencies for km ranges, it is unclear for which (ranges of) parameters Wait has verified

[2]We were able to verify this for up to 64 CPU cores.

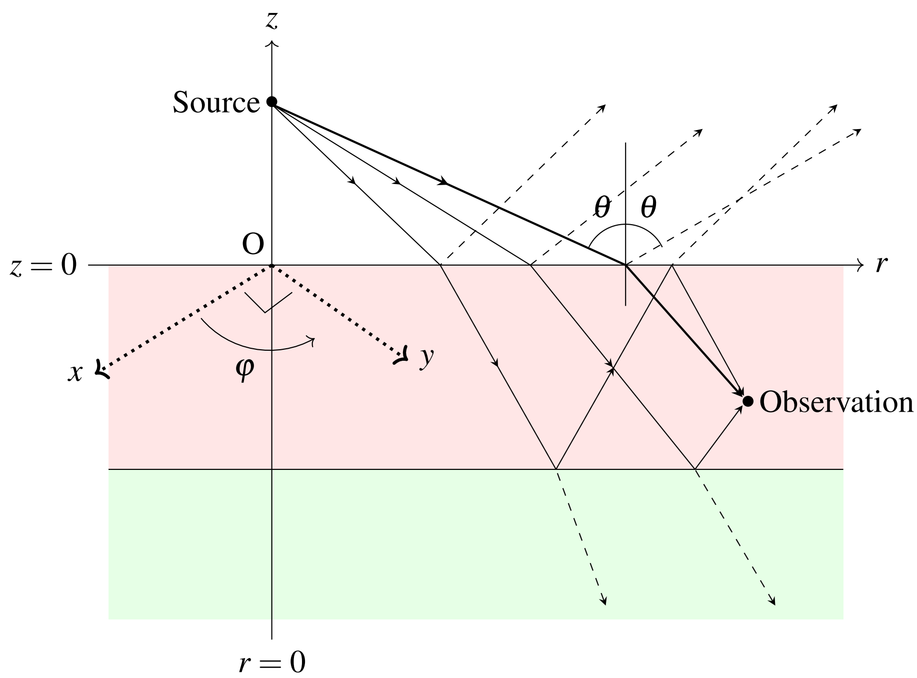

Figure 5.1: Reflection and refraction paths from a source in the presence of layered media. The direct path (thick) and several indirect paths (thin) between source and observation point can be distinguished. The layering is in the z-direction in a Cartesian (x, y, z) or cylindrical (r, φ, z) coordinate system.

the model. Furthermore, although Stoyer presents some numerical considerations, we show that these are insufficient for successful numerical integration in many of the cases presented in this work. Therefore, we pay explicit attention to the numerical implementation (in Section 5.3). Note that in [209] and [226], the z-axis runs downward, whereas we chose it to run upward, as we believe this to be more intuitive. Therefore, the equations used differ slightly from those in [209, 226].

5.2.1 General setup

We distinguish two dipole orientations: the horizontally oriented magnetic point dipole (HMD) and the VMD, depicted in Figure 5.2. The equations used for the VMD model are variations on those used for the HMD. Hence the HMD case is covered first.

The presented model is applicable to any planarly layered structure with an MPD located in an arbitrary layer. The general setup is depicted in Figure 5.3. In the model and in the figure, the MPD is located as the source in layer 0, at height $z = d$. Layer i, where $-n \leq i \leq m$, has relative permittivity $\varepsilon_{r,i}$, conductivity σ_i, and relative permeability $\mu_{r,i}$. Human tissue has a relative magnetic permeability $\mu_r = 1$ [68]. For the numerical implementation, to ensure the integrals remain finite (as will become clear in Section 5.3.2), σ_i has to be nonzero and positive. For non-conductive layers, choosing $\sigma_i = 10^{-9}$ S/m ensures successful computation

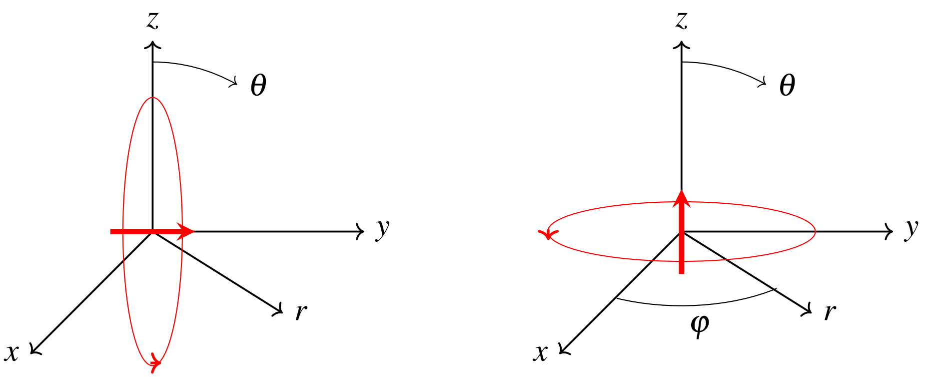

Figure 5.2: Coordinate systems and orientation of the horizontal (left) and vertical (right) magnetic dipole, shown as a red arrow. The shown single-turn wire loops (current direction indicated) can be used to approximate the magnetic point dipoles, provided that the radius is sufficiently small.

for the frequencies considered (100 kHz $\leq f \leq$ 5 GHz), without changing the result notably.

Layer i has thickness h_i, with boundaries at z_i and z_{i+1}. The top and bottom half spaces, layers m and $-n$ respectively, have one boundary at $z = \infty$ and $-\infty$, respectively, and thus have infinite thickness.

We assume that only a magnetic point source is present. In that case, we can write the electric and magnetic fields in layer i, at position $\mathbf{r}$, and at time t, in time-harmonic form as [210]:

$$\mathbf{E}_i(\mathbf{r},t) = -\mathrm{j}\omega\mu_0\mu_{r,i}\nabla \times \mathbf{\Pi}_i(\mathbf{r},t), \tag{5.1a}$$

$$\mathbf{H}_i(\mathbf{r},t) = k_i^2\mathbf{\Pi}_i(\mathbf{r},t) + \nabla\big(\nabla \cdot \mathbf{\Pi}_i(\mathbf{r},t)\big), \tag{5.1b}$$

where $\mathbf{\Pi}_i(\mathbf{r},t)$ is the magnetic Hertz potential of the source, with unit A·m, ω is the angular frequency in rad/s, and k_i is the wave number in m^{-1}, for which holds

$$k_i^2 = \omega^2\mu_0\mu_{r,i}\varepsilon_0\varepsilon_{r,i} - \mathrm{j}\omega\mu_0\mu_{r,i}\sigma_i. \tag{5.2}$$

In this work, we consider the case in which $m = 0$, with the source located in the top layer, i.e. the $m = 0$ layer. Thus, the layered media are strictly below the source $(i < 0)$. With the help of [209], the relevant equations can be obtained for the case where the source is located in a different layer, i.e. $m \neq 0$.

5.2.2 Horizontal Magnetic Point Dipole (HMD)

We chose the HMD to be positioned such that it radiates maximum energy in the y-direction. We choose a Cartesian coordinate system, as depicted in Figure 5.2. The Hertz potential in layer i can be decomposed into two orthogonal parts $\Pi_{i,y}$ and $\Pi_{i,z}$, given by [209]:

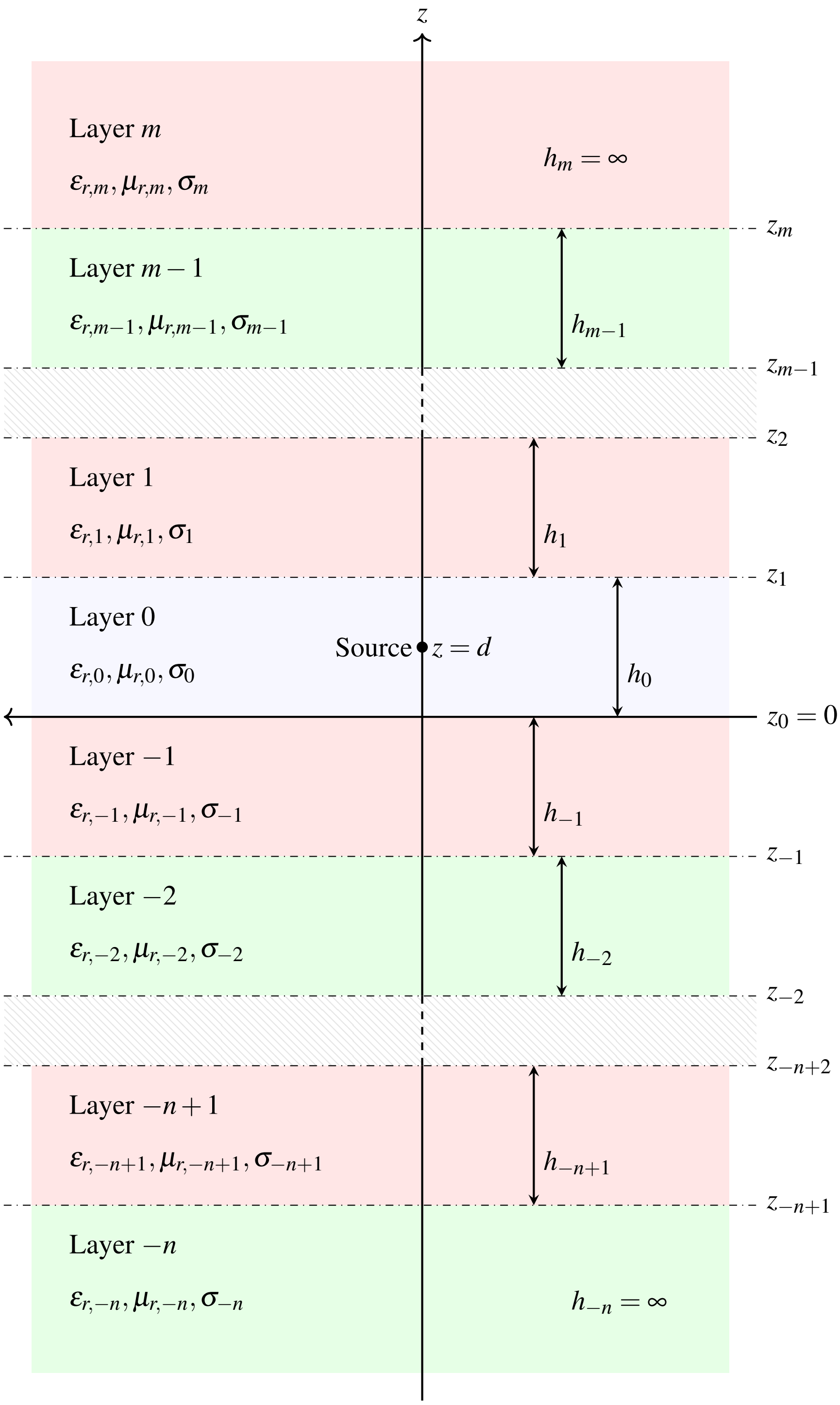

Figure 5.3: Schematic representation of the layered media in the model. The layering is in the z direction and can be described using either a Cartesian or cylindrical coordinate system.

$$\Pi_{i,y,\mathrm{HMD}} = \frac{\mathrm{j}M}{4\pi}\int_0^\infty \left[\delta(i)\frac{g}{u_0}e^{-u_0|d-z|} + D_{i,y}e^{u_iz} + U_{i,y}e^{-u_iz}\right] J_0(gr)\mathrm{d}g, \tag{5.3}$$

$$\Pi_{i,z,\mathrm{HMD}} = \frac{\mathrm{j}M}{4\pi}\frac{\delta}{\delta y}\int_0^\infty \frac{1}{g}\left[D_{i,z}e^{u_iz} + U_{i,z}e^{-u_iz}\right] J_0(gr)\mathrm{d}g, \tag{5.4}$$

where M is the magnetic moment magnitude[‡] of the MPD in $\mathrm{A}\cdot\mathrm{m}^2$, J_0 is the Bessel function of the first kind of order zero, $r = \sqrt{x^2+y^2}$ is the horizontal distance from the source, and

$$u_i = \sqrt{g^2 - k_i^2}. \tag{5.5}$$

The other variables in Eqs. (5.3) and (5.4) will be explained below.

The point dipole is represented by an integration (continuous summation) over an infinite number of plane waves traveling from the source in all directions. In these equations, g is the integration variable, that relates to the angle of incidence and reflection θ (see Figure 5.1) of the waves generated by the source via $g = k_0 \sin\theta$. In this way, it projects the propagation onto the xy-plane.

As stated earlier, the EM fields at any position are a superposition of the fields following direct and indirect paths from the source. The $\delta(i)\frac{g}{u_0}$ term represents the direct path. The $D_{i,j}$ term, with $j = y, z$, recursively represents the indirect paths traveling downward from the layers above layer i, and the $U_{i,j}$ term recursively represents the indirect paths traveling upward from the layers below layer i.

There are no layers above the source, so layer $m = 0$ is the top layer, and thus no reflections can occur above the source. Therefore, we know that

$$D_{0,y}(g) = 0, \qquad D_{0,z}(g) = 0. \tag{5.6}$$

When layer 0 is the top layer, the reflections from the layers $-n < i < -1$ are given by [209]:

$$U_{0,y}(g) = \frac{g}{u_0}R_{||0}^{-1}e^{-u_0d}, \tag{5.7}$$

$$U_{0,z}(g) = -\frac{1-\frac{k_0^2}{k_{a-1}^2}}{N_0 + Y_{-1}}\frac{g^2}{\mathrm{j}\omega\mu_{r,0}\mu_0u_0}(1+R_{||0}^{-1})e^{-u_0d}, \tag{5.8}$$

where

$$R_{||0}^{\pm1} = \frac{K_0 - Z_{\pm1}}{K_0 + Z_{\pm1}}, \tag{5.9}$$

‡The magnetic moment M in [209, 226] includes an additional $\omega\mu_{r,i}\mu_0$ term, which is incompatible with the $\mathrm{A}\cdot\mathrm{m}^2$ unit of M. This was found to cause results incompatible with both Simulia CST Studio Suite® [35] and the analytical model from Chapter 4. Therefore, this term was omitted in this chapter.

$$k_{a\pm1}^2 = \frac{g^2}{1 - Z_{\pm1}Y_{\pm1}}, \tag{5.10}$$

$$K_i = \frac{u_i}{\sigma_i + \mathrm{j}\omega\mu_{r,i}\mu_0}, \tag{5.11}$$

$$N_i = \frac{u_i}{\mathrm{j}\omega\mu_{r,i}\mu_0}, \tag{5.12}$$

$$Z_i = K_i \frac{Z_{i-1} + K_i \tanh(u_i h_i)}{K_i + Z_{i-1}\tanh(u_i h_i)}, \tag{5.13}$$

$$Y_i = N_i \frac{Y_{i-1} + N_i \tanh(u_i h_i)}{N_i + Y_{i-1}\tanh(u_i h_i)}, \tag{5.14}$$

and the $\pm$ sign denotes whether the reflection is coming from the layer(s) below $(-)$ or above $(+)$ the layer containing the source. As stated before, we consider the situation where the source is located in the top layer, meaning that the layers are located below the source. Therefore, the $\pm$ will always be $-$. Nonetheless, the $\pm$ sign is used for completeness.

In a multi-layer environment, waves bounce back and forth between boundaries, as depicted in Figure 5.1. This is analogous to the behavior of fields inside a network of cascaded transmission lines [226]. In this analogy, u_i is the propagation constant in the ith layer, K_i is the characteristic impedance, and N_i is the characteristic admittance.

$R_{||0}^{\pm1}$ is the input reflection coefficient of the layer stack, the algebraic form of which is analogous to the input reflection for parallel incidence of a plane wave, hence the $||$ denotation. Analogous to the transmission line, the input impedance Z_i of a layer depends not only on its own characteristic impedance, but also on the dielectric and spatial properties of the surrounding layers [227]. This results in recursive relations for the input impedance of layer i, given in Eq. (5.13). Similarly, the input admittance of layer i is given in Eq. (5.14).

The downward and upward contributions in the successive layers are also given by recursive relations, for the same reason. In the layers $i < 0$, these are given as [209]:

$$D_{i-1,y} = C_{i,y}^{+}\left[D_{i,y} + \delta(i)\frac{g}{u_0}e^{-u_0 d}\right]e^{(u_i - u_{i-1})z_i} + C_{i,y}^{-}U_{i,y}e^{-(u_{i-1}+u_i)z_i}, \tag{5.15}$$

$$U_{i-1,y} = C_{i,y}^{-}\left[D_{i,y} + \delta(i)\frac{g}{u_0}e^{-u_0 d}\right]e^{(u_{i-1} + u_i)z_i} + C_{i,y}^{+}U_{i,y}e^{(u_{i-1}-u_i)z_i}, \tag{5.16}$$

$$\begin{aligned} D_{i-1,z} &= C_{i,z}^{+}D_{i,z}e^{(u_i-u_{i-1})z_i} + C_{i,z}^{-}U_{i,z}e^{-(u_{i-1}+u_i)z_i} \\ &\quad - \frac{g}{2u_{i-1}}\left(1 - \frac{k_i^2}{k_{i-1}^2}\right)\left\{\left[D_{i,y} + \delta(i)\frac{g}{u_0}e^{-u_0 d}\right]e^{(u_i-u_{i-1})z_i} + U_{i,y}e^{-(u_{i-1}+u_i)z_i}\right\}, \end{aligned} \tag{5.17}$$

$$\begin{aligned} U_{i-1,z} &= C_{i,z}^{-}D_{i,z}e^{(u_{i-1}+u_i)z_i} + C_{i,z}^{+}U_{i,z}e^{(u_{i-1}-u_i)z_i} \\ &\quad - \frac{g}{2u_{i-1}}\left(1 - \frac{k_i^2}{k_{i-1}^2}\right)\left\{\left[D_{i,y} + \delta(i)\frac{g}{u_0}e^{-u_0 d}\right]e^{(u_{i-1}+u_i)z_i} + U_{i,y}e^{(u_{i-1}-u_i)z_i}\right\}, \end{aligned} \tag{5.18}$$

with the propagation factors

$$C_{i,y}^{\pm} = \frac{1}{2}\frac{\mu_{r,i}}{\mu_{r,i-1}}\left[\frac{\sigma_i + \mathrm{j}\omega\mu_{r,i}\mu_0}{\sigma_{i-1} + \mathrm{j}\omega\mu_{r,i-1}\mu_0} \pm \frac{u_i}{u_{i-1}}\right], \tag{5.19}$$

$$C_{i,z}^{\pm} = \frac{1}{2}\left[\frac{\mu_{r,i}}{\mu_{r,i-1}} \pm \frac{u_i}{u_{i-1}}\right]. \tag{5.20}$$

In the bottom layer ($i = -n$), the upward component U_{-n} is zero, since there is no lower layer for the waves to reflect off.

The electric and magnetic fields generated by the HMD can now be obtained by evaluating Eqs. (5.1a) and (5.1b), respectively, in each layer, in Cartesian coordinates. $\mathbf{\Pi}_i(\mathbf{r},t)$ is composed of Eqs. (5.3) and (5.4), its x-component is zero.

5.2.3 Vertical Magnetic Point Dipole (VMD)

The magnetic Hertz potential $\mathbf{\Pi}_{i,\mathrm{VMD}}$ for a VMD contains only a z-component. To compute the fields generated by a VMD, we substitute Eqs. (5.15), (5.16), and (5.20) into Eq. (5.3) [209], resulting in

$$\Pi_{i,\mathrm{VMD}} = \frac{\mathrm{j}M}{4\pi}\int_0^{\infty}\left[\delta(i)\frac{g}{u_0}e^{-u_0|d-z|} + D_{i,\mathrm{VMD}}e^{u_i z} + U_{i,\mathrm{VMD}}e^{-u_i z}\right]J_0(gr)\mathrm{d}g. \tag{5.21}$$

In this expression, the downward $D_{i,\mathrm{VMD}}$ and upward $U_{i,\mathrm{VMD}}$ contributions in layer i, are given by [209]:

$$D_{i-1,\mathrm{VMD}} = C_{i,z}^{+}\left[D_{i,\mathrm{VMD}} + \delta(i)\frac{g}{u_0}e^{-u_0 d}\right]e^{(u_i-u_{i-1})z_i} + C_{i,z}^{-}U_{i,\mathrm{VMD}}e^{-(u_{i-1}+u_i)z_i}, \tag{5.22}$$

$$U_{i-1,\mathrm{VMD}} = C_{i,z}^{-}\left[D_{i,\mathrm{VMD}} + \delta(i)\frac{g}{u_0}e^{-u_0 d}\right]e^{(u_{i-1}+u_i)z_i} + C_{i,z}^{+}U_{i,\mathrm{VMD}}e^{(u_{i-1}-u_i)z_i}. \tag{5.23}$$

Since the setup now exhibits rotational symmetry, we use cylindrical coordinates. In layer 0, again assuming this is the top layer ($m = 0$), we have

$$D_0(g) = 0, \tag{5.24}$$

$$U_0(g) = \frac{g}{u_0}R_{\perp 0}^{+1}e^{-u_0 d}, \tag{5.25}$$

where

$$R_{\perp 0}^{\pm 1} = \frac{N_0 - Y_{\pm 1}}{N_0 + Y_{\pm 1}}, \tag{5.26}$$

is the reflection coefficient of the layer stack, which is now algebraically analogous to the input reflection for perpendicular incidence of a plane wave, hence the $\perp$ denotation. Again, in the bottom layer $(i = -n)$, the upward component U_{-n} is zero.

The electric and magnetic fields generated by the VMD can now be obtained by evaluating Eqs. (5.1a) and (5.1b), respectively, in each layer, in cylindrical coordinates. The z-component of $\mathbf{\Pi}_i(\mathbf{r},t)$ is given by Eq. (5.21), and its other components are zero.

5.3 Numerical Implementation

We now have all necessary equations to calculate the fields at any location in any layer. No closed-form solutions are available for Eqs. (5.3), (5.4) and (5.21), or their (partial) derivatives, required in Eqs. (5.1a) and (5.1b). Therefore we have to use numerical approximations. In the following two subsections, numerical implementation details will be given for the differentiation and integration operations needed.

The values mentioned in this section assume a situation with frequencies ranging from 100 kHz to 5 GHz, distances in the order of centimeters, $\varepsilon_r \leq 60$, and $\sigma \leq 1$ S/m. These values are believed to be representative for the application under consideration, being WPT to an IMD. Details about the exact setups used can be found in Section 5.5. For applications outside these ranges, the outlined procedures can be followed to obtain workable settings for the numerical implementation.

5.3.1 Numerical differentiation

We use the central difference rule to numerically approximate spatial derivatives, given by [118]:

$$\frac{\delta}{\delta x} f(x) \approx \frac{f(x+\Delta) - f(x-\Delta)}{2\Delta}, \tag{5.27}$$

where Δ is the step size, which has to be chosen sufficiently small; if this value is chosen too small, internal round-off errors start to influence the result notably. If this value is chosen too large, the approximation error becomes too large.

Higher order and mixed derivatives are approximated by

$$\frac{\delta^2}{\delta x^2} f(x) \approx \frac{f(x+\Delta) - 2f(x) + f(x-\Delta)}{\Delta^2}, \tag{5.28}$$

$$\frac{\delta^2}{\delta x \delta y} f(x,y) \approx \frac{f(x+\Delta,y+\Delta) - f(x-\Delta,y+\Delta) - f(x+\Delta,y-\Delta) + f(x-\Delta,y-\Delta)}{4\Delta^2}, \tag{5.29}$$

and even higher order approximations can be obtained by combining Eqs. (5.27)—(5.29). The error introduced by the approximations is of order Δ^2 [118]. For our tests, $\Delta = 10^{-3}$ meter was found to result in sufficient accuracy, as decreasing the value further does not notably improve the result.

For the HMD, we can rewrite Eq. (5.1) (in Cartesian coordinates) as

$$E_{i,x} = -\mathrm{j}\omega\mu\left(\frac{\partial^2}{\partial y^2}\Pi'_{i,z} - \frac{\partial}{\partial z}\Pi_{i,y}\right), \tag{5.30}$$

$$E_{i,y} = \mathrm{j}\omega\mu\frac{\partial^2}{\partial x\partial y}\Pi'_{i,z}, \tag{5.31}$$

$$E_{i,z} = -\mathrm{j}\omega\mu\frac{\partial}{\partial x}\Pi_{i,y}, \tag{5.32}$$

$$H_{i,x} = \frac{\partial^2}{\partial x\partial y}\Pi_{i,y} + \frac{\partial^3}{\partial x\partial y\partial z}\Pi'_{i,z}, \tag{5.33}$$

$$H_{i,y} = \left(k^2 + \frac{\partial^2}{\partial y^2}\right)\Pi_{i,y} + \frac{\partial^3}{\partial y^2\partial z}\Pi'_{i,z}, \tag{5.34}$$

$$H_{i,z} = \frac{\partial^2}{\partial y\partial z}\Pi_{i,y} + \left(k^2\frac{\partial}{\partial y} + \frac{\partial^3}{\partial y\partial z^2}\right)\Pi'_{i,z}, \tag{5.35}$$

where we have introduced

$$\Pi'_{i,z} = \frac{\mathrm{j}M}{4\pi}\int_0^\infty \frac{1}{g}\left[D_{i,z}e^{u_i z} + U_{i,z}e^{-u_i z}\right]J_0(gr)\mathrm{d}g, \tag{5.36}$$

of which the numerical derivative with respect to y is to be taken to obtain $\Pi_{i,z}$ in Eq. (5.4). Using the central difference rule, we obtain

$$\Pi_{i,z} \approx \frac{\Pi'_{i,z}(x, y+\Delta, z) - \Pi'_{i,z}(x, y-\Delta, z)}{2\Delta}. \tag{5.37}$$

For the VMD, we use cylindrical coordinates. We can rewrite Eq. (5.1) as

$$H_{i,r} = \frac{\partial^2}{\partial r\partial z}\Pi_{i,\mathrm{VMD}}, \tag{5.38}$$

$$H_{i,z} = \left(k_i^2 + \frac{\partial^2}{\partial r\partial z}\right)\Pi_{i,\mathrm{VMD}}, \tag{5.39}$$

$$E_{i,\varphi} = \mathrm{j}\omega\mu_i\frac{\partial}{\partial r}\Pi_{i,\mathrm{VMD}}. \tag{5.40}$$

The other field components are zero. All derivatives are calculated using the central difference rule.

5.3.2 Numerical integration

For numerical integration, we use the built-in `integral` function of MATLAB [145, 193], which is based on an adaptive Gauss-Kronrod (7 Gauss nodes, 15 Kronrod nodes) quadrature method. This method yields sufficiently accurate results for our application.

Number of subdomains

The upper bound of Eqs. (5.3), (5.21), and (5.36) is infinite, which would result in an infinite number of subdomains for integration. Since the integrands approach zero for g approaching infinity, truncation at a large, but finite upper bound can take place, such that a finite number of subdomains can be used. The routine then adaptively determines the required number of these subdomains, based on an estimation of the approximation error.

The integrands of Eqs. (5.3), (5.21), and (5.36) are generally smooth functions, and are hence very well piecewise approximated by only a few polynomials. This implies that the expected number of subdomains required for accurate numerical integration is small. However, there is one sharp peak near $g = \frac{\omega}{c_0}$, with $c_0 = (\varepsilon_0\mu_0)^{-\frac{1}{2}}$ the speed of light in vacuum, caused by a near-singularity. This peak area is difficult to approximate by a polynomial, resulting in a high number of local subdomains, and a large number of iterations, before the approximation error is sufficiently low. This, in turn, leads to a significant increase in computation time.

A solution to this problem is to manually assign several small subdomains over the range for g where the peak is expected.

Upon evaluation of a wide range of the model parameters mentioned before, it was found that introducing 10 equidistant boundaries (9 subdomains) over the range $g \in [0.88 - 1.12]\frac{\omega}{c_0}$, is sufficient to capture the peak with an acceptably low relative approximation error (below 0.1%, estimated by a MATLAB routine). Figure 5.4 shows the subdomain boundaries with a typical integrand curve.

Upper boundary

As stated before, the integrands of Eqs. (5.3), (5.21), and (5.36) approach zero for g approaching infinity. They consist of recursive functions that contain both positive and negative exponentials. The total combination of these exponentials, multiplied with the Bessel function $J_0(gr)$, indeed approaches zero. However, in the implementation of a recursive scheme, each part is inherently evaluated separately. Some of the individual parts have a dominant positive exponential, whereas others have a dominant negative exponential. Hence, some individual parts will grow towards infinity for large g, whereas others will eventually reach zero. When a part of the integrand reaches infinity, the numerical integration procedure will fail, even though the total integrand approaches zero.

Additionally, when the argument of a negative exponential is sufficiently large, the value of this exponential approaches machine precision, but is not yet zero. In that case, unpre-

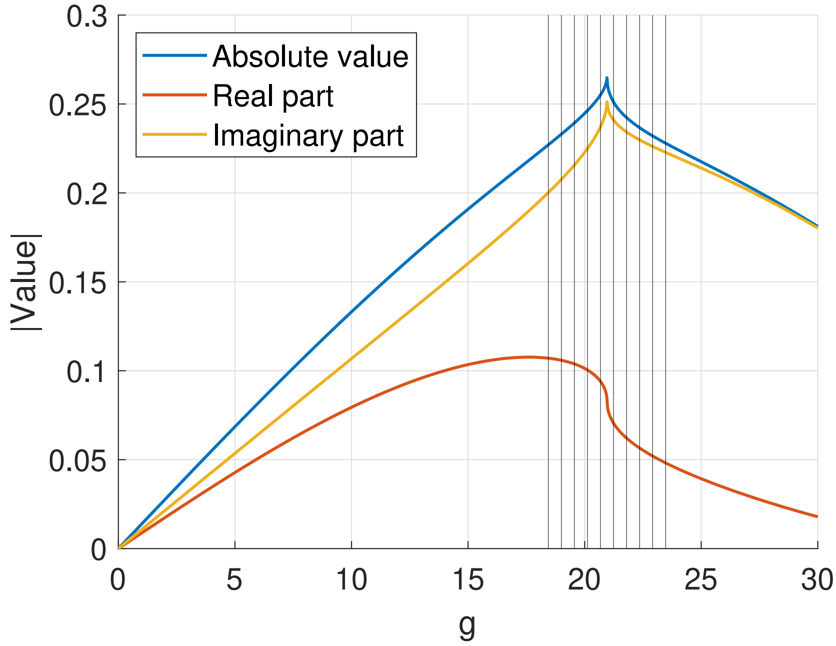

Figure 5.4: Typical VMD integrand of Π_y (Eq. (5.3)), with 10 enforced integration domain boundaries around the peak in the range $g \in [0.88 - 1.12]\frac{\omega}{c_0}$.

dictable rounding errors can occur. This implies that when individual parts of the integrand are large, yet still finite, they can magnify these rounding errors, causing erroneous results.

The solutions to these problems are different for the HMD and VMD case, as their integrands differ. The two cases are detailed next.

HMD

The infinite integration bounds for g can be replaced by the finite values g_{by} and g_{bz} for Eqs. (5.3) and (5.36), respectively, truncating the integration domain. The values should be chosen such that the integrands at these values are sufficiently small, and not yet affected by parts of the integrand growing towards or reaching infinity.

We have empirically derived values for g_{by} and g_{bz} listed in Table 5.1, which result in correct behavior for the model parameters mentioned before. Please note that these values are not critical, but serve as guidelines; changing them a few percent will not notably change the result. To determine whether these values are applicable to models with other parameters, or to determine new values in case they are not, the following procedure can be used.

We start by looking at the integrand as a function of g. Figure 5.5 shows an example of how the integration procedure fails in a 5-layer HMD situation. In Figure 5.5(a), one can clearly see that initially, for low g, the integrands in each layer decrease as g increases, which is as expected. In layers 0 and -1, the integrands keep decreasing throughout the figure, but for $g > 250$, the integrand in layer -4 starts to increase and becomes 'noisy'. The increase suggests that the positive exponentials dominate the negative ones. The noise suggests that

Table 5.1: General guidelines for choosing upper bounds g_{by} and g_{bz}.

$\mathbf{g_{by}}$	$\mathbf{g_{bz}}$	**Layer**	**z**
60060	665	$i=0$	$\lvert z-d\rvert \leq 0.3d$
6006	665	$i=0$	$0.3d < \lvert z-d\rvert \leq 1.1d$
1001	665	$i=0$	$\lvert z-d\rvert > 1.1d$
1001	665	$i=-1$	all
601	1002	$-n+1 \leq i \leq -2$	all
501	542	$i=-n$	all

the terms containing negative exponentials approach machine precision, resulting in unpredictable rounding errors.

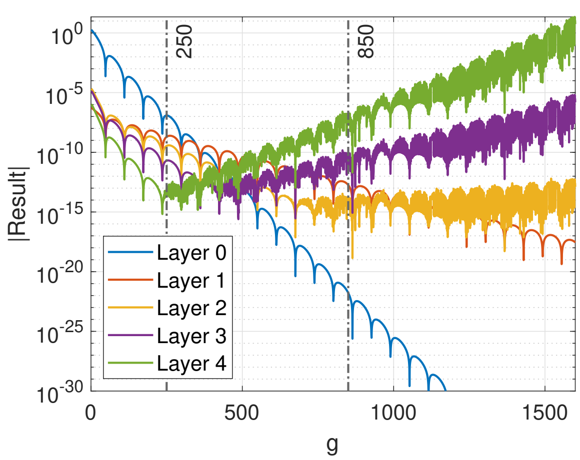

(a) Integrand of Eq. (5.3).

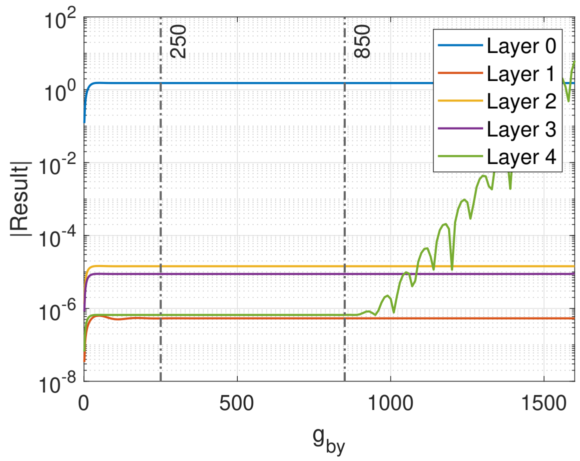

(b) Computed integral of Eq. (5.3) with upper bound g_{by}.

Figure 5.5: Effect of upper bound g_{by} on the computed value of $\Pi_{i,y}$, Eq. (5.3).

Figure 5.5(b) shows that for $g > 850$, the result of the integral is notably affected by the described phenomenon. In layer -4, g_{by} should thus be chosen smaller than 850. Figure 5.5(b) also shows that for $g > 250$, the results of the integral have approximately reached a steady state value (within 0.5%, which is considered acceptably low). The value of g_{by} in layer -4 should thus be chosen larger than 250. By repeating this procedure for different layers, coordinates, and dielectric properties, one can define a proper value for the boundaries of g_{by}. The procedure for finding g_{bz} is analogous.

In layer 0, when z is close to d, the integral converges slowly. Hence, as $|z-d|$ approaches zero, the upper bound for the integral should increase. This is included in Table 5.1.

VMD

This case is more complicated to solve, as there is a large spread in behavior of the integrand, depending on the frequency, number of layers, and r and z coordinates. Simply choosing a fixed finite upper boundary, as we did for the HMD in the previous subsection, will most probably introduce an error. To get a workable solution, asymptotic extraction is used [97]. This could also be an option for the HMD, but the solution presented above executes faster.

Suppose we have to compute $A = \int_0^\infty F(g)dg$, where $F(g)$ is difficult to evaluate numerically for large values of g. The integration interval $[0,\infty\rangle$ can be split into two parts $[0,b]$ and $[b,\infty\rangle$, such that the integral can be rewritten as

$$A = \int_0^\infty F(g)\mathrm{d}g = \int_0^b F(g)\mathrm{d}g + \int_b^\infty \tilde{F}(g)\mathrm{d}g + \int_b^\infty \big(F(g) - \tilde{F}(g)\big)\mathrm{d}g, \tag{5.41}$$

where asymptotic function $\tilde{F}(g)$ is a good approximation for $F(g)$ for large $g \geq b$, which can be computed without numerical problems. We can then write $F(g) \approx \tilde{F}(g)$ for $g \geq b$, simplifying the asymptotic extraction to

$$A \approx \int_0^b F(g)\mathrm{d}g + \int_b^\infty \tilde{F}(g)\mathrm{d}g. \tag{5.42}$$

From a plot of the integrand of Eq. (5.21), the tail of the curve is observed to look very smooth, which is the case for all configurations considered. It turns out that for g large enough (will be specified later), we can approximate Eq. (5.5) to $u_i \approx g$. This results in many of the exponentials of Eqs. (5.22) and (5.23) approaching $e^0 = 1$. Furthermore, this results in $\frac{g}{u_0} \approx 1$, $C_i^- \approx 0$, $C_i^+ \approx 1$, and $R^1_{\perp 0} \approx 0$.

Substituting the above, for g_b large enough (will be specified later), we can approximate Eq. (5.21) by

$$\Pi_{i,\mathrm{VMD}} \approx \Pi_{i,\mathrm{VMD}}\Big|_0^{g_b} + \frac{\mathrm{j}M}{4\pi}\int_{g_b}^\infty e^{-g|d-z|} J_0(gr)\mathrm{d}g, \tag{5.43}$$

which can be computed without numerical problems. $\Pi_{i,\mathrm{VMD}}\big|_0^{g_b}$ is equal to Eq. (5.21), but now the integral runs from 0 to g_b, instead of from 0 to ∞. The introduced relative error has been observed to stay below 0.1%, which is considered acceptable.

Besides mitigating numerical problems, the procedure of asymptotic extraction causes a significant speedup in the execution of the model. This speedup can be increased even further using an approximation for the Bessel function J_0. The asymptotic approximation of a Bessel function of the first kind and order 0, for $gr \gg \frac{1}{4}$, is given as [2]:

$$J_0(gr) \approx \sqrt{\frac{2}{\pi g r}} \cos\left(gr - \frac{\pi}{4}\right), \tag{5.44}$$

Figure 5.6 shows an example of the behavior of the original integrand of Eq. (5.21), the result using asymptotic extraction (5.43), and the one containing also an approximation of the Bessel function (5.44). It can be seen that indeed, for large g, the original integrand starts to increase and becomes ‘noisy’. The asymptotic extracted integral and the original one are hardly distinguishable already at $g = 40$, and around $g = 125$, the difference with the approximated Bessel function is also acceptably low.

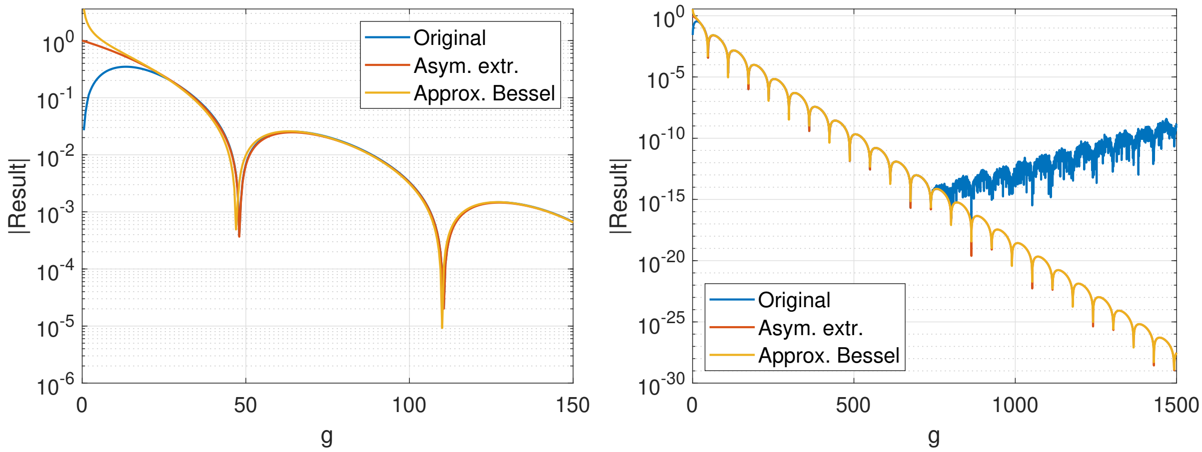

(a) Behavior for small values of g. **(b)** Behavior for larger values of g.

Figure 5.6: Example behavior of the original integrand, the result using asymptotic extraction, and the one using both asymptotic extraction and Bessel function approximation.

We can now use Eqs. (5.43) and (5.44) to make sure Eq. (5.21) can be computed successfully, without generating numerical problems and with sufficient accuracy. The complete solution can be written as

$$\Pi_i \approx \frac{\mathrm{j}M}{4\pi}\int_0^{g_b}\left[\delta(i)\frac{g}{u_0}e^{-u_0|d-z|} + D_i e^{u_i z} + U_i e^{-u_i z}\right] J_0(gr)\mathrm{d}g$$
$$+ \frac{\mathrm{j}M}{4\pi}\int_{g_b}^{g_c} e^{-g|d-z|} J_0(gr)\mathrm{d}g + \frac{\mathrm{j}M}{4\pi}\int_{g_c}^{\infty} e^{-g|d-z|}\sqrt{\frac{2}{\pi g r}}\cos(gr - \tfrac{\pi}{4})\mathrm{d}g. \qquad (5.45)$$

The values for g_b and g_c have to be chosen with care, otherwise the approximation might not be successful. The three parts of Eq. (5.45) were evaluated separately for a wide range of r, $|d-z|$, and ω, listed in Section 5.5, to obtain the range of values for g_b and g_c for which the difference between two successive parts is acceptably low. Suggested values for g_b and g_c were found empirically as

$$g_b = e^{\left(\frac{\omega}{\pi 10^{10}}\right)} \cdot \max\left[500, \min\left(\frac{3}{r}, \frac{60}{|d-z|}\right), \frac{50000}{2000|d-z|+1}\right],$$
$$g_c = \max\left[\frac{5}{r}, g_b + 1\right].$$

5.4 Model validation

The analytical model is validated by comparing the results with the results for the fields generated with the commercial 3D EM field simulation software Simulia CST Studio Suite® [35]. We will show results for nine frequencies ranging from 100 kHz to 5 GHz, corresponding to free space wavelengths ranging from 3 km to 60 mm. The model is validated for specific situations, each with a certain number of layers, dielectric parameters, and dipole orientation. Figure 5.7(a) shows the 3-layer VMD model used in the comparison, implemented in CST Studio Suite®, representing for example an air-skin-muscle setup.

5.4.1 Modeling a magnetic point dipole

Simulia CST Studio Suite® does not allow for direct excitation by ideal MPDs, but as it turns out, a current loop can be considered a good approximation for a MPD, if its circumference is small enough compared to the wavelength [223]. In the CST model, we use a current loop with a fixed diameter of 215 μm, such that the circumference is less than 2% of the wavelength at 5 GHz. This is small enough for this assumption to hold.

The model is excited by a current source, which is placed inside a 2 μm wide slit in the loop. Figure 5.7(b) shows a closeup of the loop, with the current source in the slit at the top. The current through the loop is 1.0 A, resulting in a magnetic moment magnitude of $M = 3.63 \cdot 10^{-8}$ $[\mathrm{A} \cdot \mathrm{m}^2]$.

5.4.2 Quantification of the result

To compare the fields generated by CST Studio Suite® and those generated by the analytical model, the relative difference is calculated. A relative difference below 10% is considered sufficiently accurate to use this model as a practical design tool for simulations of WPT systems in multilayered (biomedical) environments.

In order to compare any two fields, their spatial sampling grids should be identical, such that the field values can be compared at each coordinate. We chose to interpolate the coordinate grids of both the fields generated by CST Studio Suite® and those generated by the analytical model onto one new grid, to make sure the procedure is not limited by the spatial sampling of any of the original fields.

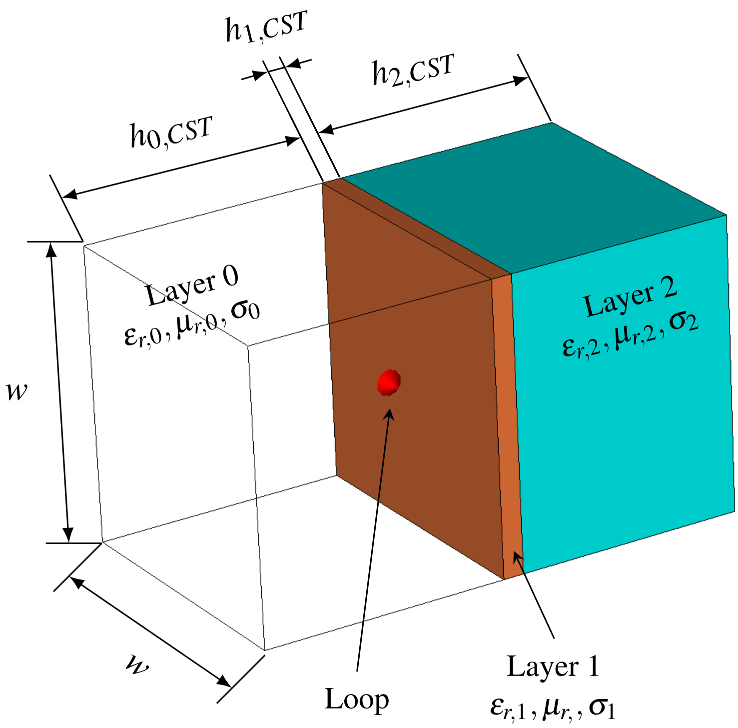

(a) Complete model, dimensions given in Section 5.5.

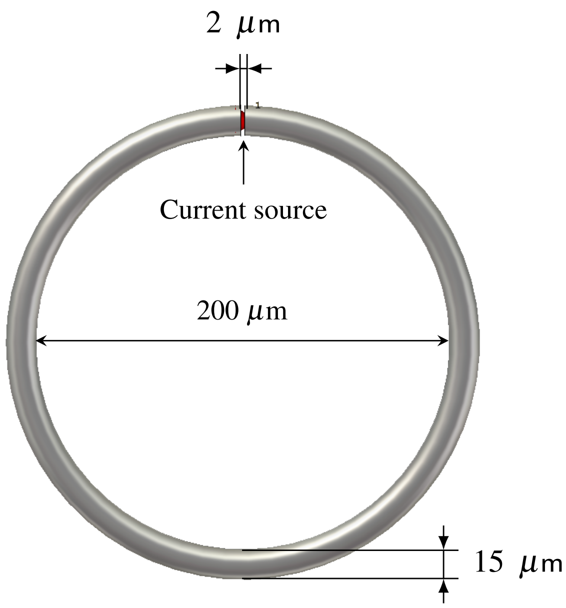

(b) Close-up of the loop.

Figure 5.7: CST model used to validate the three-layer mathematical model, representing for example an air-skin-muscle configuration.

The Modified Akima [5] algorithm is used for interpolation, as it outperforms other algorithms that were tested, such as spline, bicubic, and linear, in terms of accuracy. For each coordinate $\mathbf{r}$, the relative difference in the magnetic field strength is quantified as

$$\text{diff}(\mathbf{r}) = \frac{\big||H_{model}(\mathbf{r})| - |H_{CST}(\mathbf{r})|\big|}{|H_{CST}(\mathbf{r})|}, \tag{5.46}$$

for each field component. The approach for the electric field is analogous.

5.4.3 Behavior near boundaries

The behavior of the fields near the boundaries of the simulation domain of CST Studio Suite® requires special attention. We run our analytical model for $r \in [0, 50]$ mm. When running a CST simulation over the same domain (with ‘open’ PML boundaries), the relative difference between the fields calculated by CST Studio Suite® and those calculated by our model near the boundaries is tens to hundreds of percent, which is unacceptably high. Increasing the CST simulation domain, whilst the domain of the mathematical model remains unchanged, results in a better resemblance between the fields. In general, the larger the CST simulation domain, the smaller the difference near the original boundaries.

How much increase in domain size is required, depends among others on the problem size, MPD orientation, dielectric properties, frequency, and the solver order. However, with the increase of simulation domain, the required number of mesh cells increases as well, which increases the required memory (and simulation time). This could eventually lead to a memory overflow.

As it turns out, it is not straightforward to determine how large a domain is required. It can actually take quite some iterations before a decent simulation setup can be defined. One might consider increasing the simulation domain to such an extent that it is without doubt large enough, at the expense of a longer simulation time. However, this can increase the required memory to levels that are not available. For our simulations, the available computers were limited to 768 GB RAM, but this would not be sufficient to support this alternative solution, as can be seen in Section 5.5. Since the mathematical model needs to be validated only once, we have not attempted to generate general rules for finding the required CST simulation domain size. Instead, the simulation domain is increased until the results converged.

5.4.4 Meshing considerations

In this chapter, the transmitter coil is located at $h = 10$ mm above layer -1, and has a fixed diameter of 215 μm, whereas the simulation domain is three orders of magnitude larger, with wavelengths ranging from 60 mm to 3 km. The slit is only 2 μm wide. The mesh in and around the coil should be sufficiently fine to capture the details of its shape properly. On the other hand, the mesh size should increase further away from the source, as simulations will otherwise require too much memory. A non-uniform meshing is thus required.

5.4.5 Behavior near the source

Close to the coil, i.e. less than 3 mm away, the relative differences between the fields generated by CST Studio Suite® and those generated by the analytical model can be high, as was also observed in Chapter 4. This effect appears to be frequency-independent, which was verified for frequencies ranging from 100 kHz to 5 GHz, with the MPD located in air. Even though the small wire loop is known to behave very similar to a MPD, it is not a perfect representation.

The fields close to the source are considered less relevant for the scope of this work, again for the purpose of WPT. Therefore, we ignore a small region around the source during the calculation of the relative differences. This region extends 3 mm around the source in each direction. Figure 5.8 shows an example of how this region is excluded. In the remainder of this chapter, this procedure will be addressed as 'correction near the source'.

5.4.6 Nulls in field distribution

Another issue regards nulls in the field distribution of the MPD. Every realizable antenna or coil has directions in which it radiates little energy. For the MPD, the locations of these 'nulls' generated by CST Studio Suite® and those generated by our model match quite closely, but they do not perfectly coincide. This can cause large relative differences. This can be seen in Figure 5.8(b). The dark red areas in the relative difference correspond to areas where the calculated field is almost zero.

With the main goal of this work in mind, namely WPT for biomedical applications, we are specifically interested in areas where high power levels are present, or where high power absorption in tissue occurs. As a result, the exact field values near zero are less relevant. Therefore, we ignore the coordinates where either the simulated or the modeled field strength is lower than a certain threshold. This threshold is defined as follows. For each layer i, the maximum field value on both the top and bottom boundaries is determined. If any field value inside this layer is below -40 dB of this maximum value, the corresponding coordinate is ignored in the calculation of the average relative difference. Figure 5.9 depicts an example. In the remainder of this chapter, this procedure will be addressed as 'correction for low field values'.

5.5 Results

The EM fields generated by the analytical model presented in this chapter are compared with those generated by the commercial EM field simulation software Simulia CST Studio Suite®, as explained in Section 5.4.

In biomedical implant applications, a wide range of spatial and dielectric parameters can be encountered, especially when the frequency range is large [67], which is the case in this research. We have chosen to limit our results to a depth (z-direction) of 100 mm, and a

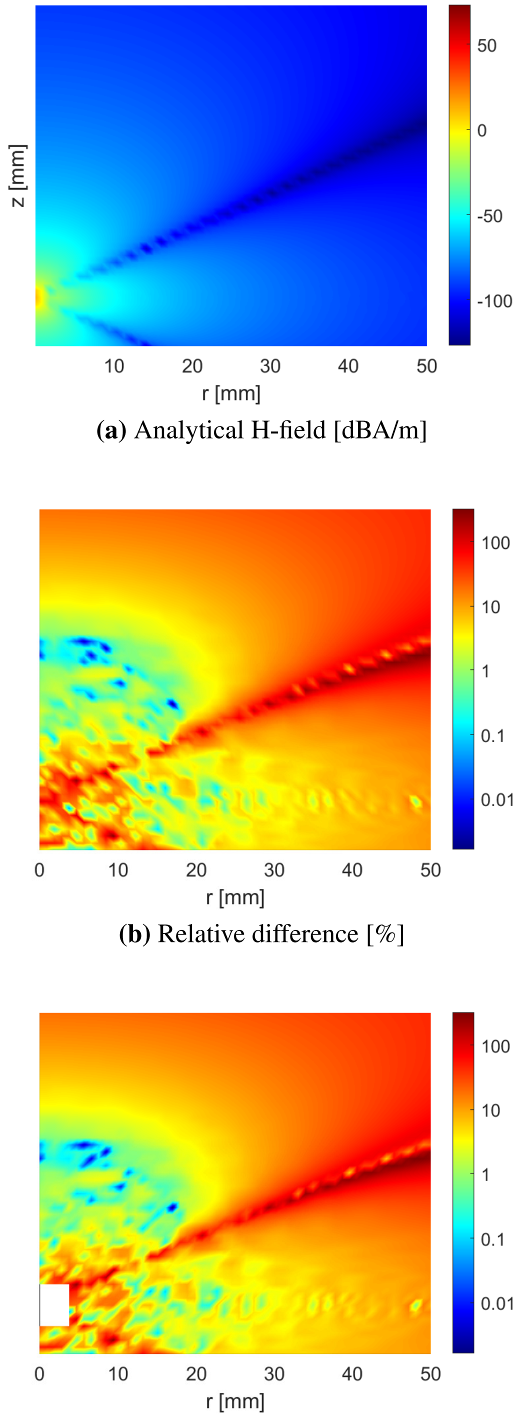

(**a**) Analytical H-field [dBA/m]

(**b**) Relative difference [%]

(**c**) Corrected difference [%]

Figure 5.8: Example of 'correction near the source', 3-layer VMD, H_z in the top layer at 13 MHz. Differences in %.

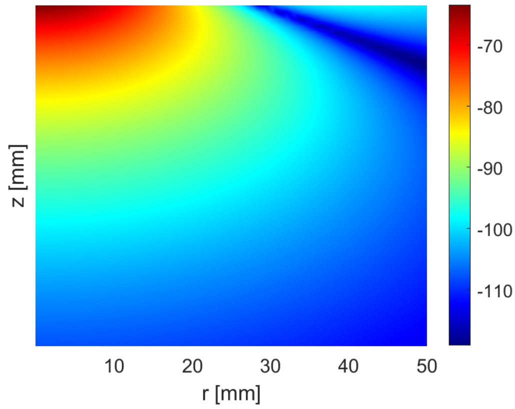

(a) Analytical H-field [dBA/m]

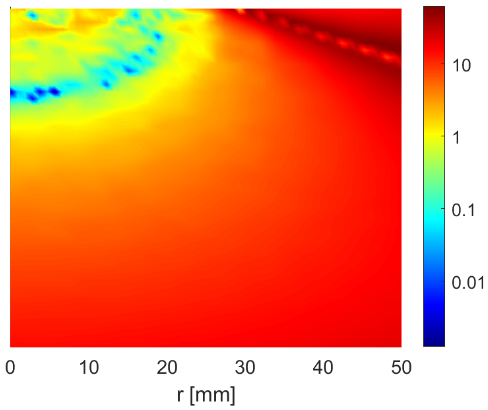

(b) Relative difference [%]

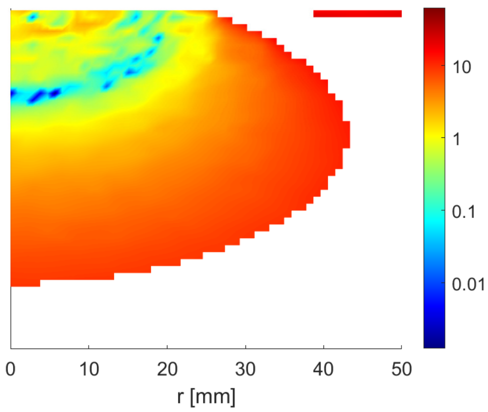

(c) Corrected difference [%]

Figure 5.9: Example of 'correction for low field values', 3-layer VMD, H_z in the bottom layer at 13 MHz. Differences in %.

misalignment (radial size) of at most 50 mm, as we believe this covers most practical cases. The relative permittivity ε_r of the layers is at most 60, and the conductivity σ is at most 1 S/m. This does not cover the full range encountered in biomedical applications, but we believe these values are sufficient to show the validity of the analytical model.

As indicated earlier, the validation is performed at nine discrete frequencies ranging from 100 kHz to 5 GHz. The VMD model is validated for 2—4 layers, the HMD is validated for 3 layers, and the use of more layers is discussed at the end of this section. The exact model parameters are listed in Tables 5.2 and 5.3. Additionally, the analytical 2-layer VMD model is compared to the previously presented 2-layer model in Chapter 4, based on work by Baños [12].

For the HMD, the results were computed for the region $x, y \in [0, 50]$ mm and $z \in [-100, 70]$ mm. Two cases are evaluated; the yz-plane, the plane in which the HMD is positioned, and the xz-plane, orthogonal to the HMD. For the VMD, the results are computed for the region $r \in [0, 50]$ mm and $z \in [-100, 70]$ mm.

In all cases, the MPD is located in layer 0, at $d = 10$ mm above layer -1. The step size in r, x, y, and z is 1 mm for the interpolation grid.

Besides the generated fields, also the computation time and memory usage are compared. The computations were performed on high performance computers [§ ¶ ‖ **].

Figures 5.10—5.12 show planar cuts of the fields generated with our model, and the relative differences with the results generated with CST Studio Suite® for three different simulation cases.

5.5.1 2, 3, and 4-layer VMD

The 2, 3, and 4-layer VMD models were executed with the parameters listed in Table 5.2. The execution details for CST Studio Suite® are stated in Table 5.3.

2-layer VMD

When comparing the current 2-layer model to the 2-layer model presented in Chapter 4, after applying the corrections detailed in Sections 5.4.5 and 5.4.6, the average relative difference is below 2.3% in layer 0, and below 0.0043% in layer -1, for all frequencies. This can be seen in Table 5.4. Both analytical 2-layer models run in about 20 (100 kHz) to 50 (5 GHz) seconds[¶], using at most 8 GB memory.

[§] using 12 cores of a 16-core 2.3 GHz Intel® Xeon® Gold 5218 CPU.

[¶] using 12 cores of a 16-core 2.1 GHz Intel® Xeon® Gold 6130 CPU.

[‖] executed on two 6-core 2.79 GHz Intel® Xeon® X5660 CPUs.

[**] using 12 cores of a 64-core 2.2 GHz AMD EPYC™ 7601 CPU.

Table 5.2: Parameters for the 2, 3, and 4-layer models.

Layers		Layer 0	Layer -1	Layer -2	Layer -3
2	$\varepsilon_{r,i}$ [$\cdot$]	1	40		
	σ_i [S/m]	10^{-7}	1.0		
	height [mm]	70	70		
	Grid points	50×70	50×70		
3	$\varepsilon_{r,i}$ [$\cdot$]	1	8	40	
	σ_i [S/m]	10^{-7}	0.2	1.0	
	height [mm]	70	10	90	
	Grid points	50×70	50×10	50×90	
4	$\varepsilon_{r,i}$ [$\cdot$]	1	8	30	50
	σ_i [S/m]	10^{-7}	0.2	0.5	1.0
	height [mm]	70	10	20	70
	Grid points	50×70	50×10	50×20	50×70

Table 5.3: Simulation volume, execution time, and required memory for the VMD in CST Studio Suite®.

		0.1—13 MHz	100—400 MHz	1 GHz	2.45 GHz	5 GHz
2 layer	x,y [mm]	240	200	200	200	200
	z [mm]	$-170,110$	$-150,90$	$-150,90$	$-150,90$	$-150,90$
	t_{exec} [s]	7920**	6240‖	6240‖	6240‖	6240‖
	Mem [GB]	192	126	126	126	126
3 layer	x,y [mm]	220	220	180	180	140
	z [mm]	$-150,90$	$-150,90$	$-130,130$	$-130,130$	$-120,120$
	t_{exec} [s]	2340‖	2340‖	3780‖	3780‖	2100‖
	Mem [GB]	73	73	99	99	53
4 layer	x,y [mm]	400	400	400	300	220
	z [mm]	$-240,120$	$-240,120$	$-240,120$	$-200,120$	$-150,100$
	t_{exec} [s]	1020¶	1020¶	1020¶	21960§	19920§
	Mem [GB]	40	40	40	577	530

Table 5.4: Relative differences [%] between the fields generated by our model and the one from Chapter 4. 2-layer. VMD. Correction near the source and correction for low field values applied.

	Layer 0			**Layer** -1		
	H_r	H_z	E_φ	H_r	H_z	E_φ
100 KHz	1.7e−2	1.2e−5	8.8e−6	3.9e−6	1.2e−5	1.2e−5
1 MHz	1.7e−2	1.1e−5	8.9e−6	4.0e−6	1.6e−4	3.4e−5
6 MHz	1.7e−2	1.7e−5	9.0e−6	3.9e−6	1.2e−5	8.9e−5
13 MHz	1.7e−2	1.6e−5	1.2e−5	4.0e−6	9.2e−6	8.3e−6
100 MHz	1.7e−2	6.8e−6	8.9e−6	4.1e−6	4.3e−4	8.8e−4
400 MHz	1.6e−2	8.7e−5	9.0e−6	4.5e−6	5.2e−5	6.3e−6
1 GHz	4.6e−2	7.0e−6	8.5e−6	7.0e−6	2.0e−5	2.2e−5
2.45 GHz	1.5e−1	3.5e−1	1.3	3.0e−5	1.3e−4	2.7e−4
5 GHz	2.2e−1	2.3	6.7e−1	3.4e−5	5.6e−4	4.3e−3

When comparing the 2-layer VMD model to CST Studio Suite®, the average relative difference between the two is given in Table 5.5. As can be seen, it is below 8.7% for all frequencies, for all field components, and in all layers. In fact, in more than half of the cases it is below 3.0%.

Table 5.5: Relative differences [%] between the fields generated by our model and those of CST. 2-layer VMD. Correction near the source and correction for low field values applied.

Layer		100 kHz	1 MHz	6 MHz	13 MHz	100 MHz	400 MHz	1 GHz	2.45 GHz	5 GHz
0	H_r	2.9	2.9	2.9	2.3	2.2	2.4	2.1	4.1	2.6
	H_z	8.0	8.5	8.7	8.7	4.7	4.0	3.9	2.3	2.6
	E_φ	1.8	1.8	1.9	2.1	3.1	1.6	4.0	2.1	2.4
-1	H_r	1.5	1.5	1.4	1.3	1.4	2.6	1.9	2.2	2.6
	H_z	1.0	3.5	4.4	4.2	4.1	3.5	2.7	1.8	3.8
	E_φ	2.3	2.3	2.9	3.2	2.5	1.5	1.9	1.9	4.4

The analytical model runs in about 20 (100 kHz) to 50 (5 GHz) seconds[¶], using at most 8 GB memory. This means that the dedicated model is 160 to 410 times faster than CST Studio Suite®, using 16 to 24 times less memory.

3-layer VMD

For the 3-layer VMD, the average relative difference between the analytical model and CST Studio Suite® is below 6.2% for all frequencies, and in all layers. In fact, in most cases it is below 3.0%. The results are listed in Table 5.6.

Figure 5.10(a) shows the E_φ field at 13 MHz, generated by the analytical model. Figure 5.10(b) shows the relative difference between the fields generated by the analytical model and those generated by CST Studio Suite®. Additionally, Figure 5.10(c) shows this relative difference after applying the corrections detailed in Sections 5.4.5 and 5.4.6. The white areas are excluded from the calculation of the average relative difference presented in this section.

The analytical model runs in about 50 (100 kHz) to 100 (5 GHz) seconds¶, using at most 8 GB memory. This means that the dedicated model is 30 to 60 times faster than CST Studio Suite®, using 6 to 12 times less memory.

Table 5.6: Relative differences [%] between the fields generated by our model and those of CST. 3-layer VMD. Correction near the source and correction for low field values applied.

Layer		100 kHz	1 MHz	6 MHz	13 MHz	100 MHz	400 MHz	1 GHz	2.45 GHz	5 GHz
	H_r	4.3	4.4	4.3	4.3	4.5	4.2	3.4	1.9	3.4
0	H_z	4.0	3.8	5.4	4.0	3.8	3.3	4.5	3.0	3.2
	E_φ	5.0	4.7	5.0	2.2	4.5	2.7	4.2	2.1	3.0
	H_r	1.7	1.5	1.6	1.6	1.6	2.1	2.5	2.2	3.5
-1	H_z	1.9	2.1	2.3	1.9	2.0	2.1	2.3	2.4	2.5
	E_φ	1.3	1.2	1.2	1.3	1.2	1.9	2.1	2.0	2.5
	H_r	1.4	1.5	1.0	1.1	1.7	2.7	2.5	1.7	3.9
-2	H_z	4.4	1.8	3.9	4.4	1.2	2.4	3.1	3.2	4.6
	E_φ	5.6	2.0	5.3	6.2	0.8	2.4	2.4	1.5	3.2

4-layer VMD

For the 4-layer VMD, for all frequencies from 100 kHz to 1 Ghz, the resulting average relative difference between this model and CST Studio Suite® is below 3.0% for each field component and in any layer. At 2.45 and 5 GHz, the average relative difference is below 8.6%. The results are listed in Table 5.7.

The analytical model runs in about 80 (100 kHz) to 240 (5 GHz) seconds¶, using at most 8 GB memory. This means that the dedicated model is 6 to 90 times faster than CST Studio Suite®, and uses 5 to 70 times less memory.

5.5.2 3-layer HMD

The 3-layer HMD model was executed with the parameters listed in Table 5.2. Details about the simulation volumes used in CST Studio Suite® are listed in Table 5.8.

Table 5.7: Relative differences [%] between the fields generated by our model and those of CST. 4-layer VMD. Correction near the source and correction for low field values applied.

Layer		100 kHz	1 MHz	6 MHz	13 MHz	100 MHz	400 MHz	1 GHz	2.45 GHz	5 GHz
0	H_r	2.7	2.7	2.7	2.7	2.8	2.2	2.4	2.6	1.8
	H_z	2.4	2.4	2.4	2.4	2.4	2.5	2.5	1.7	1.4
	E_φ	1.4	1.4	1.4	1.4	1.4	1.8	2.6	1.9	1.4
-1	H_r	2.0	2.0	2.0	2.0	2.0	2.0	2.0	2.1	3.2
	H_z	1.9	1.9	1.9	2.0	2.0	2.0	1.9	1.9	1.8
	E_φ	1.6	1.6	1.6	1.7	1.8	2.0	1.9	2.0	2.5
-2	H_r	2.1	2.1	2.1	2.1	2.1	2.2	2.1	3.4	4.0
	H_z	1.6	1.6	1.6	1.7	1.9	1.9	2.1	5.0	4.4
	E_φ	1.6	1.6	1.6	1.8	2.0	2.1	2.0	4.6	5.2
-3	H_r	1.3	1.3	1.3	1.2	1.7	2.2	1.9	4.2	6.0
	H_z	1.9	1.9	1.5	0.8	1.7	2.1	3.0	8.6	7.3
	E_φ	1.3	1.3	1.0	0.7	1.8	2.0	2.3	4.9	8.3

The validation is performed on two different planes; the yz-plane, the plane in which the HMD is positioned, and the xz-plane, orthogonal to the HMD. The average relative difference between the analytical model and CST Studio Suite® in the yz-plane is given in Table 5.9, the difference in the xz-plane is given in Table 5.10. In each of these planes, three field components are given, as the other three are zero.

Table 5.8: Simulation volumes in CST Studio Suite® for the 3-layer HMD model.

	x, y [mm]	z [mm]
0.1—100 MHz	700	$[-400, 130]$
0.4—5 GHz	320	$[-190, 130]$

For almost all frequencies, in almost all layers, the average relative differences are below 9.0%, which is considered acceptable. In fact, most of them are even below 4.0%. There are three exceptions where the average relative difference is above 10%.

The first exception is the E_z field in the xz-plane, orthogonal to the dipole orientation, in layers -1 and -2, for frequencies up to 13 MHz. However, since the E_x field is much stronger (i.e. at least three orders of magnitude) than the E_z fields in these cases, E_z can be ignored for frequencies up to 13 MHz without introducing a significant error, resulting in a relative difference below 11.5%, and most of them are even below 5.5%.

The second exception is H_z in layer -2 at 2.45 GHz, and all field components in layer -2 at 5 GHz. Contrary to what can be seen in Figures 5.10 and 5.12, where the generated fields

Table 5.9: Relative differences [%] between the fields generated by our model and those of CST. 3-layer HMD, yz-plane. Correction near the source and correction for low field values applied.

Layer		100 kHz	1 MHz	6 MHz	13 MHz	100 MHz	400 MHz	1 GHz	2.45 GHz	5 GHz
	E_x	1.6	1.6	1.9	2.0	2.3	3.5	1.1	2.6	4.5
0	H_y	2.6	2.3	2.6	2.6	3.0	2.8	2.0	2.5	4.7
	H_z	2.7	2.5	2.7	2.7	2.7	2.5	2.8	2.4	4.9
	E_x	4.1	4.4	3.2	3.3	4.1	3.3	2.1	2.7	2.7
-1	H_y	5.0	3.3	5.0	4.9	7.7	4.2	2.2	2.8	4.2
	H_z	5.2	2.7	5.4	5.2	5.8	3.2	3.0	3.4	2.8
	E_x	15.9	17.2	8.9	8.2	3.4	1.5	2.5	7.2	13.2
-2	H_y	4.5	1.2	5.3	4.5	3.9	2.4	2.5	6.5	15.2
	H_z	2.5	0.8	3.0	2.4	2.4	1.8	2.3	19.3	98.8

Table 5.10: Relative differences [%] between the fields generated by our model and those of CST. 3-layer HMD xz-plane. Correction near the source and correction for low field values applied.

Layer		100 kHz	1 MHz	6 MHz	13 MHz	100 MHz	400 MHz	1 GHz	2.45 GHz	5 GHz
	E_x	3.1	3.1	3.6	5.5	4.3	5.3	2.8	4.0	5.5
0	H_y	2.1	1.9	2.0	2.1	2.2	1.3	2.2	2.2	3.4
	E_z	2.0	1.8	1.8	1.8	1.8	2.3	1.9	1.8	3.1
	E_x	3.6	2.9	3.2	2.8	2.3	0.9	1.9	1.6	1.4
-1	H_y	2.7	2.5	2.7	2.8	2.4	1.3	2.1	1.6	2.8
	E_z	NaN	92.8	139.1	11.2	4.9	3.9	3.3	3.4	5.9
	E_x	11.1	11.5	6.2	5.5	2.3	0.5	2.2	4.8	7.6
-2	H_y	3.3	0.9	4.2	3.4	2.7	0.6	2.4	4.9	10.4
	E_z	NaN	91.0	52.4	33.4	8.1	3.4	4.5	6.0	20.4

and the relative differences behave rather smoothly, the relative difference now shows less smooth behavior, similar to what can be observed in Figure 5.11(b). The fields computed by CST Studio Suite® contain fluctuations that cause artifacts in the relative differences. This phenomenon suggests that the accuracy of CST Studio Suite® is insufficient. However, as the memory usage of the simulation approaches the maximum installed memory on the simulation server, an increase of accuracy is not possible. In other words: the relatively large difference is believed to be caused by limitations in the available hardware, not in the analytical model.

The last exception are the E_x fields in the bottom layer, at 100 kHz and 1 MHz. The average relative differences are slightly over 10%, reaching up to 17.2%. This increased difference occurs mainly where the field values are very low, but not yet low enough to be filtered out by the 'correction for low field values', as described in Section 5.4.6. Similarly to the effect described in the previous paragraph, also here these results suggests that the accuracy of CST Studio Suite® is insufficient.

In summary, the analytical model for the 3-layer HMD runs in about 430 (6 MHz) to 600 (5 GHz) seconds[¶] for frequencies ranging from 100 kHz to 5 GHz, using the parameters listed in Tables 5.2 and 5.8, using at most 8 GB memory. This means that the model is about 1.5 to 70 times faster than CST Studio Suite®, and uses 1.8 to 40 times less memory.

5.5.3 More layers

Results for more layers could not be generated with sufficient accuracy by CST Studio Suite®. At this moment, our available simulation computers are limited to 768 GB RAM. This is sufficient for the cases shown, but for an increased number of layers, this turned out to be insufficient to achieve acceptable results for most field components in the majority of cases.

However, some results have been generated successfully, such as H_y for the 4-layer HMD at 5 GHz, as can be seen in Figure 5.11, and H_z for the 5-layer VMD at 100 kHz, as can be seen in Figure 5.12. In the former, even details like a (weak) standing wave pattern can be observed in layers -1 and -2. Again, the top figures show the fields calculated by the analytical model, the middle figures show the relative difference with CST Studio Suite®, and the bottom figures show this difference after applying the corrections detailed in Sections 5.4.5 and 5.4.6.

The analytical model requires much less computing power, and has been successfully used to generate fields for the 5, 6, and 7-layer VMD, and the 4 and 5-layer HMD. As the number of layers increases, the execution time increases as well.

5.6 Discussion

The presented analytical model executes much faster than commercial EM field solvers. It is possible to make the model even faster, without compromising the accuracy of the results.

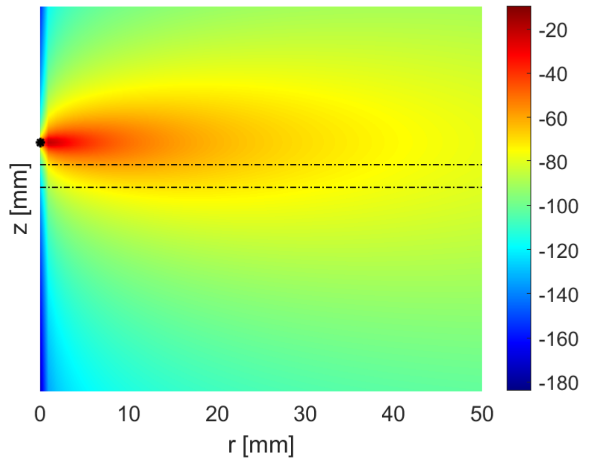

(a) $|E_\varphi|$ [dBV/m], analytical model.

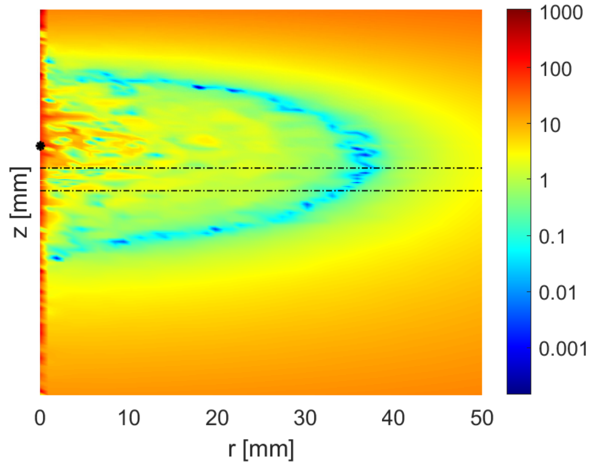

(b) Relative difference [%].

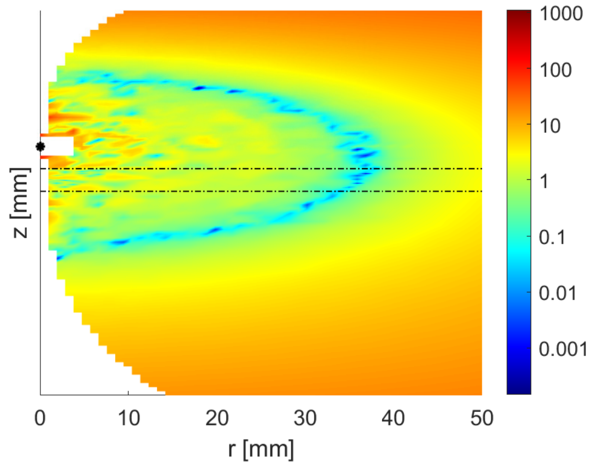

(c) Relative difference with source and low field correction [%].

Figure 5.10: E_φ generated by the mathematical model (3 layer VMD) for $f = 13$ MHz and the differences with CST Studio Suite®. Differences in %.

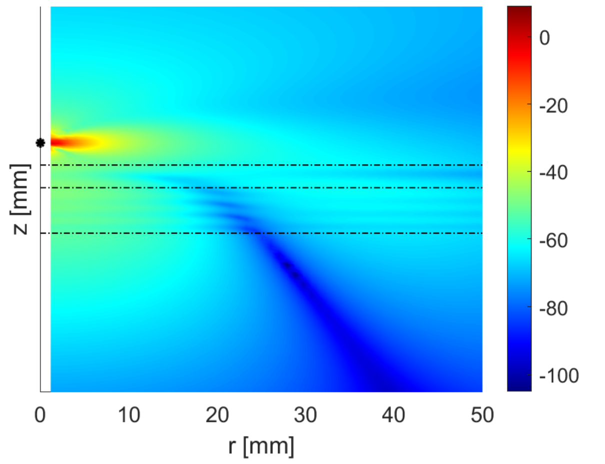

(a) $|H_y|$ [dBA/m], analytical model.

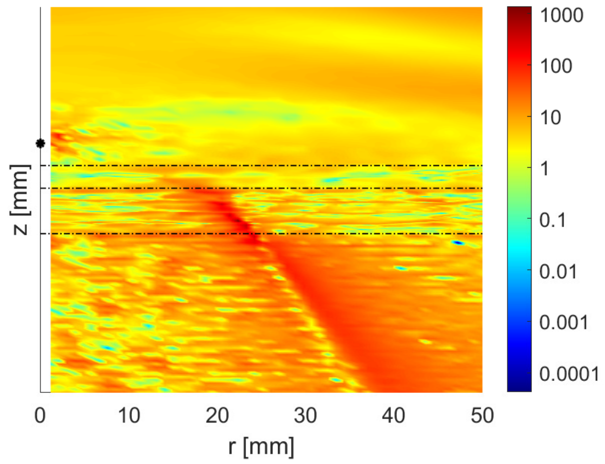

(b) Relative difference [%].

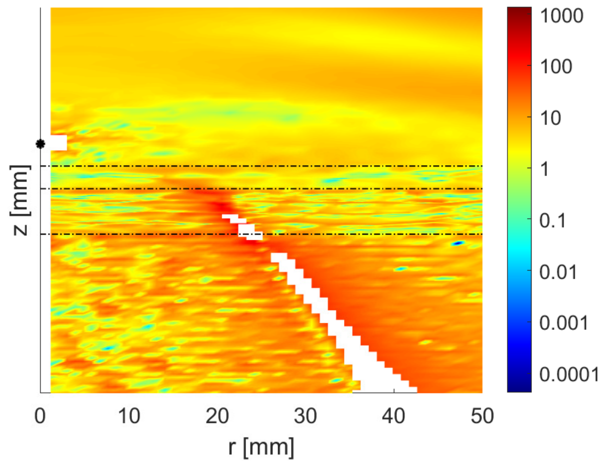

(c) Relative difference with source and low field correction [%].

Figure 5.11: H_y generated by the mathematical model (4 layer HMD) for $f = 5$ GHz and the differences with CST Studio Suite®. Differences in %.

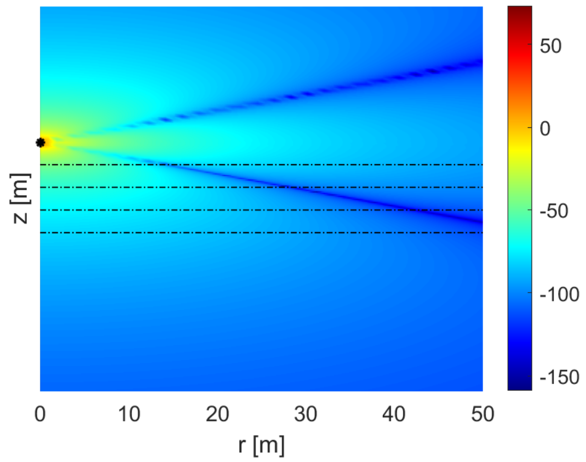

(a) $|H_z|$ [dBA/m], analytical model.

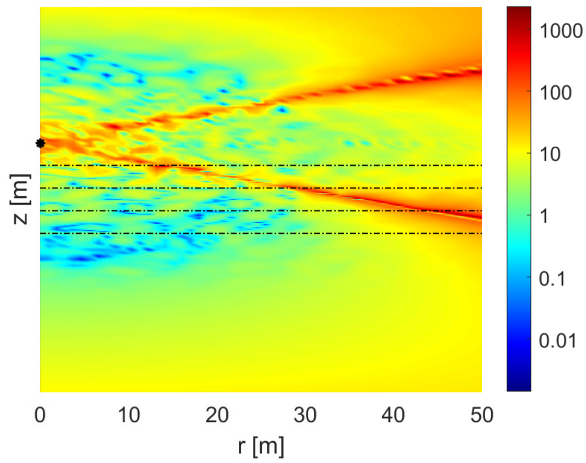

(b) Relative difference [%].

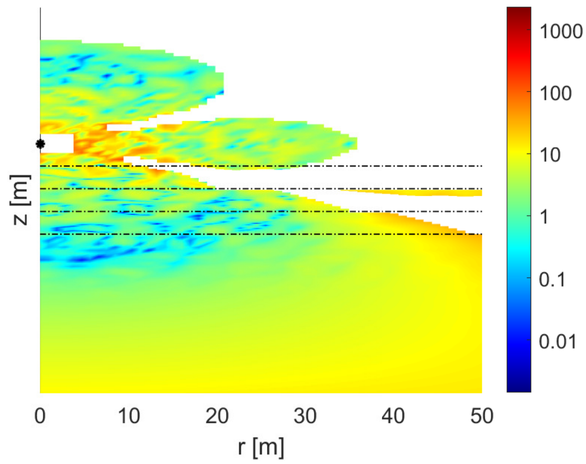

(c) Relative difference with source and low field correction [%].

Figure 5.12: H_z generated by the mathematical model (5 layer VMD) for $f = 100$ kHz and the differences with CST Studio Suite®. Differences in %.

When only the fields inside the tissue are of interest, and not the fields in air, one can choose to not calculate the fields in layer 0. Additionally, the calculation domain can be limited to the region of interest. This is in sharp contrast with commercial EM field solvers, where the complete domain has to be calculated.

If a reduction of the accuracy is acceptable, additional speedup can be achieved by using a coarser spatial resolution in r, x, y, and/or z. This is again in sharp contrast with commercial EM field solvers, where a minimum spatial resolution is required to ensure convergence of the algorithms. One could also choose to first run the model with a coarse spatial resolution, which will allow the user to identify the region(s) of interest, and then run the model a second time with an improved resolution, only for the region(s) of interest.

In this way, an additional speedup of over 10 times can easily be achieved, with a similar reduction in required memory. As the number of layers increases, the execution time increases as well. Biomedical WPT environments can often be approximated by 3 (for instance, air, skin, muscle) to 7 (for instance, air, fat, scalp, skull, CSF, grey matter, white matter) layers, and these cases will indeed benefit from this model.

Throughout this chapter, the EM fields generated by Simulia CST Studio Suite® have been used as a reference. It should be investigated how reliable those fields are, for example by extending the validation procedure to the use of additional commercial EM solvers.

5.7 Conclusion

We have presented an analytical model that can be used to calculate the electromagnetic fields generated by a magnetic point dipole located in a layered environment. The numerical implementation of the model is discussed in detail, and the resulting fields are compared to those generated by Simulia CST Studio Suite®. The model was validated for 9 frequencies ranging from 100 kHz to 5 GHz, with $|r|$, $|x|$, $|y| \leq 50$ mm, and $-100 \leq z \leq 70$ mm, all in 1 mm steps.

The average relative difference between this model and the commercial EM field solver is below 9.0% (worst case) for almost all cases discussed, and is typically even below 4.0%. We consider this accurate enough to regard the model as a useful design tool for simulations of wireless power transfer systems in multilayered (biomedical) environments. There are a few exceptions where the relative difference is larger than 10%, but these cases can almost all be explained by imperfections in the commercial software.

The analytical model used for validation runs in tens to hundreds of seconds, which is up to 430 times faster than the commercial EM field solver, and uses considerably less memory, up to 70 times. The model can easily run on a standard office PC, whereas this is certainly not the case for commercial solvers for the setups tested here. The speedup of our model scales approximately linearly with the number of processors.

Additional speedup can be achieved by using a coarser spatial resolution in r, x, y, and/or z. Furthermore, one can choose to not calculate the fields in layer 0, when only the fields inside the other layers are of interest. In this way, an additional speedup of over 10 times can easily be achieved, with a similar reduction in required memory.

A major advantage of our model is that it can be implemented in almost any standard programming language. Designers of WPT systems can use this model to speed up their design process. This model is also applicable in other areas of engineering, such as geophysical engineering, as long as the environment is (approximately) planarly layered. Appropriate boundary values for the numerical integration can be found using the described procedure.

Chapter six

Optimal frequency for maximum received power in biomedical wireless power transfer applications*

6.1 Introduction

WPT in biomedical applications often occurs at frequencies of tens of kHz to 13.56 MHz [4, 109]. It is commonly argued that operation in this frequency range yields optimal performance in terms of power transfer efficiency (PTE), as losses in biological tissue increase with frequency [67, 68]. Furthermore, when the frequency increases, whilst the distance between the coils is kept constant, the coupling between the coils will deteriorate, resulting in a decrease in efficiency.

With the recent developments in miniaturization of IMDs [39], mm-sized implants are becoming feasible. In situations where the distance between the coils is comparable to their diameter, PTEs of over 50% can be achieved [4, 109], as was also demonstrated in Chapter 3. However, in the biomedical WPT applications under consideration, the Rx coil is mm-sized, and may be located several cm inside the human body. When the transfer distance is several times the coil diameter, efficient power transfer is still possible in general [127], but the design of the coils is subject to many constraints. These relate to the required combination of coil size, wire diameter, and number of turns, which are not free to choose for mm-sized implants. Therefore, the PTE is not expected to be high.

Several researchers have used theoretical models to find solutions for WPT to a mm-sized IMD located several cm deep inside the human body [86, 87, 157, 174, 175]. Those researchers have attempted to maximize the PTE by finding the frequency at which the PTE is highest, and by optimizing the current distribution in the transmitter for that frequency. They

*This chapter is based on [P1].

have found that the PTE is maximized at (sub-)GHz frequencies. Nonetheless, the efficiency is very small, i.e. below 1%. One could argue whether optimizing such a low efficiency is the best approach, or that it would be better to maximize the absolute received power, while staying below the SAR limits [213, 245].

It was demonstrated that, when optimizing for MPL instead of MPTE, there is little benefit of using MF-WPT at (sub-)GHz frequencies versus traditional inductive coupling at low-MHz frequencies [64]. However, the model used in [64] considers the human body to be a half-space consisting of one single (equivalent) tissue, which is an oversimplified representation of realistic cases. The environment under consideration can be more accurately represented by layered media, which will introduce additional reflections and refractions of the EM fields inside the tissue. Additionally, as we have seen in Chapter 5, (weak) guided waves can appear inside the tissue layers. These effects can not be modeled using the model from [64].

By applying a more accurate model to the analysis, we can determine whether the conclusions drawn in [64] are also valid in the multi-layer environment, or that effects introduced by the additional layers cause the optimal frequency to shift to either (sub-)GHz or low-MHz frequencies.

In this chapter, the analytical model from Chapter 5 is used to determine the optimal frequency for WPT to an IMD, when optimizing for MPL, rather than for MPTE, within the applicable SAR limits. Additionally, the corresponding PTE will be calculated. The source will be a VMD, as it was shown in Chapter 5 that this generates the strongest magnetic fields inside the tissue, and thus the largest possible received power.

6.2 Maximum power transfer efficiency versus maximum received power

The circuit presented in Chapter 3 is designed to achieve MPTE, whereas in this chapter it is argued that designing for MPL makes more sense. This might sound counter-intuitive. Please note that the designs presented in both chapters are intended for different applications.

In Chapter 3, the Tx-Rx distance is smaller than the coil diameter. This corresponds to a coupling factor that is considerable, which leads to a maximum achievable link efficiency (considering only the coils, not the electronics) of over 86%, as shown in Chapter 3. Although not shown, an alternative MPL system was also designed for the same application. This system is able to transfer more power than the MPTE design indeed, at the cost of a significant decrease in link efficiency (roughly half). Furthermore, the MPTE design outperforms its MPL counterpart in terms of misalignment tolerance [224]. Both the MPL and MPTE solutions are able to transfer the required power to the implant. As the final product will be wearable, the MPTE design is preferable, because it has a better battery life and misalignment tolerance.

On the other hand, this chapter regards the case where the Tx-Rx distance is (much) larger than the Rx coil diameter, corresponding to a coupling factor that is negligible. This leads to a very low achievable link efficiency, below 1%. The transmit power is limited by the generated SAR. Consequently, the amount of received power will be very low. Optimizing for efficiency will implicitly lower the received power even further, which is undesired, as it can be very challenging to get the required amount of power to the load. It therefore makes sense to optimize for MPL.

6.3 Implementation

We will use the analytical model from Chapter 5 to determine the SAR generated by a VMD of known strength, i.e. with a known magnetic moment M. The maximum allowable SAR level is 2 W/kg for head and torso [213, 245]. This limit is used as constraint to maximize the magnetic moment of the VMD. Consequently, using this new magnetic moment value, the analytical model is used to calculate the magnetic field strength at various depths inside the tissue. These results are then used to determine the maximum possible received power, whilst still complying with the SAR regulations, for a range of frequencies, at various depths inside the tissue. This will allow us to determine the frequency at which the received power is at its maximum. Additionally, the efficiency of the resulting WPT system is presented.

6.3.1 SAR calculation

The SAR can be calculated using

$$\mathrm{SAR} = \frac{\sigma|\vec{E}|^2}{2\rho}, \tag{6.1}$$

where σ is the electrical conductivity of the tissue in [S/m], and ρ is the mass density in [kg/m^3]. The factor 2 comes from the conversion of the amplitude of the electric field strength to a RMS value. In relevant biomedical standards [213, 245], the SAR is averaged over a certain volume. These standards define the averaging volume as a $21.5 \times 21.5 \times 21.5$ mm^3 cubic volume† [92], which approximately corresponds to a mass of 10 g.

The environment under consideration consists of multiple layers in the z direction, as depicted in the model in Figure 5.3. Each layer has its own values for of σ and ρ. In other words, σ and ρ depend on z. The analytical model is able to calculate the field at discrete coordinates. To calculate the SAR using the analytical model from Chapter 5, we can thus average

$$\mathrm{SAR} = \sum_x \sum_y \sum_z \frac{\sigma(z)|\vec{E}(x,y,z)|^2}{2\rho(z)} \tag{6.2}$$

†The procedure described in this chapter can be applied to a volume of any size.

over the specified volume. The discretization of this equation is discussed next.

As discussed earlier, the maximum value of the SAR is required. Therefore, we need to find the volume $V_{\max}$ that contains the highest SAR value SAR_{max}. This volume is expected to be in the top of the layer stack (i.e. the first layer(s) of tissue), where the electric field is the strongest, as this is closest to the source. We can therefore limit ourselves to $z \in [0, -21.5]$ mm. As the fields generated by a VMD are symmetrical around the z-axis, we can choose any radial direction to find $V_{\max}$ on. We choose $y \in [-10.75, 10.75]$ mm, and sweep along the x-axis to find the location of $V_{\max}$. Because of the same symmetry, we can even choose $y \in [0, 10.75]$ mm, and evaluate the result twice.

The $21.5 \times 10.75 \times 21.5$ mm^3 volume is divided into $K \times N \times P$ cuboids[‡]. The electric field is evaluated at the geometrical center of each cuboid (x_i, y_j, z_k). Each cuboid should be sufficiently small to capture the field with enough detail, and the cuboid should be chosen such that the medium inside each cuboid is approximately homogeneous. Figure 6.1 shows a simplified representation of the grid on which the electric field is to be calculated.

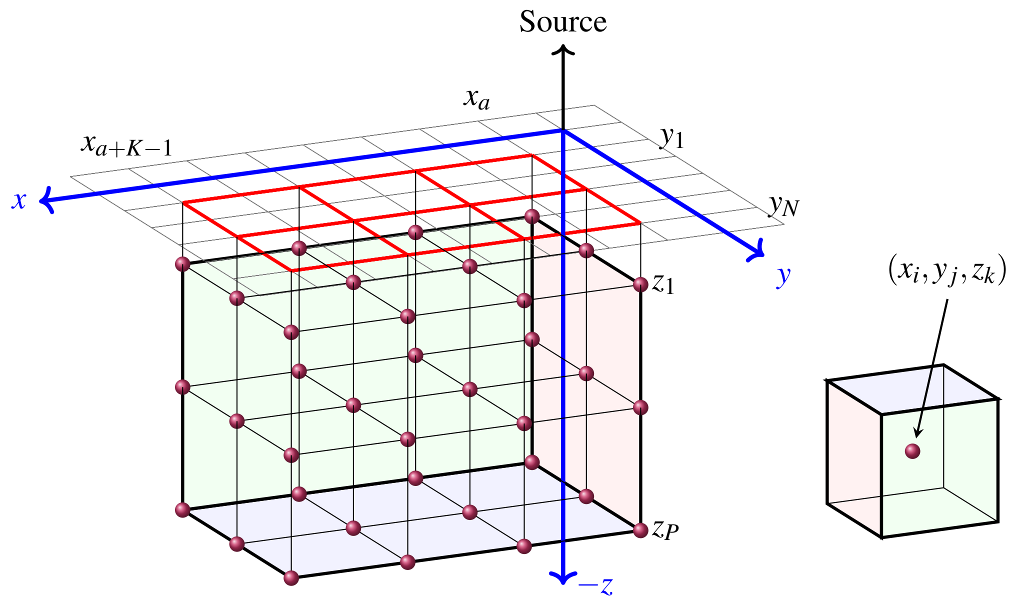

Figure 6.1: 3D grid points on which the electric field is calculated to evaluate the SAR (left) and cuboidal volume around (x_i, y_j, z_k) in which the electric field is considered homogeneous (right).

By moving the entire $21.5 \times 10.75 \times 21.5$ mm^3 volume along the x-axis, the SAR at each discrete location can be evaluated using

$$\mathrm{SAR} = \frac{1}{K}\frac{1}{N}\frac{1}{P}\sum_{k=1}^{P}\sum_{j=1}^{N}\sum_{i=a}^{(a+K-1)} \frac{\sigma(z_k)|\vec{E}(x_i, y_j, z_k)|^2}{2\rho(z_k)}, \tag{6.3}$$

[‡]This is convenient to implement, but the procedure can be applied to any type of grid.

where the value for a (i.e. the x-position) that maximizes the SAR is to be determined. The result will be denoted $\mathrm{SAR}_{max,calculated}$. The calculation of this maximum SAR value is in line with IEC/IEEE Std. 62704.1 [92].

6.3.2 Magnetic moment calculation

We know that the strength of the electric field scales linearly with the magnetic moment M of the MPD. As the SAR scales with the square of the electric field, it scales with M^2. Therefore, the value M_{max} that results in the maximum allowable SAR level is

$$M_{max} = \sqrt{\frac{\mathrm{SAR}_{limit}}{\mathrm{SAR}_{max,calculated}}} M_{old}, \tag{6.4}$$

where M_{old} is the (known) magnetic moment used to calculate $\mathrm{SAR}_{max,calculated}$ in Eq. (6.3), and SAR_{limit} is the desired limit value from [213, 245].

6.3.3 Received power calculation

The new value for the magnetic moment M_{max} can now be used in the analytical model. As the aim of this chapter is to find the maximum received power, the region with the strongest magnetic fields is of interest. From Chapter 5, we know the strongest magnetic fields generated by a VMD can be found along the z-axis, i.e. $x = y = 0$. We use the analytical model to calculate $|\vec{H}(0,0,z_r)|$ at the required receiver depth z_r.

As the aim of this work is WPT to small IMDs, the receiver will be modeled as an MPD. The induced voltage and power in an MPD, as a function of the magnetic field strength, are given by [64]:

$$|V_{emf}| = |\mu \omega A_{rx} \vec{H} \cdot \vec{n}|, \tag{6.5}$$

$$P_{rx} = \left| \frac{V_{emf}^2}{2Z_{load}} \right|, \tag{6.6}$$

where $\vec{n}$ is the normal of the receiver coil. As the field is strongest along the z-axis, we can substitute $\vec{H} \cdot \vec{n} = H_z$, resulting in the received power at receiver depth z_r as

$$P_{rx}(0,0,z_r) = \left| \frac{\mu^2 \omega^2 A_{rx}^2 H_z^2(0,0,z_r)}{2Z_{load}} \right|. \tag{6.7}$$

Note that the received power increases with ω^2, which might outweigh the fact that σ increases with ω [68]. This suggests that, indeed, an optimal frequency can exist.

6.3.4 Power transfer efficiency

The frequency at which MPL occurs, is not per definition the frequency at which the PTE is maximized. To determine the PTE, the authors in [64] make a number of assumptions. As stated before, the tissue volume is assumed to consist of one (equivalent) tissue half-space, without any additional layers. A hemisphere is defined, centered at the origin $\mathbb{O}$, which is at the air-tissue boundary, as shown in Figure 6.2. The radius is equal to the skin depth. Inside this hemisphere, the electric field strength is assumed to be constant and equal to the field strength at $\mathbb{O}$. The power dissipated in the hemisphere can now be calculated analytically. This power is assumed to be a good approximation of the total dissipated power in the complete tissue volume.

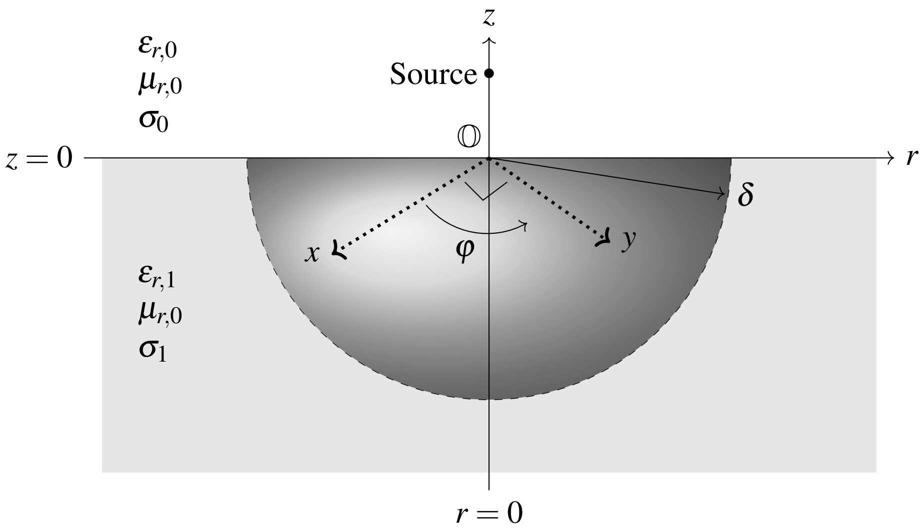

Figure 6.2: Representation of the hemispherical volume used to calculate the SAR in [64].

The PTE is now defined as the ratio between the received power and the dissipated power:

$$\eta = \frac{P_{rx}}{P_{diss,tot}}. \tag{6.8}$$

In [175], which does include additional layers, the total dissipated power is determined by integrating the analytically determined expression of the dissipated power over the complete tissue volume. Care must be taken that the tissue volume is sufficiently large, or else truncation errors will occur. The PTE is then determined similar as before, by calculating the ratio between the received power and the dissipated power.

The approach in this chapter is based on the one in [175]. As we calculate the electric field only at discrete coordinates, and thus also the dissipated power, a summation has to be used. As the fields generated by a VMD exhibit rotational symmetry, we can limit ourselves to the calculation of the electric field in the xz-plane, and revolve the plane around the z-axis, taking into account the volume of the body of revolution at each grid point, to cover the complete volume.

Figure 6.3 shows the procedure graphically. The field at coordinate (x_i, z_k) is assumed to be approximately constant over a small square area $\Delta x \times \Delta z$, denoted by the hatched area in the figure. This area is revolved around the z-axis to obtain a ring-shaped volume in which the field is approximately constant, denoted by the grey volume in the figure. By sweeping over all i and k, the complete volume can be spanned. In theory, i and k should run until infinity, but in practice, for i and k large enough, the field strength will be low enough such that it can be ignored without introducing a significant error, resulting in finite upper bounds for i and k.

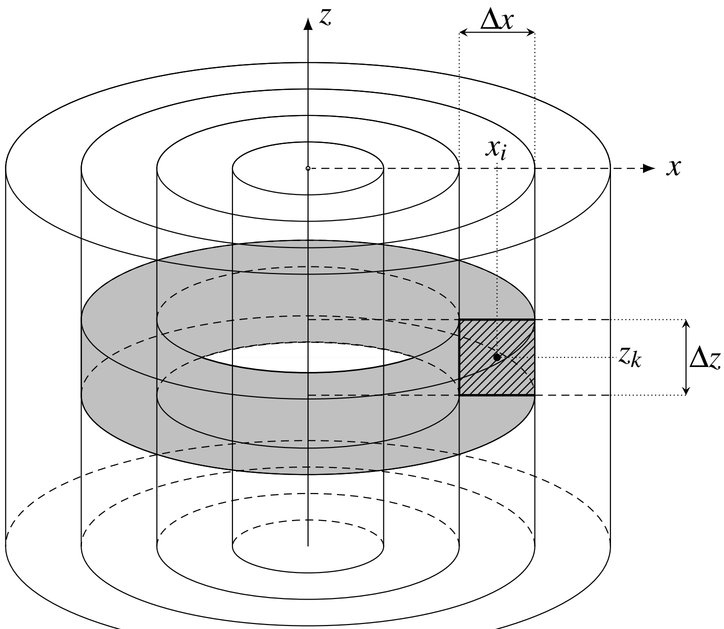

Figure 6.3: Cross section (hatched) and volume (grey) of the volume in which the field strength is approximately equal to the field at (x_i, z_k), assuming Δx and Δz are chosen sufficiently small. The VMD is located on the positive z-axis.

The the total power dissipated in the tissue can now be approximated using

$$P_{diss,tot} \approx \sum_{i=1}^{I} \sum_{k=1}^{K} \Delta V_i \frac{\sigma(z_k)|\vec{E}(x_i, 0, z_k)|^2}{2}, \tag{6.9}$$

where ΔV_i is the volume in which the field strength is assumed to be approximately constant, denoted by the grey ring-shaped volume in Figure 6.3, given by

$$\Delta V_i = \pi \left(\left(x_i + \frac{\Delta x}{2} \right)^2 - \left(x_i - \frac{\Delta x}{2} \right)^2 \right) \Delta z, \tag{6.10}$$

$x_i = (i - \frac{1}{2})\Delta x$ and $z_k = (k - \frac{1}{2})\Delta z$ are the coordinates at which the electric field is evaluated,

$\Delta x = |x_2 - x_1|$ is the step size in the x-direction, and $\Delta z = |z_2 - z_1|$ is the step size in the z-direction, assuming uniform sampling. I and K should be chosen such that the electric field strength at $x > x_I$ or $z < z_K$ is negligible compared to the field strength at the origin.

The PTE η can now be approximated using Eq. (6.8).

6.4 Validation

The analytical model was already validated in Chapter 5, but that validation did not include the calculation of the SAR. Therefore, the calculation of the SAR, using the analytical model, is verified by comparing the results to the maximum SAR calculated by Simulia CST Studio Suite® [35], as will be outlined next.

The calculation of the SAR, as described in Section 6.3, was added to the analytical model as a post processing step. In the analytical model, the $21.5 \times 10.75 \times 21.5$ mm^3 volume was divided into $28 \times 14 \times 28 = 10976$ cubes, each of which measure $0.75 \times 0.75 \times 0.75$ mm^3. This was found to be sufficient to capture the details in the electric field with acceptable accuracy, as a further decrease in the cell size did not result in a significant change in the calculated SAR value.

The validation was performed for a 4 layer case. The case consists of an air–skin–fat–muscle layer stack, where the skin layer was chosen to be 3 mm thick, the fat measures 6 mm. These values are in the range that can be encountered in the human body [160].

The validation was performed for frequencies ranging from 100 kHz to 2.45 GHz. The material properties of the tissues used [68, 82] are listed in Table 6.1.

Full-wave EM simulations were performed in Simulia CST Studio Suite® [35], for a model similar to the one used in the verification procedure described in Chapter 5, with the parameters from Table 6.1. The magnetic moment M was chosen such that the current through the VMD is 1 A. It should be noted that the validation, i.e. the results generated with CST, as well as the calculation of the maximum SAR value, is independent of the initial value of M, as this value is corrected for through Eq. (6.4).

The maximum SAR values calculated by the analytical model are compared to those calculated by CST, according to IEC/IEEE Std. 62704.1 [92]. The SAR values, as well as the difference between the two, are given in Table 6.2. It can be seen that the difference is below 25%.

We will see later that this difference is small enough to not affect the determination of the frequency that is optimal for receiving the maximum power.

6.5 Results

The model is now used to calculate the received power and corresponding PTE for a total of 31 discrete frequencies ranging from 100 kHz to 10 GHz, for multiple receiver depths

Table 6.1: Mass densities and dielectric properties of the layered model used to validate the SAR calculation [68, 82]. The source is located in air at $d = 10$ mm above the air–skin boundary.

		Air	Skin	Fat	Muscle
Density	ρ [kg/m^3]	1.2	1109	911	1090
Thickness	h_i [mm]	∞	3	6	∞
100 kHz	ε_r' [–]	1	1119	101	8089
	σ [S/m]	10^{-7}	$4.5 \cdot 10^{-4}$	0.043	0.36
1 MHz	ε_r' [–]	1	991	50.8	1836
	σ [S/m]	10^{-7}	0.013	0.044	0.50
6 MHz	ε_r' [–]	1	518	36.6	260
	σ [S/m]	10^{-7}	0.13	0.049	0.60
13 MHz	ε_r' [–]	1	316	26.9	153
	σ [S/m]	10^{-7}	0.22	0.054	0.62
100 MHz	ε_r' [–]	1	72.9	12.7	66.0
	σ [S/m]	10^{-7}	0.49	0.068	0.71
400 MHz	ε_r' [–]	1	46.8	11.6	57.1
	σ [S/m]	10^{-7}	0.69	0.081	0.80
1 GHz	ε_r' [–]	1	40.9	11.3	54.8
	σ [S/m]	10^{-7}	0.90	0.12	0.98
2.45 GHz	ε_r' [–]	1	38.1	10.8	52.7
	σ [S/m]	10^{-7}	1.48	0.27	1.76

Table 6.2: Maximum SAR calculated by the 4 layer analytical model, as well as by Simulia CST Studio Suite® [35], by a VMD located $d = 10$ mm above the layer stack. The material parameters are listed in Table 6.1.

Frequency [MHz]	SAR analytical [W/kg]	SAR CST [W/kg]	Difference [%]
0.1	$2.484 \cdot 10^{-16}$	$1.991 \cdot 10^{-16}$	24.8
1	$3.411 \cdot 10^{-14}$	$2.750 \cdot 10^{-14}$	24.0
6	$2.205 \cdot 10^{-12}$	$2.056 \cdot 10^{-12}$	7.3
13	$1.440 \cdot 10^{-11}$	$1.410 \cdot 10^{-11}$	2.1
100	$1.556 \cdot 10^{-9}$	$1.615 \cdot 10^{-9}$	3.7
400	$3.718 \cdot 10^{-8}$	$3.943 \cdot 10^{-8}$	5.7
1000	$3.979 \cdot 10^{-7}$	$4.290 \cdot 10^{-7}$	7.3
2450	$7.022 \cdot 10^{-6}$	$8.573 \cdot 10^{-6}$	18.1

z_r ranging from -10 to -85 mm. For each depth, the frequency that achieves maximum received power can then be found.

Two cases are used for the analysis: the previously described 4 layer air–skin–fat–muscle case, and a 7 layer case consisting of the layers air–skin–fat–bone–CSF–grey matter–white matter, representing WPT to an IMD located inside the brain. Table 6.3 lists the parameters of the 7 layer model, the dielectric properties for the biological tissues at each frequency can be found partly in Table 6.1, those for the missing tissues can be found in [68, 82].

Table 6.3: Thicknesses and mass densities of the layers in the 7 layer model [82]. Thicknesses were derived from the HUGO human voxel model in Simulia CST Studio Suite® [35].

Layer	Air	Skin	Fat	Bone	CSF	Grey matter	White matter
Thickness h [mm]	∞	1.5	5.25	7.5	0.75	2.25	∞
Mass density ρ [kg/m^3]	1.2	1109	911	1908	1007	1045	1041

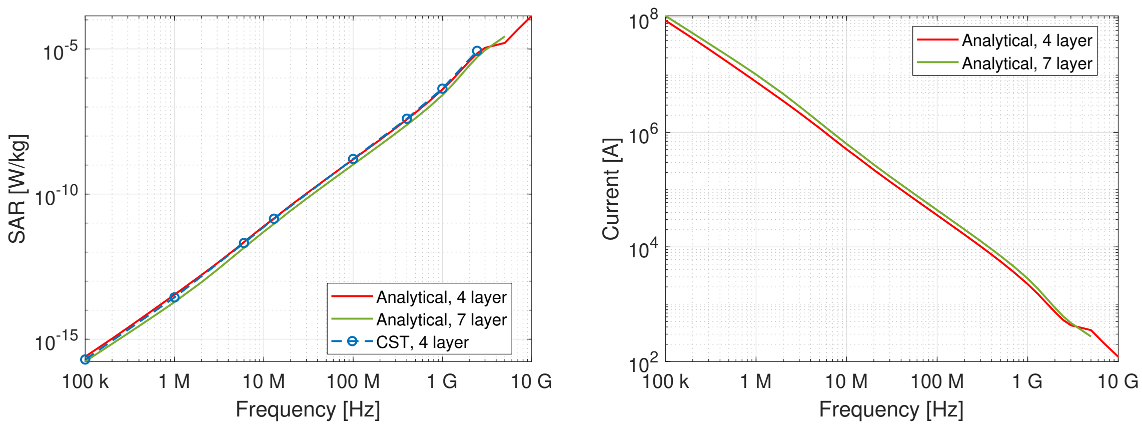

(a) SAR [W/kg]. **(b)** Current [A].

Figure 6.4: (a) SAR generated by a VMD current of 1 A, calculated using the analytical model and CST, and (b) the corresponding current that generates a SAR of 2 W/kg, calculated using Eq. (6.4). The analysis is performed from 100 kHz to 10 GHz.

Figure 6.4(a) shows the maximum SAR, calculated using Eq. (6.3). The model uses a magnetic moment M that corresponds to a VMD current of 1 A. As stated before, the exact value of M is irrelevant at this stage, as this value is corrected for in Eq. (6.4). It can be seen that the SAR generated by the 4 layer analytical model and those generated by CST follow the same trend, as was already seen in the validation in Section 6.4. Also, the data for the 4 and 7 layer setups follow the same trend for frequencies up to about 2.5 GHz; for higher frequencies, they start to differ. Furthermore, the SAR is strictly increasing with frequency, which is to be expected, as the losses increase with frequency.

Figure 6.4(b) shows the VMD current that will result in a SAR of 2 W/kg, calculated using Eq. (6.4). The current might seem unusually high at first glance, with values up to 10^8 A, but it should be noted that this is for a 215 μm diameter Tx coil, as was also used in Chapter 5. When we compare this, for example, to the 55 mm Tx coil in Chapter 3, we see that the area of this coil is about $5 \cdot 10^4$ larger, and it has 10 turns instead of 1. When the values from Figure 6.4(b) are corrected for this difference in size and number of turns, we see that the currents are actually in the same order of magnitude.

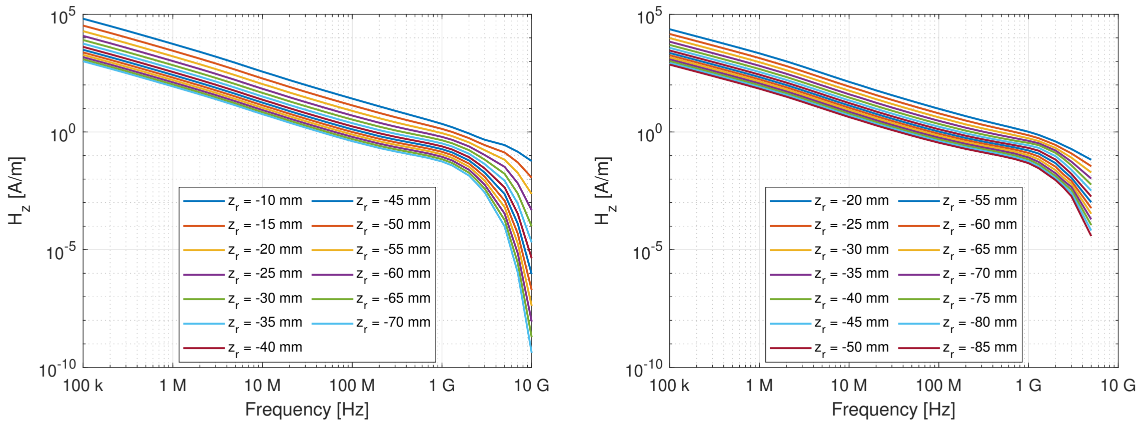

(a) 4-layer **(b)** 7-layer

Figure 6.5: Magnetic field strength H_z [A/m] for the magnetic moment M that results in a SAR of 2 W/kg, at receiver depths z_r ranging from -85 to -10 mm, for (a) the 4 layer model, and (b) the 7 layer model.

6.5.1 Magnetic field strength at max SAR

The VMD current that will result in a SAR of 2 W/kg, as shown in Figure 6.4(b), can now be used to calculate the magnetic field strength H_z at several depths inside the tissue layer stack. Figure 6.5 shows H_z, calculated using the magnetic moment M_{max} of the source that results in maximum SAR in the analytical model of Chapter 5. The 4 layer results are given for depths in the range $-70 \leq z_r \leq -10$ mm, the range for the 7 layer case is $-85 \leq z_r \leq -20$ mm.

The magnetic field strength decreases with frequency, which is to be expected, as the magnetic moment M_{max} of the source decreases with frequency. Around 1 GHz, a slight local peak can be distinguished, especially at deeper locations. This could imply the existence of a locally optimal frequency. Above 1 GHz, the magnetic field strength drops rapidly.

In Chapter 5, numerical problems were encountered when implementing Eq. (5.21) in MATLAB [145]. These problems were solved in Section 5.3.2, resulting in Eq. (5.45). As H_z is now evaluated only on the z-axis, at $x = y = 0$, Eq. (5.21) can actually be evaluated without numerical problems, hence Eq. (5.45) is no longer needed, and the original Eq. (5.21) can be used.

6.5.2 Maximum received power

The magnetic field strength H_z from Figure 6.5 can be used in Eq. (6.7) to calculate the received power P_{rx} at depth z_r, for an Rx coil with area A_{rx}, and load impedance Z_{load}. The results for both the 4 layer and 7 layer cases are shown in Figure 6.6, normalized for the maximum P_{rx}, which can be received closest to the source.

The presented results are generated using $A_{rx} = 1$ mm^2, and $Z_{load} = 1$ kΩ. The received power depends on the receiver size and load impedance, Eq. (6.7) can be used to scale the presented results accordingly. The maximum P_{rx} at $z_r = -10$ mm is 1.3 μW for the 4 layer case. For the 7 layer case, the maximum P_{rx} at $z_r = -20$ mm is 170 nW.

In both cases, at all implant depths shown, the maximum P_{rx} is found at 100 kHz, the lowest frequency investigated. Around 1 GHz, a local maximum can be distinguished, which corresponds to the local maximum in H_z observed previously. This will be elaborated upon in the discussion in Section 6.6. Above 1 GHz, depending on the depth z_r, the received power decreases rapidly, which corresponds to the decrease in H_z observed previously.

6.5.3 Practical guidelines for sizing the receiver coil

The Rx coil size used to generate the presented results has size $A_{rx} = 1$ mm^2. From Eq. (6.7), we know that the received power scales with the square of A_{rx}. Increasing the Rx coil size is thus a way of increasing the received power level, provided the physical increase in IMD size is permitted for the application.

The Rx coil size can not be increased indefinitely. How much increase is relevant, from an application point of view, depends on the magnetic field distribution. For various implant depths z_r, we have already determined the maximum field strength, as was shown in Figure 6.5. These were calculated on the z-axis, i.e. at $x = y = 0$. The further we move away from the z-axis, the more the magnetic field strength decreases.

The received power depends on the total magnetic flux passing through the Rx coil surface area. Eq. (6.7) can be applied to the available Rx coil area to calculate the maximum achievable received power. This approach can also be reversed, such that it can be used to find the required minimum Rx coil area for a given desired received power level.

As stated before, the magnetic field strength decreases with the distance from the z-axis. There might thus exist a maximum coil radius above which the magnetic field strength has decreased to such levels, that a further increase in coil radius has only limited effect on the received power, depending on the application. To get insight in this phenomenon, we determine the coil areas for which the received power has decreased with 10 and 20% of the maximum value, respectively.

We determine at which distance from the z-axis the received power P_{rx} has decreased to 90 and 80% of its maximum value. From Eq. (6.7), we know that this corresponds to finding the value of x for which H_z is $\sqrt{0.9} \approx 0.95$ and $\sqrt{0.8} \approx 0.89$ of the maximum value. When the Rx coil radius is limited to this distance, the received power fluctuates at most 10% and

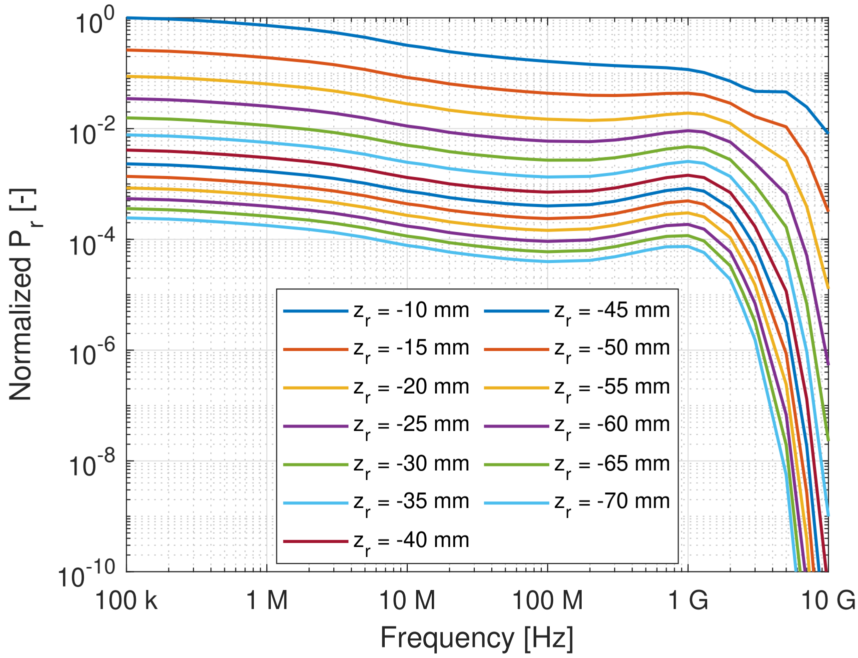

(a) 4 layer model.

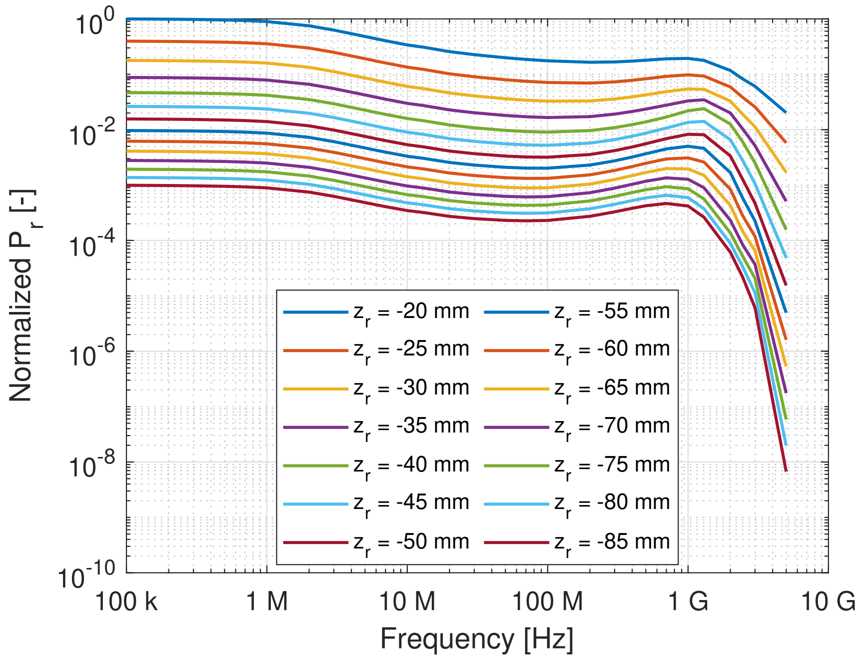

(b) 7 layer model.

Figure 6.6: Normalized received power at receiver, for (a) the 4 layer model at depths z_r ranging from -10 to -70 mm, and (b) the 7 layer model, for z_r ranging from -20 to -85 mm.

20% over the full Rx coil area. These results give insight in the maximum Rx coil size that can be used in practical applications.

Figure 6.7(a) shows the maximum Rx coil radius for which the received power is within 10% of the maximum value. Results are presented for the 4 layer model (solid) and 7 layer model (dash-dot), for Rx coil depths of $-50 \leq z_r \leq -10$ mm. It can be seen that, for frequencies up to 10 MHz, the difference between the 4 and 7 layer models is hardly distinguishable. At a depth of $z_r = -10$ mm, at 100 kHz, the maximum allowed coil radius is 2.6 mm, and it increases by approximately 1.3 mm for every additional 10 mm depth. At a depth of $z_r = -50$ mm, at 100 kHz, the allowed coil radius is 8.0 mm.

Figure 6.7(b) shows the maximum Rx coil radius for which the received power is within 20% of the maximum value. Results are presented for the 4 layer model (solid) and 7 layer model (dash-dot), for Rx coil depths of $-50 \leq z_r \leq -10$ mm. The curves follow the same trends as in Figure 6.7(a). At a depth of $z_r = -10$ mm, at 100 kHz, the maximum allowed coil radius is 5.6 mm, and it increases by approximately 1.7 mm for every additional 10 mm depth. At a depth of $z_r = -50$ mm, at 100 kHz, the allowed coil radius is 12.3 mm. The difference between Figures 6.7(a) and (b) is 3.0 mm for $z_r = -10$ mm, to 4.3 mm for $z_r = -50$ mm.

For the 7-layer model, as the frequency increases above about 10 MHz, the maximum Rx coil radius starts to increase, whereas this is hardly the case for the 4-layer model. This is likely caused by the increase in the number of layers, causing additional reflections between the layers. As we already observed in Chapter 5, this can cause (weak) guided wave propagation in the radial direction at higher frequencies.

At higher frequencies, starting from around 1 GHz, the maximum Rx coil radius decreases fast. As seen before, the received power also decreases fast at those frequencies, which is likely the cause of this behavior.

For practical applications with mm-sized receivers located several cm inside the human body, the presented results show that the fluctuation of the magnetic field over the complete Rx coil area A_{rx} is small, meaning that the received power over the area fluctuates with less than 10%. As the received power scales with the square of A_{rx}, an increase of the Rx coil radius by only a few mm, can result in an increase of several orders of magnitude in the received power presented in Section 6.5.2. Consequently, the PTE, presented next, will improve with the same factor.

6.5.4 Power transfer efficiency

The PTE is determined for several implant depths z_r, using Eq. (6.8). The magnitude of the magnetic moment M at each frequency is chosen such that maximum SAR is achieved, as explained before. Again, we take $A_{rx} = 1$ mm^2, and $Z_{load} = 1$ kΩ. Figure 6.8 shows the PTE for the 4 and 7 layer models, for depths up to 80 mm.

In the figure, it can be seen that the maximum PTE is found at 100 kHz for all implant depths, for both the 4 and the 7-layer models. For increasing depths, a peak around 1 GHz can

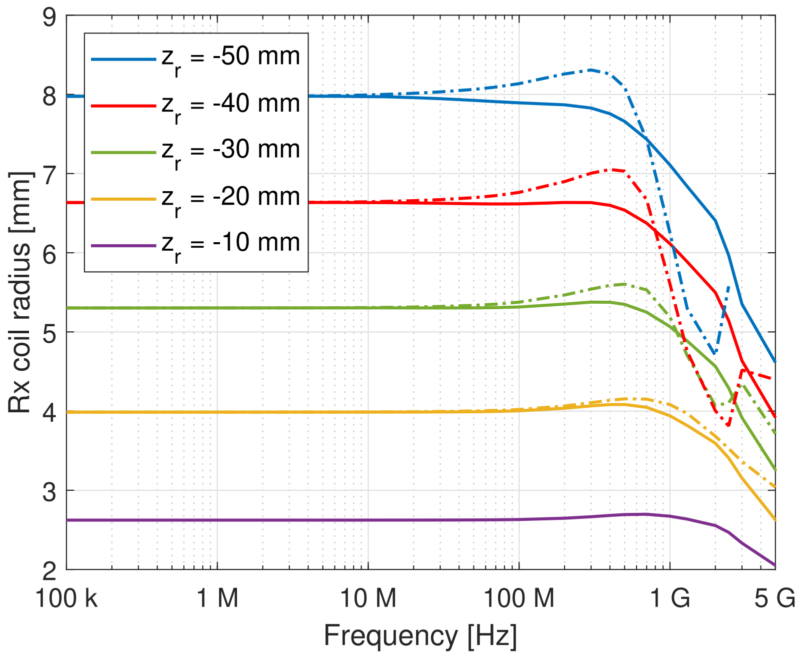

(a) Received power within 10% of the maximum power.

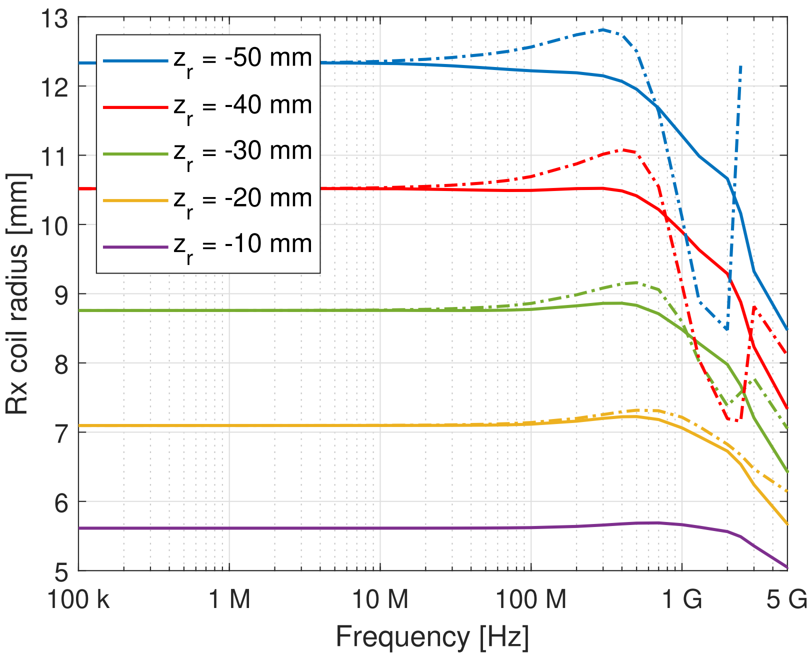

(b) Received power within 20% of the maximum power.

Figure 6.7: Maximum Rx coil radius for which the received power P_{rx} is within (a) 10%, and (b) 20% of the maximum received power, over the full coil area, at receiver depths z_r ranging from -10 to -50 mm for the 4 layer model (solid), and z_r ranging from -20 to -50 mm for the 7 layer model (dash-dot).

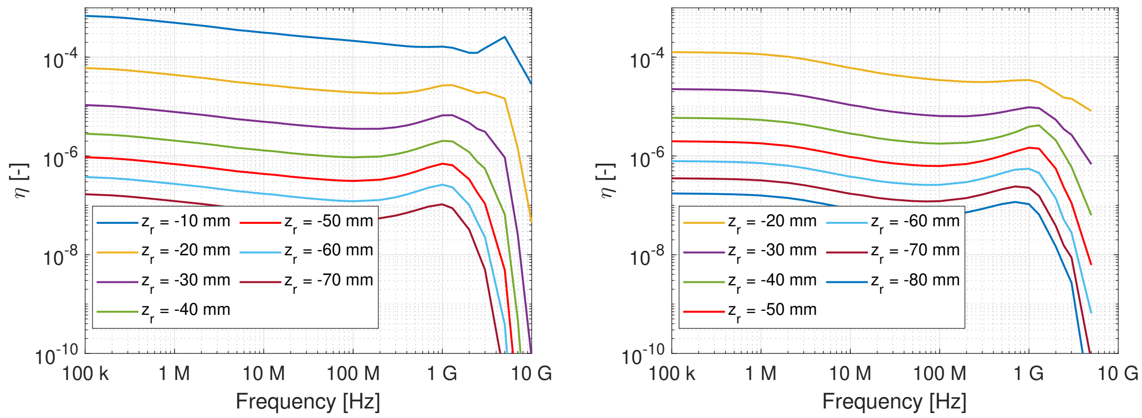

(a) 4 layer model. **(b)** 7 layer model.

Figure 6.8: Calculated PTE versus frequency for (a) the 4 layer model, for receiver depths z_r ranging from -10 to -70 mm, and (b) the 7 layer model, for z_r ranging from -20 to -80 mm.

clearly be distinguished, and the corresponding PTE approaches the maximum PTE, which occurs at 100 kHz. However, it never exceeds the PTE at 100 kHz. This will be discussed further in Section 6.6.

When the receiver area A_{rx} is increased, the received power increases with the square of A_{rx}, as presented in the previous section. Consequently, the PTE increases with the same factor.

6.5.5 Frequencies below 100 kHz

The presented results are generated for frequencies ranging from 100 kHz to 10 GHz. In Figure 6.6, we have seen that above approximately 1 GHz, depending on the receiver depth z_r, the received power levels decrease rapidly with increasing frequency. Therefore, we do not expect the received power levels at those frequencies to exceed the values around 100 kHz.

On the lower end of the used frequency spectrum, near 100 kHz, the presented results suggest that the received power levels reach a plateau. However, data at frequencies below 100 kHz are required to determine whether this is really the case. Therefore, the analysis was extended to 10 kHz.

The received power at 10 kHz is 2.0% higher than at 100 kHz. This is the case for all receiver depths z_r considered in this chapter. Hence, strictly speaking, WPT at 10 kHz outperforms operation at 100 kHz, in terms of MPL. However, the difference is small. In fact, for all frequencies ranging from 10 to 300 kHz, the difference is less than 4%, whereas the difference between operation at 10 kHz and the peak around 1 GHz is at least 41%, depending on the depth z_r. We can thus state that, even though operation at 10 kHz is optimal, operation at any frequency between 10 and 300 kHz achieves approximately similar (optimal) performance.

6.6 Discussion

In Figure 6.6, a peak in the received power can be clearly observed around 1 GHz, for both the 4 and 7 layer cases. This peak corresponds to the increased efficiency, as shown in Section 6.5.4 and discussed in [175]. However, this increase in efficiency is not sufficient to outweigh the increased tissue losses, combined with the decreased Tx current, at those frequencies, when the system is designed for MPL.

From Figure 6.6, the relative height of the peak around 1 GHz appears to increase as the implant depth z_r increases. This could mean that, after a certain depth, the received power at (sub-)GHz frequencies could be higher than the power around 100 kHz. The presented analysis was repeated for depths up to 150 mm, for both the 4 and the 7 layer case, but the received power is always highest around 100 kHz, by at least a factor of 2. Furthermore, the absolute received power at those depths is in the (sub-)nW range, which is too low for practical WPT applications.

In the validation, a difference of up to 25% was observed between the SAR calculated using the analytical model, and the values calculated using CST Studio Suite® [35]. These percentages can be added to the presented data as an uncertainty. This does not change the determination of the optimal frequency, both for MPL and for MPTE; they remain at 10 kHz.

The absolute received power, which is in the 100 nW to μW range, is sufficient to power various kinds of IMDs [72, 130, 196]. Furthermore, it is possible to charge an IMD for several minutes, after which it wakes up, performs a task for a short amount of time, and returns to the idle state, where the charging cycle starts again [225]. The received power scales with A_{rx}^2, implying that it should be possible to receive tens to hundreds of μW with an Rx coil area of only a few mm^2, depending on the implant depth.

In [86, 175], it was argued that the optimal frequency for WPT into biomedical tissue is in the GHz range. The analysis in [175] is limited to frequencies from 10 MHz to 10 GHz, and [86] is limited to frequencies from 100 MHz to 6 GHz. When these frequency ranges are applied to Figure 6.8, indeed the PTE exhibits a maximum around 1 GHz. However, when the lower end of the frequency range is extended to 10 kHz, the frequency at which the PTE is maximized shifts to 10 kHz. Extending the frequency range to even lower frequencies might result in an even lower optimal frequency, but since the performance from 10 to 300 kHz is approximately constant, the difference with even lower frequencies is not expected to be significant.

The main difference in approach between this work and that by Poon *et al.*[175], is that Poon *et al.* first determine the frequency at which maximum MPTE is achieved, and then scale M such that the SAR is maximized, to determine the maximum power that can be received at this frequency. On the other hand, we first determine M such that the SAR is maximized for each individual frequency, and then determine the frequency at which maximum power can be received. Our approach thus results in a higher received power level.

The presented analysis is not limited to biomedical applications. It is applicable to many applications where the environment can be approximated using a finite number of discrete planar layers, and where the receiver is small compared to the transmit distance. For these situations, it might be challenging to achieve sufficient received power levels. In many of these cases, SAR or similar limits will not be relevant, allowing for more freedom in the design process. Depending on the application, it might be beneficial to aim for MPTE or for MPL. Possible applications include, for example, moisture sensors distributed throughout crop fields, flow or temperature sensors attached to underground pipes, identification tags or temperature sensors for underground cables, temperature sensors distributed through (fresh) cargo, dike monitoring, or various kinds of sensors floating freely in chemical reactors.

6.7 Conclusion

The analytical model presented in Chapter 5 was extended to calculate the SAR generated by the dipole source. The model was validated by comparing the calculated SAR of the analytical model and Simulia CST Studio Suite® [35]. These show the same overall trend, and the difference between both is below 25%. A possible cause for these differences was not further investigated, since they did not hinder the research carried out and described in this chapter.

This model was then used to calculate the magnetic moment M that will result in achieving the maximum allowable SAR inside human tissue, for a range of frequencies. Consequently, for each frequency, this value for M was used to calculate the received power at various implant depths, after which the frequency that results in the maximum received power was determined. The analysis was performed for two cases: a 4 layer air–skin–fat–muscle case, and a 7 layer air–skin–fat–bone–CSF–grey matter–white matter case. The optimal frequency for maximum received power into biological tissue is 10 kHz, the lowest frequency investigated, and is approximately constant for frequencies ranging from 10 to 300 kHz; the difference is at most 4%. Frequencies below 10 kHz were not tested, but judging from the behavior from 10 to 300 kHz, no significant changes are expected below 10 kHz.

For both cases considered, the frequency that results in maximum received power is 10 kHz, the lowest frequency investigated. This is true for implant depths up to 150 mm, after which the level of received power is too low for any practical applications. The amount of power that can be transferred to a receiver located several cm deep inside the human body is sufficient for various practical applications. The difference between the 4 and 7 layer cases is less than a factor 2 for the full frequency range, suggesting that the optimal frequency for MPL is quite robust, since it does not depend heavily on the chosen biological environment.

Additionally, the power transfer efficiency was calculated. It was shown that this efficiency is highest at 10 kHz, and is again approximately constant for frequencies ranging from 10 to 300 kHz. It should be noted that, at increased depth in the tissue, the efficiency around 1 GHz approaches the efficiency around 10 kHz.

Freeman *et al.* [64] concluded that there is little benefit in using frequencies around 1 GHz compared to (sub-)MHz frequencies, when optimizing for MPL. Their conclusions are based on an environment with just a single (equivalent) tissue layer. This chapter shows that the introduction of additional layers results in an optimal frequency that is clearly in the sub-MHz range. Poon *et al.* [175] argued that the optimal frequency for WPT into biomedical tissue is in the GHz range. Their analysis is limited to frequencies from 10 MHz to 10 GHz. When these frequency ranges are applied to Figure 6.8, indeed the PTE exhibits a maximum around 1 GHz. However, when the lower end of the frequency range is extended to 10 kHz, the frequency at which the PTE moves to the sub-MHz range.

CHAPTER SEVEN

Liquid electromagnetic phantoms for biomedical experiments*

7.1 Introduction

For the development of IMDs, it is essential to validate their behavior in an environment that is as realistic as possible, as the behavior of implanted antennae and coils is affected by the surrounding tissue [71, 83, 104, 242]. Biomedical phantoms can be used to create an environment with dielectric properties that mimic those of actual human tissues. Furthermore, these phantoms can be used to experimentally verify the analytical models presented in Chapters 4 and 5.

For some applications, TSLs such as Triton X100, TX150, and TX151 [27, 79, 128], can be bought in specialized (web)shops. However, the range of application is limited, in terms of frequency range and tha variety of different tissues that can be mimicked, and these solutions can be expensive. The availability of recipes for TSLs, using only cheap COTS ingredients, which can be tailored to mimic the dielectric properties of specific biological tissue at a frequency of interest, will be desirable for a wide portion of the WPT community.

With the use of COTS ingredients like deionized water, sugar, salt, gelatin, agar, polyethylene glycol, and sodium alginate, human tissues can be mimicked [42, 69, 81, 96, 173]. However, detailed instructions on how to make phantom material, mimicking a specific tissue for a certain frequency, are hard to find. The few papers that are available are either limited in applicability in terms of frequency or tissue type, or use exotic, hard to obtain ingredients. One such ingredient is sodium azide, which is poisonous, and due to its recent web-recommended use for suicide, very difficult to obtain. Furthermore, little can be found on stability, preparation, handling, and shelf life of the phantom materials.

The work presented in this chapter lists recipes for TSLs mimicking various human tis-

*This chapter is based on [P3].

sues at different frequencies. Details about the preparation of the liquids are also given. Furthermore, it describes how the recipes can be changed to adapt the dielectric properties, for example to mimic those of other human tissue, or to change the frequency at which they match. TSLs made with the presented recipes have a shelf life of at least 10 days at room temperature.

Additionally, we describe how to make a permittivity measurement probe from a piece of semi-rigid coaxial cable, and how to calibrate it, avoiding the use of a short. Not only will this allow for an alternative to a COTS measurement probe, it will also allow for low-budget, disposable measurement probes that can be incorporated in phantoms for monitoring the permittivity over time.

7.2 Phantom recipes

To create tissue mimicking fluids and gels, we only want to use COTS ingredients, ideally products available in regular shops, like supermarkets. As a basis we use deionized water. We add gelatin or agar as a jelling agent or to produce self-shaping phantoms, respectively. Table salt (sodium chloride) is used to tune the conductivity σ, and sugar (sucrose) to tune the real part of the relative permittivity ε_r'.

The aim for the first batch of recipes was that they should be kept as simple as possible, in terms of ingredients and manufacturing. Therefore, no preservatives were added. As will be shown, it is perfectly possible to create phantoms with a fair shelf life without using preservatives. Therefore, we have chosen to also not add preservatives in later batches.

7.2.1 Permittivity measurement

Before going into the recipes and procedures to create body tissue mimicking fluids and gels, we first need to discuss the measurement of the relative permittivity. Relative permittivity is a complex valued quantity:

$$\varepsilon_r = \frac{\varepsilon(\omega)}{\varepsilon_0} = \varepsilon_r'(\omega) + \mathrm{j}\varepsilon_r''(\omega) = \varepsilon_r'(\omega) + \mathrm{j}\frac{\sigma(\omega)}{\omega\varepsilon_0}, \tag{7.1}$$

where ω is the angular frequency, ε_0 is the free space permittivity and σ is the conductivity of the medium.

The complex permittivity of fluids and gels can be measured reliably by measuring the complex reflection coefficient of an open-ended coaxial line, thus obtaining the aperture admittance [204]. A calibration using three standards, usually incorporating water, air (open) and a short, is needed before measurement of the material under investigation can be performed. After calibration, the probe and its cable should remain stationary, as the measurement is very sensitive, and can as such be influenced by movements in the cable.

For the measurements in this chapter, we have made use of the Agilent 85070E High Temperature probe [115] (open-ended coaxial line) attached to an Agilent E5061B VNA [116]. This enables measurements in the frequency range from 300 MHz to 3 GHz. The probe is connected to the VNA using a phase-stable coaxial cable. For correct results, it is also important that all calibration standards and fluids as well as the test sample have the same temperature. Leaving everything overnight in the test laboratory is an easy way to accomplish this.

7.2.2 Procedure for making the phantom material

To create the phantom material, a large supply of deionized water is heated to just below 100° C (not cooking). This temperature is not overly critical. It needs to be in excess of 40° C to dissolve gelatin, and in excess of 95° C to dissolve agar. Gelatin is added as a jelling agent, agar is added to solidify the phantom material.

The desired quantity of water (grams or milliliters) is taken from this heated water supply and put into a separate mixing container, where the right quantities (masses) of sugar and salt are added. The ingredients are thoroughly mixed using a hand-held electrical blender. During this step, gelatin or agar can be added. The amount of gelatin can be be determined visually: stop adding gelatin when the required degree of viscosity is reached. Agar will solidify during the cooling process, hence it is not possible to determine the right amount of viscosity in the warm liquid. From experience, about 40 g/l agar is sufficient to create a solid phantom.

The liquid in the mixing container can now be poured into the final container. This can be a general container when a large homogeneous volume of TSL is required, but it can also be a custom shaped container, for example in the shape of a specific organ. Custom shaped containers will be discussed further in Chapter 8.

The final container with the solution is then closed with a lid or sealed using cling film or aluminum foil, and left to cool down, see Figure 7.1. Closing is important for maintaining the desired permittivity; not closing the container leads to evaporation of water, which leads to a severe change of permittivity and conductivity.

7.2.3 Influence of sugar and salt

To test how different concentrations of salt and sugar influence ε_r', we have first changed the sugar (weight) concentration and measured the relative permittivity for 400 MHz and 2.45 GHz. Different samples were measured to test reproducibility, and were measured on several consecutive days after producing the samples to test for shelf life. In all solutions, we have applied gelatin in a concentration of 24 g per 1000 g water, and salt in a concentration of 20 g per 1000 g water. Figure 7.2 shows ε_r' and σ as a function of sugar concentration.

We do see an excellent reproducibility, proving the suitability of the mixing procedure and a shelf life (at room temperature) of at least three days. In fact, none of our many samples showed a significant change in measured dielectric properties within the first ten days after production. We also see that adding sugar decreases ε_r'. The value of σ also decreases when

Figure 7.1: Various paper and plastic cups containing liquid samples used in the permittivity measurements.

adding sugar. This might be due to the fact that the salt concentration decreases slightly, as the total mass increases when the sugar content increases, whilst the mass of salt stays the same.

Figure 7.3 shows ε_r' and σ as a function of sugar (weight) concentration (30% and 47%) for three different salt (weight) concentrations (0%, 0.6%, and 1.15%), at frequencies of 400 MHz and 2.45 GHz. These graphs confirm that adding sugar decreases ε_r', whilst σ is less affected. Adding salt increases the conductivity of the mixture, but slightly lowers the relative permittivity.

Figure 7.4 shows ε_r' and σ as a function of salt (weight) concentration for different sugar (weight) concentrations, at frequencies of 400 MHz and 2.45 GHz. These graphs confirm that ε_r' is hardly affected by the salt concentration. Adding salt increases the conductivity of the mixture. A higher sugar concentration results in a less steep increase in conductivity with increasing salt concentration.

The graphs indicate that water with sugar and salt in the right concentrations can be used to mimic human tissue and that, even without the use of preservatives, the dielectric characteristics will remain stable for several days. The graphs can be used to predict the required amounts of salt and sugar to obtain a TSL with certain desired dielectric properties. This will be elaborated in Section 7.5.

7.2.4 Specific recipes

Based on the identified trends, we have proposed recipes for phantoms mimicking the relative permittivity of muscle, stomach and kidney tissue as well as blood, for the frequencies 402, 433, 915, and 2450 MHz [68, 82]. The recipes are listed in Table 7.1. These frequencies were chosen as they are commonly used frequencies for MedRadio, industrial, scientific and medical (ISM), GSM, and Wi-Fi, within the measurement range of our dielectric measurement

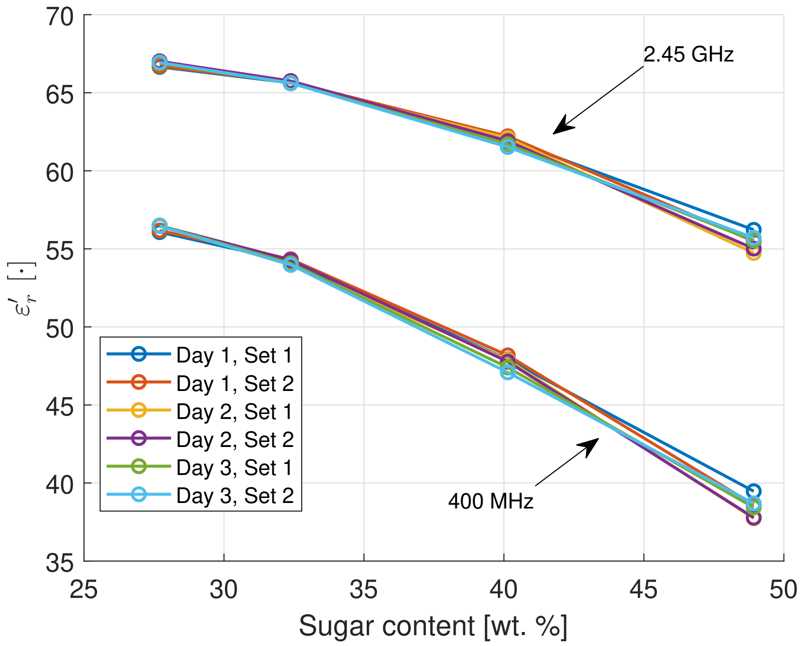

(a) Relative permittivity ε_r'.

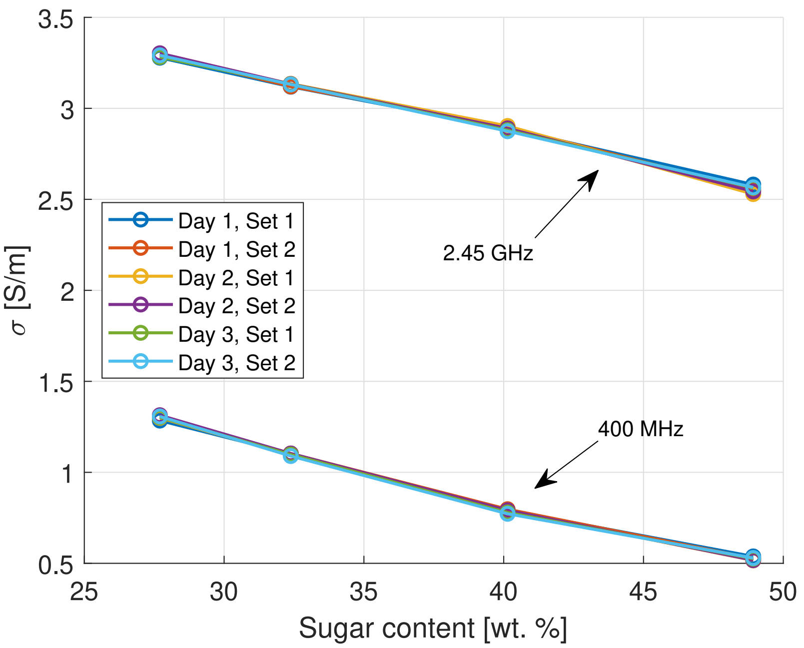

(b) Conductivity σ [S/m].

Figure 7.2: Relative permittivity ε_r' as a function of sugar (weight) concentration for phantoms consisting of 1000 g water, 20 g salt, and 24 g gelatin, at 400 MHz and 2.45 GHz.

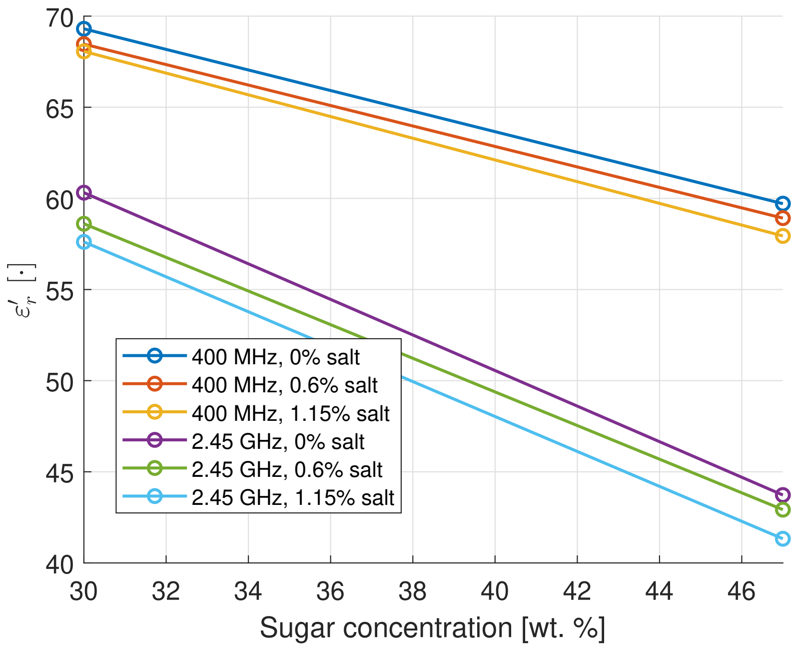

(a) Relative permittivity ε_r'.

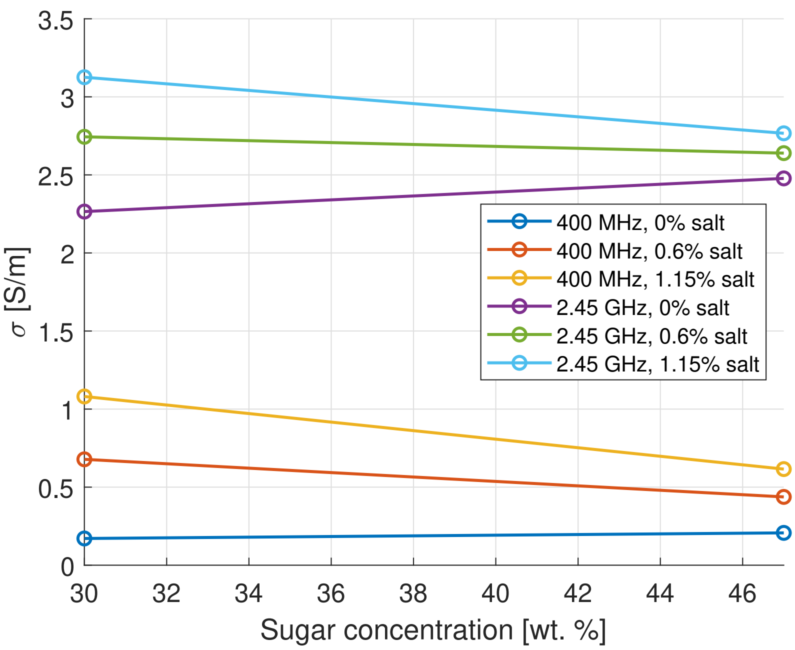

(b) Conductivity σ [S/m].

Figure 7.3: Dielectric properties as a function of sugar (weight) concentration, for different salt (weight) concentrations, for a phantom consisting of 1000 g water, and 24 g gelatin, at 400 MHz and 2.45 GHz. (a) Relative permittivity ε_r'. (b) Conductivity σ.

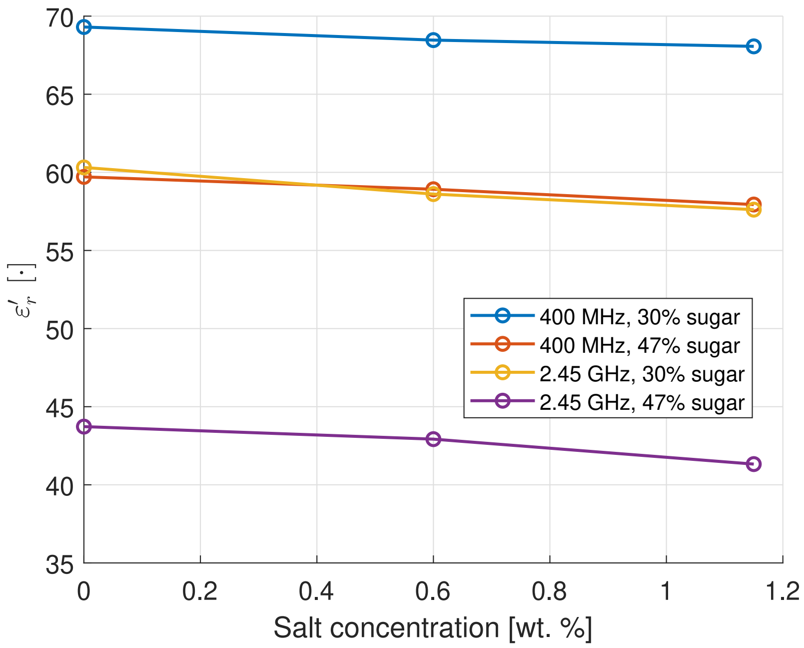

(a) Relative permittivity ε_r'.

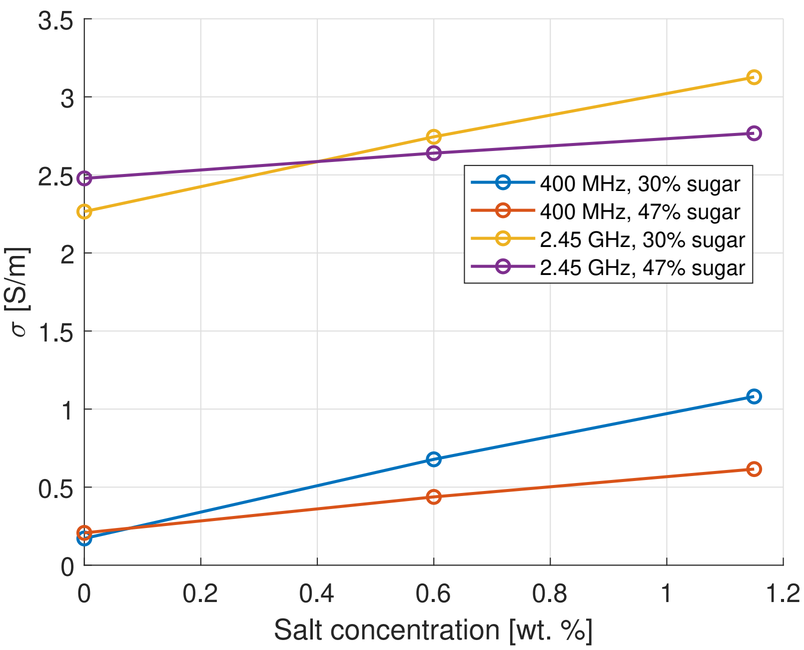

(b) Conductivity σ [S/m].

Figure 7.4: Dielectric properties as a function of salt (weight) concentration, for different sugar (weight) concentrations, for a phantom consisting of 1000 g water, and 24 g gelatin, at 400 MHz and 2.45 GHz. (a) Relative permittivity ε_r'. (b) Conductivity σ.

equipment.

Table 7.1: Dielectric properties of several human tissues at different frequencies [68, 82], and proposed recipes for their tissue mimicking liquids. Each recipe assumes 24 g gelatin per 1000 g water.

Tissue	Freq [MHz]	ε_r' [-]	σ [S/m]	Sugar [wt.%]	NaCl [wt.%]
Muscle	402	57.1	0.797	47.0	1.75
Muscle	433	56.9	0.805	48.0	1.55
Muscle	915	55.0	0.948	43.5	0.65
Stomach	402	67.5	1.00	30.0	1.15
Stomach	433	67.2	1.01	31.0	1.00
Stomach	915	65.0	1.19	31.0	0.80
Stomach	2450	62.2	2.21	26.5	0.00
Blood	433	63.8	1.36	36.5	2.10
Blood	915	61.3	1.54	34.5	1.55
Blood	2450	58.3	2.54	31.0	0.35
Kidney	433	65.5	1.12	34.0	1.40
Kidney	915	58.6	1.40	38.0	1.55
Kidney	2450	52.7	2.43	37.0	0.10

As a next step, six different samples were created and measured, based on the previously mentioned samples at 400 MHz and 2450 MHz, but now their dielectric properties are presented for the full frequency range from 300 MHz to 3 GHz, to give a broadband characterization of the behavior of the TSLs. The recipes have sugar concentrations of 30 and 47 wt.%, and salt concentrations of 0, 0.6, and 1.15 wt.%. Figure 7.5 shows the measured relative permittivity ε_r', Figure 7.6 shows the conductivity σ as a function of frequency. The reference data of six different biological reference materials, taken from the Gabriel database [68], are also shown.

It can be seen that the dielectric properties of stomach can be accurately mimicked by the recipe listed in Table 7.1 at 402 MHz. The error in ε_r' is 4%, the error in σ is 7%. The data and analysis presented in this section can be used to aid others into designing recipes for TSLs for different tissues at different frequencies. The graphs can be used to predict the required amounts of salt and sugar to obtain a TSL with certain desired dielectric properties.

7.3 DIY probe

Dielectric measurement equipment for liquids is delicate. Their principle of operation is based on measuring the input reflection (S_{11}) of an open-ended coaxial cable, which depends on the medium in which the open end is submerged. This implies that the measurement is sensitive

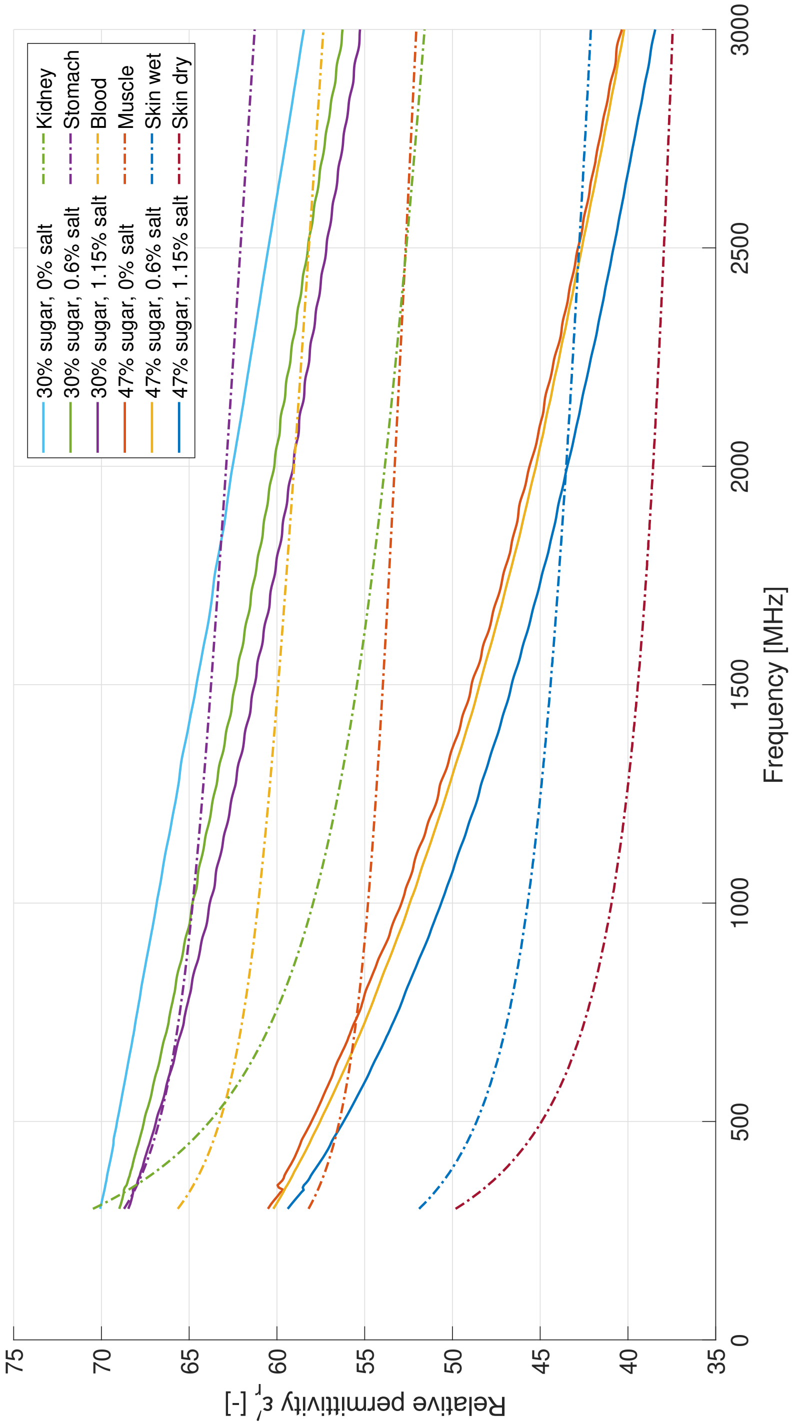

Figure 7.5: Measured average real part of the relative permittivity ε_r' [-] of six different liquid phantoms, as well as reference curves [68] for six human tissues. All liquids contain 24 g gelatin per 1000 g water.

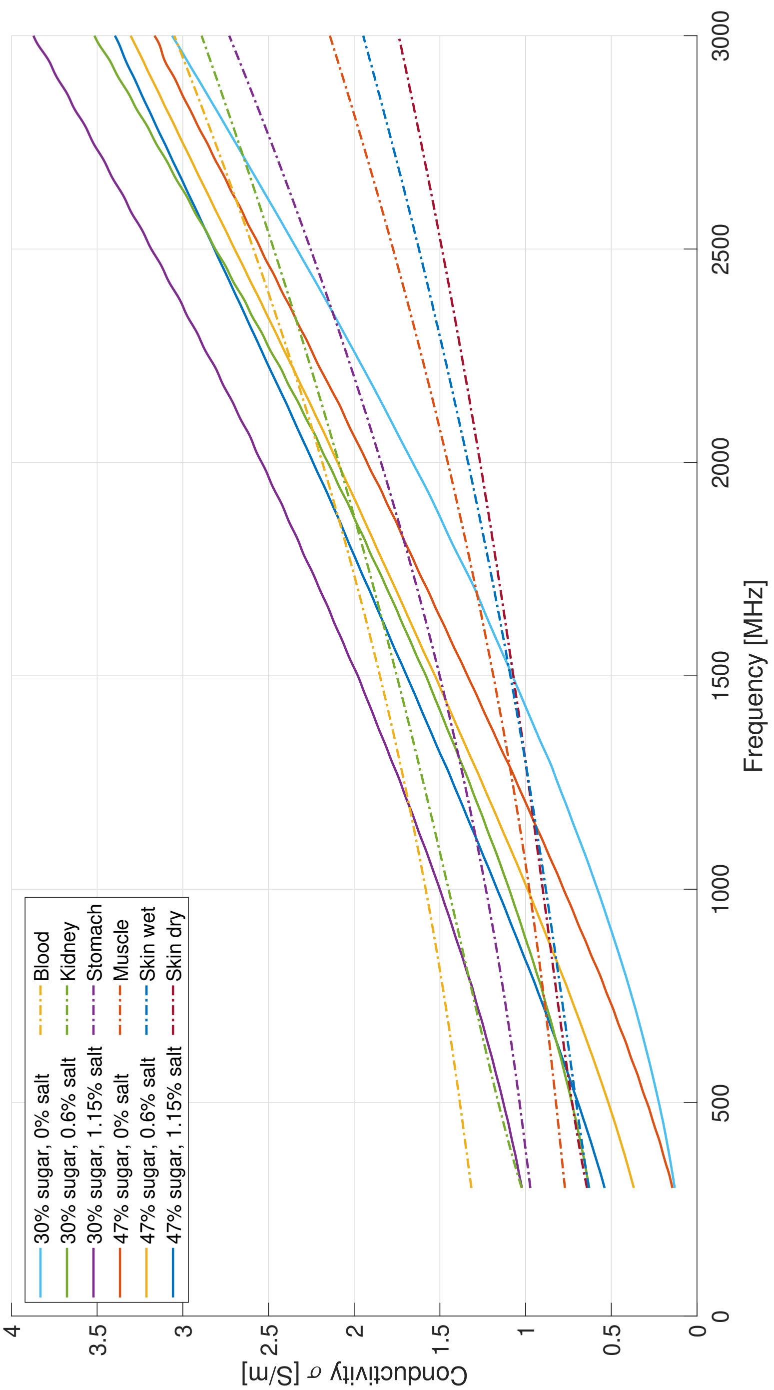

Figure 7.6: Measured average conductivity σ [S/m] of six different liquid phantoms, as well as reference curves [68] for six human tissues. All liquids contain 24 g gelatin per 1000 g water.

to changes in the cable, as well as damage to the open-ended surface.

One of the calibration steps is to press a piece of copper firmly against the open end, creating a short circuit. This procedure is prone to error, as the quality of the calibration depends on the surface quality of the copper, as well as the force used to press the copper calibration sample against the open end.

Our COTS measurement probe got damaged beyond repair, mainly due to the attachment of the short-calibration-piece. Replacing the equipment is costly. Therefore, we have investigated whether it is possible to develop our own measurement probes, based on a length of RG405 semi-rigid coaxial cable with pre-assembled SMA connector, see Figure 7.7. These probes are so low-cost (about €5 each) that we can use them as integral and disposable part of our phantoms to monitor the relative permittivity over time.

Figure 7.7: Measurement probe constructed from a piece of RG405 semi-rigid coaxial cable with pre-assembled SMA connector.

A multitool with a grinding disk was used to slowly cut the cable with two assembled SMA connectors (carefully held into a vice) in half, obtaining two probes. After that, the multitool with a sanding bit was used to sand both open ends of the coaxial cable smooth and flat. Sanding can be performed again to renew the probe after it has been used for some time.

The measurement procedure follows the procedure described in [149, 204, 244]. For the calibration, three references are needed. Usually for these references, air (open), deionized water and a short are used. Here, we have circumvented the use of a short, since this would require a precise mechanical attachment, which is prone to the the same errors as with the COTS measurement probe described above. Instead we have chosen for a second calibration liquid next to deionized water.

7.3.1 Calibration liquid

The three calibration samples should have sufficiently different dielectric properties. Air has a low permittivity and conductivity. Deionized water has a high permittivity and medium conductivity. For the third calibration liquid, we would like to have a liquid with a medium, known permittivity and a high, known conductivity. The liquid we have used is made by adding 928 g sugar (sucrose) and 22.7 g of salt (NaCl) to 1000 g of deionized water. The relative permittivity of this liquid has been measured using an Agilent 85070E High Temperature probe and is fitted as a function of frequency f $(3.0 \cdot 10^8 \text{ Hz} \leq f \leq 3.0 \cdot 10^9 \text{ Hz})$ by

$$\varepsilon_r = \sum_{n=0}^{N} p_n f^n, \tag{7.2}$$

where $N = 7$ was found to be sufficient to achieve an approximation with an error below 0.1%. The polynomial coefficients p_n $(n = 0, 1, 2, ..., 7)$ are given by

$$\begin{aligned}
p_0 &= 66.8053 - \mathrm{j}68.4170, \\
p_1 &= -2.1881 \cdot 10^{-8} + \mathrm{j}1.9371 \cdot 10^{-7}, \\
p_2 &= 1.2322 \cdot 10^{-17} - \mathrm{j}3.4940 \cdot 10^{-16}, \\
p_3 &= -5.4360 \cdot 10^{-27} + \mathrm{j}3.5044 \cdot 10^{-25}, \\
p_4 &= 1.3400 \cdot 10^{-36} - \mathrm{j}2.0694 \cdot 10^{-34}, \\
p_5 &= -1.3543 \cdot 10^{-46} + \mathrm{j}7.1345 \cdot 10^{-44}, \\
p_6 &= -\mathrm{j}1.3268 \cdot 10^{-53}, \\
p_7 &= \mathrm{j}1.0274 \cdot 10^{-63}.
\end{aligned} \tag{7.3}$$

In performing the calibration, using liquids, the formation of air bubbles on the probe surface should be carefully avoided. These bubbles might be difficult to spot. To validate whether or not the calibration is performed well, best perform a calibration measurement, clean the probe using deionized water from a second source, and repeat the measurement. If the results are not (nearly) identical, most probably air bubbles were formed on the surface of the probe.

7.3.2 Measurement

For calibration and measurement, the probe is fixed in a holder and samples are placed under the probe, submerging the probe into the liquid, see Figure 7.8. The probe and the cable should not be moved during the full duration of the experiment. Instead, the samples should be elevated from below, until the probe tip is sufficiently submerged.

For both calibration and measurements, we advise to have the tip of the probe at least 5 mm submerged and at least 10 mm displaced from the walls and/or bottom of the sample container. After each measurement, the probe must be wiped clean with a tissue, cleaned using deionized water, and wiped dry.

7.3.3 Results

The dielectric properties measured with the RG405-based DIY probe are obtained following the theory of the procedure described in [204]. They are compared to the values obtained through measuring with the COTS Agilent 85070E High Temperature Probe [115]. The results are presented for frequencies ranging from 300 MHz to 3 GHz, as explained before.

Figure 7.8: Application of the DIY probe. The probe is fixed in position and attached to the VNA using a phase-stable cable. Measurement samples are brought underneath the probe such that the probe aperture is submerged into the sample.

Figure 7.9(a) shows the relative permittivity and conductivity versus frequency of a sample of (contaminated) ethanol. Figures 7.9(b) and 7.9(c) show the absolute and relative error in the DIY-probe measurements versus the COTS-probe measurements, respectively.

Figure 7.10(a) shows the relative permittivity and conductivity versus frequency for a sample taken from a mixture of 908 g sugar dissolved in 1000 g deionized water with 24 g gelatin (i.e. 47 wt.% sugar). Figures 7.10(b) and 7.10(c) show the absolute and relative error in the DIY-probe measurements relative to the COTS-probe measurements, respectively.

The absolute error in ε_r' is below 2.0 for the complete frequency band, for both measurements. For σ, it is below 0.14. This relates to a relative error in ε_r' between 2.5 and 9.5%, and for σ it is between 0.3 and 20.5%. The relative error in σ is highest at the lower end of the frequency range. For frequencies above 500 MHz, the relative error in σ is between 0.3 and 14.4%. These results are considered accurate enough for most lab experiments.

7.4 Challenges with model validation

Biomedical phantoms can be used to validate the work presented in Chapters 4 and 5 experimentally, as well as to validate and reproduce the work reported in [175, 176]. For this validation, we have designed several pairs of Tx and Rx coils spanning a frequency range from 100 MHz to 2.7 GHz, see Figure 7.11. The Rx coil can be submerged in the TSL at

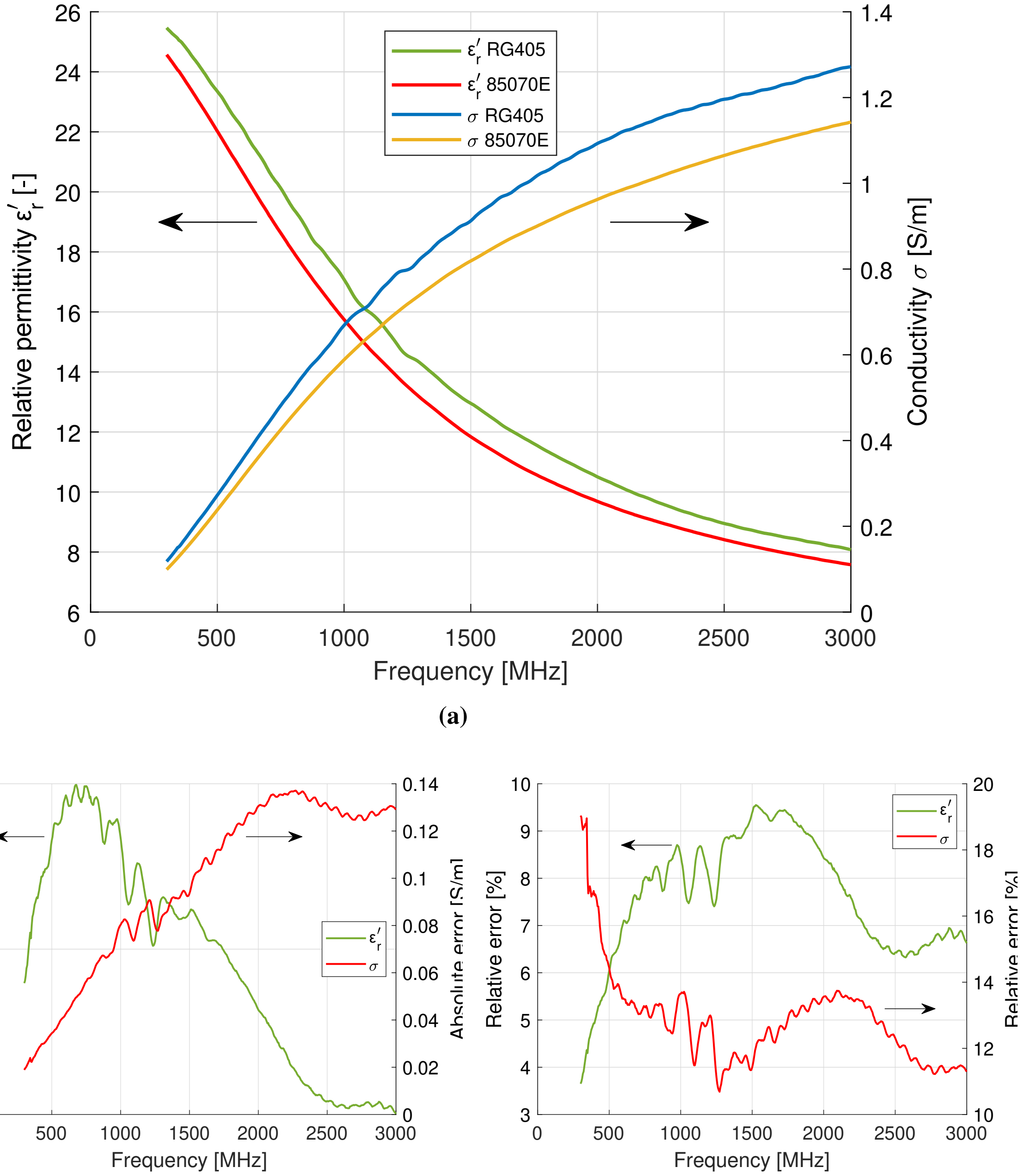

(a)

(b)

(c)

Figure 7.9: Relative permittivity and conductivity of (contaminated) ethanol vs. frequency. (a) Values measured with an RG405-based DIY probe and measured with an Agilent 85070E High Temperature Probe. (b) Absolute and (c) relative error between the DIY probe measurement values and the Agilent probe measurements.

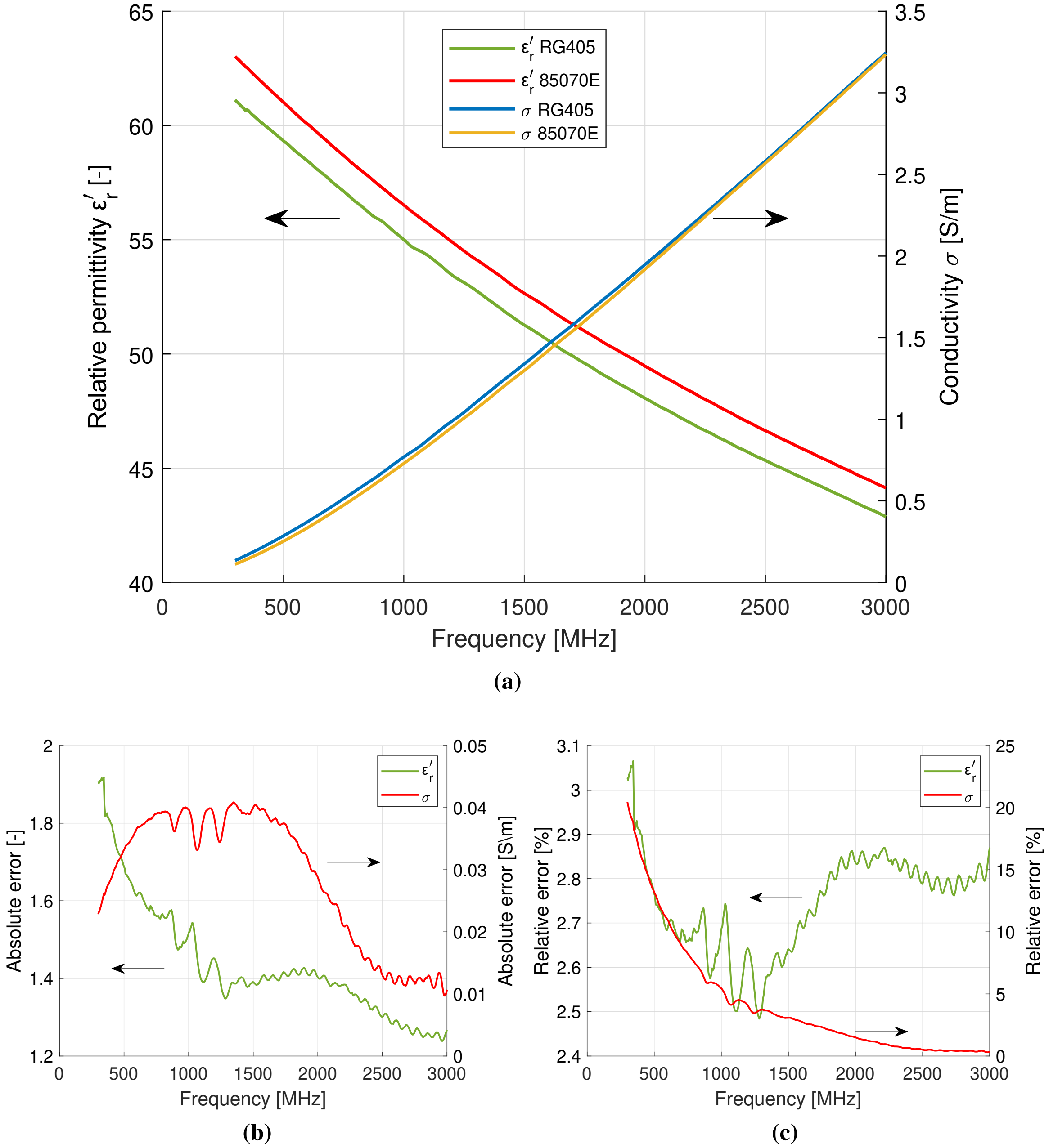

Figure 7.10: Relative permittivity and conductivity of sugar-water-mixture vs. frequency. (a) Values measured with an RG405-based DIY probe and measured with an Agilent 85070E High Temperature Probe. (b) Absolute and (c) relative error between the DIY probe measurement values and the Agilent probe measurements.

certain locations, where it receives power transmitted by the Tx coil located outside the TSL. These results can be compared to the received power calculated by the analytical model, as outlined in Chapter 6.

The coils are realized on PCB. They consist of a single turn, realised by a copper trace. They are designed such that their circumference is less than 10% of the free space wavelength, which means that they can be considered to behave as MPDs, as explained in [223] and validated in Chapter 4. Their input impedance is matched to 50 Ω, such that the accepted power of the ports is maximized. The 100 and 500 MHz coils have discrete LC-matching circuits that can be soldered by hand, the 2.7 GHz coils have a matching circuit realised in microstrip technology [177]. Their values were optimized using Simulia CST Studio Suite® [35].

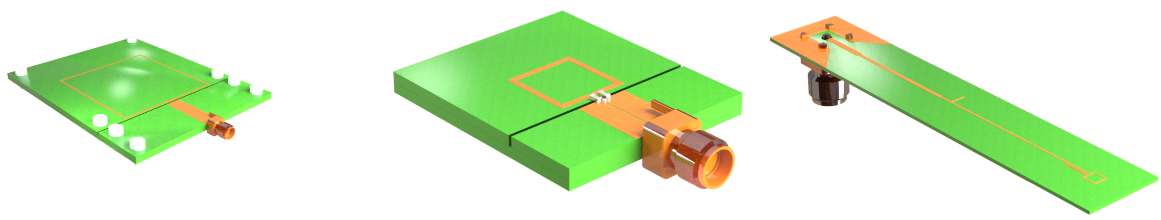

(a) 100 MHz (50 × 50 mm) **(b)** 500 MHz (10 × 10 mm) **(c)** 2.7 GHz (2 × 2 mm)

Figure 7.11: Printed PCB coils which can be used to validate analytical field models.

The coils were manufactured, and the S-parameters of each pair were measured in free space. These corresponded well with the simulated values. However, the practical implementation of the validation procedure, where one of the coils needs to be submerged in phantom material, has proven to be rather difficult. The input reflection of the submerged coil is severely affected by the surrounding medium, even when an insulating layer is applied to the metal parts of the coils. This lowers the radiation efficiency significantly, leading to situations where the received power becomes too low to be detected reliably by the VNA.

Surrounding the coil with a material with dielectric properties close to those of air, will reduce the influence of the phantom material on the coil. This can be a layer of foam, for example. However, this implies that only the fields inside the foam layer can be measured, and not the field inside the other TSL layer(s), which severely limits the application. Furthermore, adding a layer of foam means the introduction of an additional layer, and thus additional boundaries, to the TSL. This affects the propagation of the EM waves through the layer stack, and should thus be incorporated in the analytical model.

Future work should focus on overcoming these limitations. One possible approach could be to match one coil in free space, and the other coil in the specific medium in which it is submerged. Another approach could be to use a power amplifier to boost the transmitted energy, such that the received power becomes detectable again. Furthermore, it would be valuable to have coils available at additional frequencies, to reduce the frequency steps between the coil pairs. Suggestions for future work will be elaborated in Chapter 9.

7.5 Discussion

The obtained measurement results can be used to create TSLs for a wide range of biological tissues. By interpolated and extrapolating the presented data regarding the influence of adding sugar and salt, one can predict the required concentrations of both to obtain a TSL with the required values for ε' and σ. This approach was used to create the proposed recipes in Table 7.1.

From Figures 7.5 and 7.6, we know that the trends in ε' and σ of biological tissues are in general not the same as those of TSLs created using sugar and salt. This implies that, although the presented method can be used to create a broad range of TSLs, the frequency range in which the dielectric properties (approximately) match those of the biological reference data will be limited. In other words, the generated TSLs will be narrow band. Figures 7.5 and 7.6 can be used to estimate the bandwidth of each TSL. From the figures, it is estimated that a bandwidth of a few hundred MHz can be achieved within a 5% error margin, depending on the frequency and the tissue that is mimicked.

7.6 Conclusion

We have shown that it is possible to create body-tissue-mimicking fluids, for frequencies ranging from UHF to microwaves, by mixing deionized water, sugar and salt according to the proposed recipes. By adding gelatin, the fluid can be made jelly-like, adding agar makes the solution solid. Even without adding preservatives, all samples made for this research maintained the dielectric characteristics for at least ten days when stored at room temperature.

The presented data can be interpolated and extrapolated to obtain the concentrations of sugar and salt required for creating a TSL with specific dielectric properties. The bandwidth of the TSL will be limited, but a few hundred MHz can be achieved within a 5% error margin, depending on the frequency and the tissue that is mimicked.

Low-cost permittivity measurement probes can be easily constructed from pieces of RG405, semi-rigid coaxial waveguide. Calibration needs air (open), deionized water and a sugar-salt-water mixture. Measured reflection data need to be processed following a procedure described in [204]. The maximum absolute error relative to a using a COTS probe and software is less than 2.0 for ε_r', and less than 0.14 for σ, for frequencies ranging from 300 MHz to 3 GHz.

Chapter eight

Solid electromagnetic phantoms for biomedical experiments*

8.1 Introduction

In the previous chapter, various recipes for tissue simulating liquids (TSLs) have been presented, using COTS ingredients like deionized water, sugar, salt, gelatin, and agar. These can be used to mimic a large variety of biological tissues, and have been used frequently in the lab, but they have two main limitations.

The first limitation is that the TSLs are water based, which means that the relative permittivity ε_r' of the phantom will approximately be between 30 and 80. Additionally, the conductivity σ will be equal to or larger than the conductivity of water. This is adequate to mimic the dielectric properties for a large range of organs and muscle, but not for, for example, bone or fat. The use of materials with a low permittivity could increase the range of biological tissues that can be mimicked. Affordable COTS examples of such materials are, for example, plastics.

The second limitation of the TSLs presented in the previous chapter, is that the amount of detail realised with them is limited to a container filled with a homogeneous material. This can be sufficient for certain types of experiments, but might present too little detail for other experiments.

An increase in the level of detail of biomedical phantoms, by, for example, introducing a more realistic geometry or multiple tissue layers, will result in more realistic measurements and will broaden the range of applications. To achieve more detail, it can be beneficial to add solid structures to the phantom, for example to mimic bone or teeth structures. These solid parts can be added to an existing liquid phantom, which will result in a more realistic EM

*This chapter is based on [P6]. The research described in this chapter has been conducted in close collaboration with Steven Beumer.

contrast. Alternatively, when a higher permittivity and/or conductivity is required, molds can be used to create phantom parts (such as organs) with realistic shapes [173], filled with a TSL with the desired dielectric properties, combined with a gelifying agent such as agar.

This chapter presents the dielectric properties of various COTS 3D printable materials, including several kinds with added carbon, metal, and stone particles. Their properties are compared to those of reference biological data [68] to determine their applicability.

8.1.1 3D printing of biological phantoms

3D printing is a cheap and accessible way of creating these structures from models available online or by segmenting medical images. Two main 3D printing technologies exist on the market today: fused deposition modeling (FDM) (sometimes also referred to as fused filament fabrication (FFF)) and resin printing using a stereolithography apparatus (SLA). An FDM printer works with a heated nozzle that melts the raw material (a filament wire). The nozzle travels through the build volume, and deposits the material at the desired locations, layer by layer. In an SLA printer, the raw material is a liquid resin solution. A controllable light source solidifies the resin at the desired locations, layer by layer.

An SLA printer outperforms its FDM counterpart in terms of accuracy, rigidity, and print speed of the final result. However, the raw printing material of SLA printers is more expensive, more difficult to handle because of toxicity, and the variety of available materials is severely limited. Furthermore, an FDM printer is generally much cheaper than an SLA printer, although the difference is getting smaller over the last few years.

The dielectric properties of the resins used in SLA printing [168] are not in or near the range of those of biological tissue [68]. Carbon filled filament for FDM 3D printers [143, 147, 172] has been demonstrated to exhibit dielectric properties closer to those of biological tissue [68]. Furthermore, several other types of COTS filament with added metal or stone particles are available. These materials could prove to be useful as well, even though no dielectric information has been found yet.

This suggests that FDM 3D printers are more suitable than SLA ones for our application. The accuracy of an FDM printer, which is in the order of 100 μm [221] (depending on the printer quality) is considered sufficient for bone or teeth, and for molds for organs, as the accuracy is much smaller than the object size, and also much smaller than the wavelength of EM fields in biological tissue, at least for frequencies up to 20 GHz, which is the upper frequency limit for practical purposes.

8.1.2 Dielectric properties of 3D printing materials

For the creation of solid biological phantoms, it is essential to know the dielectric properties of COTS 3D printing materials. Various sources have reported measurements of dielectric properties of several 3D printing materials. Table 8.1 lists the dielectric properties of 3D printing materials presented in recent literature. The gray cells correspond to one of the reasons for non-applicability in our situation, as will be discussed next.

Table 8.1: Dielectric properties of 3D printing materials in recent literature.

Ref.	Freq. [GHz]	ε_r'	ε_r''	σ [S/m]	$\tan\delta$	Tech.	Material
[17]	$1.9-2.4$	$1.3-4.3$	-	-	$0.001-0.004$	FDM	COTS
[57]	$0.5-20, 40, 60$	$2.74-3.05$	-	-	$0.011-0.017$	FDM	COTS
[143]	$8.2-12.4$	$6-8$	$10-12$	-	-	FDM	COTS
[144]	$2-20$	$3.13-3.18$	-	-	$0.042-0.052$	FDM	COTS
[147]	$0.5-8.5$	$4-120$	-	$0.5-10$	-	FDM	DIY
[168]	$20-60$	$2.45-3.10$	-	-	$0.007-0.025$	SLA	COTS
[172]	DC-13	$6-100$	$8-100$	-	-	FDM	COTS
[179]	DC-8	$1.0-3.5$	-	-	-	FDM	COTS
[183]	$3-50$	$2.03-3.73$	-	-	$0.0002-0.066$	FDM	COTS
[241]	$1-10$	$2.55-2.95$	-	-	$0.007-0.08$	FDM	COTS

As can be seen in the table, several publications report materials with a relatively low permittivity ($\varepsilon_r' \leq 4.3$) and low loss ($\tan\delta \leq 0.08$), which is much lower than the dielectric properties of biological tissue [68], as we will see later in this chapter.

The sources that report materials with a higher permittivity ($\varepsilon_r' \geq 8$) [143, 147, 172] all use carbon-filled filament. Their values for σ and ε_r'' are of the same order of magnitude as those of biomedical tissue [68], which indicates that carbon-filled filament could be a suitable material for the 3D printing of solid biomedical phantoms.

We prefer to use COTS material, as DIY fabrication of 3D printable filament requires specific expertise and equipment [147]. The frequency band of [143] is limited to $8.2-12.4$ GHz, whereas we would like to perform experiments also at commonly used (medical) frequencies such as 6.78, 402, and 2450 MHz, and possibly also around 28 GHz for future 5G experiments. The data in [172] can be useful for most of these experiments. However, the presented imaginary part of the relative permittivity ε_r'' is much higher than that of biological tissue [68].

Additionally, we have found several COTS 3D printing filaments with different carbon concentrations [1, 182] than the ones listed in Table 8.1. Based on the dielectric properties of the carbon-filled filaments in Table 8.1, we would like to verify whether or not the dielectric properties of these are too in the range of biological tissue [68]. Furthermore, COTS filaments enriched with different kinds of metal [28, 29, 30] and stone [61], were found. As we could not find reference data for these materials, we would like to investigate what range of dielectric properties these materials have, to determine whether or not they are in the range of biological tissue [68]. Moreover, as the measurement equipment available in our lab allows for dielectric measurements up to 20 GHz, we can extend the readily available data to a larger frequency range.

This chapter presents an overview the dielectric properties of COTS materials that can be used in standard FDM or FFF 3D printers, for frequencies ranging from 4 MHz to 20 GHz, measured with the SPEAG DAK-TL2 dielectric assessment kit [37]. We present results for relatively common materials, such as, acrylate styrene acrylonitrile (ASA) [60], polyethylene terephthalate glycol (PETG) [217], regular and tough polylactic acid (PLA) [218, 220]. Additionally, the properties of special COTS PLA and PETG filaments enriched with bronze [28], carbon [1, 182], clay [61], concrete [61], copper [29], granite [61], steel [30], and terracotta [61] particles are measured. Based on our results, a researcher can select the material with dielectric properties that are closest to the desired biological material properties [68].

8.2 Experimental Method

For each of the materials listed in Table 8.2, three $50 \times 50 \times 2$ mm^3 samples are printed using a 0.2 mm layer height and 100% infill [†] on an Ultimaker S5 FDM 3D printer [221]. The print settings were as specified by the manufacturer for each material. The filament was stored in a dedicated low humidity environment, to prevent deterioration. The standard materials are printed using a 0.4 mm standard printing head [219]. The materials with additions are printed using a 0.6 mm hardened steel CC head [219], due to the abrasive nature of these filaments. The printer is set to iron the top of each sample as a post processing step.

After ironing, the top of each sample is sanded manually (from 120 to 4000 grit in eleven steps) to obtain a flat and smooth surface with a surface roughness of at least N5, which is recommended by the manufacturer of the SPEAG DAK-TL2 dielectric assessment kit [37].

The measurement probe is pressed against the sample with a force of 200 N. Each sample is measured at different probe locations over its surface, to validate the intra-sample uniformity of the results. Each measurement is repeated ten times. The results are averaged and their standard deviation is calculated. In this chapter, the real part of the relative permittivity ε_r' and the conductivity σ are used, as this is commonly the case in biological reference data [68]. Using the following relations, the dissipation factor $\tan\delta$ or the imaginary part of the relative permittivity ε_r'' can be determined.

$$\hat{\varepsilon}_r = \varepsilon_r' + \mathrm{j}\varepsilon_r'' = \varepsilon_r' + \mathrm{j}\frac{\sigma}{\omega\varepsilon_0} = \varepsilon_r'(1 + \mathrm{j}\tan\delta), \tag{8.1}$$

where $\omega = 2\pi f$ is the angular frequency in rad/s.

[†] A 3D model is typically printed with a solid outer shell, whilst the internal volume contains some sort of scaffolding structure, also referred to as ‘infill’. The infill density represents the ratio between the volume of the scaffolding material and empty space inside the final print; a part with 0% infill is completely hollow, and 100% corresponds to a completely solid part. Different infill patterns exist, 3D printing software Cura [216] contains 14 different ones. The strength of the final print is determined by the outer wall thickness, the infill density, and the infill pattern. These can also affect the print time and material consumption significantly.

Table 8.2: List of 3D printing filament materials measured.

Material	Addition	Brand
ASA	-	Formfutura ApolloX™[60]
PLA	Bronze	colorFabb Bronzefill [28]
PETG	15% carbon	REAL PC-PETG [182]
PETG	20% carbon	123-3D PETG Jupiter [1]
PLA	50% Pottery clay	Formfutura StoneFil™[61]
PLA	50% Concrete	Formfutura StoneFil™[61]
PLA	Copper	colorFabb Copperfill [29]
PLA	50% Granite	Formfutura StoneFil™[61]
PETG	-	Ultimaker PETG red [217]
PLA	-	Ultimaker PLA blue + magenta [218]
PLA	-	Ultimaker tough PLA black [220]
PLA	Steel	colorFabb Steelfill [30]
PLA	50% Terracotta	Formfutura StoneFil™[61]

For some of the PLA samples, as well as the materials that contain additives, like carbon, stone or metal, the dielectric properties of an additional sample of 5 mm thick are measured to verify whether or not the thickness affects the results significantly.

8.3 Results

Figure 8.1 shows the measured average relative permittivity ε_r' of the 3D printed samples, Figure 8.2 the conductivity σ. The dielectric properties are measured with two probes, the first of which measures from 4 to 600 MHz, and the second from 200 MHz to 20 GHz. The reference data of four biological tissues are given [68]: cortical bone, fat, and red and yellow bone marrow. Tooth is not shown, as it has identical properties as cortical bone.

8.3.1 Relative permittivity

The measured relative permittivity ε_r' of each of the carbon-filled and metal-filled samples crosses at least three of the four reference curves. Table 8.3 lists the discrete frequencies at which the measured ε_r' matches the reference data.

The crossings between the measured and reference data are found for frequencies either below 68.2 MHz or above 7230 MHz, meaning that no crossings occur in a frequency span of little over two decades. For yellow bone marrow, all crossings occur below 68.2 MHz. For the other reference curves, the crossings with carbon-filled PETG occur below 68.2 MHz, and the crossings with metal-filled PLA occur above 7230 MHz.

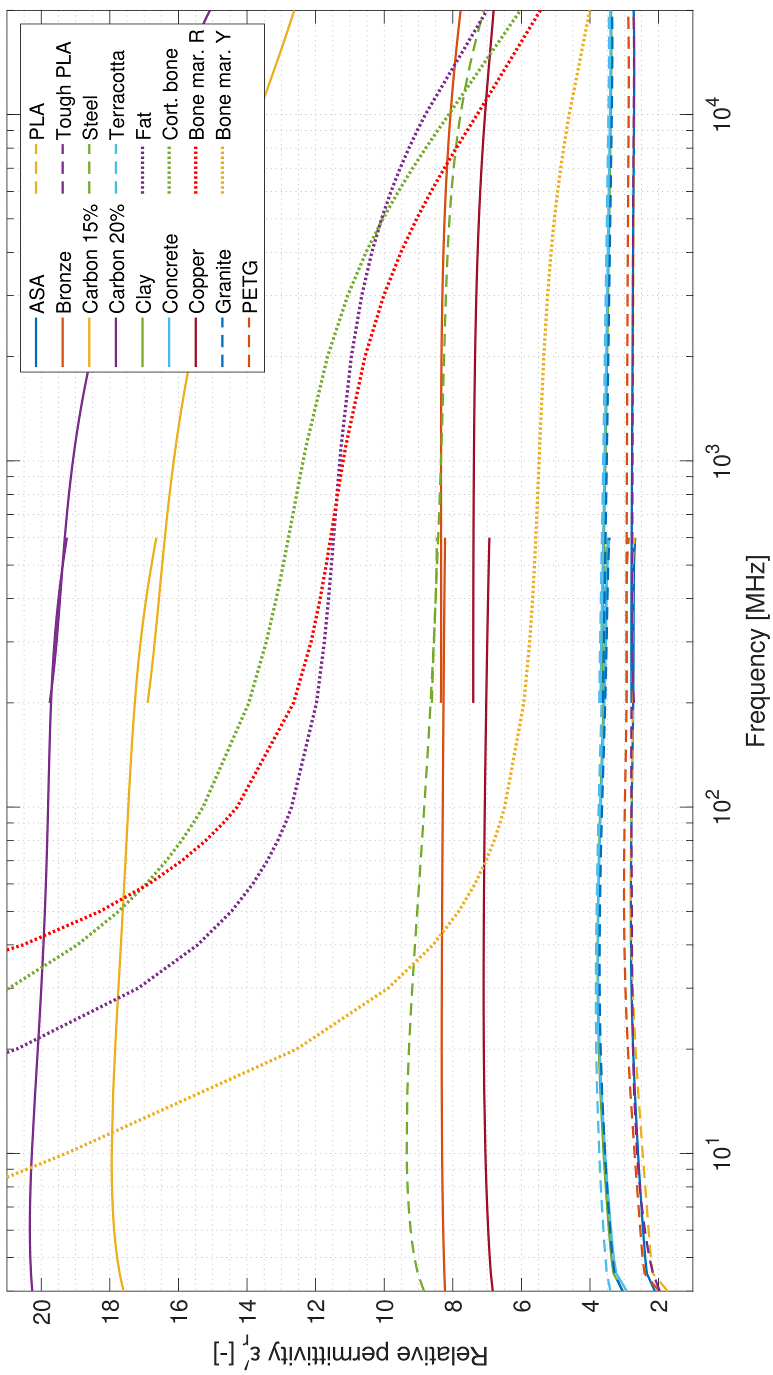

Figure 8.1: Measured average real part of the relative permittivity ε_r' [-] of the 3D printed samples, as well as reference curves [68] for four human tissues.

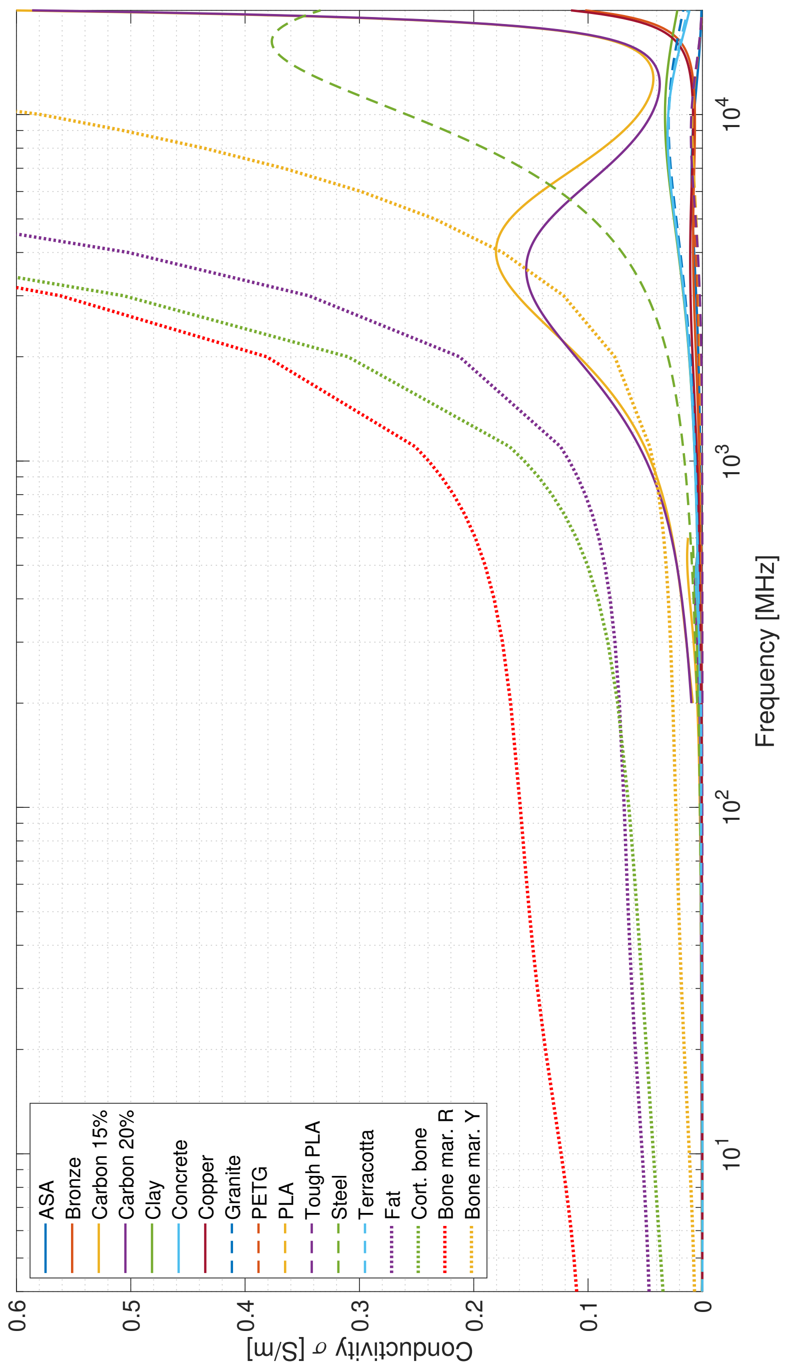

Figure 8.2: Measured average conductivity σ [S/m] of the 3D printed samples, as well as reference curves [68] for four human tissues.

Table 8.3: Frequency at which the measured ε_r' matches the reference data [68].

Material	Frequency of reference data match			
	Fat	Cortical bone	Bone marrow Red	Bone marrow Yellow
Bronze-filled PLA	10.9 GHz	10.2 GHz	7230 MHz	43.2 MHz
Carbon-filled PETG 15%	28.0 MHz	51.5 MHz	54.6 MHz	11.5 MHz
Carbon-filled PETG 20%	21.5 MHz	34.5 MHz	42.5 MHz	9.1 MHz
Copper-filled PLA	21.8 GHz	14.9 GHz	11.0 GHz	68.2 MHz
Steel-filled PLA	18.8 GHz	11.7 GHz	7952 MHz	35.3 MHz

The stone-filled PLA samples all have approximately similar values for ε_r', which approaches that of yellow bone marrow for 20 GHz, but are too low for the lower frequencies and the other reference tissues. The relative permittivity of regular ASA ($\varepsilon_r' \leq 2.81$), PETG ($\varepsilon_r' \leq 3.01$), and PLA ($\varepsilon_r' \leq 2.81$) are not close to the reference data.

The standard deviation of ε_r' is $< 1.4\%$ for all materials for all frequencies measured, except for bronze and copper filled PLA, for which it is $< 3.5\%$, which is still considered acceptably low.

8.3.2 Conductivity

The conductivity σ of the carbon-filled PETG samples is close to that of yellow bone marrow for frequencies ranging from 800 to 4100 MHz, but the difference at other frequencies is quite substantial. The σ values of none of the samples is close to the other reference data at any frequency within the measured frequency range; it is at least two times too low at any frequency, with differences of at least sixteen times for $f \leq 200$ MHz.

The standard deviation of σ is $< 30\%$ for $f > 30$ MHz for all materials except regular and tough PLA. Below 30 MHz, the standard deviation can reach up to 90%, which is caused by both intra-sample and inter-sample variability. A possible explanation is the fact that the measured values for σ are relatively low, which means (small) measurement errors can result in significantly different results.

8.3.3 Stone-filled PLA samples

After the initial measurements, the stone-filled PLA samples were submerged in deionized water for over 24 hours, to investigate whether or not they would absorb any water, and as such their dielectric properties would change accordingly. The measured dielectric properties did not show a significant difference compared to the dry material, though. Furthermore, the weight of the sample did not increase notably, suggesting little to no water was absorbed.

8.4 Discussion

The measured ε_r' values indicate that, above 9 MHz, there are several (small) frequency bands in which ε_r' of the filament approximately matches that of the reference data from biological tissue. However, the conductivity of almost all of the measured samples is much lower than the biological reference data. This means that experiments performed using phantoms created with these materials might underestimate the losses.

Even when the dielectric properties of the selected phantom material are not a good match to those of biological tissue, they might still be used to get useful insight. For example, the contrast in ε_r' between bone and skin or muscle is high. This means that the resulting reflection coefficient will be large. When ε_r' of the phantom bone is not accurate, the reflection coefficient will still be large. Alternatively, the problem could be scaled to a different frequency,such that the multi-layer phantom represents the correct contrast at the scaled frequency. The size of the phantom and antennas should be scaled accordingly.

8.4.1 Effect of infill percentage

Even though the relative permittivity ε_r' of the samples matches the biological reference data for small frequency bands only, it should still be possible to use 3D printing to manufacture biological phantoms with realistic ε_r' outside these bands, by varying the infill. A 3D printed object usually consists of a solid outer shell, which can be as small as 1 to 2 mm thick, and the rest of the volume is filled with a supporting structure, called 'infill'. This results in a significant reduction in print time, model weight, and material use. The higher the infill percentage, the more material is used for the supporting structure, giving the model more strength. The 3D printed samples created in this research are solid, i.e. the infill percentage is 100%.

Research indicates that the effective relative permittivity $\varepsilon_{r,\text{eff}}'$ of 3D printed material scales almost linearly with infill percentage [17, 144], i.e. a model printed with arbitrary infill percentage η_{infill} will have an effective permittivity of approximately

$$\varepsilon_{r,\text{eff}}' \approx \eta_{\text{infill}} \cdot \varepsilon_{r,\text{filament}}' + (1 - \eta_{\text{infill}}) \cdot \varepsilon_{r,\text{air}}'. \tag{8.2}$$

Even though the presented data in [17, 144] suggest such a linear relationship, more research is needed to determine whether that is indeed applicable to the general case, or that a different relation is valid, for example one of the mixing equations discussed in [110, 134]. Also, more research is needed to determine whether or not this relationship also holds for the conductivity σ.

The resulting phantom will not be homogeneous, as the volume will be part filament, part air. More research is needed to determine which infill pattern achieves the best performance. The chosen pattern should result in a good isotropy, and the error introduced by the inhomogeneity of the model should be as small as possible. More research is also needed to investigate the effect of filling the empty space inside the model with a TSL, instead of with air, as this could possibly be used to increase the dielectric properties of the model in a predictive way. In this case, $\varepsilon'_{r,\mathrm{air}}$ in Eq. (8.2) should be changed to $\varepsilon'_{r,\mathrm{TSL}}$

A dual or triple extruder can even be used to manufacture a phantom consisting of different materials, such as a bone with bone marrow inside, or a skull with cortical and spongy bone, to increase the level of detail even further [243]. Alternatively, a phantom can be printed with multiple materials alternately, effectively mixing their dielectric properties.

8.4.2 Sample preparation issues

Several samples were excluded from the presented data, as their measured ε'_r differed significantly ($\geq 25\%$) from the other samples. In these samples, a large intra-sample variability was measured. All of the discarded samples had notable imperfections on either their bottom or top surface, violating the surface roughness requirement for the measurement system. New samples with smooth surfaces were manufactured, which resulted in better reproducible measurements. Therefore, we believe the initial differences in measured dielectric properties were caused by the preparation of the samples, and not by the samples themselves.

For the carbon-filled materials, the 2 mm thick samples could not be printed with sufficient quality, i.e. the 2 mm samples were prone to small print errors leading to an uneven surface, so only 5 mm samples were used.

The used dielectric measurement equipment requires the surface of the samples to have a surface roughness of at least N5. Quite some labor is required to obtain such a smooth surface, and as stated above, the process is sensitive to errors. For biomedical experiments, however, this should be much less of a problem, as the 3D printed structures required for these experiments are usually orders of magnitude larger than the size of these imperfections. When required, sanding the phantom with 120 grit sanding paper should be sufficient to smooth curves and get rid of possible surface defects, and thus give reliable results.

8.5 Conclusion

We presented the measured relative permittivity ε'_r and conductivity σ of various cubes made of COTS 3D printing filaments, for frequencies ranging from 4 MHz to 20 GHz. These materials can be used to increase the level of detail in biomedical phantoms, by not only using TSLs, but also 3D printed structures mimicking for example bone or teeth. This will allow for experiments that are closer to reality, and thus produce more valuable results.

The measured dielectric properties are compared to those of cortical bone, fat, and red and yellow bone marrow. The relative permittivity ε'_r of the metal and carbon filled samples matches the biological reference data for small frequency bands. The measured σ is too low for all materials and frequencies, except for yellow bone marrow from 800 to 4100 MHz.

More research is needed to increase the applicability of 3D printing techniques in the creation of biomedical phantoms. In particular, varying the infill percentage, and filling the empty space inside the model with a TSL, instead of with air, could turn out to be promising techniques to tune the dielectric properties of the 3D printed model predictably. Additionally, when a 3D printer with a dual or triple extruder is available, a single part could be fabricated with multiple materials to increase the level of detail even further, such as bones with bone marrow inside.

Chapter nine

Conclusions and Recommendations

In wireless power transfer (WPT) to biomedical implants, numerous aspects play a role. In this thesis, we have looked at the design, realization and validation of a WPT system for a visual prosthesis. In addition, a general, efficient modelling approach for electromagnetic (EM) wave propagation in planarly layered media had been developed. Furthermore, liquid and solid phantoms for biomedical EM experiments have been investigated.

In Chapters 2 and 3, we have presented an approach for the design of a WPT system consisting of a class E inverter, a class DE rectifier, and two coupled coils, optimized for maximum power transfer efficiency (MPTE). The hardware design was simulated and validated in a case study for the NESTOR project, where a brain implant is connected to the visual cortex. EM and thermal simulations were performed to verify compliance with relevant safety standards.

Chapters 4 and 5 describe two analytical models that can calculate the EM-fields generated by an magnetic point dipole (MPD) in a layered environment. The first regards a two-layer environment, for instance air and (equivalent) biological tissue. The second model regards a multilayered environment, containing any number of layers. The numerical implementation of the models is discussed in detail. The models were validated by comparing them with simulations in commercial software.

These analytical models were extended in Chapter 6, such that the specific absorption rate (SAR) generated by the transmitting MPD can be calculated, as well as the received power and the total power dissipated in the tissue. This was then used to calculate the transmit power that will result in achieving the maximum allowable SAR, whilst complying with the relevant safety standards. Consequently, for each frequency, this transmit power was used to calculate the corresponding received power at various implant depths, as well as the transfer efficiency. The frequency that maximizes the received power and the transfer efficiency is then found.

In Chapter 7, we have presented several recipes for liquid biomedical phantoms, consisting of deionized water, sugar, salt, and gelling agents like gelatin or agar. The relative permittivity ε_r' and conductivity σ have been measured, and their variation over time and shelf-live have been assessed. The measured dielectric properties were compared to reference data of biological tissue. Additionally, a low-cost permittivity probe has been constructed, and its performance is compared to a commercial off-the-shelf (COTS) permittivity probe.

Finally, we have measured the relative permittivity ε_r' and conductivity σ of various slabs made of COTS 3D printing filaments, the results of which are given in Chapter 8. These were compared to the dielectric properties of human tissue. Regular filaments were measured, as well as filaments with added carbon, metal, and stone particles.

The conclusions for the topics mentioned above will be described in the next sections. Recommendations based on our work will be given in Section 9.4.

9.1 Hardware development for wireless power transfer to implantable medical devices

The designed WPT system can transcutaneously transfer 80 mW at 7 V to a biomedical brain implant at 6.78 MHz. The link efficiency is 86 to 95%, depending on the coil alignment. The transfer efficiency, including the efficiency of the inverter and rectifier, is between 52 and 68%. The end-to-end efficiency, taking into account also the oscillator and gate driver, is 39 to 57%. The WPT system is compared to related literature in Table 9.1. Compared to the related work, our design is the only one that operates at a frequency permitted for WPT, transfers at least 80 mW, presents the end-to-end efficiency, is validated in a realistic environment, and complies with the relevant safety regulations.

Circuit simulations were performed in LTspice. There is a mismatch of up to 17% in output voltage between the simulations and the measurements. However, the results do exhibit similar trends, regarding the transferred power versus coupling factor k. When the results are shifted by $\Delta k = 0.053$, the difference drops to 4%. In this case, the difference in input current is at most 8%. This shift of $\Delta k = 0.053$ is believed to be caused by inaccuracies in the spice models for the MOSFET, which operates at only 4% of its rated voltage and current, and by the fact that the self-resonance frequencies (SRFs) of the coils are close to the frequency of operation. The presented design procedure can be used for other applications as well, both medical and other.

EM and thermal simulations were performed in Simulia CST Studio Suite®. The system complies with IEEE Std C95.1, ICNIRP, ETSI EN 303 417, EN-45502-1, and ISO 14708-3 standards for distances between the coils of $8 \leq h \leq 15$ mm, and misalignment from $0 \leq d \leq 15$ mm. The system designed for the case study is thus suitable for WPT to the visual prosthesis in the NESTOR project.

In designing such a system, the total efficiency needs to be optimized, not just the link efficiency. The presented design procedure and prototype were designed to maximize the transfer efficiency, including the inverter and the rectifier, rather than maximizing the efficiency of the individual sub-systems separately. Misalignment tolerance should be part of the

Table 9.1: Comparison of the WPT system presented in this thesis with systems published in literature.

Ref.	f [MHz]	P_{rx} [mW]	Link η [%]	Transfer η [%]	End-to-end η [%]	h [mm]	Env.	SAR
[10]	6.785	$1-10$		$51-74$		$1-10$	Saline	
[22]	0.7	50	51	36		30	Air	
[99]	1	100		≤ 66		$5-10$	Rat	HFSS + meas.
[101]	13.56	100	$33-85$		≤ 66	$5-15$	Air	
[114]	1	250			$51-67$	$2-15$	Air	
[135]	10	24			$35-42$	$4-8$	Air	
[169]	$6.5-7.5$	115	≤ 89		≤ 53	$5-8$	Phantom + Pork	
[211]	39.86	115	47			10	Pork	HFSS
[230]	1	$40-250$		$33-66$		$7-15$	Air	
This work	6.78	80	$86-95$	$52-68$	$39-57$	$8-15$	Phantom	CST

design. This was found to affect the compliance with the relevant (medical) standards, e.g. a system that meets the SAR limit for perfect alignment, might not meet it when misalignment is introduced.

9.2 Electromagnetic field modeling in layered media

The two-layer model from Chapter 4 was validated for frequencies ranging from 13 MHz to 5 GHz, with a simulation domain of $r \leq 50$ mm, and $-70 \leq z \leq 70$ mm, with a spatial resolution of 1 mm. The relative differences between the EM fields calculated by the analytical model and those calculated by Simulia CST Studio Suite® are small, i.e. below 8% on average.

The multi-layer model from Chapter 5 was validated for 9 frequencies ranging from 100 kHz to 5 GHz, with a simulation domain of r, $|x|$, $|y| \leq 50$ mm, and $-100 \leq z \leq 70$ mm, with a spatial resolution of 1 mm. It was verified for up to 4 layers, as reference CST data could not be generated with sufficient accuracy for more layers. The relative differences between the EM fields calculated by the analytical model and those calculated by Simulia CST Studio Suite® are small, i.e. below 9% (worst case) for all vertically oriented magnetic point dipole (VMD) cases and almost all horizontally oriented magnetic point dipole (HMD) cases discussed, and is typically below 4%. We consider this accurate enough to regard the model as a useful design tool in the design process of WPT systems in multilayered (biomedical) environments. There are a few exceptions where the relative difference for the HMD is larger than 9%, but these cases can almost all be explained by imperfections in the commercial software.

The analytical models run in tens to hundreds of seconds, which is up to 800 times faster than the corresponding CST simulations, and use up to 70 times less memory. The models can easily run on a standard office personal computer (PC), whereas this is certainly not the case for commercial solvers for the setups tested here. The execution time can be further reduced by using multiple processors. The speedup of our models scales approximately linearly with the number of processors.

The presented analytical models for EM field propagation in planarly layered media are dedicated for very specific cases, they can be used to get quick insight in for example the expected field distribution and received power levels at certain locations of interest. Results can be generated in a few minutes, which is generally much faster than commercial full-wave EM solvers can, which are designed to solve general EM problems. The models can be used stand-alone, or as a preliminary tool for rapid design iteration, speeding up the initial iterations of the design process. Furthermore, they can be used to answer fundamental questions, like determining the optimal frequency for WPT to implantable medical devices (IMDs).

A major advantage of our models is that they can be implemented in almost any standard programming language. The models are also applicable in other areas of engineering, such as geophysical engineering, as long as the environment is (approximately) planarly layered.

Optimal frequency for biomedical wireless power transfer

The difference between the SAR calculated by the analytical model and CST is below 25%, which is small enough to not influence the conclusions drawn in this section. The differences are believed to be at least partially caused by imperfections in the SAR calculation in CST.

Two cases were considered: a 4 layer air–skin–fat–muscle case, and a 7 layer case consisting of the layers air–skin–fat–bone–cerebro-spinal fluid (CSF)–grey matter–white matter, representing WPT to an IMD located inside the brain. The received power and transfer efficiency were calculated for frequencies ranging from 10 kHz to 10 GHz. For both cases, the highest received power is found at 10 kHz, the lowest frequency investigated. Additionally, for all frequencies in the range from 10 kHz to 300 kHz, the performance is similar; the performance decrease is less than 4% compared to the one at 10 kHz. This is true for implant depths up to 150 mm, after which the level of received power is too low for practical applications. The amount of power that can be transferred to a mm-sized receiver located several cm deep inside the human body is sufficient for various practical applications. The difference between the 4 and 7 layer cases is less than a factor 2 for the full frequency range, suggesting that the optimal frequency for maximum power on the load (MPL) does not depend heavily on the chosen biological environment.

The transfer efficiency is highest at 10 kHz, and is again approximately constant for frequencies up to 300 kHz. It should be noted that, at increased depth in the tissue, the efficiency around 1 GHz approaches the efficiency at 10 kHz.

The presented analytical model can be used to calculate the SAR, received power, and power transfer efficiency of WPT to a mm-sized receiver located several cm deep inside the human body. Additionally, the model is also applicable in other areas of engineering, such as sensors embedded in soil or floating freely in liquid, as long as the environment is (approximately) planarly layered. This data can be used to determine the optimal frequency for maximum received power and power transfer efficiency.

9.3 Realistic environments for biomedical electromagnetic experiments

We have shown that it is possible to create both liquid and solid materials with relative permittivity ε_r and conductivity σ close to those of actual biological tissues, for frequencies ranging from UHF to microwaves, using commonly available and non-toxic ingredients. The liquid phantoms are ready to be used in biomedical experiments, whereas more research is needed to make the solid phantoms usable.

The liquid phantoms consist of deionized water, sugar, salt, and gelling agents like gelatin or agar. Increasing the sugar concentration decreases the permittivity and has little effect on the conductivity. Alternatively, increasing the salt concentration increases the conductivity, and has little effect on the permittivity. By adding gelatin, the fluid can be made jelly-like, adding agar makes the solution solid. Even without adding preservatives, all samples made for this research maintained the dielectric characteristics for at least ten days when stored at room temperature in a sealed container.

The presented data can be interpolated and extrapolated to obtain the concentrations of sugar and salt required for creating a tissue simulating liquid (TSL) with specific dielectric properties. The dielectric properties match the biological data for a limited frequency band, hence the recipe needs to be tailored to the frequency of operation. The band in which the dielectric properties match (within 5%) is limited to a few hundred MHz, depending on the frequency and the tissue that is being mimicked.

Additionally, a DIY permittivity probe was constructed from a piece of RG405 semi-rigid coaxial cable. The maximum absolute error relative to a using a COTS probe and software is less than 2.0 for ε_r', and less than 0.14 S/m for σ, for frequencies ranging from 300 MHz to 3 GHz. Using only basic mechanical tools, a permittivity measurement probe can be constructed for a fraction of the price of a COTS system. The accuracy of the probe is adequate for the validation of liquid body mimicking phantoms.

The dielectric properties of various COTS 3D printing materials were measured, and compared to those of cortical bone, fat, and red and yellow bone marrow. Standard materials were measured, as well as materials with added metal, carbon, and stone particles. The relative permittivity ε_r' of the metal and carbon filled samples matches the biological reference data for small frequency bands. The measured σ is too low for all materials and frequencies, except for yellow bone marrow from 800 to 4100 MHz.

3D printed structures can be used to make molds that can be filled with a solidifying TSL, in order to increase the level of detail in biomedical phantoms. More research is needed into filaments that have dielectric properties similar to those of human tissue, or other ways of increasing the conductivity of 3D printed structures. These can then be used to add teeth and bone structures to phantoms, for example.

9.4 Recommendations

9.4.1 Hardware development for wireless power transfer to implantable medical devices

The WPT link has been tested as a stand alone system, but the final product will contain much more electronics, such as wireless data transfer systems, data processing, and interfacing of the electrodes. It should be verified that the WPT system does not affect the performance of the other electronics, and vice versa.

The MOSFET operates at about 4% of its rated current and voltage. Future work can benefit from the development of spice models that are more accurate at the relatively low power levels under consideration.

The MOSFET was selected to be a gallium nitride (GaN) type, which is particularly suited for switching at MHz frequencies. It was selected for its low gate capacitance. The GaN MOSFETs available on the market today are generally designed for use with voltages over 100 V and currents of several A. It should be investigated whether a less powerful MOSFET can be used resulting in a similar or better efficiency, but with better resemblance between the simulations and measurements.

No research was performed to improve the oscillator and gate driver. It should be investigated whether more energy efficient components can be found, without compromising the performance of the WPT link. Additionally, the optimal number of NOT-gates should be determined, especially when a less powerful MOSFET is used, as discussed before.

Furthermore, the behavior of the feed inductor L_f should be more accurately represented in the circuit simulation, for this specific application, where the current flowing through it is a combination of DC, saturating the core, and AC, the frequency of which is sufficiently close to the self-resonance frequency (SRF) of the inductor to influence its inductance.

Additionally, it is assumed in this work that the self and mutual inductance (and thus the coupling factor) between two coils, one of which is submerged in a saline solution, the other one in the vicinity of the saline solution, can be considered the same as two coils in free space. It should be verified whether this is indeed the case.

Finally, it should be investigated whether it is possible to add data transfer to the designed WPT link, without compromising the WPT efficiency too much.

9.4.2 Electromagnetic field modeling in layered media

The presented analytical models are able to generate results significantly faster than commercial solvers. Additional speedup can be achieved by using a coarser spatial resolution in r, x, y, and/or z. Furthermore, one can choose to not calculate the fields in air (layer 0), when only the fields inside the tissue are of interest. Using these techniques, an additional speedup of over 10 times can easily be achieved, with a similar reduction in required memory.

The analytical models were validated for frequencies up to 5 GHz. For higher frequencies, we were unable to generate reliable reference data in Simulia CST Studio Suite®. We have shown that biomedical WPT applications at frequencies above roughly 2 GHz are highly inefficient, which justifies the upper frequency limit of 5 GHz in this case. However, there are certainly applications that could benefit from the analytical calculation of EM fields at higher frequencies, for example 5G/6G, satellite communication, and various radar applications that operate at frequencies of several tens to over one hundred GHz. Validating the analytical models at these frequencies will expand their range of applicability.

The range of applicability can be expanded even further when the analytical models are also validated for the electric point dipole (EPD), such that for example dipole and patch antennas can also be modeled. The equations for the EPD are variations of those used in the MPD models.

In this thesis, Simulia CST Studio Suite® is used as the ground truth in terms of generated EM fields. Several limitations of CST have been observed and discussed. However, as the differences between the analytical models and CST are small for a wide range of frequencies and model parameters, we have no direct reason to doubt the validation procedure. Nonetheless, it should be investigated how accurate the EM fields generated by Simulia CST Studio Suite® are. Therefore, they should be compared to those calculated by additional EM field solver packages, such as COMSOL Multiphysics®, IMST EMPIRE XPU, Sim4Life, Ansys HFSS, or Altair® Feko®.

It should be possible to model realistic sources with MPDs using the superposition principle, requiring only a small increase in computational cost. A realistic source can be spanned by MPDs, the fields of which only have to be calculated once, and can be translated consequently. A workflow for this superposition should be devised and verified. Additionally, in the presented models, it is assumed that the receiver has no influence on the transmitter, i.e. the coupling factor is negligible. For coupled coils in inductive WPT, this is not realistic. It should be investigated if and how this influence can be incorporated in the models.

In Chapter 6, the receiver (Rx) coil is located on the z-axis, directly underneath the source, where the magnetic field strength H_z is highest. It should be verified whether this is indeed the best location to achieve MPL, whilst complying to the SAR limit. In particular, it should be verified whether a combination of the VMD and HMD, representing a source at a certain angle, yields better performance. Additionally, future research could focus on combining multiple sources, spread out over a certain area. This spreads the SAR over a larger volume, thus the combined transmit power can be increased. The sources should be positioned and controlled such that the energy is focused at the Rx coil deep inside the tissue.

Besides biomedical WPT, there are many more possible applications for the presented analytical model, as outlined in Section 6.6. As the dielectric properties of the layers are different in these environments, the optimal frequency for maximum power on the load (MPL) and maximum power transfer efficiency (MPTE) will likely change. In biological tissue, the conductivity σ increases rapidly above a few hundred MHz, depending on the tissue [68, 82]. When the model is used with materials that have a conductivity that increases less with frequency, it might be the case that the optimal frequency is actually in the GHz range [175].

9.4.3 Realistic environments for biomedical EM experiments

The dielectric properties of the presented recipes for liquid phantoms should be measured for a broader frequency range, to increase the range of applicability of the tissue simulating liquids (TSLs). Furthermore, measurements should be performed on the dielectric properties of additional COTS liquids and solutions, preferably consisting of non-toxic ingredients that can be bought in regular shops. Also, general equations should be devised, that predict the dielectric properties of any solution of sugar and salt in deionized water, at any frequency of interest.

Regarding 3D printed phantoms, the market should be regularly monitored for new types of COTS 3D printing filament. Especially types with special additions, such as metal or carbon, could be useful in the creation of solid biomedical phantoms with realistic dielectric properties.

In this thesis, all 3D printed objects were printed completely solid, i.e. with an infill of 100%. The data presented in [17, 144] suggest that the infill of a 3D printed object affects the effective ε_r'. In particular, the relationship appears to be linear, and can be represented by Eq. (8.2). More research is needed to determine whether that is indeed applicable to the general case, or that a different relation is valid, for example one of the mixing equations discussed in [110, 134]. It should also be investigated whether this relationship also holds for the conductivity σ, like data from [17, 110, 134, 144] suggests.

The resulting phantom will not be homogeneous, as the volume will be part filament, part air. More research is needed into how this affects the effective dielectric parameters, and which infill patterns yields optimal performance in terms of homogeneity and isotropy of the dielectric properties. Furthermore, it should be investigated how the effective dielectric parameters are affected when the volume in between the infill pattern is filled with water or a TSL, rather than with air.

A dual or triple extruder can be used to manufacture heterogeneous phantoms consisting of different materials, such as a bone with bone marrow inside, or a skull with cortical and spongy bone, to increase the level of detail even further [243]. Alternatively, a phantom can be printed with multiple materials alternately, effectively mixing their dielectric properties.

List of Publications

Journal publications

[P1] **Tom van Nunen**, Rob Mestrom, Hubregt Visser, "Wireless Power Transfer to Biomedical Implants using a Class-E inverter and a Class-DE rectifier," in *IEEE Journal of Electromagnetics, RF and Microwaves in Medicine and Biology (J-ERM)*, Submitted.

[P2] **Tom van Nunen**, Rob Mestrom, Hubregt Visser, "Electromagnetic Field Calculation for Biomedical Wireless Power Transfer in Multilayer Applications," in *IEEE Transactions on Antennas and Propagation*, Submitted.

Conference publications

[P3] **Tom van Nunen**, Esmee Huismans, Rob Mestrom, Mark Bentum, Hubregt Visser, "DIY Electromagnetic Phantoms for Biomedical Wireless Power Transfer Experiments," *IEEE Wireless Power Transfer Conference (WPTC)*, London, 2019, pp. 399-404.

[P4] **Tom van Nunen**, Rob Mestrom, Mark Bentum, Hubregt Visser, "Electromagnetic Field Modeling for Wireless Power Transfer in Biological Tissue," *14^{th} European Conference on Antennas and Propagation (EuCAP)*, Copenhagen, 2020.

[P5] **Tom van Nunen**, Rob Mestrom, Hubregt Visser, "Wireless Power Transfer to a Visual Prosthesis: 100 mW at 6.78 MHz," *IEEE International Symposium on Antennas and Propagation (AP-S)*, Singapore, 2021, pp. 269-270.

[P6] **Tom van Nunen**, Steven Beumer, Rob Mestrom, Hubregt Visser, "Characterization of Dielectric Properties of 3D-printing Materials for Solid Biomedical Phantoms," *IEEE Asia-Pacific Microwave Conference (APMC)*, Yokohama, 2022.

Bibliography

[1] 123-3D. *123-3D Filament carbon 2,85 mm PETG 0,5 kg (Jupiter serie)*. URL: www.123-3d.nl/123-3D-Filament-carbon-2-85-mm-PETG-0-5-kg-Jupiter-serie-i1535-t9717.html.

[2] M. Abramowitz and I. A. Stegun. *Handbook of Mathematical Functions with Formulas, Graphs, and Mathematical Tables*. 9th ed. Dover Publications, 1964.

[3] „Accelerating CST MWS Performance with GPU and MPI Computing". In: *CST workshop series*. 2010.

[4] K. Agarwal, R. Jegadeesan, Y. X. Guo, and N. V. Thakor. „Wireless Power Transfer Strategies for Implantable Bioelectronics". In: *IEEE Reviews in Biomedical Engineering* 10 (2017), pp. 136–161. ISSN: 19411189. DOI: 10.1109/RBME.2017.2683520.

[5] H. Akima. „Algorithm 760: Rectangular-Grid-Data Surface Fitting that Has the Accurancy of a Bicubic Polynomial". In: *ACM Trans. Mathematical Software* 22.3 (1996), pp. 357–361.

[6] S. Aldhaher, D. C. Yates, and P. D. Mitcheson. „Modeling and Analysis of Class EF and Class E/F Inverters with Series-Tuned Resonant Networks". In: *IEEE Transactions on Power Electronics* 31.5 (2016), pp. 3415–3430. ISSN: 08858993. DOI: 10.1109/TPEL.2015.2460997.

[7] A. B. Amar, A. B. Kouki, and H. Cao. „Power Approaches for Implantable Medical Devices". In: *Sensors* 15 (2015), pp. 28889–28914. ISSN: 14248220. DOI: 10.3390/s151128889.

[8] L. N. Ayton, N. Barnes, G. Dagnelie, T. Fujikado, et al. „An Update on Retinal Prostheses". In: *Clinical Neurophysiology* 131.6 (2020), pp. 1383–1398. ISSN: 18728952. DOI: 10.1016/j.clinph.2019.11.029.

[9] L. N. Ayton, P. J. Blamey, R. H. Guymer, C. D. Luu, et al. „First-in-human trial of a novel suprachoroidal retinal prosthesis". In: *PLoS ONE* 9.12 (2014), pp. 1–26. ISSN: 19326203. DOI: 10.1371/journal.pone.0115239.

[10] M. W. Baker and R. Sarpeshkar. „Feedback analysis and design of RF power links for low-power bionic systems". In: *IEEE Transactions on Biomedical Circuits and Systems* 1.1 (2007), pp. 28–38. ISSN: 19324545. DOI: 10.1109/TBCAS.2007.893180.

[11] C. A. Balanis. *Antenna Theory: Analysis and Design*. 3rd ed. New York: John Wiley & Sons, Inc., 2005. ISBN: 0-471-66782-X.

[12] A. J. Baños. *Dipole Radiation in the Presence of a Conducting Half-Space*. Ed. by A. Cullen, V. Fock, and J. Wait. 1st ed. Pergamon Press Inc., 1966.

[13] G. L. Barbruni, P. M. Ros, D. Demarchi, S. Carrara, and D. Ghezzi. „Miniaturised Wireless Power Transfer Systems for Neurostimulation: A Review". In: *IEEE Transactions on Biomedical Circuits and Systems* 14.6 (2020), pp. 1160–1178. ISSN: 19409990. DOI: 10.1109/TBCAS.2020.3038599.

[14] J. C. Barrese, N. Rao, K. Paroo, C. Triebwasser, et al. „Failure mode analysis of silicon-based intracortical microelectrode arrays in non-human primates". In: *Journal of Neural Engineering* 10.6 (2013). DOI: 10.1088/1741-2560/10/6/066014.

[15] Y. Baskharoun, A. Trehan, N. K. Nikolova, and M. D. Noseworthy. „Physical phantoms for microwave imaging of the breast". In: *IEEE Topical Conference on Biomedical Wireless Technologies, Networks, and Sensing Systems, BioWireleSS*. IEEE, 2012, pp. 73–76. ISBN: 9781457711541. DOI: 10.1109/BioWireless.2012.6172736.

[16] N. C. Benson, D. Yoon, D. Forenzo, S. A. Engel, J. Winawer, and K. N. Kay. „Surface area and cortical magnification of V1, V2, and V3 in a large sample of human observers". In: *Journal of Vision* 19.10 (2019), 41a. ISSN: 1534-7362. DOI: 10.1167/19.10.41a.

[17] B. Biemacki, S. Zhang, and W. Whittow. „3D Printed Substrates with Graded Dielectric Properties and their Application to Patch Antennas". In: *Loughborough Antennas and Propagation Conference (LAPC)*. Loughborough: IEEE, 2017. ISBN: 9781509007820. DOI: 10.1109/LAPC.2016.7807603.

[18] W. H. Bosking, P. Sun, M. Ozker, X. Pei, et al. „Saturation in phosphene size with increasing current levels delivered to human visual cortex". In: *Journal of Neuroscience* 37.30 (2017), pp. 7188–7197. ISSN: 15292401. DOI: 10.1523/JNEUROSCI.2896-16.2017.

[19] R. R. Bourne, J. D. Steinmetz, S. R. Flaxman, P. S. Briant, et al. „Trends in prevalence of blindness and distance and near vision impairment over 30 years: An analysis for the Global Burden of Disease Study". In: *The Lancet Global Health* 9.2 (2021), e130–e143. ISSN: 2214109X. DOI: 10.1016/S2214-109X(20)30425-3.

[20] A. Büchner and L. Gärtner. „Technische Entwicklungen bei Cochleaimplantaten". In: *HNO* 65.4 (2017), pp. 276–289. ISSN: 0017-6192. DOI: 10.1007/s00106-017-0339-7.

[21] Caelynx. *CST Studio Suite - Electromagnetic Simulation Software*. 2020. URL: https://caelynx.com/product/cst-studio-suite/.

[22] M. Catrysse, B. Hermans, and R. Puers. „An inductive power system with integrated bi-directional data-transmission". In: *Sensors and Actuators, A: Physical* 115.2-3 SPEC. ISS. (2004), pp. 221–229. ISSN: 09244247. DOI: 10.1016/j.sna.2004.02.016.

[23] M. S. Chae, Z. Yang, M. R. Yuce, L. Hoang, and W. Liu. „A 128-channel 6 mW wireless neural recording IC with spike feature extraction and UWB transmitter". In: *IEEE Transactions on Neural Systems and Rehabilitation Engineering* 17.4 (2009), pp. 312–321. ISSN: 15344320. DOI: 10.1109/TNSRE.2009.2021607.

[24] J. Charthad, M. J. Weber, T. C. Chang, and A. Arbabian. „A mm-Sized Implantable Medical Device (IMD) With Ultrasonic Power Transfer and a Hybrid Bi-Directional Data Link". In: *IEEE Journal of Solid-State Circuits* 50.8 (2015), pp. 1741–1753. ISSN: 00189200. DOI: 10.1109/JSSC.2015.2427336.

[25] K. Chen, Z. Yang, L. Hoang, J. D. Weiland, M. S. Humayun, and W. Liu. „An integrated 256-channel epiretinal prosthesis". In: *IEEE Journal of Solid-State Circuits* 45.9 (2010), pp. 1946–1956. ISSN: 00189200. DOI: 10.1109/JSSC.2010.2055371.

[26] X. Chen, F. Wang, E. Fernández, and P. R. Roelfsema. „Shape perception via a high-channel-count neuroprosthesis in monkey visual cortex". In: *Science* 370.6521 (2020), pp. 1191–1196. ISSN: 10959203. DOI: 10.1126/science.abd7435.

[27] C.-K. Chou, G.-W. Chen, A. W. Guy, and K. H. Luk. „Formulas for preparing phantom muscle tissue at various radiofrequencies". In: *Bioelectromagnetics* 5.4 (1984), pp. 435–441. DOI: 10.1002/bem.2250050408.

[28] ColorFabb. *bronzeFill*. URL: https://colorfabb.com/bronzefill (visited on 08/30/2022).

[29] ColorFabb. *copperFill*. URL: https://colorfabb.com/copperfill (visited on 08/30/2022).

[30] ColorFabb. *steelFill*. URL: https://colorfabb.com/steelfill (visited on 08/30/2022).

[31] E. C. Committee. „ERC Recommendation 70-03 Relating to the use of Short Range Devices (SRD)". In: (2021).

[32] A. Costanzo, M. Dionigi, F. Mastri, M. Mongiardo, et al. „Conditions for a Load-Independent Operating Regime in Resonant Inductive WPT". In: *IEEE Transactions on Microwave Theory and Techniques* 65.4 (2017), pp. 1066–1076. ISSN: 00189480. DOI: 10.1109/TMTT.2017.2669987.

[33] J. Coulombe, M. Sawan, and J. F. Gervais. „A Highly Flexible System for Microstimulation of the Visual Cortex: Design and Implementation". In: *IEEE Transactions on Biomedical Circuits and Systems* 1.4 (2007), pp. 258–269. ISSN: 19324545. DOI: 10.1109/TBCAS.2007.916026.

[34] S. C. Cripps. *RF Power Amplifiers for Wireless Communications*. Vol. 40. 6. 2006, p. 456. ISBN: 9781596930186. DOI: 10.1002/1521-3773(20010316)40:6⟨9823::AID-ANIE9823⟩3.3.CO;2-C. arXiv: arXiv:1011.1669v3.

[35] *CST Studio Suite*. 2022. URL: www.3ds.com/products-services/simulia/products/cst-studio-suite/.

[36] „CST Studio Suite: High Performance Computing Techniques". In: *CST information leaflet*. 2012. DOI: 10.1080/10618562.2020.1833151.

[37] *DAK-TL2 SPEAG, Schmid & Partner Engineering AG*. URL: https://speag.swiss/products/dak/dak-tl-2/.

[38] A. A. Danilov, E. A. Mindubaev, R. R. Aubakirov, K. O. Gurov, O. Surkov, and S. V. Selishchev. „Strategy for Design of Misalignment Tolerant Inductive Powering System for Medical Implants". In: *IEEE PELS Workshop on Emerging Technologies: Wireless Power Transfer (WoW)*. London: IEEE, 2019, pp. 111–115. ISBN: 9781538675144. DOI: 10.1109/WoW45936.2019.9030623.

[39] R. Das, F. Moradi, and H. Heidari. „Biointegrated and Wirelessly Powered Implantable Brain Devices: A Review". In: *IEEE Transactions on Biomedical Circuits and Systems* 14.2 (2020), pp. 343–358. ISSN: 19409990. DOI: 10.1109/TBCAS.2020.2966920.

[40] J. de Ruyter van Steveninck, T. van Gestel, P. Koenders, G. van der Ham, et al. „Real-world indoor mobility with simulated prosthetic vision: The benefits and feasibility of contour-based scene simplification at different phosphene resolutions". In: *Journal of Vision* 22.2 (2022), pp. 1–14. ISSN: 15347362. DOI: 10.1167/JOV.22.2.1.

[41] W. F. DeForge. „Cardiac pacemakers: a basic review of the history and current technology". In: *Journal of Veterinary Cardiology* 22 (2019), pp. 40–50. ISSN: 18750834. DOI: 10.1016/j.jvc.2019.01.001.

[42] S. Di Meo, E. Massoni, L. Silvestri, J. Obbad, et al. „Dielectric characterization of material for 3D-printed breast phantoms up to 50 GHz: Preliminary experimental results". In: *International Microwave Workshop Series on Advanced Materials and Processes for RF and THz Applications (IMWS-AMP)*. IEEE, 2017. ISBN: 9781538604809. DOI: 10.1109/IMWS-AMP.2017.8247371.

[43] K. Ding, Y. Yu, and H. Lin. „Wireless Midfield Scheme for Power Transfer and Bidirectional Data Transmission for Capsule Endoscopy". In: *IEEE International Conference on Communication Technology (ICCT)*. 2015, pp. 522–524.

[44] M. Dionigi, M. Mongiardo, and R. Perfetti. „Regorous Network and Full-Wave Electromagnetic Modeling of Wireless Power Transfer Links". In: *IEEE Transactions on Microwave Theory and Techniques* 63.1 (2015), pp. 65–75. ISSN: 00189480. DOI: 10.1109/TMTT.2014.2376555.

[45] W. H. Dobelle, M. G. Mladejovsky, J. R. Evans, T. S. Roberts, and J. P. Girvin. „Braille reading by a blind volunteer by visual cortex stimulation". In: *Nature* 259.5539 (1976), pp. 111–112. ISSN: 00280836. DOI: 10.1038/259111a0.

[46] W. H. Dobelle, M. G. Mladejovsky, and J. P. Girvin. „Artificial Vision for the Blind: Electrical Stimulation of Visual Cortex Offers Hope for a Functional Prosthesis". In: *Science* 183.4123 (1974), pp. 440–444. DOI: 10.1126/science.183.4123.440.

[47] M. Donohoe, S. Balasubramaniam, B. Jennings, and J. M. Jornet. „Powering In-Body Nanosensors With Ultrasounds". In: *IEEE Transactions on Nanotechnology* 15.2 (2016), pp. 151–154. ISSN: 1536125X. DOI: 10.1109/TNANO.2015.2509029.

[48] J. Dowling. „Current and future prospects for optoelectronic retinal prostheses". In: *Eye* 23.10 (2009), pp. 1999–2005. ISSN: 0950-222X. DOI: 10.1038/eye.2008.385.

[49] J. Dragas, V. Viswam, A. Shadmani, Y. Chen, et al. „In Vitro Multi-Functional Microelectrode Array Featuring 59 760 Electrodes, 2048 Electrophysiology Channels, Stimulation, Impedance Measurement, and Neurotransmitter Detection Channels". In: *IEEE Journal of Solid-State Circuits* 52.6 (2017), pp. 1576–1590. ISSN: 00189200. DOI: 10.1109/JSSC.2017.2686580.

[50] „Durable miniaturized bioelectronics". In: *Nature Biomedical Engineering* 1.3 (2017), p. 2017. ISSN: 2157846X. DOI: 10.1038/s41551-017-0053.

[51] K. A. Eckert, M. J. Carter, V. C. Lansingh, D. A. Wilson, et al. „A Simple Method for Estimating the Economic Cost of Productivity Loss Due to Blindness and Moderate to Severe Visual Impairment". In: *Ophthalmic Epidemiology* 22.5 (2015), pp. 349–355. ISSN: 17445086. DOI: 10.3109/09286586.2015.1066394.

[52] *EN-45502-1:2015 — Implants for surgery - Active implantable medical devices; European Standard.*

[53] R. Erfani, F. Marefat, A. M. Sodagar, and P. Mohseni. „Transcutaneous capacitive wireless power transfer (C-WPT) for biomedical implants". In: *Proceedings - IEEE International Symposium on Circuits and Systems* (2017), pp. 4–7. ISSN: 02714310. DOI: 10.1109/ISCAS.2017.8050940.

[54] M. Etemadrezaei. „Wireless Power Transfer". In: *Power Electronics Handbook*. Ed. by M. H. Rashid. 4th ed. Elsevier Inc., 2018. Chap. 22, pp. 711–722. ISBN: 9780128114070. DOI: 10.1016/B978-0-12-811407-0.00024-6.

[55] ETSI. *ETSI EN 303 417 V1.1.1 (2017-09) Wireless Power Transmission Systems; Harmonised European Standard.*

[56] ETSI. *ETSI TR 103 493 - V1.1.1 (2019-02) - System Reference document (SRdoc); Wireless Power Transmission (WPT) systems operating below 30 MHz; Technical Report.*

[57] J. M. Felício, C. A. Fernandes, and J. R. Costa. „Complex permittivity and anisotropy measurement of 3D-printed PLA at microwaves and millimeter-waves". In: *International Conference on Applied Electromagnetics and Communications (ICECom)*. Dubrovnik: IEEE, 2016. ISBN: 9789536037728. DOI: 10.1109/ICECom.2016.7843900.

[58] A. D. Flaxman, J. S. Wittenborn, T. Robalik, R. Gulia, et al. „Prevalence of Visual Acuity Loss or Blindness in the US: A Bayesian Meta-analysis". In: *JAMA Ophthalmology* 139.7 (2021), pp. 717–723. ISSN: 21686173. DOI: 10.1001/jamaophthalmol.2021.0527.

[59] S. R. Flaxman, R. R. Bourne, S. Resnikoff, P. Ackland, et al. „Global Causes of Blindness and Distance Vision Impairment 1990–2020: a Systematic Review and Meta-Analysis". In: *The Lancet Global Health* 5.12 (2017), e1221–e1234. ISSN: 2214109X. DOI: 10.1016/S2214-109X(17)30393-5.

[60] FormFutura 3D printing Materials. *AppoloX*. URL: www.formfutura.com/shop/product/apollox-2779?category=453 (visited on 08/30/2022).

[61] FormFutura 3D printing Materials. *StoneFil*. URL: www.formfutura.com/shop/product/stonefil-2842?category=465.

[62] K. Fotopoulou and B. W. Flynn. „Wireless power transfer in loosely coupled links: Coil misalignment model". In: *IEEE Transactions on Magnetics* 47.2 (2011), pp. 416–430. ISSN: 00189464. DOI: 10.1109/TMAG.2010.2093534.

[63] J. G. Fraser. „Cochlear Implants: Current Status and Future Directions". In: *IEE Colloquium on Cochlear Implants in the UK*. London: IET, 1991, pp. 55–56.

[64] D. K. Freeman and S. J. Byrnes. „Optimal Frequency for Wireless Power Transmission Into the Body: Efficiency Versus Received Power". In: *IEEE Transactions on Antennas and Propagation* 67.6 (2019), pp. 4073–4083. ISSN: 0018-926X. DOI: 10.1109/TAP.2019.2905672.

[65] K. Fukui and H. Koizumi. „Analysis of half-wave class DE low dv/dt rectifier at any duty ratio". In: *IEEE Transactions on Power Electronics* 29.1 (2014), pp. 234–245. ISSN: 08858993. DOI: 10.1109/TPEL.2013.2252367.

[66] K. Fukui and H. Koizumi. „Half-wave Class DE Low dv/dt rectifier". In: *IEEE Asia-Pacific Conference on Circuits and Systems (APCCAS)* 1 (2012), pp. 69–72. DOI: 10.1109/APCCAS.2012.6418973.

[67] S. Gabriel, R. W. Lau, and C. Gabriel. „The dielectric properties of biological tissues: II. Measurements in the frequency range 10 Hz to 20 GHz". In: *Physics in Medicine and Biology* 41.11 (1996), pp. 2251–2269. ISSN: 00319155. DOI: 10.1088/0031-9155/41/11/002.

[68] S. Gabriel, R. W. Lau, and C. Gabriel. „The dielectric properties of biological tissues: III. Parametric models for the dielectric spectrum of tissues". In: *Phys. Med. Biol* 41 (1996), pp. 2271–2293.

[69] D. H. Gadani, V. A. Rana, S. P. Bhatnagar, A. N. Prajapati, and A. D. Vyas. *Effect of salinity on the dielectric properties of water*. Tech. rep. 1. 2012, pp. 104–111.

[70] J. D. Garrett. „Average Dielectric Property Analysis of Non-Uniform Structures: Tissue Phantom Development, Ultra-Wideband Transmission Measurements, and Signal Processing Techniques". Master thesis. University of Calgary, 2014. DOI: 10.11575/PRISM/25086.

[71] J. Gemio, J. Parrón, and J. Soler. „Human body effects on implantable antennas for ism bands applications: Models comparison and propagation losses study". In: *Progress in Electromagnetics Research* 110.January 2010 (2010), pp. 437–452. ISSN: 15598985. DOI: 10.2528/PIER10102604.

[72] M. H. Ghaed, G. Chen, R. U. Haque, M. Wieckowski, et al. „Circuits for a cubic-millimeter energy-autonomous wireless intraocular pressure monitor". In: *IEEE Transactions on Circuits and Systems I: Regular Papers* 60.12 (2013), pp. 3152–3162. ISSN: 15498328. DOI: 10.1109/TCSI.2013.2265973.

[73] C. Gilbert, R. Bowman, and A. N. Malik. „The epidemiology of blindness in children: changing priorities". In: *Community Eye Health Journal* 30.100 (2017), pp. 74–77. ISSN: ISSN 0950-222X.

[74] D. Goswami, D. Saha, A. Saha, R. Ganguly, and A. Chakraborty. „A brief review of deep brain stimulation for treatment of neurological diseases". In: *International Conference and Workshop on Computing and Communication, IEMCON*. IEEE, 2015. ISBN: 9781479969081. DOI: 10.1109/IEMCON.2015.7344513.

[75] K. Goto, T. Nakagawa, O. Nakamura, and S. Kawata. „An implantable power supply with an optically rechargeable lithium battery". In: *IEEE Transactions on Biomedical Engineering* 48.7 (2001), pp. 830–833. ISSN: 00189294. DOI: 10.1109/10.930908.

[76] G. Green. „An Essay on the Application of mathematical Analysis to the theories of Electricity and Magnetism". In: *Journal fur die Reine und Angewandte Mathematik* 1852.44 (1852), pp. 356–374. ISSN: 14355345. DOI: 10.1515/crll.1852.44.356. arXiv: 0807.0088.

[77] Grepow. *Ultra Thin Battery*. URL: www.grepow.com/page/ultra-thin-battery.html (visited on 08/30/2022).

[78] S. A. P. Haddad, R. P. M. Houben, and W. A. Serdijn. „The Evolution of Pacemakers". In: *IEEE Engineering in Medicine and Biology Magazine* 25.3 (2006), pp. 38–48. ISSN: 0739-5175. DOI: 10.1109/MEMB.2006.1636350.

[79] P. S. Hall and Y. Hao. *Antennas and Propagation for Body-centric Wireless Communications*. 2nd ed. Norwood: Artech House, 2012, pp. 17–28. ISBN: 978-1-60807-376-4.

[80] D. C. Hamill. „Class DE inverters and rectifiers for DC-DC conversion". In: *PESC Record - IEEE Annual Power Electronics Specialists Conference* 1 (1996), pp. 854–860. ISSN: 02759306. DOI: 10.1109/PESC.1996.548681.

[81] G. Hartsgrove, A. Kraszewski, and A. Surowiec. „Simulated biological materials for electromagnetic radiation absorption studies". In: *Bioelectromagnetics* 8.1 (1987), pp. 29–36. ISSN: 1521186X. DOI: 10.1002/bem.2250080105.

[82] P. Hasgall, E. Neufeld, M. Gosselin, A. Klingenböck, and N. Kusten. *IT'IS Database for thermal and electromagnetic parameters of biological tissues*. 2013. URL: www.itis.ethz.ch/virtual-population/tissue-properties/database/.

[83] B. Hattenhorst, M. Mallach, C. Baer, T. Musch, J. Barowski, and I. Rolfes. „Dielectric Phantom Materials for Broadband Biomedical Applications". In: *International Microwave Bio Conference (IMBioC)*. IEEE, 2017. ISBN: 9781538617137. DOI: 10.1109/IMBIOC.2017.7965802.

[84] T. J. Heesterbeek, H. P. van der Aa, G. H. van Rens, J. W. Twisk, and R. M. van Nispen. „The incidence and predictors of depressive and anxiety symptoms in older adults with vision impairment: a longitudinal prospective cohort study". In: *Ophthalmic and Physiological Optics* 37.4 (2017), pp. 385–398. ISSN: 14751313. DOI: 10.1111/opo.12388.

[85] J. S. Ho, S. Kim, and A. S. Y. Poon. „Midfield Wireless Powering for Implantable Systems". In: *Proceedings of the IEEE* 101.6 (2013), pp. 1369–1378.

[86] J. S. Ho and A. S. Poon. „Energy transfer for implantable electronics in the electromagnetic midfield". In: *Progress in Electromagnetics Research* 148.July (2014), pp. 151–158. ISSN: 15598985. DOI: 10.2528/PIER14070603.

[87] J. S. Ho, A. J. Yeh, S. Kim, and A. S. Y. Poon. „Wireless Powering for Miniature Implantable Systems". In: *Neural Computation, Neural Devices, and Neural Prosthesis*. Ed. by Z. Yang. Springer, 2014. Chap. 13, pp. 313–334. ISBN: 9781461481515. DOI: 10.1007/978-1-4614-8151-5_13. arXiv: arXiv:1011.1669v3.

[88] J. S. Ho, A. J. Yeh, E. Neofytou, S. Kim, et al. „Wireless Power Transfer to Deep-Tissue Microimplants." In: *Proceedings of the National Academy of Sciences of the United States of America* 111.22 (2014), pp. 7974–9. ISSN: 1091-6490. DOI: 10.1073/pnas.1403002111.

[89] H. Hori, G. Moretti, A. Rebora, and F. Crovato. „The Thickness of Human Scalp: Normal and Bald". In: *Journal of Investigative Dermatology* 58.6 (1972), pp. 396–399.

[90] F. J. Huang, C. M. Lee, C. L. Chang, L. K. Chen, T. C. Yo, and C. H. Luo. „Rectenna application of miniaturized implantable antenna design for triple-band biotelemetry communication". In: *IEEE Transactions on Antennas and Propagation* 59.7 (2011), pp. 2646–2653. DOI: 10.1109/TAP.2011.2152317.

[91] *IEC 60601-1 - Medical electrical equipment - Part 1: General requirements for basic safety and essential performance*. 2005.

[92] „IEC/IEEE Std 62704.1™-2017 'Determining the peak spatial-average specific absorption rate (SAR) in the human body from wireless communications devices, 30 MHz to 6 GHz - Part 1: General requirements for using the finite-difference time-domain (FDTD) metho". In: *IEEE* (2017). DOI: 10.1109/IEEESTD.2017.8088404.

[93] T. Inaba, H. Koizumi, and H. Sekiya. „Design of Wireless Power Transfer System with Class E Inverter and Half-Bridge Class DE Rectifier at Any Fixed Coupling Coefficient". In: *International Future Energy Electronics Conference and ECCE Asia, IFEEC - ECCE Asia* 1.d (2017), pp. 185–189. DOI: 10.1109/IFEEC.2017.7992440.

[94] Integer. *Implantable Batteries*. URL: www.integer.net/products/implantable-batteries/default.aspx (visited on 08/30/2022).

[95] *ISO 14708-3:2008 Implants for surgery — Active implantable medical devices — Part 3: Implantable neurostimulators*. 2008.

[96] K. Ito, K. Furuya, Y. Okano, and L. Hamada. „Development and characteristics of a biological tissue-equivalent phantom for microwaves". In: *Electronics and Communications in Japan, Part I: Communications (English translation of Denshi Tsushin Gakkai Ronbunshi)* 84.4 (2001), pp. 67–77. DOI: 10.1002/1520-6424(200104)84:4⟨67::AID-ECJA8⟩3.0.CO;2-D.

[97] D. R. Jackson and N. G. Alexópoulos. „An Asymptotic Extraction Technique for Evaluating Sommerfeld-Type Integrals". In: *IEEE Transactions on Antennas and Propagation* AP-34.8610053 (1986), pp. 24–25.

[98] R. Jegadeesan, K. Agarwal, Y. X. Guo, S.-C. Yen, and N. V. Thakor. „Wireless Power Delivery to Flexible Subcutaneous Implants Using Capacitive Coupling". In: *IEEE Transactions on Microwave Theory and Techniques* 65.1 (2017), pp. 280–292. DOI: 10.1109/TMTT.2016.2615623.

[99] R. Jegadeesan, S. Nag, K. Agarwal, N. V. Thakor, and Y. X. Guo. „Enabling Wireless Powering and Telemetry for Peripheral Nerve Implants". In: *IEEE Journal of Biomedical and Health Informatics* 19.3 (2015). DOI: 10.1109/JBHI.2015.2424985.

[100] Z. Jia, G. Yan, Jiangpingping, Z. Wang, and H. Liu. „Efficiency optimization of wireless power transmission systems for active capsule endoscopes". In: *Physiological Measurement* 32.10 (2011), pp. 1561–1573. ISSN: 13616579. DOI: 10.1088/0967-3334/32/10/005.

[101] D. Jiang, D. Cirmirakis, M. Schormans, T. A. Perkins, N. Donaldson, and A. Demosthenous. „An Integrated Passive Phase-Shift Keying Modulator for Biomedical Implants with Power Telemetry over a Single Inductive Link". In: *IEEE Transactions on Biomedical Circuits and Systems* 11.1 (2017), pp. 64–77. ISSN: 19324545. DOI: 10.1109/TBCAS.2016.2580513.

[102] B. Jing, M. L. Tomov, A. N. Wijntjes, S. R. Bhamidipati, et al. „Synthesis of ultrasound-compatible embryonic heart tube phantom using water-soluble 3D printed model for 3D ultrasound flow velocimetry". In: *International Ultrasonics Symposium (IUS)*. IEEE, 2020. ISBN: 9781728154480. DOI: 10.1109/IUS46767.2020.9251443.

[103] A. Y. S. Jou, H. Shan, H. Pajouhi, M. S. Tsai, et al. „A single-chip wireless microelectrode array for neural recording and stimulation". In: *IEEE MTT-S International Microwave Symposium Digest* (2017), pp. 1248–1250. ISSN: 0149645X. DOI: 10.1109/MWSYM.2017.8058833.

[104] U. M. Jow and M. Ghovanloo. „Modeling and optimization of printed spiral coils in air and muscle tissue environments". In: *Conference of the IEEE Engineering in Medicine and Biology Society (EMBC)*. Vol. 3. 5. 2009, pp. 6387–6390. ISBN: 9781424432967. DOI: 10.1109/IEMBS.2009.5333876.

[105] A. I. Al-Kalbani, M. R. Yuce, and J. M. Redoute. „Safe SAR levels in inductively powered brain implanted visual prostheses". In: *IEEE International Symposium on Electromagnetic Compatibility*. Rome: IEEE, 2012. ISBN: 9781467307185. DOI: 10.1109/EMCEurope.2012.6396784.

[106] M. Kamon, J. K. White, and M. J. Tsuk. „FASTHENRY: A Multipole-Accelerated 3-D Inductance Extraction Program". In: *IEEE Transactions on Microwave Theory and Techniques* 42.9 (1994), pp. 1750–1758. ISSN: 15579670. DOI: 10.1109/22.310584.

[107] M. Y. Kanda, M. Ballen, S. Salins, C.-K. Chou, and Q. Balzano. „Formulation and characterization of tissue equivalent liquids used for RF densitometry and dosimetry measurements". In: *IEEE Transactions on Microwave Theory and Techniques* 52.8 II (2004), pp. 2046–2056. ISSN: 00189480. DOI: 10.1109/TMTT.2004.832001.

[108] L. Karapanos, C. J. Abbott, L. N. Ayton, M. Kolic, et al. „Functional vision in the real-world environment with a second-generation (44-channel) suprachoroidal retinal prosthesis". In: *Translational Vision Science and Technology* 10.10 (2021), pp. 1–13. ISSN: 21642591. DOI: 10.1167/tvst.10.10.7.

[109] M. J. Karimi, A. Schmid, and C. Dehollain. „Wireless Power and Data Transmission for Implanted Devices via Inductive Links: A Systematic Review". In: *IEEE Sensors Journal* 21.6 (2021), pp. 7145–7161. ISSN: 15581748. DOI: 10.1109/JSEN.2021.3049918.

[110] K. K. Kärkkäinen. „Effective permittivity of mixtures: numerical validation by the FDTD method". In: *IEEE Transactions on Geoscience and Remote Sensing* 38.3 (2000), pp. 1303–1308. ISSN: 01962892. DOI: 10.1109/36.843023.

[111] M. K. Kazimierczuk. „Analysis of Class E Zero-Voltage-Switching Rectifier". In: *IEEE Transactions on Circuits and Systems* 37.6 (1990), pp. 747–755. ISSN: 00984094. DOI: 10.1109/31.55033.

[112] M. K. Kazimierczuk and D. Czarkowski. *Resonant Power Converters*. 1st ed. New York: John Wiley & Sons, Inc., 1995.

[113] K. S. Keerthi, K. Ilango, G. N. Manjula, and G. Nair Manjula. „Study of Mid-field Wireless Power Transfer for Implantable Medical Devices". In: *International Conference on Biomedical Engineering (IBIOMED)*. IEEE, 2018, pp. 44–47. ISBN: 9781538647363. DOI: 10.1109/IBIOMED.2018.8534820.

[114] G. A. Kendir, W. Liu, G. Wang, M. Sivaprakasam, et al. „An optimal design methodology for inductive power link with Class-E amplifier". In: *IEEE Transactions on Circuits and Systems I: Regular Papers* 52.5 (2005), pp. 857–866. ISSN: 10577122. DOI: 10.1109/TCSI.2005.846208.

[115] *Keysight 85070E Dielectric Probe Kit*. URL: www.keysight.com/en/pd-304506-pn-85070E.

[116] *Keysight E5061B, ENA Vector Network Analyzer*. URL: https://literature.cdn.keysight.com/litweb/pdf/5990-4392EN.pdf.

[117] S. R. Khan, S. K. Pavuluri, G. Cummins, and M. P. Desmulliez. „Wireless power transfer techniques for implantable medical devices: A review". In: *Sensors (Switzerland)* 20.12 (2020), pp. 1–58. ISSN: 14248220. DOI: 10.3390/s20123487.

[118] A. Kharab and R. B. Guenther. *An introduction to numerical methods: A MATLAB® approach, second edition*. 3rd ed. CRC Press, 2005. ISBN: 9781420057058.

[119] H. J. Kim, H. Hirayama, S. Kim, K. J. Han, R. Zhang, and J. W. Choi. „Review of Near-Field Wireless Power and Communication for Biomedical Applications". In: *IEEE Access* 5 (2017). ISSN: 21693536. DOI: 10.1109/ACCESS.2017.2757267.

[120] J. Kim, R. Ghaffari, and D. H. Kim. „The quest for miniaturized soft bioelectronic devices". In: *Nature Biomedical Engineering* 1.3 (2017), pp. 1–4. ISSN: 2157846X. DOI: 10.1038/s41551-017-0049.

[121] S. Kim, J. S. Ho, and A. S. Y. Poon. „Wireless Power Transfer to Miniature Implants : Transmitter Optimization". In: *IEEE Transactions on Antennas and Propagation* 60.10 (2012), pp. 4838–4845. DOI: 10.1109/TAP.2012.2207341.

[122] S. Kim, R. A. Normann, R. R. Harrison, and F. Solzbacher. „Preliminary study of the thermal impact of a microelectrode array implanted in the brain". In: *Annual International Conference of the IEEE Engineering in Medicine and Biology Society* (2006), pp. 2986–2989. ISSN: 05891019. DOI: 10.1109/IEMBS.2006.260307.

[123] S. Klauke, M. Goertz, S. Rein, D. Hoehl, et al. „Stimulation with a wireless intraocular epiretinal implant elicits visual percepts in blind humans". In: *Investigative Ophthalmology and Visual Science* 52.1 (2011), pp. 449–455. ISSN: 01460404. DOI: 10.1167/iovs.09-4410.

[124] L. Kranold, J. Boparai, L. Fortaleza, and M. Popovic. „Comparative Study of Tissue-Mimicking Phantoms for Microwave Breast Cancer Screening Systems". In: *International Microwave Biomedical Conference (IMBioC)*. 2020. ISBN: 9781728158662. DOI: 10.1109/IMBIoC47321.2020.9385029.

[125] R. Kubowicz. „A class-E power amplifier". In: *IEEE Transactions on Microwave Theory and Techniques* CAS-24.1 (2000).

[126] F. W. Kuo, S. Binsfeld Ferreira, H. N. R. Chen, L. C. Cho, et al. „A Bluetooth Low-Energy Transceiver with 3.7-mW All-Digital Transmitter, 2.75-mW High-IF Discrete-Time Receiver, and TX/RX Switchable On-Chip Matching Network". In: *IEEE Journal of Solid-State Circuits* 52.4 (2017), pp. 1144–1162. ISSN: 00189200. DOI: 10.1109/JSSC.2017.2654322.

[127] A. Kurs, A. Karalis, R. Moffatt, J. D. Joannopoulos, P. Fisher, and M. Soljačić. „Wireless power transfer via strongly coupled magnetic resonances". In: *Science* 317.5834 (2007), pp. 83–86. ISSN: 00368075. DOI: 10.1126/science.1143254.

[128] M. Lazebnik, E. L. Madsen, G. R. Frank, and S. C. Hagness. „Tissue-mimicking phantom materials for narrowband and ultrawideband microwave applications". In: *Physics in Medicine and Biology* 50.18 (2005), pp. 4245–4258. DOI: 10.1088/0031-9155/50/18/001.

[129] G. Lazzi. „Thermal effects of bioimplants". In: *IEEE Engineering in Medicine and Biology Magazine* 24.5 (2005), pp. 75–81. ISSN: 07395175. DOI: 10.1109/MEMB.2005.1511503.

[130] M. C. Lee, A. Karimi-Bidhendi, O. Malekzadeh-Arasteh, P. T. Wang, et al. „A CMOS MedRadio transceiver with supply-modulated power saving technique for an implantable brain-machine interface system". In: *IEEE Journal of Solid-State Circuits* 54.6 (2019), pp. 1541–1552. ISSN: 1558173X. DOI: 10.1109/JSSC.2019.2899521.

[131] T. Lee, M. K. Kim, H. J. Lee, and M. Je. „A 5.7μW/Channel Folded-Current-Mirror-Based Reconfigurable Multimodal Neural Recording IC with Improved Hardware Availability". In: (2021), pp. 1–4. DOI: 10.1109/iscas51556.2021.9401740.

[132] P. M. Lewis, H. M. Ackland, A. J. Lowery, and J. V. Rosenfeld. „Restoration of vision in blind individuals using bionic devices: A review with a focus on cortical visual prostheses". In: *Brain Research* 1595 (2015), pp. 51–73. ISSN: 18726240. DOI: 10.1016/j.brainres.2014.11.020.

[133] C. Liu, Y. X. Guo, H. Sun, and S. Xiao. „Design and safety considerations of an implantable rectenna for far-field wireless power transfer". In: *IEEE Transactions on Antennas and Propagation* 62.11 (2014), pp. 5798–5806. DOI: 10.1109/TAP.2014.2352363.

[134] H. Looyenga. „Dielectric constants of heterogeneous mixtures". In: *Physica* 31.3 (1965), pp. 401–406. ISSN: 00318914. DOI: 10.1016/0031-8914(65)90045-5.

[135] M. Lotfi Navaii, H. Sadjedi, and A. Sarrafzadeh. „Efficient ASK Data and Power Transmission by the Class-E with a Switchable Tuned Network". In: *IEEE Transactions on Circuits and Systems I: Regular Papers* 65.10 (2018), pp. 3255–3266. ISSN: 15580806. DOI: 10.1109/TCSI.2018.2808189.

[136] A. M. Lozano, N. Lipsman, H. Bergman, P. Brown, et al. „Deep Brain Stimulation: Current Challenges and Future Directions". In: *Nature Reviews Neurology* 15.3 (2019), pp. 148–160. ISSN: 17594766. DOI: 10.1038/s41582-018-0128-2.

[137] A. Lozano, J. S. Suárez, C. Soto-Sánchez, J. Garrigós, et al. „Neurolight: A Deep Learning Neural Interface for Cortical Visual Prostheses". In: *International Journal of Neural Systems* 30.9 (2020). ISSN: 17936462. DOI: 10.1142/S0129065720500458.

[138] *LTspice simulator*. URL: www.analog.com/en/design-center/design-tools-and-calculators/ltspice-simulator.html.

[139] L. Lucke and V. Bluvshtein. „Safety Considerations for Wireless Delivery of Continuous Power to Implanted Medical Devices". In: *Conference of the IEEE Engineering in Medicine and Biology Society*. 2014, pp. 286–289. ISBN: 9781424479290. DOI: 10.1109/EMBC.2014.6943585.

[140] Y. H. L. Luo and L. da Cruz. „The Argus® II Retinal Prosthesis System". In: *Progress in Retinal and Eye Research* 50 (2016), pp. 89–107. ISSN: 18731635. DOI: 10.1016/j.preteyeres.2015.09.003.

[141] A. Ma and A. S. Y. Poon. „Midfield Wireless Power Transfer for Bioelectronics". In: *IEEE Circuits and Systems Magazine* 2.2 (2015), pp. 54–60. ISSN: 1531-636X. DOI: 10.1109/MCAS.2015.2418999.

[142] *Macula of retina*. 2012. URL: https://medical-dictionary.thefreedictionary.com/macula+of+retina.

[143] Z. Manzoor, M. T. Ghasr, and K. M. Donnell. „Microwave Characterization of 3D Printed Conductive Composite Materials". In: *IEEE International Instrumentation and Measurement Technology Conference (I2MTC)*. Houston: IEEE, 2018, pp. 1–5. ISBN: 9781538622223. DOI: 10.1109/I2MTC.2018.8409627.

[144] E. Massoni, L. Silvestri, M. Bozzi, L. Perregrini, et al. „Characterization of 3D-printed dielectric substrates with different infill for microwave applications". In: *International Microwave Workshop Series on Advanced Materials and Processes for RF and THz Applications (IMWS-AMP)*. Chengdu: IEEE, 2016, pp. 1–4. ISBN: 9781509020171. DOI: 10.1109/imws-amp.2016.7588330.

[145] *Mathworks MATLAB*. 2022. URL: www.mathworks.com/products/matlab.html.

[146] D. McCreery, V. Pikov, and P. R. Troyk. „Neuronal loss due to prolonged controlled-current stimulation with chronically implanted microelectrodes in the cat cerebral cortex". In: *Journal of Neural Engineering* 7.3 (2010). ISSN: 17412560. DOI: 10.1088/1741-2560/7/3/036005.

[147] B. McDermott, E. Porter, M. Orhalloran, A. Poudel, et al. „3D Printable Solid Tissue-Mimicking Material for Microwave Phantoms". In: *Conference on Biomedical Applications of Electromagnetic Fields (EMF-Med)*. Split, 2018, pp. 2–3. ISBN: 9789532900798. DOI: 10.23919/EMF-MED.2018.8526005.

[148] S. A. Mirbozorgi, P. Yeon, and M. Ghovanloo. „Robust Wireless Power Transmission to mm-Sized Free-Floating Distributed Implants". In: *IEEE Transactions on Biomedical Circuits and Systems* 11.3 (2017), pp. 692–702. ISSN: 19324545. DOI: 10.1109/TBCAS.2017.2663358.

[149] D. K. Misra. „A Quasi-Static Analysis of Open-Ended Coaxial Lines". In: *IEEE Transactions on Microwave Theory and Techniques* 1.5 (1987), pp. 10–13.

[150] P. D. Mitcheson, E. M. Yeatman, G. K. Rao, A. S. Holmes, and T. C. Green. „Energy harvesting from human and machine motion for wireless electronic devices". In: *Proceedings of the IEEE* 96.9 (2008), pp. 1457–1486. ISSN: 00189219. DOI: 10.1109/JPROC.2008.927494.

[151] J. Moll, D. Wcortge, V. Krozer, A. Santorelli, et al. „Quality control of carbon-rubber tissue phantoms: Comparative MRI, CT, X-ray and UWB microwave measurements". In: *European Conference on Antennas and Propagation (EUCAP)*. 2017, pp. 2723–2727. ISBN: 9788890701870. DOI: 10.23919/EuCAP.2017.7928186.

[152] T. Nagashima, X. Wei, E. Bou, E. Alarcón, and H. Sekiya. „Analytical Design for Resonant Inductive Coupling Wireless Power Transfer System with Class-E Inverter and Class-DE Rectifier". In: *IEEE International Symposium on Circuits and Systems*. Vol. 2015-July. 2015, pp. 686–689. ISBN: 9781479983919. DOI: 10.1109/ISCAS.2015.7168726.

[153] A. Najarpour Foroushani, C. C. Pack, and M. Sawan. „Cortical visual prostheses: From microstimulation to functional percept". In: *Journal of Neural Engineering* 15.2 (2018). ISSN: 17412552. DOI: 10.1088/1741-2552/aaa904.

[154] NESTOR. *NESTOR - Neuronal Stimulation for Recovery of Function*. 2022. URL: www.nestor-sight.com.

[155] A. L. Neves, L. Leroi, N. Cochinaire, R. Abdeddaim, P. Sabouroux, and A. Vignaud. „A simple approach towards a multi-frequency MRI head phantom". In: *European Conference on Antennas and Propagation (EUCAP)*. Euraap, 2017, pp. 1823–1827. ISBN: 9788890701870. DOI: 10.23919/EuCAP.2017.7928361.

[156] K. S. Nikita. „Handbook of Biomedical Telemetry". In: *Handbook of Biomedical Telemetry* (2014), pp. 1–702. DOI: 10.1002/9781118893715.

[157] D. Nikolayev, M. Zhadobov, P. Karban, and R. Sauleau. „Electromagnetic Radiation Efficiency of Body-Implanted Devices". In: *Physical Review Applied* 9.2 (2018), p. 24033. ISSN: 23317019. DOI: 10.1103/PhysRevApplied.9.024033.

[158] S. O'Driscoll, S. Korhummel, P. Cong, Y. Zou, et al. „A 200μm x 200μm x 100μm, 63nW, 2.4GHz Injectable Fully-Monolithic Wireless Bio-Sensing System". In: *IEEE Radio Frequency Integrated Circuits Symposium (RFIC)*. 2017, pp. 256–259. ISBN: 9781509046263. DOI: 10.1109/RFIC.2017.7969066.

[159] S. O'Driscoll and T. H. Meng. „Adaptive Signal Acquisition and Wireless Power Transfer for an Implantable Prosthesis Processor". In: *IEEE International Symposium on Circuits and Systems*. 2010, pp. 3589–3592.

[160] P. Oltulu, B. Ince, N. Kokbudak, S. Findik, and F. Kilinc. „Measurement of Epidermis, Dermis, and Total Skin Thicknesses from Six Different Body Regions with a new Ethical Histometric Technique". In: *Turkish Journal of Plastic Surgery* 26.2 (2018), pp. 56–61. DOI: 10.4103/tjps.tjps_2_17.

[161] A. E. Omisakin. „Bi-directional Transcutaneous Wireless Communication System for Intracortical Visual Prosthesis". PhD thesis. Eindhoven University of Technology, 2022.

[162] A. E. Omisakin, R. M. C. Mestrom, and M. J. Bentum. „Low-Power BPSK Inductive Data Link for an Implanted Intracortical Visual Prosthesis". In: *Conference of the IEEE Engineering in Medicine and Biology Society (EMBC)*. IEEE, 2019, pp. 1–5. ISBN: 9781538613115.

[163] A. E. Omisakin, R. M. C. Mestrom, and M. J. Bentum. „Low-Power Communication for an Implanted Intracortical Visual Prosthesis". In: *European Conference on Antennas and Propagation (EuCAP)*. European Association on Antennas and Propagation, 2019, pp. 1–4. ISBN: 9788890701887.

[164] A. E. Omisakin, R. M. C. Mestrom, and M. J. Bentum. „System Design of a Low-power Wireless Link for Neural Recording in a Visual Prosthesis". In: *IEEE AFRICON Conference*. 2019. ISBN: 9781728132891. DOI: 10.1109/AFRICON46755.2019.9133916.

[165] A. E. Omisakin, R. M. C. Mestrom, G. Radulov, and M. J. Bentum. „Sub-milliwatt Transceiver IC for Transcutaneous Communication of an Intracortical Visual Prosthesis". In: *Electronics (Switzerland)* 11.1 (2022). ISSN: 20799292. DOI: 10.3390/electronics11010024.

[166] S. Ozeri and D. Shmilovitz. „Ultrasonic Transcutaneous Energy Transfer for Powering Implanted Devices". In: *Ultrasonics* 50.6 (2010), pp. 556–566. ISSN: 0041624X. DOI: 10.1016/j.ultras.2009.11.004.

[167] D. Palanker, A. Vankov, P. Huie, and S. Baccus. „Design of a high-resolution optoelectronic retinal prosthesis". In: *Journal of Neural Engineering* 2.1 (2005). ISSN: 17412560. DOI: 10.1088/1741-2560/2/1/012.

[168] A. C. Paolella, C. Corey, D. Foster, J. Desjardins, C. Smith, and L. Walters. „Broadband Millimeter Wave Characterization of 3-D Printed Materials". In: *International Microwave Symposium (IMS)*. Vol. 2018-June. Philadelphia: IEEE, 2018, pp. 1565–1568. ISBN: 9781538650677. DOI: 10.1109/MWSYM.2018.8439634.

[169] Y. Park, S.-t. Koh, J. Lee, H. Kim, et al. „A Frequency-Splitting-Based Wireless Power and Data Transfer IC for Neural Prostheses with Simultaneous 115mW Power and 2.5Mb/s Forward Data Delivery". In: *ISSCC*. San Fransisco, 2021, pp. 472–474. ISBN: 9781728195490.

[170] J. S. Pezaris and R. C. Reid. „Demonstration of Artificial Visual Percepts Generated through Thalamic Microstimulation". In: *Proceedings of the National Academy of Sciences of the United States of America* 104.18 (2007), pp. 7670–7675. ISSN: 00278424. DOI: 10.1073/pnas.0608563104.

[171] M. Pinuela, D. C. Yates, S. Lucyszyn, and P. D. Mitcheson. „Maximizing DC-to-load efficiency for inductive power transfer". In: *IEEE Transactions on Power Electronics* 28.5 (2013), pp. 2437–2447. ISSN: 08858993. DOI: 10.1109/TPEL.2012.2215887.

[172] T. Plüss, F. Zimmer, T. Hehn, and A. Murk. „Characterisation and Comparison of Material Parameters of 3D-Printable Absorbing Materials". In: *Materials* 15.4 (2022), p. 1503. DOI: 10.3390/ma15041503.

[173] T. Pokorny and J. Tesarik. „3D Printed Multi-layer Molds of Human Head Tissue Phantoms for Microwave Stroke Detection". In: *PhotonIcs & Electromagnetics Research Symposium - Spring (PIERS-Spring)*. Rome: IEEE, 2019, pp. 1424–1427. ISBN: 9781728134031. DOI: 10.1109/PIERS-Spring46901.2019.9017648.

[174] A. S. Y. Poon. „Electromagnetic Field Focusing for Short-Range Wireless Power Transmission". In: *IEEE Radio and Wireless Symposium*. 2012, pp. 115–118. ISBN: 9781457711558. DOI: 10.1109/RWS.2012.6175400.

[175] A. S. Y. Poon, S. O'Driscoll, and T. H. Meng. „Optimal Frequency for Wireless Power Transmission into Dispersive Tissue". In: *IEEE Transactions on Antennas and Propagation* 58.5 (2010), pp. 1739–1750. ISSN: 0018-926X. DOI: 10.1109/TAP.2010.2044310.

[176] A. S. Y. Poon, S. O'Driscoll, and T. H. Meng. „Optimal Operating Frequency in Wireless Power Transmission for Implantable Devices". In: *Annual International Conference of the IEEE Engineering in Medicine and Biology Society*. Vol. 29. 2007, pp. 5673–5678. ISBN: 1424407885.

[177] D. M. Pozar. *Microwave engineering*. 4th ed. 2012, p. 732. ISBN: 9780470631553.

[178] L. Radziemski and I. R. S. Makin. „In vivo demonstration of ultrasound power delivery to charge implanted medical devices via acute and survival porcine studies". In: *Ultrasonics* 64 (2016), pp. 1–9. DOI: 10.1016/j.ultras.2015.07.012.In.

[179] G. A. Ramirez Arroyave and J. L. Araque Quijano. „Broadband Characterization of 3D Printed Samples with Graded Permittivity". In: *International Conference on Electromagnetics in Advanced Applications (ICEAA)*. Cartagena, 2018, pp. 584–588. ISBN: 9781538667620. DOI: 10.1109/ICEAA.2018.8520349.

[180] S. Rao and J. C. Chiao. „Body electric: Wireless power transfer for implant applications". In: *IEEE Microwave Magazine* 16.2 (2015), pp. 54–64. ISSN: 15273342. DOI: 10.1109/MMM.2014.2377586.

[181] S. U. Rehman, A. M. Kamboh, and Y. Yang. „A 79μW 0.24mm2 8-channel neural signal recording front-end integrated circuit". In: *International Conference on Applied Electronics* (2017), pp. 24–27. ISSN: 18037232. DOI: 10.23919/AE.2017.8053611.

[182] RepRapWorld. *PC-PETG filament Zwart 2.85 mm / 1 kg Real*. URL: https://reprapworld.nl/3d-filament/carbon/2-85-real-filament-pc-petg-zwart-1kg/.

[183] N. Reyes, F. Casado, V. Tapia, C. Jarufe, R. Finger, and L. Bronfman. „Complex Dielectric Permittivity of Engineering and 3D-Printing Polymers at Q-Band". In: *Journal of Infrared, Millimeter, and Terahertz Waves* 39.11 (2018), pp. 1140–1147. ISSN: 18666906. DOI: 10.1007/s10762-018-0528-9.

[184] J. F. Rizzo. „Update on retinal prosthetic research: The Boston retinal implant project". In: *Journal of Neuro-Ophthalmology* 31.2 (2011), pp. 160–168. ISSN: 10708022. DOI: 10.1097/WNO.0b013e31821eb79e.

[185] J. F. Rizzo, J. L. Wyatt, J. Loewenstein, S. K. Kelly, and D. B. Shire. „Methods and Perceptual Thresholds for Short-Term Electrical Stimulation of Human Retina with Microelectrode Arrays". In: *Investigative Ophthalmology and Visual Science* 44.12 (2003), pp. 5355–5361. ISSN: 01460404. DOI: 10.1167/iovs.02-0819.

[186] S. Rizzo, P.-O. Barale, S. Ayello-Scheer, R. G. Devenyi, et al. „Adverse Events of the Argus II Retinal Prosthesis". In: *Retina* 40.2 (2020), pp. 303–311. DOI: 10.1097/IAE.0000000000002394.

[187] P. J. Rousche and R. A. Normann. „Chronic recording capability of the utah intracortical electrode array in cat sensory cortex". In: *Journal of Neuroscience Methods* 82.1 (1998), pp. 1–15. ISSN: 01650270. DOI: 10.1016/S0165-0270(98)00031-4.

[188] S. Roy, A. N. M. W. Azad, S. Baidya, and F. Khan. „A Comprehensive Review on Rectifiers, Linear Regulators, and Switched-Mode Power Processing Techniques for Biomedical Sensors and Implants Utilizing in-Body Energy Harvesting and External Power Delivery". In: *IEEE Transactions on Power Electronics* 36.11 (2021), pp. 12721–12745. ISSN: 19410107. DOI: 10.1109/TPEL.2021.3075245.

[189] K. Sankaragomathi, L. Perez, R. Mirjalili, B. Parviz, and B. Otis. „A 27μW subcutaneous wireless biosensing platform with optical power and data transfer". In: *IEEE Custom Integrated Circuits Conference (CICC)*. IEEE, 2014, pp. 6–9. ISBN: 9781479932863. DOI: 10.1109/CICC.2014.6946089.

[190] K. van Schuylenberg and R. Puers. *Inductive powering*. Springer, 2009. ISBN: 9789048124114.

[191] K. Servick. *Next-generation artificial vision comes into view*. 2019. DOI: 10.1126/science.366.6466.671.

[192] F. Shahrokhi, K. Abdelhalim, D. Serletis, P. L. Carlen, and R. Genov. „The 128-channel fully differential digital integrated neural recording and stimulation interface". In: *IEEE Transactions on Biomedical Circuits and Systems* 4.3 (2010), pp. 149–161. ISSN: 19324545. DOI: 10.1109/TBCAS.2010.2041350.

[193] L. F. Shampine. „Vectorized Adaptive Quadrature in Matlab". In: *Journal of Computational and Applied Mathematics* 211 (2008), pp. 131–140.

[194] T. Sharf, T. Kalakuntla, D. J. Lee, and K. K. Gokoffski. „Electrical Devices for Visual Restoration". In: *Survey of Ophthalmology* (2021). ISSN: 00396257. DOI: 10.1016/j.survophthal.2021.08.008.

[195] A. Sharma, L. Rieth, P. Tathireddy, R. R. Harrison, et al. „Evaluation of the packaging and encapsulation reliability in fully integrated, fully wireless 100 channel Utah Slant Electrode Array (USEA): Implications for long term functionality". In: *Bone* 23.1 (2014), pp. 1–7. ISSN: 15378276. DOI: 10.1016/j.sna.2011.11.015.Evaluation. arXiv: NIHMS150003.

[196] Y. Shi, M. Choi, Z. Li, G. Kim, et al. „A 10mm3 Syringe-Implantable Near-Field Radio System on Glass Substrate". In: *IEEE International Solid-State Circuits Conference (ISSCC)*. Vol. 26. 7. San Fransisco: IEEE, 2016, pp. 448–450. ISBN: 9781467394673. DOI: 10.1109/ISSCC.2016.7418100.

[197] D. B. Shire, S. K. Kelly, W. A. Drohan, J. Chen, et al. „Development and Implantation of a Minimally Invasive Wireless Subretinal Neurostimulator". In: *IEEE Transactions on Biomedical Engineering* 56.10 (2009), pp. 2502–2511. ISSN: 15582531. DOI: 10.1109/TBME.2009.2021401.

[198] *Sim4Life V7.0*. Zurich, 2022. URL: https://zmt.swiss/sim4life/.

[199] A. K. Skrivervik, M. Bosiljevac, and Z. Sipus. „Design Considerations for Implantable and Wearable Antennas". In: *TELSIKS* (2017), pp. 83–86.

[200] M. Song, M. Ding, E. Tiurin, K. Xu, et al. „A Millimeter-Scale Crystal-Less MICS Transceiver for Insertable Smart Pills". In: *IEEE Transactions on Biomedical Circuits and Systems* 14.6 (2020), pp. 1218–1229. ISSN: 19409990. DOI: 10.1109/TBCAS.2020.3036905.

[201] S. Sonmezoglu, J. R. Fineman, E. Maltepe, and M. M. Maharbiz. „Monitoring deep-tissue oxygenation with a millimeter-scale ultrasonic implant". In: *Nature Biotechnology* 39.7 (2021), pp. 855–864. DOI: 10.1038/s41587-021-00866-y.

[202] F. Spelman. „The past, present, and future of cochlear prostheses". In: *IEEE Engineering in Medicine and Biology Magazine* 18.3 (1999), pp. 27–33. ISSN: 0739-5175. DOI: 10.1109/51.765186.

[203] P. R. Stauffer, F. Rossetto, M. Prakash, D. G. Neuman, and T. Lee. „Phantom and animal tissues for modelling the electrical properties of human liver". In: *International Journal of Hyperthermia* 19.1 (2003), pp. 89–101. ISSN: 02656736. DOI: 10.1080/0265673021000017064.

[204] K. F. Steabell and D. K. Misra. „An Experimental Technique for In Vivo Permittivity Measurement of Materials as Microwave Frequencies". In: *IEEE Transactions on Microwave Theory and Techniques* 38.3 (1990).

[205] G. A. Stevens, R. A. White, S. R. Flaxman, H. Price, et al. „Global Prevalence of Vision Impairment and Blindness: Magnitude and Temporal Trends, 1990-2010". In: *Ophthalmology* 120.12 (2013), pp. 2377–2384. ISSN: 01616420. DOI: 10.1016/j.ophtha.2013.05.025.

[206] K. Stingl, K. U. Bartz-Schmidt, D. Besch, A. Braun, et al. „Artificial vision with wirelessly powered subretinal electronic implant alpha-IMS". In: *Proceedings of the Royal Society B: Biological Sciences* 280.1757 (2013), pp. 1–8. ISSN: 14712954. DOI: 10.1098/rspb.2013.0077.

[207] K. Stingl, K. U. Bartz-Schmidt, A. Braun, F. Gekeler, et al. „Transfer characteristics of subretinal visual implants: corneally recorded implant responses". In: *Documenta Ophthalmologica* 133.2 (2016), pp. 81–90. ISSN: 15732622. DOI: 10.1007/s10633-016-9557-7.

[208] K. Stokes, G. Jiang, D. D. Zhou, O. Auciello, et al. *Implantable Neural Prostheses 2: Techniques and Engineering Approaches*. Ed. by D. D. Zhou and E. Greenbaum. Springer, 2010, pp. 27–61. ISBN: 9780387981192. DOI: 10.1007/978-0-387-98120-8.

[209] C. H. Stoyer. „Electromagnetic Fields of Dipoles in Stratified Media". In: *IEEE Transactions on Antennas and Propagation* July (1977), pp. 547–552.

[210] J. A. Stratton. *Electromagnetic Theory*. New York: McGraw-Hill, 1941.

[211] G. Sun, B. Muneer, Y. Li, and Q. Zhu. „Ultracompact Implantable Design With Integrated Wireless Power Transfer and RF Transmission Capabilities". In: *IEEE Transactions on Biomedical Circuits and Systems* 12.2 (2018), pp. 1–11. ISSN: 1932-4545. DOI: 10.1109/TBCAS.2017.2787649.

[212] T. Sunaga, H. Ikehira, S. Furukawa, M. Tamura, et al. „Development of a Dielectric Equivalent Gel for Better Impedance Matching for Human Skin". In: *Bioelectromagnetics* 24.3 (2003), pp. 214–217. ISSN: 01978462. DOI: 10.1002/bem.10080.

[213] „Synopsis of IEEE Std C95.1™-2019 'IEEE Standard for Safety Levels with Respect to Human Exposure to Electric, Magnetic, and Electromagnetic Fields, 0 Hz to 300 GHz'". In: *IEEE Access* (2019). ISSN: 21693536. DOI: 10.1109/ACCESS.2019.2954823.

[214] J. Taipale, A. Mikhailova, M. Ojamo, J. Nättinen, et al. „Low vision status and declining vision decrease Health-Related Quality of Life: Results from a nationwide 11-year follow-up study". In: *Quality of Life Research* 28.12 (2019), pp. 3225–3236. ISSN: 15732649. DOI: 10.1007/s11136-019-02260-3.

[215] P. R. Troyk, M. Bak, J. Berg, D. Bradley, et al. „A Model for Intracortical Visual Prosthesis Research". In: *Artificial Organs* 27.11 (2003), pp. 1005–1015. ISSN: 0160564X. DOI: 10.1046/j.1525-1594.2003.07308.x.

[216] Ultimaker. *Cura 4.13*. URL: https://ultimaker.com/software/ultimaker-cura.

[217] Ultimaker. *PETG*. URL: https://ultimaker.com/materials/petg (visited on 08/30/2022).

[218] Ultimaker. *PLA*. URL: https://ultimaker.com/materials/pla.

[219] Ultimaker. *Print cores and add-ons*. URL: https://ultimaker.com/en/3d-printers/ultimaker-print-cores-and-addons.

[220] Ultimaker. *Tough PLA*. URL: https://ultimaker.com/materials/tough-pla (visited on 08/30/2022).

[221] *Ultimaker S5: Reliability at scale*. URL: www.ultimaker.com/3d-printers/ultimaker-s5.

[222] J. Villalobos, D. A. X. Nayagam, P. J. Allen, P. McKelvie, et al. „A wide-field suprachoroidal retinal prosthesis is stable and well tolerated following chronic implantation." In: *Investigative ophthalmology & visual science* 54.5 (2013), pp. 3751–3762. ISSN: 15525783. DOI: 10.1167/iovs.12-10843.

[223] H. J. Visser. *Approximate Antena Analysis for CAD*. 1st ed. Chichester: John Wiley & Sons, Inc., 2009. ISBN: 978-0-470-51293-7. DOI: 10.1002/9780470986394.

[224] H. J. Visser. „Optimum Tolerance for Load Mismatch and Coil Misalignment in Resonant Inductive WPT". In: *IEEE Wireless Power Transfer Conference (WPTC)*. Bordeaux, 2022.

[225] H. J. Visser, H. W. Pflug, and S. Keyrouz. „Rectenna demonstrators at Holst Centre/IMEC and Eindhoven University of Technology". In: *Conference on Antennas and Propagation (EuCAP)*. Lisbon: EurAAP, 2015. ISBN: 9788890701856.

[226] J. R. Wait. *Electromagnetic Waves in Stratified Media*. 2nd ed. Pergamon Press Ltd., 1970.

[227] J. R. Wait. „Propagation of Radio Waves over a Stratified Ground". In: *Geophysics* 18.2 (1953), pp. 416–422.

[228] B. Wang, W. Yerazunis, and K. H. Teo. „Wireless power transfer: Metamaterials and array of coupled resonators". In: *Proceedings of the IEEE* 101.6 (2013), pp. 1359–1368. ISSN: 1558-2256. DOI: 10.1109/JPROC.2013.2245611. arXiv: 1509.00940.

[229] C. Wang, E. Brunton, S. Haghgooie, K. Cassells, A. Lowery, and R. Rajan. „Characteristics of electrode impedance and stimulation efficacy of a chronic cortical implant using novel annulus electrodes in rat motor cortex". In: *Journal of Neural Engineering* 10.4 (2013). ISSN: 17412560. DOI: 10.1088/1741-2560/10/4/046010.

[230] G. Wang, W. Liu, M. Sivaprakasam, and G. A. Kendir. „Design and analysis of an adaptive transcutaneous power telemetry for biomedical implants". In: *IEEE Transactions on Circuits and Systems I: Regular Papers* 52.10 (2005), pp. 2109–2117. ISSN: 1558-0806. DOI: 10.1109/TCSI.2005.852923.

[231] W. Watson. „An account of Mr. Benjamin Franklin's treatise, lately published, intituled, Experiments and observations on electricity, made at Philadelphia in America". In: *Philosophical Transactions of the Royal Society* 47 (1752), pp. 202–211. DOI: 10.1098/rstl.1751.0032.

[232] Website. *Wireless Charging Technology & Standards — AirFuel Alliance*. URL: https://airfuel.org/ (visited on 08/30/2022).

[233] Website. *Wireless Power Consortium*. URL: www.wirelesspowerconsortium.com/ (visited on 08/30/2022).

[234] X. Wei, L. Luan, Z. Zhao, X. Li, et al. „Nanofabricated Ultraflexible Electrode Arrays for High-Density Intracortical Recording". In: *Advanced Science* 5.6 (2018). ISSN: 21983844. DOI: 10.1002/advs.201700625.

[235] K. Wendel-Mitoraj, D. Stoliar, J. Malmivuo, and J. A. Hyttinen. „Measuring Tissue Thicknesses of the Human Head Using Centralized and Normalized Trajectories". In: *Consciousness and its Measures*. May 2014. Limassol, 2009, pp. 112–113.

[236] D. Wessels. „Implantable Pacemakers and Defibrillators: Device Overview & EMI considerations". In: *IEEE International Symposium on Electromagnetic Compatibility*. Minneapolis, 2002, pp. 911–915. ISBN: 0-7803-7264-6. DOI: 10.1109/ISEMC.2002.1032815.

[237] *World report on vision*. Geneva: World Health Organization. 2019. Licence: CC BY-NC-SA 3.0 IGO. ISBN: 9789241516570.

[238] Z. Yang, W. Liu, and E. Basham. „Inductor modeling in wireless links for implantable electronics". In: *IEEE Transactions on Magnetics* 43.10 (2007), pp. 3851–3860. ISSN: 00189464. DOI: 10.1109/TMAG.2007.904189.

[239] F. Zanella. „3D Full Wave EM Simulations Accelerated by GPU Computing". In: *GPU Technology Conference*. San Jose, 2010.

[240] M. Zargham and P. G. Gulak. „Fully integrated on-chip coil in 0.13 μm CMOS for wireless power transfer through biological media". In: *IEEE Transactions on Biomedical Circuits and Systems* 9.2 (2015). ISSN: 19324545. DOI: 10.1109/TBCAS.2014.2328318.

[241] J. Zechmeister and J. Lacik. „Complex Relative Permittivity Measurement of Selected 3D-Printed Materials up to 10 GHz". In: *Conference on Microwave Techniques (COMITE)*. 3. Pardubice: IEEE, 2019, pp. 4–7. ISBN: 9781538693377. DOI: 10.1109/COMITE.2019.8733590.

[242] M. Zhadobov, A. Guraliuc, N. Chahat, and R. Sauleau. „Tissue-equivalent Phantoms in the 60-GHz Band and their Application to the Body-centric Propagation Studies". In: *International Microwave Workshop Series on: RF and Wireless Technologies for Biomedical and Healthcare Applications (IMWS-Bio)*. IEEE, 2015. ISBN: 9781479954476. DOI: 10.1109/IMWS-BIO.2014.7032417.

[243] J. Zhang, B. Yang, H. Li, F. Fu, et al. „A novel 3D-printed head phantom with anatomically realistic geometry and continuously varying skull resistivity distribution for electrical impedance tomography". In: *Scientific Reports* 7.1 (2017), pp. 1–9. ISSN: 20452322. DOI: 10.1038/s41598-017-05006-8.

[244] H. Zheng and C. E. Smith. „Permittivity Measurements Using a Short Open-Ended Coaxial Line Probe". In: *IEEE Microwave and Guided Wave Letters* (1991), pp. 337–339.

[245] G. Ziegelberger, R. Croft, M. Feychting, A. C. Green, et al. *ICNIRP Guidelines for Limiting Exposure to Electromagnetic Fields (100 kHz to 300 GHz)*. Vol. 118. 5. International Commission on Non-Ionizing Radiation Protection (ICNIRP), 2020, pp. 483–524. DOI: 10.1097/HP.0000000000001210.

Acknowledgments

There are many people who have contributed to this thesis one way or another. It all started during my internship, during which I considered pursuing a PhD for the first time. Many thanks to **Ramiro Serra** and **Franz Schlagenhaufer** for the supervision and for planting this seed. Also thanks to the others back in Perth, who have all contributed to the great social and scientific atmosphere that eventually lead to this decision.

Considering doing a PhD is one thing, but being asked to do so is of course an important part of the process. Thanks **Rob Mestrom** and **Mark Bentum** for considering me. Also thanks for the friends who have suggested them to contact me in the first place.

I am grateful for the supervision I received from **Huib Visser** and **Rob Mestrom**. Our weekly meetings obviously contained many technical discussions, which I enjoyed a lot. In particular, the mutual respect, involvement, and open atmosphere were things I really admired. Having a weekly meeting with your supervisors at four o'clock on Friday afternoon might be considered tricky by some. However, our overlapping senses of humor, as well as other common interests, made that this was certainly not the case. I could not have wished for better supervision. Thanks for everything.

I had the possibility to work on a truly awesome project, as part of a great multidisciplinary team. Thanks **Pieter Roelfsema** for starting the NESTOR project and getting everybody together, and thanks to all team members for sharing their knowledge and scientific contributions, as well as for making the associated activities much fun. Thanks STW, part of NWO, for funding the project. I also thank the patient organisations who were involved in the project for providing insight into what it means to be blind. A special thanks to **Jens Naumann** and **Jeroen Pels** for sharing your experience with visual prostheses. Your stories have inspired and motivated me beyond imagination, I will never forget them.

Over the past years, I've come to know the EM group as a great place within our faculty. On the professional side, cutting edge research is being performed on a large variety of subjects, I have learned so much from you all on many occasions. On the social side, there are so many great people who make the atmosphere in this group so nice. I especially enjoyed the joint lunches, birthday treats, random visits to Het Walhalla, group outings, meerkamp, (un)official PhD activities, and unofficial after-parties in our office, as well as getting to know the different cultures of my colleagues. I especially thank the fellow inhabitants of Flux 9.078

Adedayo, Elles, Kevin, Kirill, Martijn, Nazanin, Niels, Paola, Radovan, Stefan, Thomas, it was a pleasure sharing an office with you. I wish you lots of Smint for the future, and please take good care of the plants. Also thanks to the EM4C&C members and to others with whom I've had much contact during my PhD.

I could easily fill an entire second thesis with all the great times we had as EM PhDs, but I have chosen to keep those stories unwritten, and as such I won't mention everybody individually. Even though, I'd like to highlight a few people. **Teun**, thanks for everything you've learned me, and for the template used to make this thesis (adapted from Rob's version). **Elles**, thanks for learning me about the biological side of things, for the help with my posters, and for the renders of my designs. **Steven**, thanks for sharing your WPT experience with me. I enjoyed setting up the EM4C&C lab together. **Leroy**, thanks for taking over the supervision of the servers, and for being kind of my successor in the field of neural prostheses. Thanks to you all, and of course all others, for being my colleagues.

Suzanne, you deserve a special mention. Thanks for arranging everything, including the things we didn't even think of, and thanks for the many nice conversations we had. You are the backbone of the group.

I have enjoyed participating in education at our faculty. Thanks to everyone involved in Numerical Methods and Rock Your Baby, as well as to the students who enrolled. A special thanks goes to **Esmee**, **Jules**, and **Alexandra**, the students who accepted the challenge of investigating some parts that I did not have the time for. It was a pleasure working together, you certainly contributed to my journey.

Music is a valuable aspect of life. Thanks to my fellow percussionists of the **Koninklijke Harmonie Deurne**, as well as all members of the **Jazzcombo Ludwig Attevelt**, for the many hours of music we made together. Also thanks to all the artists and composers I had the pleasure of listening to, both live and on record, and thanks everyone for your suggestions.

Being able to take your mind off things from time to time is essential. I thank the friends I know through **e.t.s.v. Thor** and **Het Walhalla**, in particular my friends of the **54$^{\text{th}}$ Board**, for the necessary distraction, and for the trust you've put in me. Also thanks to all my friends I know through **Jongerensociëteit Walhalla** and the **Walhalla Zomerfeesten** for the great times, and for letting me do my thing undisturbed. Being part of Walhalla and Thor has added unbelievably much to my life and shaped me into the person I am today.

I thank my former and current flatmates for their companionship. Sharing a house with each of you has been a true pleasure. Thanks also to the visitors, with whom we have shared many beers and moments to never forget. Especially in times of a lockdown, during which it required more effort to maintain social relationships, meeting you meant a lot.

My family has always been there for me. Even though you obviously couldn't help me with the technical details of my project, I've always felt your unconditional support. Dad, a special thanks for fueling my interest in technology from the day I was born. I am eternally grateful to you all.

Publiekssamenvatting

Wereldwijd zijn meer dan 43 miljoen mensen blind. In de afgelopen 30 jaar is dat aantal gestegen met grofweg 50%. Voor de komende 30 jaar wordt een vergelijkbare groei verwacht. Veruit de meeste blinden worden geboren met normaal functionerend zicht en verliezen hun zicht na verloop van tijd, door bijvoorbeeld een ziekte of een ongeluk. De signalen afkomstig van de ogen kunnen bij deze mensen, om uiteenlopende redenen, de visuele cortex niet meer bereiken, terwijl deze vaak nog wel in staat is dergelijke signalen te interpreteren.

Elektrische stimulatie van de visuele cortex kan leiden tot het ervaren van visuele stimuli, die we ‘fosfenen’ noemen. Dat is zelfs het geval bij blinden, vooropgesteld dat zij tijdens hun leven ooit hebben kunnen zien. Door een externe bron, bijvoorbeeld een camera, via enkele bewerkingsstappen te verbinden met elektrodes geïmplanteerd in de visuele cortex, kunnen kunstmatige visuele waarnemingen worden gegenereerd, zelfs wanneer er uitgebreide schade aan het oog of de oogzenuw is. Dat zicht is niet te vergelijken met normaal functionerend zicht – het heeft wat weg van een matrixbord boven een snelweg – maar kan desalniettemin een zeer waardevolle toevoeging zijn aan het leven van blinden. Binnen het NESTOR project ontwikkelen we een hersenimplantaat wat hen op deze manier een ruwe vorm van zicht teruggeeft. Het uiteindelijke implantaat bevat onder andere systemen voor draadloze dataoverdracht, het aansturen van de elektrodes en draadloze energieoverdracht. Het onderzoek gepresenteerd in dit proefschrift richt zit op de ontwikkeling van dat laatste.

Het eerste gedeelte van het gepresenteerde onderzoek omvat het ontwerp van een systeem voor draadloze energieoverdracht, alsook de ontwikkeling van een prototype. De gepresenteerde methode is breed toepasbaar, maar wordt hier specifiek voor biomedische implantaten gebruikt. Het ontwerpproces is dusdanig dat de totale efficiëntie van het systeem wordt geoptimaliseerd, in plaats van die van de losse onderdelen.

Er zijn enkele bijzonderheden die komen kijken bij de toepassing in medische implantaten. Om schade aan het omliggende weefsel te voorkomen moeten de opgewekte elektromagnetische velden onder bepaalde grenswaarden blijven en moet de opwarming van de geïmplanteerde elektronica binnen de perken blijven. Daarnaast is inductieve draadloze energieoverdracht slechts toegestaan op enkele frequenties. Vanzelfsprekend is de beschikbare ruimte beperkt en zijn de afstand en uitlijning tussen de zend- en ontvangstspoel afhankelijk van externe factoren. Bovendien is het verwachte energieverbruik van het hersenimplantaat relatief hoog in vergelijking met bestaande medische implantaten. Het gepresenteerde prototype draagt het benodigde vermogen betrouwbaar over en presteert beter dan tot nu toe gepresenteerde vergelijkbare systemen.

Miniaturisatie is een voortdurende ontwikkeling in de wereld van medische implantaten. Niet alleen worden bestaande applicaties hierdoor kleiner, wat diverse voordelen met zich meebrengt, maar ontstaan er ook nieuwe toepassingsmogelijkheden. In het geval van een implantaat van enkele millimeters groot, geplaatst op enkele centimeters diepte in het lichaam, suggereert bestaande literatuur dat de efficiëntie van draadloze energieoverdracht optimaal is bij GHz-frequenties. Echter, de efficiëntie zal hoe dan ook erg laag zijn. Daarom is het denkbaar dat het maximaliseren van het ontvangen vermogen een betere aanpak is dan het maximaliseren van efficiëntie. Het is de vraag bij welke frequentie dit gebeurt.

In het tweede deel van dit proefschrift wordt de implementatie van twee analytische modellen gepresenteerd waarmee de elektromagnetische velden in gelaagde media berekend kunnen worden. Het eerste model werkt voor twee lagen, het tweede model voor een arbitrair aantal lagen. Beide modellen geven vele malen sneller resultaten dan bestaande computerprogramma's. Vervolgens zijn deze modellen uitgebreid zodat zij gebruikt kunnen worden voor de berekening van het vermogen wat wordt ontvangen door een ontvanger van enkele millimeters groot, alsook de energie geabsorbeerd in het weefsel. Zo kan bepaald worden bij welke frequentie het ontvangen vermogen gemaximaliseerd wordt, binnen de geldende limieten voor opwarming van het weefsel. Met deze modellen is vastgesteld dat dit gebeurt door gebruik te maken van frequenties beneden de 1 MHz.

Het valideren van medische elektronica dient te gebeuren in een omgeving die de werkelijkheid zo goed mogelijk nabootst. Een dergelijke omgeving kan snel, goedkoop en betrouwbaar worden gecreëerd door gebruik te maken van biomedische fantomen.

In het derde deel van dit proefschrift worden diverse fantoomrecepten gepresenteerd die gebaseerd zijn op gemakkelijk verkrijgbare ingrediënten, zoals water, suiker en zout. Er is slechts standaard keukenapparatuur nodig voor de vervaardiging. De recepten kunnen worden aangepast naar gelang de gebruikte frequentie en het type weefsel dat nagebootst dient te worden. De eigenschappen blijven nagenoeg constant voor ten minste tien dagen.

Dit proefschrift presenteert tevens een zelfgemaakte sensor waarmee de diëlektrische eigenschappen van fantomen gemeten kunnen worden. Deze sensor is minder nauwkeurig dan de commerciële variant, maar wel ordegroottes goedkoper. De nauwkeurigheid is toereikend voor de fabricage van fantomen.

De hierboven omschreven fantomen zijn homogeen. Voor sommige toepassingen kan het wenselijk zijn om inhomogene details toe te voegen. Door middel van 3D-printtechnologie kunnen vaste objecten, zoals tanden en botstructuren, worden toegevoegd. Onderzocht is of er commercieel verkrijgbare materialen bestaan waarmee de eigenschappen van dergelijke objecten realistisch na te bootsen zijn. Eerste resultaten tonen aan dat hier meer onderzoek voor nodig is.

Curriculum Vitae

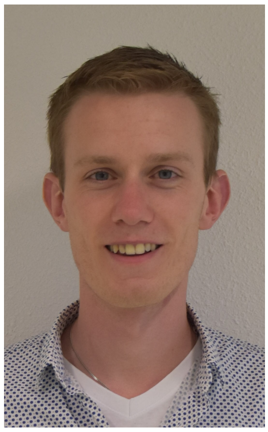

Thomas Petrus Gerardus (Tom) van Nunen was born on the 6th of September, 1990, in Helmond, The Netherlands. After graduating from St. Willibrord Gymnasium in Deurne in 2008, he started studying Electrical Engineering at Eindhoven University of Technology (TU/e), where he received his MSc degree in 2017.

As part of his MSc program, he was an intern at Curtin Institute of Radio Astronomy (CIRA) and International Centre for Radio Astronomy Research (ICRAR) in Perth, Australia, under the supervision of dr. Franz Schlagenhaufer. His graduation research was carried out within the Electrical Engineering Systems group at the TU/e, under the supervision of dr. Ramiro Serra.

In January 2018, Tom started his PhD project in the Electromagnetics group of the department of Electrical Engineering of the TU/e, under the supervision of Huib Visser, Mark Bentum, and Rob Mestrom. The main results of the research are described in this thesis. It is supported by the Dutch Technology Foundation STW, which is part of the Netherlands Organization for Scientific Research (NWO), project 5 of the NESTOR program (P15-42).